UNIVERSITAT DE BARCELONA

DEPARTAMENT DE FÍSICA APLICADA I ÒPTICA
Martí i Franquès 1, 08028 Barcelona

# Study of the laser forward transfer for the preparation of miniaturized biosensors

Martí Duocastella Solà

Memòria presentada per optar al grau de doctor
Barcelona, Març 2010

UNIVERSITAT DE BARCELONA

DEPARTAMENT DE FÍSICA APLICADA I ÒPTICA
Martí i Franquès 1, 08028 Barcelona

# Study of the laser forward transfer for the preparation of miniaturized biosensors

Martí Duocastella Solà

**Programa de Doctorat en Física**

**Director: Pere Serra Coromina**

Memòria presentada per optar al grau de doctor
Barcelona, Març 2010

The present work has been performed in the Departament de Física Aplicada i Òptica of the Universitat de Barcelona, in the frame of a research program funded by Ministerio de Ciencia y Tecnología (Projects No. MAT2004-03741, MAT2007-62357 and CSD2008-00023), and thanks to a scholarship *Formación de personal investigador*, from the same ministry.

Als meus pares i germans, que fan de la paraula *casa* una singularitat exquisida

# Acknowledgments

The present thesis would have not been possible without the invaluable help of colleagues, friends and relatives. Among them, I would like to specially thank:

-Prof. José Luis Morenza, director of the *Grup de Capes Fines i Enginyeria de Superfícies* for the opportunity he gave me to initiate this thesis, for his kind welcome and his wise advices.

-Dr. Pere Serra, my advisor and friend, with whom I have learnt how to become a researcher and have spent a wonderful time. For his patience during the corrections, and his support during the difficult moments.

-Dr. Juan Marcos Fernández, for his technical help in the lab, especially in the resurrection of the computer of the time-resolved imaging setup.

-Dr. Fabien Guillemot, from the *Insitut National de la Santé et de la Recherche Medical* of Bordeaux (France) for the opportunity he offered me to learn how to harvest and deposit living cells.

-Dr. Alberto Piqué, from the *Naval Research Laboratory* (USA) for the opportunity that he gave me to visit his lab and for his kind welcome.

-Jorge Montes and Adrian Patrascioiu, for their help in the performance of my last experiments in Barcelona.

-All the people from the *Departament de Física Aplicada i Òptica of Universitat de Barcelona*, including professors, PhD students, and staff, for their help whenever I needed it.

-My friends from the *Facultat de Fisica*, for the funny lunches and suppers we have shared, and for the amazing time we have spent together (including the victories of F.C. Barcelona).

-My friends from Calaf, with whom I have spent wonderful weekends, and I have laughed until crying.

-Silvia Bengoetxea, for all the magic moments we have shared.

# Contents

# Introduction

The laser invention in 1960 [Maiman 1960] provided the scientists with the *magic* tool with which they had always been dreaming about: lasers could be used to deposit controlled amounts of energy in any desired place. Among the other characteristics of the laser radiation, such as the long coherence length, the low divergence, or the monochromaticity, this possibility to "drop energy on place" made lasers ideal for material processing: irradiating a material with a laser could result in permanent modifications on the surface or in the bulk of the material. This issue has been used in industrial processes such as welding, cutting, marking or drilling. Moreover, optical systems can be used to focus the laser radiation into tiny volumes of some cubic micrometers, allowing the performance of any of the previous operations in the microscopic world, which makes lasers suitable for microfabrication.

The design of miniaturized devices offers several advantages in areas such as electronics [Craighead 2000], chemical analysis [Janasek *et al.* 2006] or medicine [Voldman *et al.* 1999]. This has prompted the development of microfabrication techniques capable of producing these devices. Among them, laser-based techniques are especially adequate when a fast transition between device design and production is required. The most extended laser-based microfabrication technique is laser micromachining [Ion 2005, Cerami *et al.* 2007], based on the design of micropatterns by the selective removal (or ablation) of small parts (3D volumetric pixels, referred to as voxels) of a substrate material. However, it is not the only one: lasers can also be used to fabricate micropatterns by the addition of material [Arnold *et al.* 2007]. In this case, the energy that lasers can deliver in a very controlled way is used to accurately and precisely transfer material from a source to a well-defined location on a substrate.

Laser-induced forward transfer (LIFT) is a laser-based additive technique in which laser pulses are used to deposit material from a donor film to a receptor substrate. This technique is especially interesting due to the possibility that it offers to print droplets of solutions containing functional materials with a high resolution [Arnold *et al.* 2007]. Moreover, it has additional advantages such as the capability to work in air (at atmospheric pressure and room temperature), the fact that it is a non-contact technique that avoids contamination problems, and the possibility to combine it with laser micromachining.

At the beginning of this thesis work, the feasibility of LIFT to print different complex materials had already been tested. In addition, several studies had been reported about the effects that different parameters have on the printed solutions [Wu *et al* 2003, Serra *et al.* 2004a, Colina *et al.* 2006]. However, not all the LIFT parameters had been systematically studied, neither the correlations found between the parameters variation and the morphology of the deposits had been analyzed in depth. And, which is most important, the mechanism of the LIFT printing process still remained unknown.

The goal of this thesis is to perform a complete study of the LIFT of liquid solutions in order to achieve a better understanding of this technique and to find the optimum printing conditions. Such study comprises the analysis of the role that some of the most important experimental parameters have on the printed droplets, as well as the analysis of the mechanisms involved in the ejection and deposition of material through LIFT. This is accomplished by means of both the morphological characterization of the printed droplets and the time-resolved imaging of the LIFT process. The present work has provided a complete picture of the LIFT process: the experimental conditions adequate for droplet printing have been set up, and the mechanisms responsible for the generation of droplets have been unveiled. Moreover, it has also been found that the preparation of the liquid film in thin form is the major problem that the technique faces. This last aspect has motivated the research of a new technique capable of dispensing with the preparation of the liquid film. This novel technique has been successfully developed and tested in this thesis work.

The thesis is divided into 5 chapters. A further description of each chapter is described next:

Chapter 1 begins with an outline of the different microfabrication techniques, followed by a description of some direct-writing techniques. Next, the chapter is focused on LIFT, presenting a summary of the historical development of the technique, and then moving to the earliest achievements obtained with it. After describing some drawbacks of the LIFT using solid films, the state of the art of the technique for depositing liquids is reported.

Chapter 2 describes the experimental setup used to carry out the LIFT experiments. The different materials employed in the experiments, and the characterization techniques used to determine the properties of the deposited specimens are also reported in this chapter.

Chapter 3 presents an investigation of the role that different experimental parameters play on the properties of the printed material. This allows optimizing the conditions of the deposition process, although it also evidences that other characterization techniques are necessary in order to achieve a further understanding of the LIFT mechanisms.

Chapter 4 is focused on the time-resolved imaging study of the evolution of liquid transfer and deposition through LIFT. Acquiring images of these processes at different conditions, and correlating them with the printed material at those conditions, provides a complete description of the dynamics involved in the material ejection, transport and deposition. This has allowed unveiling for the first time the mechanisms involved in the LIFT printing process.

Chapter 5 presents the development of a new and original laser-printing technique, which overcomes the main problem associated with LIFT: the preparation of the liquid film. The development of this novel technique is presented in this chapter, as well as the first experiments carried out with it,

which involve both the printing of arrays as well as the feasibility test of the technique for biomolecule printing.

# Chapter 1

# Overview of the laser-induced forward transfer technique

In this chapter, a general overview of different direct-writing microfabrication techniques is presented. Special attention is given to LIFT, since this technique comprises the main topic of this thesis. The chapter is divided into three different sections. The first one concerns the different approaches used to carry out microfabrication. The second one is focused on direct-writing techniques, especially on ink-jet printing. Finally, the LIFT technique is presented. This last section begins with a presentation of LIFT historical origins, then moves to the early achievements of the technique, and finally presents the last results which form the most recent state of the art.

## 1.1 Microfabrication

The technological revolution of the last decades of the twentieth century would not have been possible without techniques adequate for the fabrication of miniaturized electronic devices. The microelectronics industry would not have existed without micropatterning techniques capable of producing a large amount of active and passive elements (such as transistors, resistors, capacitors, or even power sources), and ensemble them in small and compact devices.

The challenge for the twenty first century is either to develop new techniques or to adapt those from the electronics industry, so that micropatterning of more sensitive functional materials can be achieved. This could have a positive impact in several areas. For example, it could play an important role in the manufacturing of organic electronics due to the flexibility and the potential for

low production costs that it offers [Loo *et al.* 2008]. It could also set a new era in tissue engineering applications, allowing the construction of artificial organs combining the deposition of cells and biomaterials, in the so-called organ printing [Boland *et al.* 2006]. And, among others, it could allow the fabrication of miniaturized devices in areas like biosensing and biochemical analysis, in which miniaturization presents advantages such as multianalyte detection, minimization of sample volumes or lab-on-a-chip integration [Janasek *et al.* 2006].

The use of these sensitive materials imposes certain restrictions on the fabrication techniques. Apart from the high fabrication speed desired in any process and the high accuracy and resolution demanded for microfabrication, these techniques must assure the functionality of the transferred material. This is especially relevant for biological samples due to their fragility. Moreover, in this case contamination problems must also be considered since they can easily affect the specimens.

Two different approaches can be considered concerning the types of microfabrication techniques which accomplish the previous requirements. The first one involves the so-called *pattern-transfer techniques* [Nagel 2002]. In this set of techniques, the pattern is generated onto the substrate as a whole: all its constituent parts are transferred at the same time. In pattern-transfer techniques, which most representative technologies are photolithography and microcontact printing, a mask or mold is previously generated from the pattern design, and the pattern is directly transferred from this element. This kind of techniques is adequate for large-scale manufacturing, since they allow the parallel production of identical units. Moreover, advances in the lithographic technologies, such as the use of extreme ultraviolet light sources, allow achieving very high resolutions, even in the nanometer range [Bratton *et al.* 2006]. However, when a fast transition between design and production is required, which usually occurs in the initial stages of the product development, the mask/mold fabrication is expensive and time-consuming. In addition, pattern-

transfer techniques are complex and generally restrictive concerning the substrates that can be used (they are usually limited to the use of rigid flat substrates). For rapid prototyping applications and for the cases in which a high versatility is required, a different approach is convenient: d*irect-writing techniques* (DW). DW techniques, as its name indicates, directly transfer the material to the substrate without the use of masks or molds. They are serial in nature, that is, the different parts of the pattern are transferred one after each other in a sequential way. This provides them with a higher flexibility than pattern-transfer techniques. Moreover, the reduction of processing steps, for instance the preparation of masks/molds, makes them cheaper and more affordable even in the case in which low product units are required.

## 1.2 Direct-writing techniques

Several direct-writing techniques are suitable for the deposition of sensitive materials. These can be very different from each other in nature, and include ink-jet printing, dip-pen lithography, microspotting, and laser-based techniques, among others. A description of all these DW techniques is out of the scope of this work, but more information can be found in Hon *et al.* 2008. However, due to the relevance of ink-jet printing, being the most extended DW technique [Sirringhaus *et al.* 2003], further details of this technology are provided next.

Ink-jet printing consists in the deposition of ink droplets generated after the breakup of a jet by forcing the ink through a small nozzle. There are basically two ink-jet printing technologies, termed continuous inkjet (CIJ) and drop-on-demand (DOD). Schematic illustrations of the principle of operation of both methods are presented in Fig. 1.1. In CIJ, the jet of ink ejected from the nozzle breaks up into several small droplets due to surface tension effects (the so-called Plateau-Rayleigh instability). Then, the droplets pass through a controllable electrical field which induces them a charge that depends on the intensity of the applied field. A steady electric field deflects then the droplets depending on the magnitude of their induced charge: uncharged (and thus undeflected) droplets

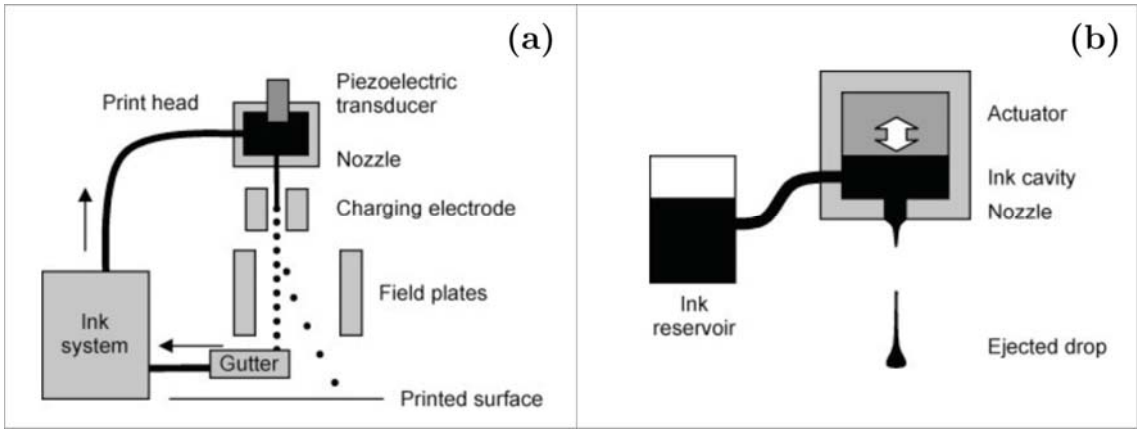


**Fig. 1.1.** Scheme of the principle of operation of: (a) a continuous inkjet printer; (b) a drop on demand printer. From Hon *et al.* 2008.

are collected in a gutter and recycled, while charged droplets arrive to the substrate forming the printed pixels. Although CIJ can produce droplets with a size of typically 2 times the diameter of the nozzle, and at a high repetition rate, it presents some drawbacks which limit its use: the technology required to fabricate the CIJ setup is complicated and expensive, only certain inks with very specific rheological properties are suitable for this technique, and large volumes of ink are necessary [Calvert 2001].

DOD has clearly surpassed CIJ in terms of reliability, price and performances in general. In this method, the ink is kept in a reservoir, and the sudden increase of the pressure inside the reservoir forces the ink through the nozzle. Then, a jet is ejected and breaks into a single droplet. Two different techniques share the DOD approach, depending on the strategy used to generate the pressure increase: thermal inkjet, in which heating a resistance inside the reservoir produces a vapor bubble; and piezoelectric inkjet, which uses a piezoelectric device to generate a pressure wave which ejects the jet. With DOD inkjet printers, various functional materials have been successfully deposited [Sirringhaus *et al.* 2003]. The resolution that is routinely achieved with this technique is about 75 µm [Barron *et al.* 2005a], although under laboratory conditions droplets as small as 5 µm have been obtained [Park *et al.* 2007]. However, this technique is not free from drawbacks. Clogging problems can

easily occur by dried ink in the nozzle, and the rheological properties of the inks are a crucial parameter: the viscosity must be low enough to allow the channel to be refilled in about 100 µs, and the ink surface tension must be high enough to produce the desired jet breakup and, after that, to hold the ink in the nozzle without dripping [Calvert 2001].

All these inconveniences have prompted the research of alternatives to ink-jet printing. One of them is laser-induced forward transfer (LIFT), a direct-write addition process which has recently been demonstrated to have a large potential for printing complex materials [Arnold *et al.* 2007].

## 1.3 Laser-induced forward transfer

The LIFT technique is a laser deposition method which makes use of laser pulses to transfer tiny amounts of material from a donor film (previously deposited on a support transparent to the laser radiation, in the following the donor substrate) to a receptor substrate, in a configuration like that depicted in Fig. 1.2: the laser pulses are focused on the donor film through the donor substrate. Therefore, under the action of the laser pulse a small fraction of the donor film is forward transferred to the receptor substrate, which is in close proximity to the donor substrate. This leads to the deposition of a voxel. Through the interdependent translation of both donor and receptor substrates, micropatterns of any two dimensional geometry can be prepared, at speeds typically limited by the speed of the translation stages. This technique does not require special vacuum or cleanroom equipment, but is usually performed under standard laboratory conditions.

The first report about this technique was a patent filled in 1967 [Brisbane *et al.* 1971], and the first publication dates from 1970 [Levene *et al.* 1970]. In that work, a pulsed laser was used to deposit different dried inks to a glass substrate, with the purpose to develop a laser-based printing process for the graphic industry. However, these first two reports fall into oblivion, and it was not until

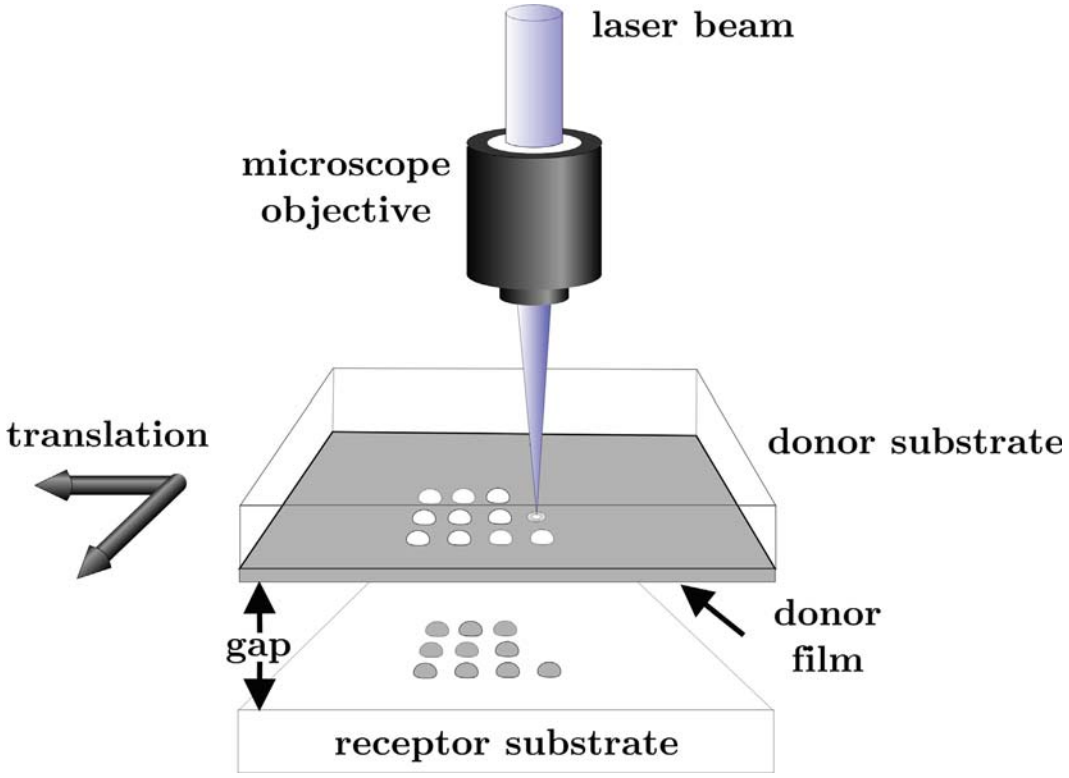


**Fig. 1.2.** Scheme of the principle of operation of the LIFT technique.

1986 when Bohandy's group [Bohandy *et al.* 1986] used the same method to deposit copper metal patterns onto fused silica substrates. They performed the operation under vacuum conditions, and called it laser-induced forward transfer (LIFT). Two years later, the same group demonstrated that the process could be carried out under atmospheric conditions [Bohandy *et al.* 1988].

### 1.3.1 Laser-induced forward transfer of solid films

In the years following the publications of Bohandy *et al.*, LIFT gained acceptance as a technique for depositing inorganic materials, mainly metals, from solid donor films. LIFT was used to successfully transfer gold [Baseman *et al.*], aluminium [Schultze *et al.* 1991], titanium [Kántor *et al.* 1992], tungsten [Kántor *et al.* 1994, 1995a, 1995b], nickel [Sano *et al.* 2002] and germanium/selenium thin film structures [Tóth *et al.* 1993]. Those works were successfully performed with lasers of a wide variety of wavelengths, ranging from ultraviolet to infrared. It should also be pointed out that most of the lasers

employed had a pulse duration of several nanoseconds (except those used in the transfer of tungsten features, which were microsecond lasers). More recently, LIFT with ultrashort laser pulses (sub-picosecond and femtosecond lasers) have also been applied to diverse metals, such as chromium [Zergioti *et al.* 1998, Zergioti *et al.* 2003, Banks *et al.* 2006], or platinum [Papakonstantinou *et al.* 1999].

Despite most of the reported works about LIFT were focused on metals, solid donor films of oxides such as $Al_2O_3$ [Greer *et al.* 1988], $In_2O_3$ [Zergioti *et al.* 1998 and 2002], $V_2O_5$ [Chakraborty *et al.* 2007], or the high-temperature superconductors YBaCuO and BiSrCaCuO [Fogarassy *et al.* 1989], were also used for deposition through this technique. However, it is worth mentioning that, especially in the last case, the quality of the transferred material was not as good as that of materials deposited by traditional film growth techniques.

Concerning the mechanisms involved in the LIFT process of solid donor films, it should be noted that there exist different possible scenarios depending on the incident laser fluence. Although most of the previous works produce melting and vaporization of the irradiated area, other situations can occur (Fig. 1.3), which are next summarized:

1- At low laser fluences (which produce a temperature increase in the material interface below its melting point), transfer in the solid state is possible [Kántor *et al.* 1994]. Two different mechanisms have been proposed to account for this situation [Veiko *et al.* 2006]. The first one relies on the creation of a vapor pocket in the film-support interface which exerts a pressure on the solid film. When the force corresponding to this pressure overcomes the fracture limit of the film, a portion of the film is released towards the receptor (Fig. 1.3a). Such vapor pocket would be created by desorption of gases absorbed by the donor surface defects. The second mechanism consists in the thermal radial expansion after laser heating, which creates a radial compression force exerted by its surroundings. This causes a transversal tension in the film (normal to the film surface) which

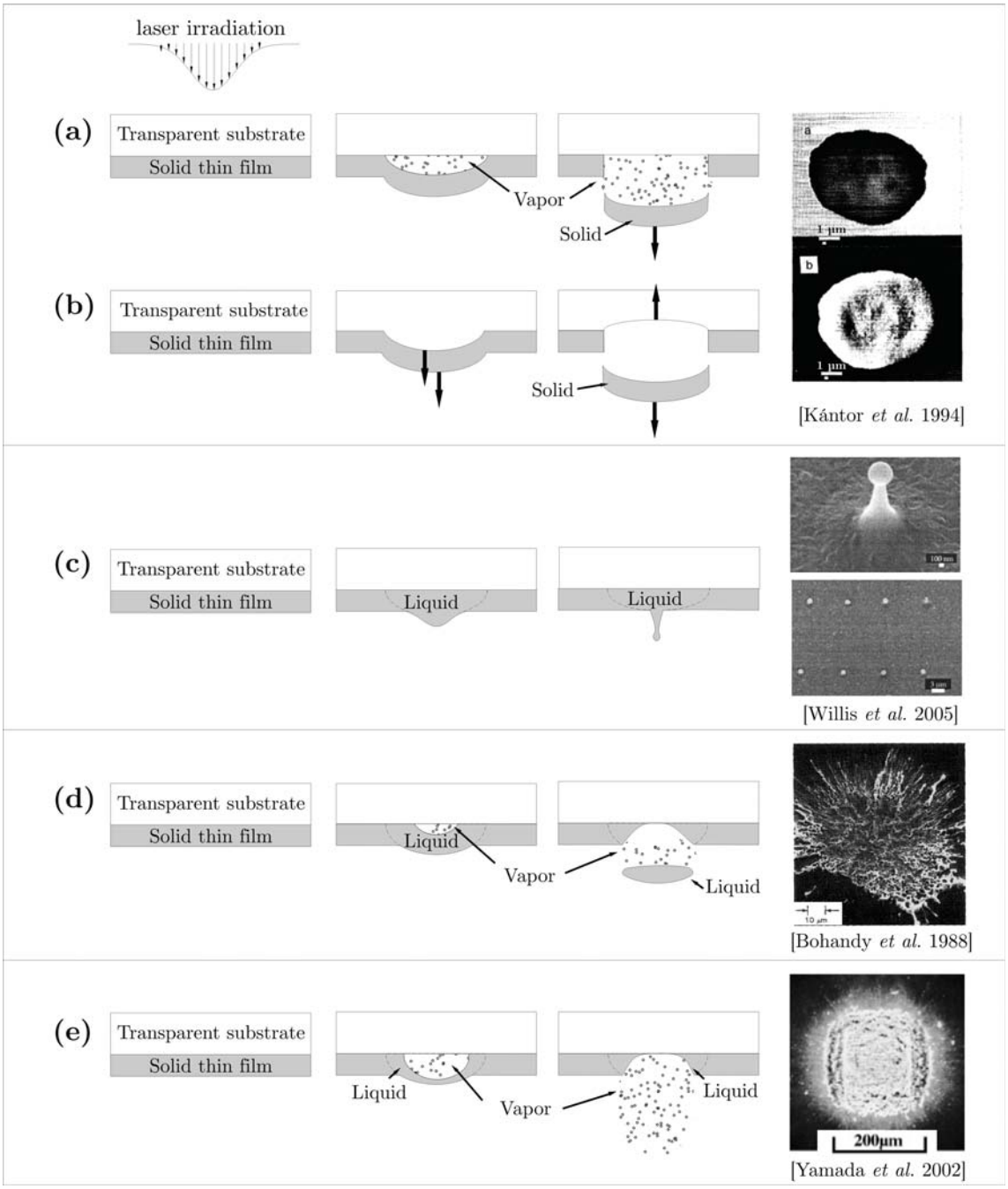


**Fig. 1.3.** Scheme of the possible transfer mechanisms in the LIFT of solids, depending on the laser fluence. The images on the right of each drawing correspond to examples of material deposited through the described mechanism. The upper images for Kántor *et al.* 1994 and Willis *et al.* 2005 correspond to the donor substrate.

leads to film exfoliation (Fig. 1.3b). Although the portion of the irradiated material can be transferred as a whole in both mechanisms, with well-defined edges and independent of the donor film-receptor substrate separation, the

deposited features suffer poor adhesion on the receptor [Veiko *et al.* 2006], thus limiting its applicability.

2- At fluences which lead to melting of the donor film, but low enough to prevent vaporization of material in the film-support interface, a different mechanism occurs (Fig. 1.3c). This was first reported by Willis and coworkers [Willis *et al.* 2005], and it is based on the melting of the film material in the interface due to the laser radiation. Then, due to a different density between the solid phase and the liquid phase, being less dense the last phase, the material expands as it melts. The expansion is constrained by the surrounding material during the melt through process, until the melt front reaches the free surface. At this moment the melt front is no longer constrained in the interface, allowing the formation of a protrusion from that point which finally results in a droplet. This mechanism leads to the deposition of well-defined hemispherical droplets [Yang *et al.* 2006, Narazaki *et al.* 2008], which dimensions can be smaller than the laser irradiated area: droplets as small as 300 nm have been deposited in this way [Banks *et al.* 2006].

3- At fluences which lead to melting and also vaporization of the interface material, the mechanism proposed by Bohandy *et al.* in 1986 occurs (Fig. 1.3d). According to this, the laser pulse heats the film-support interface, generating a molten front which propagates towards the film free surface, and attains it. When the material at the interface reaches the boiling temperature, this leads to the formation of a high-pressure vapor pocket which propels the molten material towards the receptor substrate. This explanation is supported by evidence of molten and resolidified material on the deposited features (Fig. 1.3d) [Bohandy *et al.* 1988, Adrian *et al.*, 1987, Baseman *et al.* 1990]. This mechanism is considered the responsible for feature deposition in most of the works reported on the LIFT of solids.

4- At high enough laser fluences, the irradiated material can be completely vaporized (Fig. 1.3e). The molten material reaches its boiling temperature,

and thus the material is released in the form of a vapor, as it was analyzed through time-resolved imaging by Sano *et al.* 2002 and Nakata *et al.* 2004. The violence of this process results in debris and parasite molten droplets on the receptor. Moreover, the vapor is ejected with a certain angular distribution, which forces situating the receptor substrate in close contact with the donor film in order to reduce the material dispersion.

Although the LIFT of solids has been successfully applied in some instances, like the reparation of chromium photolithographic masks, several shortcomings limit the applicability of this process [Chrisey *et al.* 2002]: for example, the preparation of the solid films requires vacuum deposition techniques and other expensive processes. But most important, since the transferred material suffers phase changes (melting or vaporization, and the posterior recondensation on the receptor), its properties can be seriously affected, as it occurs in the case of most metals, which can be easily oxidized. It is especially this latter issue, the phase transformation of the material undergoing laser transfer, which makes the mechanisms involved in the LIFT of solids unfeasible for depositing complex and more sensitive materials. For these cases, two different approaches can be carried out, as it is detailed next.

### 1.3.2 Laser-induced forward transfer of complex materials

The first group to demonstrate the feasibility of the LIFT technique for depositing complex materials was from the Naval Research Laboratory (NRL) in Washington D.C. In order to solve the problems related to vaporization and melting in the classical LIFT of solids, researches from NRL used a donor film which consisted in a mixture of powder of the material to be deposited with a solid phase organic binder (termed matrix). Then, the mixture was applied as a uniform coating on the support, forming a dry donor film of around 5 µm thick [Piqué *et al.* 1999]. In this system, most of the laser radiation is pretended to be absorbed by the organic binder, which decomposes resulting in ejection of the powder towards the receptor substrate. Since the laser fluences in this process

are lower than the ablation threshold of the powder materials, it is possible to avoid any material phase transformation. Thus, the functionality of the transferred specimens is preserved. This technique, although it is a variant of the LIFT of solids, in the literature is referred to as matrix-assisted pulsed laser evaporation direct-write (MAPLE-DW[1]), as researches from NRL initially thought of it as a modification of MAPLE [Chrisey *et al.* 2003], a variation of pulsed laser deposition (PLD) which used frozen targets of organic materials dissolved in a volatile solvent.

Different inorganic compounds have been successfully transferred with this technique, such as $BaTiO_3$ or NiCr [Chrisey *et al.* 2000] to fabricate circuit elements for microelectronics; $Y_2O_3$:Eu and $Zn_2SiO_4$:Mn [Fitz-Gerald *et al.* 2000] to produce phosphor screens; $MnO_2$, and $LiCoO_2$ [Wartena *et al.* 2004] to develop miniature sensors and micro-batteries; or $TiO_2$ [Kim *et al.* 2004, 2006] to fabricate dye-sensitized solar cells. In addition, inorganic/organic materials, like epoxy resin with carbon black and silver [Modi *et al.* 2001] or carbon/ polyepichlorohydrin [Piqué *et al.* 2003] have also been deposited for the fabrication of polymer thick film resistors and chemical sensors, respectively. However, the wide range of materials that can be employed with this approach is eclipsed by some serious drawbacks. The adhesion of the transferred material tends to be poor, and the organic binder remains after the transfer, thus high temperature calcination steps are necessary to remove the binder and achieve some degree of densification. This also makes the deposition of even more sensitive materials, such as biologicals, inadequate for this approach.

The same group in NRL tried to solve this last problem moving away from phase solid binder materials towards multiphase and multicomponent liquid or gel systems. In such approach, the material to be deposited is suspended or dissolved in a liquid to form an ink or a paste, and then spread on the donor substrate. Since the donor film is already liquid, there is no need to melt the film. Moreover, the shear forces required to dislodge and release a portion of the

[1] The name MAPLE-DW has sometimes been inappropriately employed to refer to any variation of LIFT, even in the case in which no matrix was employed.

donor film are drastically reduced compared to the other cases. Actually, in this approach the laser radiation is absorbed in a small fraction of the ink or paste, generating a vapor pocket which acts as a propeller, impelling an unaffected fraction of the donor film towards the receptor in a gentle way. This has provided a qualitative step forward in the LIFT technique since, finally, complex fragile materials can be successfully deposited. This includes solutions which contain biomolecules or even living cells [Wu *et al.* 2001, Ringeisen *et al.* 2002a, Chrisey *et al.* 2003], or also electrochemically sensitive materials [Arnold *et al.* 2004a]. It is worth mentioning that this approach, usually named LIFT of liquids or in some instances laser direct write (LDW), presents a problem: most of the solutions used are composed of water based solvents transparent to a wide range of laser wavelengths, for instance, the second and third harmonics of Nd:YAG lasers. This has been solved through the placement of a layer between the donor liquid film and its substrate. In this case, the intermediate layer acts as an absorbing layer, thus providing the thrust for ejection of a fraction of the liquid towards the receptor substrate.

The first reports of LIFT using an absorbing layer were performed with solid donor films by Tolbert and coworkers [Tolbert *et al.* 1993a, 1993b]. In those works, in which the absorbing layer is referred to as the dynamic release layer (DRL), the multilayer structure (in solid phase) was intended for high speed laser color printing applications, and was called laser ablation transfer (LAT). Actually, the company *Latran Technologies* has been commercializing printers for proofing based on this technique. The role of the DRL applied to solid donor films was to preserve the transferred material to the direct exposure of the laser radiation, and to decrease the ablation thresholds. Although in the last years several works have appeared using the DRL for solid donor films [Fardel *et al.* 2007, Ko *et al.* 2008, Kaur *et al.* 2009, Kattamis *et al.* 2009], it is in the printing of biological solutions where the absorbing layer has been extensively used. In that case, it has become a requirement due to the transparency of those solutions to most of the common laser wavelengths. The materials that have been used as absorbing layers for printing biologicals are diverse, from metals

such as titanium [Fernandez-Pradas *et al.* 2004, Barron *et al.* 2004b], gold [Barron *et al.* 2004a] or silver [Hopp *et al.* 2004, 2005], to polymers [Doraiswamy *et al.* 2006, Kattamis *et al.* 2007]. In the latter, two different approaches have been intended: to completely vaporize the polymer in the irradiated area [Doraiswamy *et al.* 2006], or to elastically deform it avoiding ablation [Kattamis *et al.* 2007]. It should be pointed out that this modification of the LIFT of liquids has received different names, such as biological laser printing (BioLP) [Barron *et al.* 2004a] or absorbing film assisted LIFT (AFA-LIFT) [Hopp *et al.* 2005a].

In the next section, a summary of the most significant achievements obtained with the LIFT of liquids (mainly using absorbing layers) is presented.

### 1.3.3 State of the art in the LIFT of liquids

The studies of the LIFT of liquids have been mainly devoted to the demonstration of the feasibility of the technique to transfer functional materials without damaging their desired properties, and also to the analysis of the effects that different experimental parameters have on the morphology of the deposited material. Some time-resolved imaging studies have also been carried out. However, in all cases the obtained results are partial and do not allow unveiling the mechanism that leads to the deposition of well-defined droplets.

Concerning the works focused on the capacity of the technique for printing functional materials, they basically consist in presenting the LIFT deposited features of different functional materials, and then analyzing whether the properties suitable for a specific application were preserved or not. In this way, ink or pastes of electrochemical materials have been deposited for the fabrication of ultracapacitors [Arnold *et al.* 2003], batteries [Arnold *et al.* 2004a, 2004b, Piqué *et al.* 2004, Kim *et al.* 2007], chemical sensors [Boutopoulos *et al.* 2008a], and electrodes for organic thin-film transistors [Kim *et al.* 2009, 2010], and the respective capacitance, energy density, and power output of these devices have been measured, demonstrating the preservation of the materials

electrochemical activity and structural integrity. A summary of the most representative LIFT works using non-biological inks or pastes is presented in Table 1.1. Biological solutions have also been deposited for biosensors or tissue engineering applications. In these cases, the biological specimens are dissolved in a solution which provides a suitable environment that grants their chemical stability, and after transfer the solvent is evaporated, leaving the biological specimens lying onto the receptor substrate (usually special substrates, such as chemically-treated glass slides, porous membranes, or gels, which assure a good adhesion of the specimens). Different kinds of biomolecules have been deposited through LIFT, and after submitting them to hybridization or immunofluorescence assays, the preservation of their activity has been demonstrated. Actually, quantitative analyses have revealed that the fraction of biomolecules damaged by the action of the laser pulse is never high [Colina *et al.* 2005, Dinca *et al.* 2008a]. In fact, even a large variety of cells [Ringeisen *et al.* 2006] and the living microorganism Trichoderma conidia [Hopp *et al.* 2004] have been transferred without harm, since they successfully reproduced after deposition. A summary of the most representative LIFT works using biological solutions is presented in Table 1.2.

The studies of the dependence of the properties of the deposited material on the different experimental parameters initially corresponded to reports of the effects of parameters like the laser pulse energy or fluence on the transferred features. In this way, it was found that under certain energy conditions, the transferred material consisted in well defined droplets [Wu *et al.* 2003, Serra *et al.* 2004a], which diameter and volume increased when increasing the laser fluence [Wu *et al.* 2003, Barron *et al.* 2004a, Serra *et al.* 2004a]. However, the first quantification of the amount of deposited material at different laser pulse energies was not reported until 2006 [Colina *et al.* 2006]. A further analysis of that work must be carried out, since it establishes the basis of the study reported in chapter 3. In that work, not only the laser pulse energy effects on the deposited material were analyzed, but also the focusing conditions. Different arrays were prepared, each one at a certain focusing condition, varying the laser

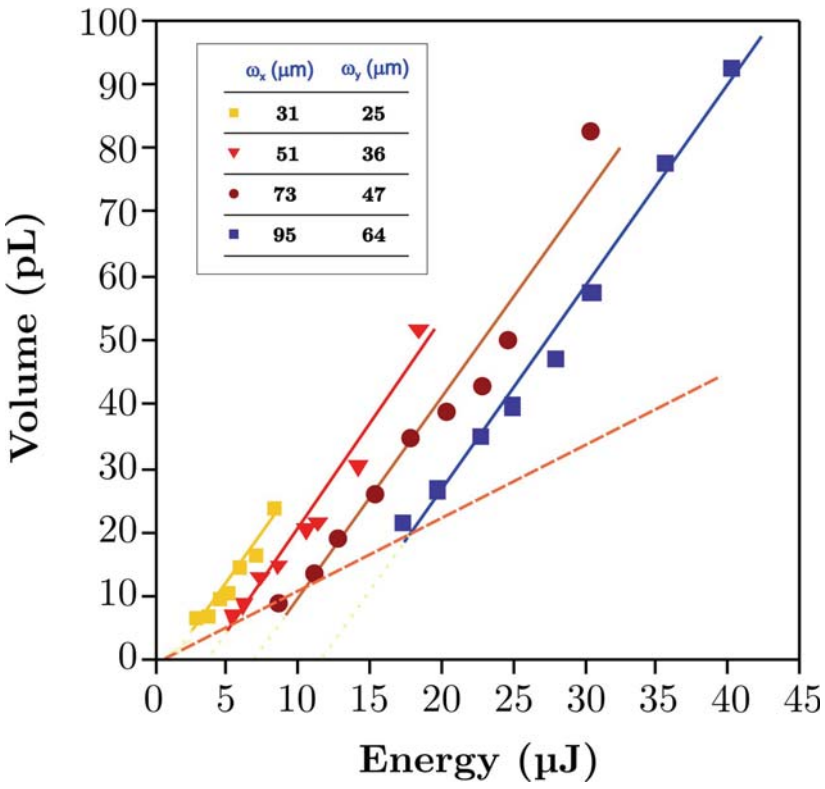


**Fig. 1.4.** Plot of the volume of droplets printed at different focusing conditions versus the laser pulse energy that produced its deposition. The straight lines correspond to linear fits. The dashed line is also a linear fit which shows that $E_{min}$ increases quite linearly when increasing the beam size. From Colina *et al.* 2006.

pulse energy from row to row. Droplets of different sizes were printed, which diameter increased for increasing laser pulse energy and beam size (elliptical Gaussian beam). The volume of the deposited droplets of each array was then measured and plotted versus the laser pulse energy (Fig. 1.4). It was found that for each focusing condition a certain minimum energy ($E_{min}$) should be surpassed in order to deposit a droplet. For energies higher than $E_{min}$, the volume increased linearly with the energy, and the values could be fitted to the expression:

$$V = K(E - E_0) \tag{1.1}$$

where $V$ is the volume of the transferred droplet, $E$ the laser pulse energy, and $K$ and $E_0$ the fitting parameters for each focusing condition. The $K$ parameter was interpreted as the process efficiency, and it presented a similar value in all cases. The $E_0$ parameter required a further analysis, as it is presented next.

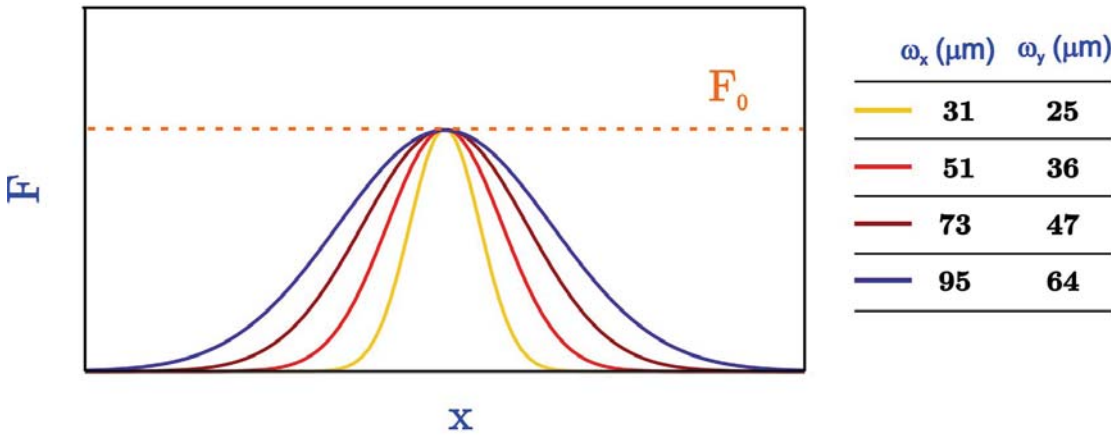


**Fig. 1.5.** Plot of the Gaussian profiles corresponding to the energy $E_0$ for the different focusing conditions described in Fig. 1.4.

The energy density distribution *F(x,y)* of an elliptical laser Gaussian beam with energy $E_0$ is given by:

$$F(x,y) = \frac{2E_0}{\pi\omega_x\omega_y} e^{-2\left(\frac{x^2}{\omega_x^2}+\frac{y^2}{\omega_y^2}\right)} \tag{1.2}$$

where $\omega_x$ and $\omega_y$ are the beam major and minor radii, and $x$ and $y$ are the Cartesian coordinates along the major an minor axis, respectively. Plotting *F(x,y)* versus one of the Cartesian coordinates (Fig. 1.5) for the different focusing conditions, reveals that all the Gaussian beams with energy $E_0$ have the same energy density peak $F_0$. In fact, the relationship between $F_0$ and $E_0$ can be written as:

$$E_0 = \frac{\pi\omega_x\omega_y F_0}{2} \rightarrow F_0 = \frac{2E_0}{\pi\omega_x\omega_y} \tag{1.3}$$

Therefore, the energy density peak $F_0$ is actually an energy density threshold. It turns out that $F_0$ is a necessary but not sufficient condition for transfer to occur: the peak of *F(x,y)* of the incoming laser pulse should surpass $F_0$ in order to produce a perturbation in the liquid film (generation of a vapor bubble), but a droplet would only be deposited if the total energy of the pulse reached the value $E_{min}$. This is illustrated in Fig. 1.6. In the same work, a model was

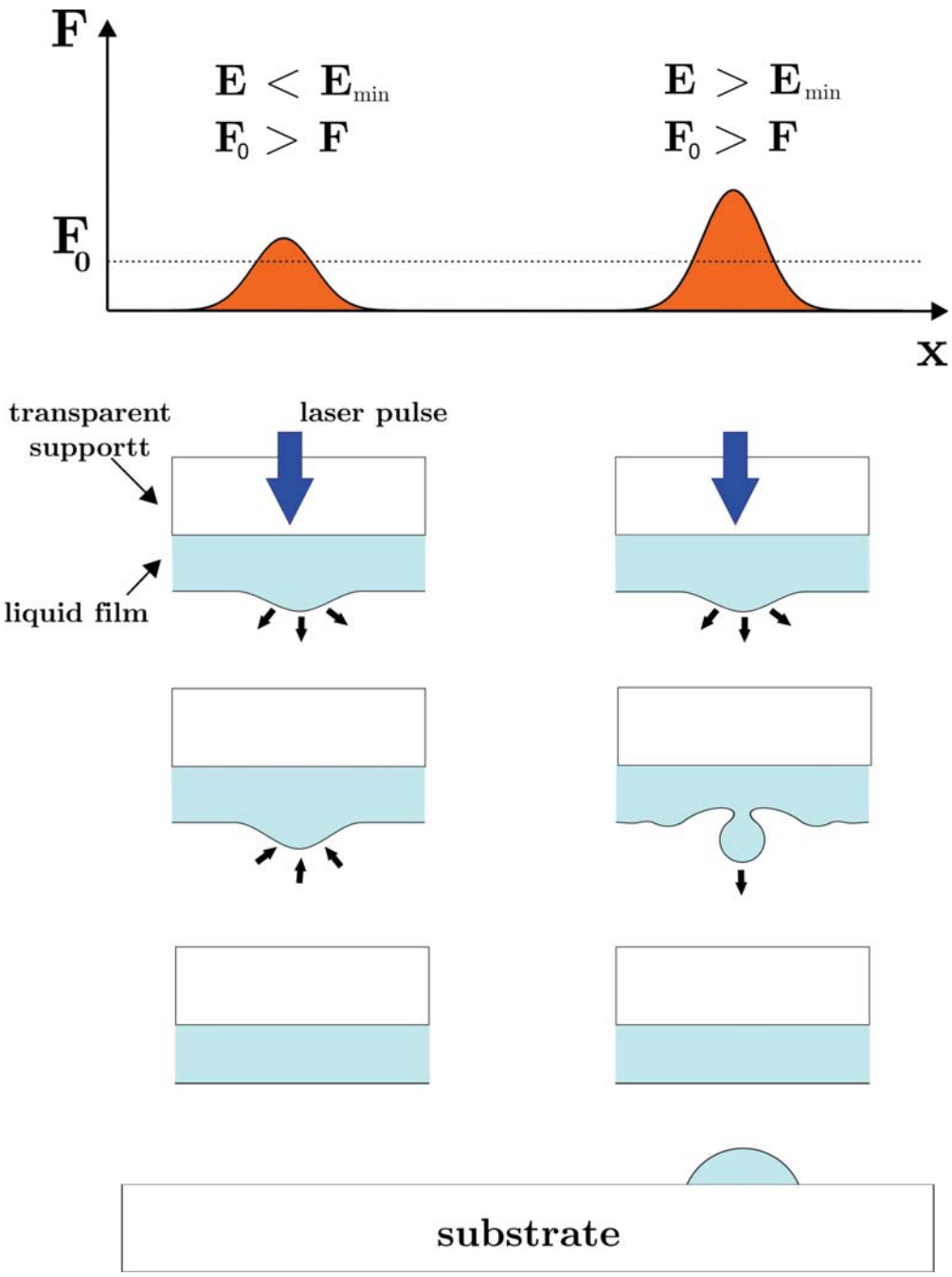


**Fig. 1.6.** Scheme of the liquid ejection mechanism through LIFT at different conditions.

successfully proposed which related the volume of the deposited material to dimensional parameters determined by $F_0$. According to it, the deposited volume corresponds to a cylinder which base is the zone in which the local energy density ($F$) surpasses $F_0$ and its height is the liquid film thickness (Fig. 1.7).

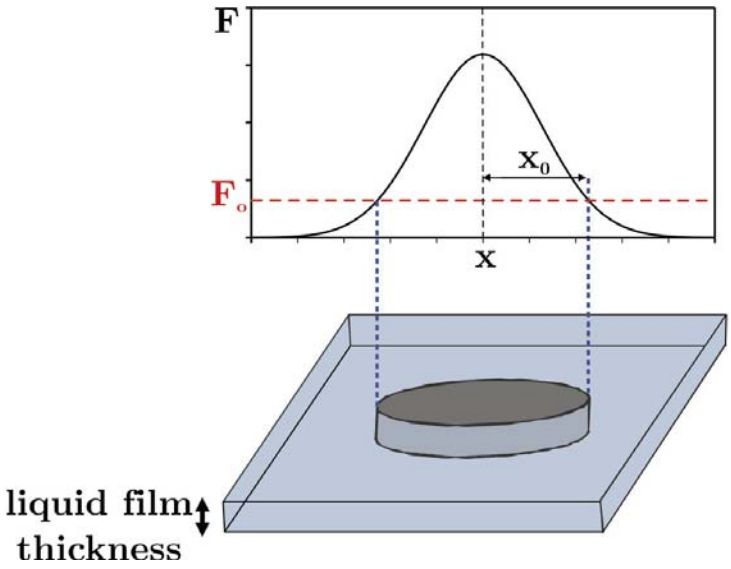


**Fig. 1.7.** Scheme of the cylinder model proposed to describe the LIFT process

Other especially relevant works which analyzed the effects of other experimental parameters on the deposited material are those of Wu *et al.* 2003 and Dinca *et al.* 2008b. The first one reported by the first time that varying the donor film-receptor substrate separation did not result in a significant variation of the deposited droplet diameter, contrary to the LIFT of solids. The work by Dinca *et al.* 2008b used different protein containing solutions (Biotin, Avidin and Titin) to study the effects on the printed material of parameters like the laser pulse energy and length, the donor film thickness and the receptor wettability and liquid viscosity. The study revealed once more the behavior previously found: the deposited droplet diameter increased when increasing the laser pulse energy. Concerning the laser pulse length, the printed material using nanosecond and femtosecond pulses presented very similar characteristics. The other parameters analyzed allowed finding that the thinner the liquid film, the smaller the diameter of the deposited droplet, and that viscous solutions and hydrophobic substrates result in smaller droplets. However, a complete interpretation of those results was not reported.

Finally, a last remark is required concerning the works in which time-resolved imaging was used to study the transfer dynamics in the LIFT of liquids. The

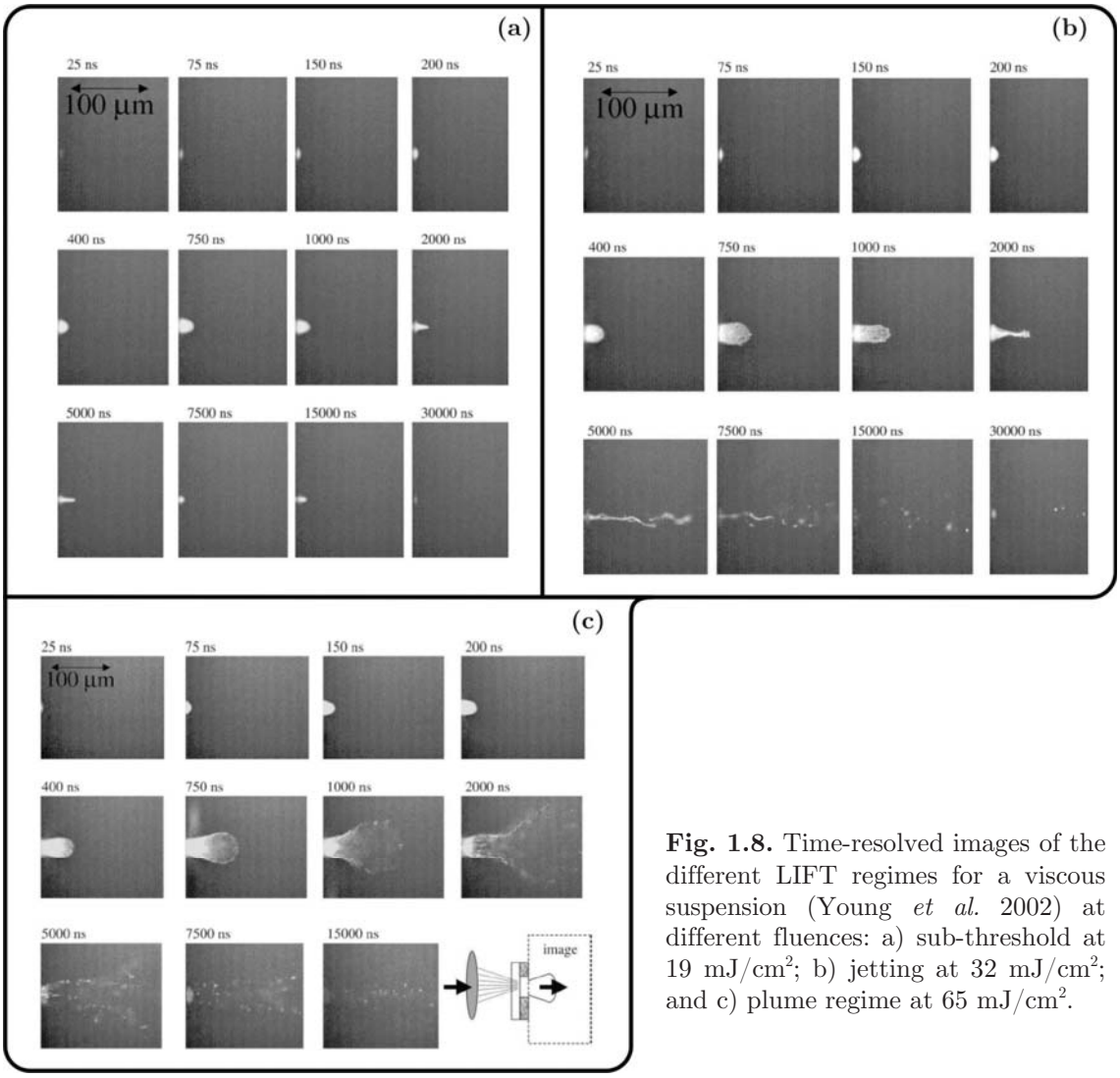


**Fig. 1.8.** Time-resolved images of the different LIFT regimes for a viscous suspension (Young *et al.* 2002) at different fluences: a) sub-threshold at 19 mJ/cm$^2$; b) jetting at 32 mJ/cm$^2$; and c) plume regime at 65 mJ/cm$^2$.

first two works in which such study was reported were those of Young and coworkers [Young *et al.* 2001, 2002]. In those works, a viscous nanopodwer suspension (barium titanate powders solved in α-terpineol) was irradiated with a nanosecond laser beam and time-resolved images of the transfer process were acquired. It was observed that depending on the laser fluences used three different regimes could be distinguished (Fig. 1.8): at low fluences, the so-called sub-threshold regime occurred, in which a protrusion was generated but it was not energetic enough to detach any material, and it collapsed back. At intermediate fluences, the jetting regime took place, characterized by the development of an irregular and turbulent jet which broke up into multiple parts when it had travelled a very short length. Finally, at higher fluences a protrusion was also generated, but in this occasion it burst producing the

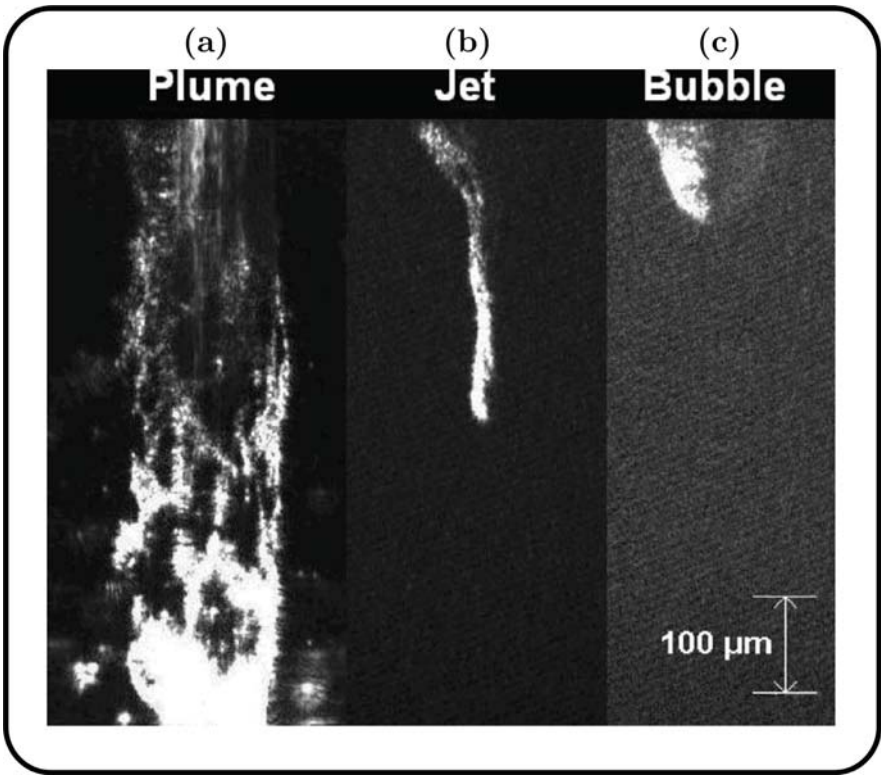


**Fig. 1.9.** Images of the LIFT process of a viscous ink at different laser fluences: a) plume regime, b) jet regime, and c) sub-threshold regime, reffered to as bubble regime( Lewis *et al.* 2006).

violent ejection of material (a process that the authors inappropiately called plume regime).

However, none of the previous regimes accounted for the deposition of well-defined droplets: the sub-threshold regime was characterized by the lack of deposited material; the jetting regime resulted in multiple and disperse droplets; and only complete splashing was observed in the plume regime. Therefore, that work did not clarify which was the mechanism which generates the well-defined droplets found in the LIFT of liquids.

Some years later, and also using a viscous ink (a paste developed for screen printing that contained silver microparticles), Lewis and coworkers [Lewis *et al.* 2006] demonstrated that if the receptor was placed in very close proximity to the donor film, the protrusion generated in the sub-threshold regime (termed by Lewis *et al.* bubble-regime, due to the shape of the protrusion) could reach the

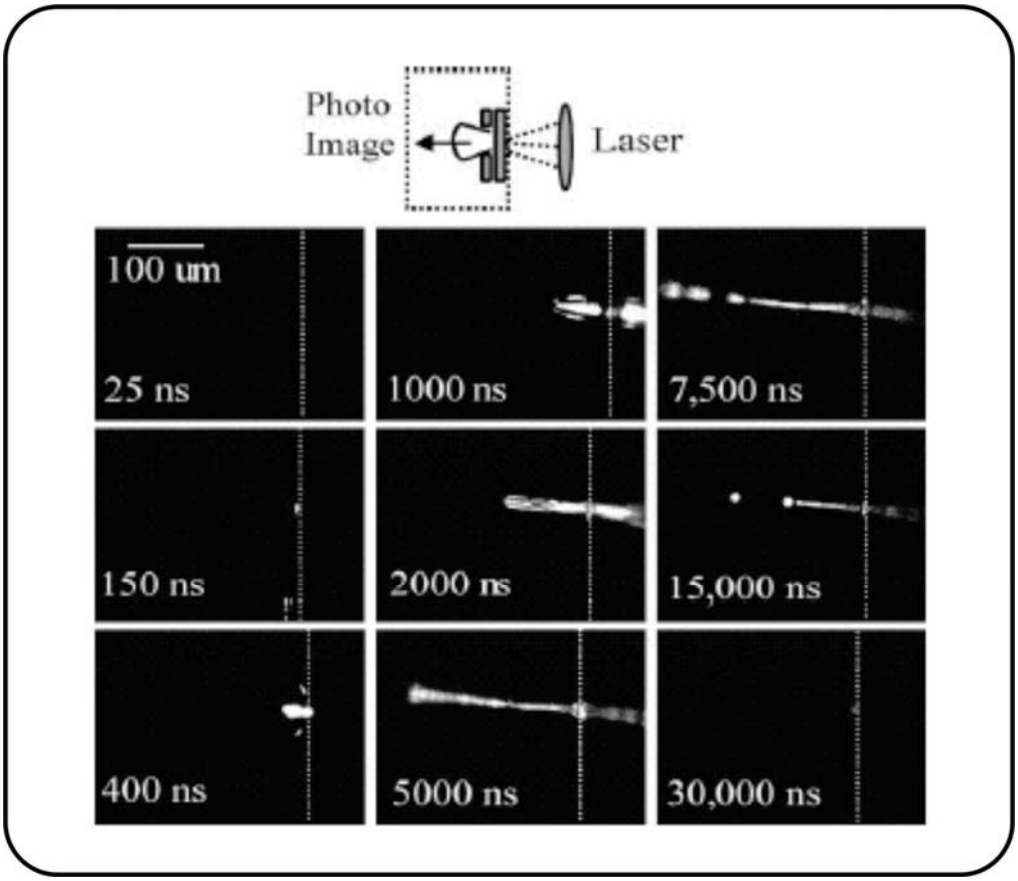


**Fig. 1.10.** Time-resolved images of the LIFT process for an aqueous solution (Barron *et al.* 2005a) at a fluence of 26 mJ/cm$^2$.

receptor substrate and result in the deposition of a droplet (Fig. 1.9). Although this result was significant from a technological point of view, it was a particular case of the previously described sub-threshold regime, and the question concerning the mechanism of the formation of droplets at high separation distances still remained open.

The most important step towards the elucidation of the transfer dynamics in the LIFT of liquids was made by Barron and coworkers [Barron *et al.* 2005a]. In that work, time-resolved images of the transfer process using a BSA solution were acquired. It was observed that some microseconds after the absorption of the laser pulse by the donor substrate, a jet developed (Fig. 1.10). However, that jet became unstable short after its formation (5–7 µs), breaking into several free droplets when the jet had a length of about 200 µm. The authors

interpreted that the deposition of a single sessile droplet at distances greater than 200 µm resulted from a single flying droplet, despite the observation of the jet breakup into multiple droplets. This mistake can be probably attributed to the extended assumption that the formation of well-defined droplets in the LIFT of liquids was due to single flying droplets [Barron *et al.* 2005a, Colina *et al.* 2006]. In fact, such assumption was so deeply-root that even when the true deposition mechanism was clarified thanks to the time-resolved study presented in chapter 4 the flying droplet was still considered to be the transfer mechanism by some authors [Lin *et al.* 2009]. It should be pointed out that the multiple droplets observed by Barron *et al.* 2005a are improbable to result in a single sessile droplet on the receptor substrate, especially at long donor film-receptor substrate separations. Moreover, it has to be noted that the LIFT setup employed during the acquisition of those images was different from that used for droplet printing, making use of different laser systems as well as different conditions. Thus, the results of Barron *et al.* 2005a, although revealing at the time in which they were obtained, do not provide with a definitive explanation of the transfer mechanism in the LIFT of liquids. Therefore, at the beginning of this thesis, the transfer and deposition mechanisms of the technique were still unknown.

**Table 1.1** LIFT experiments consisting in the deposition of non-biological inks or pastes.

| **non-biological ink or paste deposited** | **laser** | **substrate** | **absorbing film** | **reference** |
|---|---|---|---|---|
| $BaTiO_3$ nanopowder dispersed in an α-terpineol suspension | Nd:YAG (355 nm, 150 ns) | —— | —— | Young *et al.* 2001 |
| barium–zirconium titanate powder dispersed in an α –terpineol suspension | Nd:YAG (355 nm, 10 ns) | —— | —— | Young *et al.* 2002 |
| hydrous ruthenium oxide power solved in water and $H_2SO_4$ | Nd:YAG (355 nm, 150 ns) | Au coated quarz wafer | —— | Arnold *et al.* 2003, Arnold *et al.* 2004a |
| $Ag_2O$ in a solution of PVdF-HFP binder in propylene carbonate | Nd:$YVO_4$ (355 nm, 30 ns) | Au coated alumina | —— | Arnold *et al.* 2004b |
| Zn in a solution of PVdF-HFP binder in dibasic ester | Nd:$YVO_4$ (355 nm, 30 ns) | Au coated alumina | —— | Arnold *et al.* 2004b |
| $LiCoO_2$, graphite and carbon black in a solution of PVdF–HFP binder in dibasic ester | Nd:$YVO_4$ (355 nm, 30 ns) | Cu film (50 µm thick) | —— | Kim *et al.* 2007 |

| **non-biological ink or paste deposited** | **laser** | **substrate** | **absorbing film** | **reference** |
|---|---|---|---|---|
| carbon, carbon black, dissolved in dibasic ester. | Nd:$YVO_4$ (355 nm, 30 ns) | Al film (50 µm thick) | —— | Kim *et al.* 2007 |
| conducting polymer (PEDOT-PSS) | Nd:YAG (1064 nm and 532 nm, 8 ns and 50 ps), KrF(248 nm, 25 ns), Diode-pumped Yb:YKW (1025 nm, 400 fs) | Si, schott borosilicate crown glass, quartz suprasil | —— | Thomas *et al.* 2007, Rapp *et al.* 2009b |
| $P_4VP$ in $H_2O$ glycerol | Nd:YAG (266 nm, 4 ns) | low temperature oxide on Si | cromium (40 nm) | Boutopoulos *et al.* 2008a |
| PHEMA in etlyl-lactete | Nd:YAG (266 nm, 4 ns) | low temperature oxide on Si | cromium (40 nm) | Boutopoulos *et al.* 2008a |
| PAA in $H_2O$ glycerol, | Nd:YAG (266 nm, 4 ns) | low temperature oxide on Si | cromium (40 nm) | Boutopoulos *et al.* 2008a |
| organic luminophores (AM and $Alq_3$) suspended in N-methyl-2-pyrrolidone | Nd:$YVO_4$ (355 nm, 15 ns) | glass slide | polyimide (6 µm) | Kattamis *et al.* 2009 |
| silver nanoparticle ink | Nd:$YVO_4$ (355 nm, 30 ns) | glass slide, PVP dielectric layer, pentacene layer | —— | Kim *et al.* 2009, Kim *et al.* 2010 |
| | Nd:YAG (355 nm, 50 ps) | Si covered by a thin layer of $SiO_2$ | —— | Rapp *et al.* 2009a |

**Table 1.2** LIFT experiments consisting in the deposition of biomolecules or cells.

| biomolecule or cell type deposited | laser | substrate | absorbing film | reference |
|---|---|---|---|---|
| salmon sperm DNA | Nd:YAG (355 nm, 10 ns) | poly-L-lysine coated slide | titanium (60 nm) | Fernández-Pradas *et al.* 2004 |
| human cDNA | Nd:YAG (355 nm, 10 ns) | poly-L-lysine coated slide | titanium (50 nm) | Serra *et al.* 2004b, Colina *et al.* 2005 |
| lambda bacteriophage DNA | KrF (248 nm, 500 fs) | glass slides | —— | Zergioti *et al.* 2005 |
| polyphenol oxidase (PPO) | ArF (193 nm, 20 ns) | Pt microelectrode | —— | Wu *et al.* 2001 |
| | ArF (193 nm, 20 ns) | polystyrene plate, quartz plate, digene silanated slide | gelatin | Chrisey *et al.* 2003, Wu *et al.* 2003 |
| bovine serum albumin (BSA) | ArF (193 nm, 20 ns) | nitrocellulose coated glass slide | —— | Ringeisen *et al.* 2002a |
| | Nd:YAG (266nm, 3-5 ns), KrF (248 nm, 2.5 ns) | matrigel coated slides, silinated glass slides | gold (35 nm), titanium (75 nm), titanium oxide (85 nm) | Barron *et al.* 2004a |
| | KrF (248 nm, 2.5 ns) | nitrocellulose coated glass slide | gold (100 nm), titanium (75 nm), titanium oxide (85 nm) | Barron *et al.* 2005a |
| | KrF (248 nm, 500 fs) | glass slides | —— | Zergioti *et al.* 2005 |
| anti-BSA | ArF (193 nm, 20 ns) | polystyrene plate, quartz plate, digene silanated slide | gelatin | Chrisey *et al.* 2003, Wu *et al.* 2003 |

| biomolecule or cell type deposited | laser | substrate | absorbing film | reference |
|---|---|---|---|---|
| Treponema pallidum 17 kDa antigen | Nd:YAG (355 nm, 10 ns) | nylon-coated glass slide | titanium (60 nm) | Serra *et al.* 2004a |
| alkaline phosphatase | KrF (248 nm, 2.5 ns) | nitrocellulose coated glass slide | gold (100 nm), titanium (75 nm), titanium oxide (85 nm) | Barron *et al.* 2005a |
| glutathione t–transferase (GST) | KrF (248 nm, 500 fs) | glass slides | ——— | Zergioti *et al.* 2005 |
| enzyme horseradish peroxidase | KrF (248 nm, 15 ns – 500 fs) | nitrocellulose coated glass slides | gold (10 nm) | Dinca *et al.* 2008b |
| escherichia coli | ArF (193 nm, 20 ns) | Si glass slides, nutrient agar culture plates | ——— | Ringeisen *et al.* 2002b |
| | KrF (248 nm, 2.5 ns) | agar-coated glass slide, solid LB Petri dish, microtiter plate | gold (35 nm), titanium (75 nm) | Barron *et al.* 2004b |
| prostate tissue | ArF (193 nm, 20 ns) | polystyrene plate, quartz plate, digene silanated slide | gelatin | Chrisey *et al.* 2003, Wu *et al.* 2003 |
| fungus (trichoderma conidia) | KrF (248 nm, 30 ns) | cell media coated plate | silver (50 nm) | Hopp *et al.* 2004 |
| photobiotin | KrF (248 nm, 15 ns - 500 fs) | glass slides, nitrocellulose coated glass slides, agarose and ORMOCER treated glass slides | gold (10 nm) | Dinca *et al.* 2007b, 2008c |
| streptavidin | ArF (193 nm, 30 ns) | glass slides | ——— | Dinu *et al.* 2007 |
| peptides (from the adenovirus fiber) | KrF (248 nm, 15 ns) | gold coated glass slides | gold (10 nm) | Dinca *et al.* 2007a |
| avidin | KrF (248 nm, 15 ns – 500 fs) | glass slides and nitrocellulose coated glass slides | gold (10 nm) | Dinca *et al.* 2008a |

| biomolecule or cell type deposited | laser | substrate | absorbing film | reference |
|---|---|---|---|---|
| titin | KrF (248 nm, 15 ns – 500 fs) | glass slides and nitrocellulose coated glass slides | gold (10 nm) | Dinca *et al.* 2008a |
| | KrF (248 nm, 15 ns – 500 fs) | nitrocellulose coated glass slides | gold (10 nm) | Dinca *et al.* 2008b |
| biotin | KrF (248 nm, 15 ns – 500 fs) | glass slides and nitrocellulose coated glass slides | gold (10 nm) | Dinca *et al.* 2008a |
| | Nd:YAG (266 nm, 4 ns) | Si and Low Temperature Oxide on Si (LTO/Si) | cromium (40 nm) | Boutopoulos *et al.* 2008 |
| amyloid peptide | KrF (248 nm, 15 ns) | ORMOCER coated glass slides | gold (10 nm) | Dinca *et al.* 2008c |
| chinese hamster ovaries | ArF (193 nm, 20 ns) | quartz plate | —— | Wu *et al.* 2001 |
| human osteosarcoma cells | ArF (193 nm, 20 ns) | polystyrene plate, quartz plate, digene silanated slide | gelatin | Chrisey *et al.* 2003, Wu *et al.* 2003 |
| | ArF (193 nm, 20 ns) | Matrigel coated slides | —— | Barron *et al.* 2004c |
| | Nd:YAG (266 nm, 5 ns) | Matrigel coated slides | titanium, titanium oxide (75-85 nm) | Barron *et al.* 2004d |
| | Nd:YAG (266nm, 3-5 ns), KrF (248 nm, 2.5 ns) | Matrigel coated slides, silinated glass slides | gold (35 nm), titanium (75 nm), titanium oxide (85 nm) | Barron *et al.* 2004a |
| | KrF (248 nm, 2.5 ns) | Matrigel coated slides | gold (35 nm), titanium (75 nm) | Barron *et al.* 2005b |
| rat cardiac cells | ArF (193 nm, 20 ns) | Matrigel coated slides | —— | Chrisey *et al.* 2003, Barron *et al.* 2004c |

| biomolecule or cell type deposited | laser | substrate | absorbing film | reference |
|---|---|---|---|---|
| rat Schwann cells | KrF (248 nm, 30 ns) | glass plates coated with a thin wet gelatin layer | silver (100 nm) | Hopp *et al.* 2005 |
| pig lens epithelial cells | KrF (248 nm, 30 ns) | glass plates coated with a thin wet gelatin layer | silver (100 nm) | Hopp *et al.* 2005 |
| astrogial cells | KrF (248 nm, 30 ns) | glass plates coated with a thin wet gelatin layer | silver (100 nm) | Hopp *et al.* 2005 |
| bovine aortic endothelial cells | KrF (248 nm, 2.5 ns) | Matrigel coated slides, cell media coated slides | metal or metal oxide (10-100 nm) | Chen *et al.* 2006 |
| rat neuroblasts cells | ArF (193 nm, 10 ns) | basement membrane (Matrigel) coated slides | —— | Doraiswamy *et al.* 2006 |
| bovine embryonic stem cells | Nd:$YVO_4$ (355 nm, 15 ns) | Matrigel coated Petri dish | polyimide (4 µm) | Kattamis *et al.* 2007 |
| human dermal fibroblasts | ArF (193 nm, 20 ns) | Matrigel coated Petri dish | —— | Schiele *et al.* 2008 |
| bovine pulmonary artery endothelial cells | ArF (193 nm, 20 ns) | Matrigel coated Petri dish | —— | Schiele *et al.* 2008 |
| human breast cancer cells | ArF (193 nm, 20 ns) | Matrigel coated Petri dish | —— | Schiele *et al.* 2008 |
| rat neural stem cells | ArF (193 nm, 20 ns) | Matrigel coated Petri dish | —— | Schiele *et al.* 2008 |
| mouse myoblasts | ArF (193 nm, 20 ns) | Matrigel coated Petri dish | —— | Schiele *et al.* 2008 |
| rat olfactory ensheathing cells | Nd:YAG (266 nm, 5 ns) | cell culture chamber coated with poly(l-lysine) and filled with medium, Matrigel coated slides | titanium, titanium oxide (30-40 nm) | Othon *et al.* 2008b |
| human endothelial cells | Nd:YAG (1064 nm, 30 ns) | quartz disc | gold (20-30 nm) | Guillemot *et al.* 2009 |

## Chapter 2

# Experimental setup

In this chapter, the setup used to carry out the different experiments on laser printing is presented. The materials and methods employed are described, as well as the different techniques used to characterize the deposited materials.

The chapter is divided into five sections. The first one includes a detailed description of the laser direct writing setup with all its different elements. The sample preparation process before printing is presented in the second section. The third section is focused on the time-resolved imaging setup used to study the dynamics of the LIFT process. The fourth section describes the rest of the characterization techniques that have been employed to analyze the printed material. Finally, the fifth section ends up the chapter with a description of two particular measuring methods.

## 2.1 Laser direct writing setup

The printing experiments were all performed using the setup composed of the elements illustrated in Fig. 2.1: a laser source, an optical system to guide and focus the radiation on the donor substrate, and computer-controlled XYZ translation stages to allow the translation of both donor and receptor substrates with respect to the laser beam. All these elements, which are detailed below, were assembled on top of an optical table (*Melles Griot*, 250 cm long, 125 cm wide). The triple-plate construction of the table, with its internal dampers, plus the four legs with air suspension mechanisms which formed the support system, provided a rigid and an almost vibration-free working surface. Moreover, the upper plate of the table had mounting holes to provide a good fixation of the different elements of the direct writing setup.

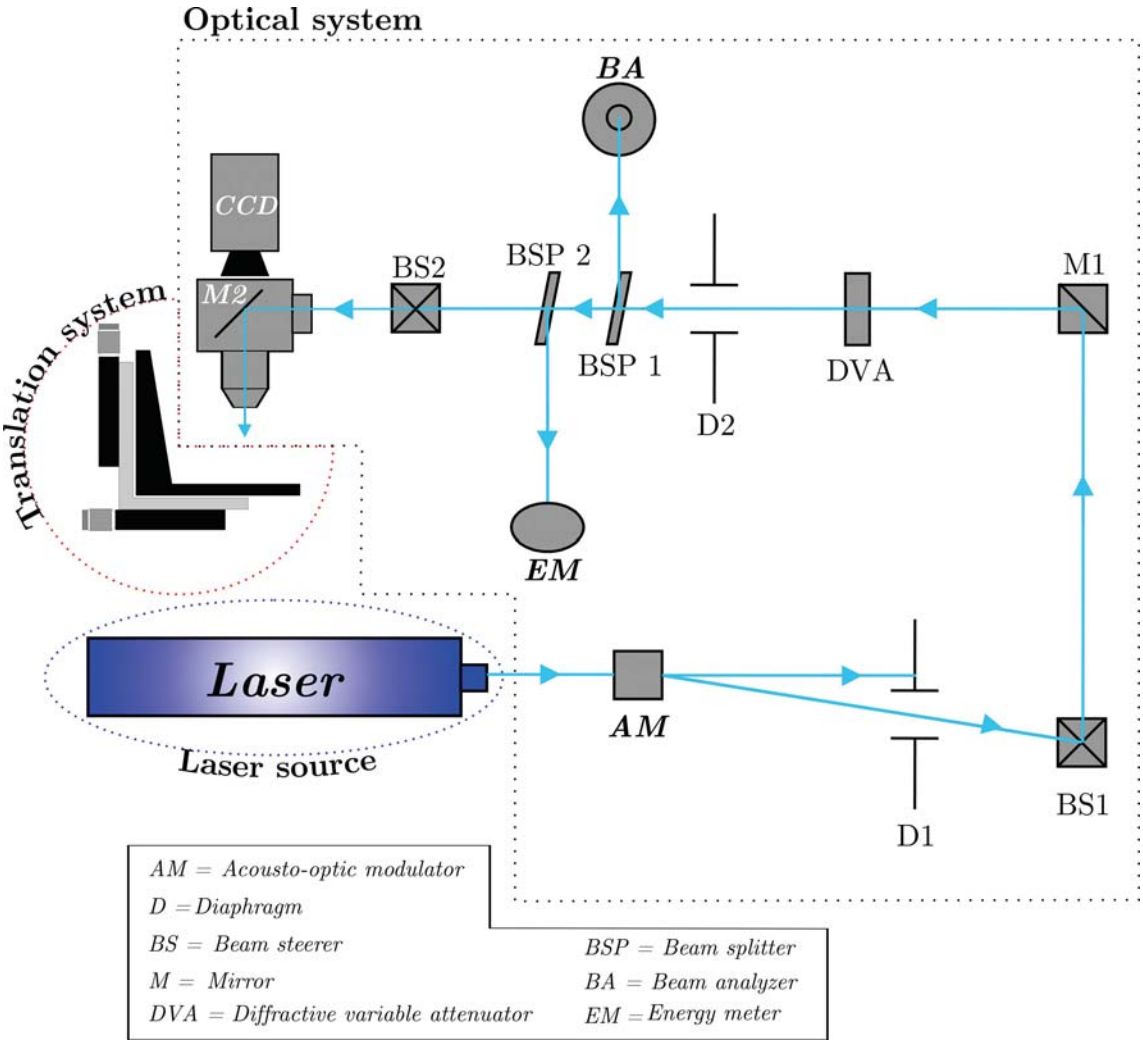


**Fig. 2.1.** Scheme of the laser direct writing setup.

### 2.1.1 Laser source

Two different laser sources could be employed in the direct writing setup: a nanosecond (ns) laser and a femtosecond (fs) laser. The first one was used in the experiments of chapters 3 and 4, whereas the second one was used in those of chapter 5. A description of these lasers is provided next.

#### Nanosecond laser source

The nanosecond laser source was a pulsed Nd:YAG laser (*Spectron Laser Systems, Mini-Q SLMQIT-20*) with a fundamental wavelength of 1064 nm

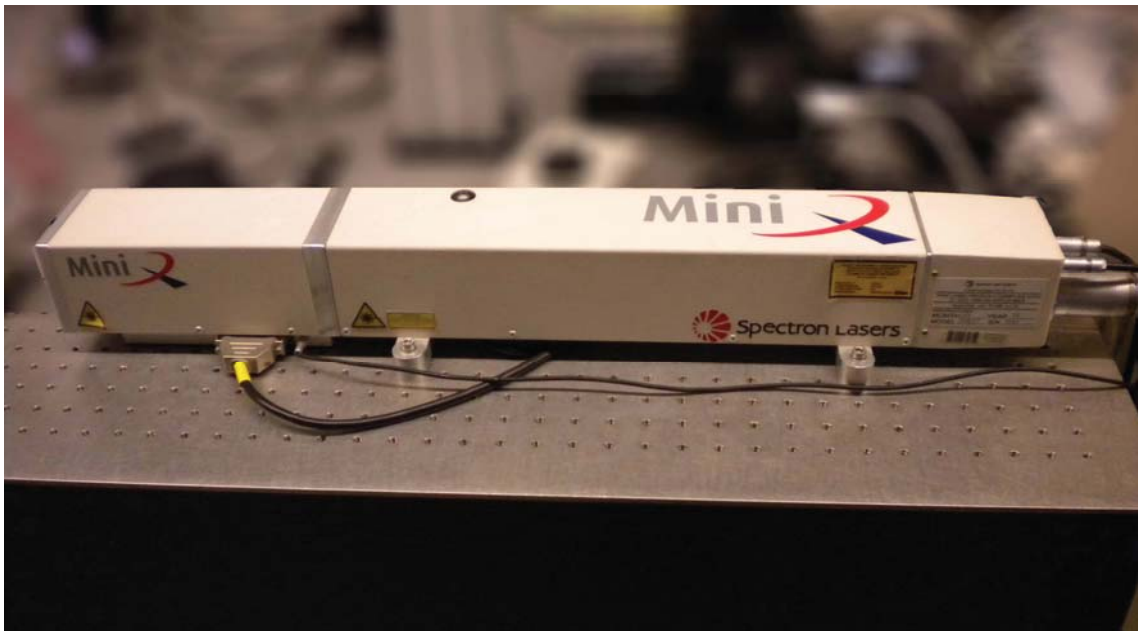


**Fig. 2.2.** Photograph of the nanosecond laser used in the LIFT experiments mounted on the optical table.

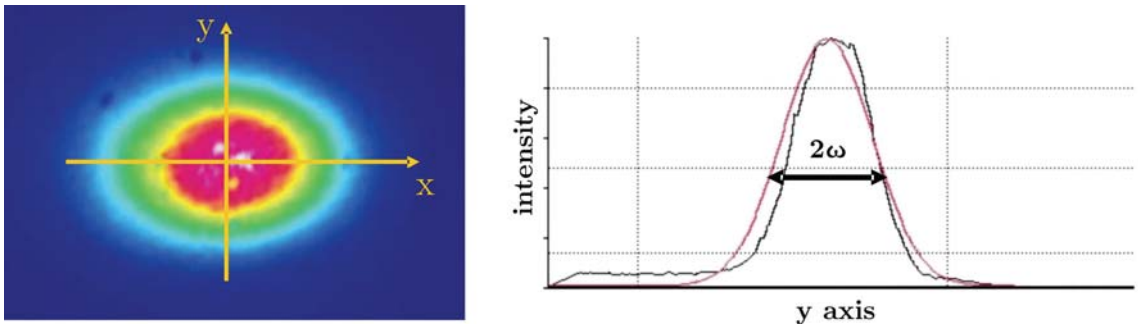


**Fig. 2.3.** Image of the energy density distribution of the laser beam. The black curve on the right plot is the real intensity profile along the y direction, whereas the red one corresponds to a perfect Gaussian distribution.

(infrared), a repetition rate range between 0.5 and 20 Hz, and a pulse duration of 10 ns (Fig. 2.2). The pulsed output beam was obtained by means of active Q-switching, more specifically a Pockels cell with a polarizer situated inside the resonant cavity. Outside the laser cavity, frequency doubling and frequency tripling crystals of potassium dihydrogen phosphate (KDP) allowed obtaining laser pulses of 532 (green) or 355 nm (ultraviolet) in wavelength. The results presented in chapters 3 and 4 were all obtained at a laser wavelength of 355 nm. Such beam had a diameter of around 2 mm at its exit point, with a divergence

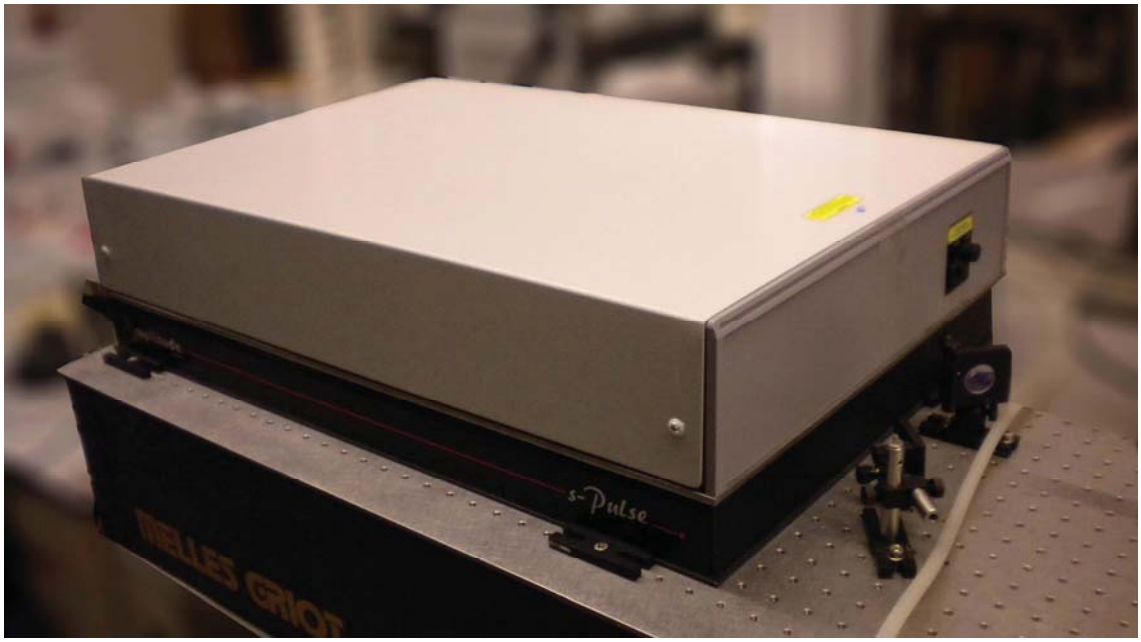


**Fig. 2.4.** Photograph of the femtosecond laser mounted on the optical table.

of 1.3 mrad, and with a nearly Gaussian intensity profile of elliptical section (Fig. 2.3). After the KDP crystals, a motorized polarizer allowed modulating the laser pulse energy, which could be varied from 1 nJ to 1 mJ.

### Femtosecond laser source

The femsotecond laser source (Fig. 2.4) was a diode pumped ytterbium (Yb:YKW, potassium yttrium tungstate) laser (*Amplitude Systemes, s-Pulse*) with a fundamental wavelength of 1027 nm (infrared), an spectral width of 4 nm, a repetition rate range between 1 and 10 kHz, and a pulse duration of 450 fs. The exit beam presented a rather Gaussian intensity profile (Fig. 2.5) with a diameter of around 5 mm. The pulsed output beam was obtained after four different stages, depicted in Fig. 2.6: laser oscillator (L1), pulse stretcher (L2), laser amplifier (L3) and finally pulse compressor (L4).

The laser oscillator part (L1) was composed of a cw laser diode, a ytterbium doped crystal, different mirrors and a saturable absorber (semiconductor saturable absorber mirror, SESAM). Initially, the crystal was pumped by the laser diode, and the emitted radiation was sent through the different optics until

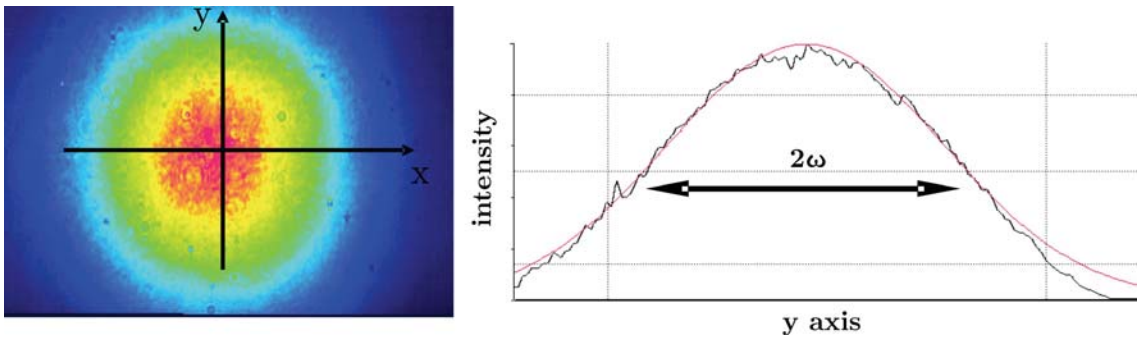


**Fig. 2.5.** Image of the energy density distribution of the femtosecond laser beam. The black curve on the right corresponds to the real intensity profile along the y direction, whereas the red one corresponds to a perfect Gaussian distribution.

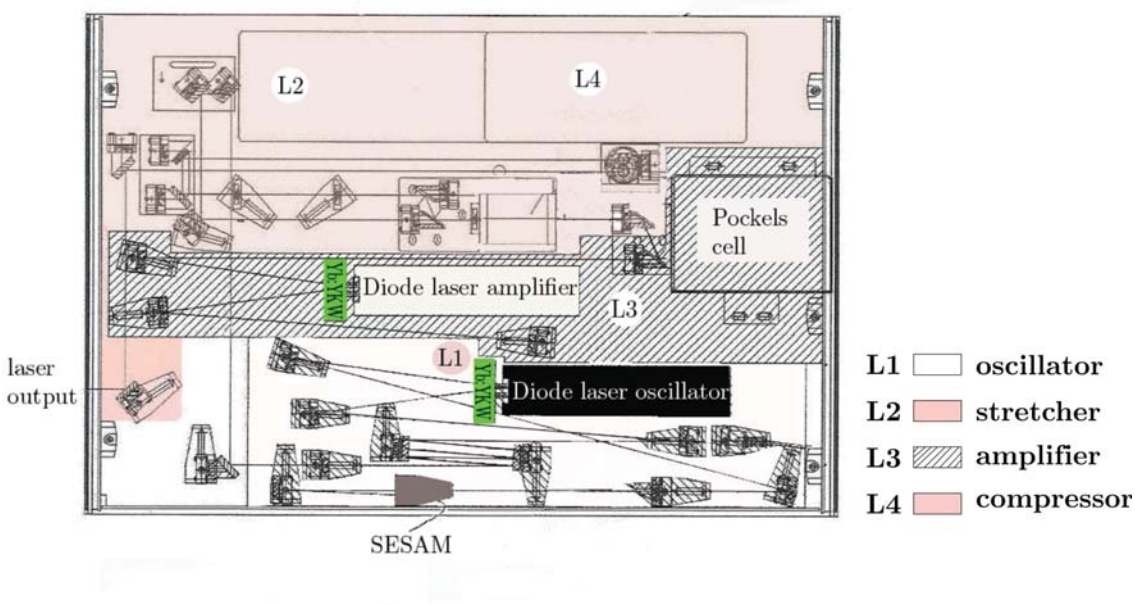


**Fig. 2.6.** Scheme of the femtosecond laser and its different parts.

reaching the SESAM[2]. The emitted crystal radiation showed very strong intensity fluctuations. Due to the SESAM behavior, the strongest intensity maxima of the radiation tended to saturate the SESAM and thus be reflected, whereas the rest of the radiation was attenuated. As a result, a laser pulse was formed, which traveled through the cavity. Once the laser pulse returned to the SESAM, the leading edge of the pulse was attenuated since it did not have enough intensity to saturate the SESAM, whereas the rest of the laser pulse

[2] The SESAM has the property to absorb the low intensity radiation and reflect the high intensity one.

could saturate the SESAM and be reflected. Thus, the laser pulse was shortened. This process was repeated during several cavity trips until a final steady stage was reached characterized by a laser pulse with a very short duration (femtoseconds) and an energy of 10-20 nJ. It has to be noted that this method allowed obtaining femtosecond laser pulses at a repetition rate of 50 MHz, which was the time during which a laser pulse could make 3 round trips in the cavity. This method of obtaining short pulses is known as *mode-locking*, because selecting a single intensity maximum in the time domain is equivalent to establishing a phase relation between the longitudinal cavity modes in the frequency domain (to lock the modes) [Ducasse *et al.* 2004].

The femtosecond pulses generated in the oscillator were not energetic enough for any materials processing application, and thus its amplification was required. However, amplifying such short pulses would damage the laser internal optics, due to the extremely high intensities of such short pulses. Thus, before the amplification stage the short pulses passed through a pulse stretcher (L2), which stretched them out temporally (reducing the laser pulse intensity). The stretcher was basically a diffraction grating with some mirrors. The stretched pulses arrived then to the laser amplifier (L3), which was composed of a Pockels cell, a ytterbium doped crystal, and different mirrors. In the amplifier the Pockels cell selected a single pulse (by changing its polarization during some tenths of nanoseconds, a shorter time than the time separation between consecutive laser pulses) and amplified it sequentially by successive round trips in the amplifier resonant cavity. Once the laser pulse had reached enough energy, the Pockels cell sent it to a pulse compressor (L4), which reversed the effect made by the pulse stretcher (also using a diffraction grating), and the laser pulse was finally sent outside the cavity.

### 2.1.2 Optical system

The optical system (Fig. 2.1) was composed of a series of mirrors, beamsplitters and lenses which allowed guiding and focusing the laser radiation on the donor substrate, and also synchronizing the laser pulses with the translation of the

XYZ stages, as well as simultaneously measuring the laser pulse energy and beam distribution.

After the motorized polarizer, an *acousto-optic modulator* (AM) allowed diffracting the laser beam when a radiofrequency signal was applied to it. Such signal was provided by a radiofrequency generator (*Neos Technology, model 38085-15DS*). The modulator (*Neos Technology, model N35085-10-350*), composed of a fused silica optical cell with a lithium niobate transducer, was optimized for wavelengths from 355 to 514 nm, and for beam diameters of 10 mm or less.

After the modulator, a *diaphragm* (D1) properly situated allowed passing only the first-order of the diffracted beam, blocking the other orders (the modulator was adjusted so that the first-order of diffraction was the most intense). The separation between the modulator and the diaphragm was of 1.5 m, which is the distance at which the different diffractive orders can be clearly distinguished. Such configuration allowed the external control of the laser radiation arrival to the rest of the optical system: when a signal was sent to the modulator, the beam was diffracted and so it could pass through D1, arriving to the rest of the optical system; when no signal was applied, the beam was blocked by D1[3]. This system was then used to synchronize the laser pulses with the translation of the XYZ stages through an appropriate computer program, which will be further detailed.

Once the first-order of the diffracted beam passed through the diaphragm, a *beam steering system* (BS1, composed of two mirrors) changed the height of the laser beam trajectory and its direction. Then, another *mirror* (M1), directed the beam to the *diffractive variable attenuator* (DVA), which allowed a very fine control of the laser pulse energy that arrived to the donor substrate. The DVA is a circular diffractive grating divided into different regions, each one with a specific grating parameter. When the laser beam passed through the DVA, it

[3] The combination of AM with D1 constituted a beam-deflection device which acted as a beam shutter. The device was not required for femtosecond laser generation.

was diffracted depending on the grating parameter of the selected region. Then, a *diaphragm* (D2) situated after the DVA blocked all the diffractive orders except the zero one, thus producing the desired attenuation of the zero order beam. Since the region of the DVA exposed to the laser beam could be manually selected, the degree of attenuation of the zero order beam could be controlled. The attenuation factor ranged between 5% and 100%.

The next elements after the diaphragm were two *beam splitters* (BSP1, BSP2). Each of them transmits 70% of the incoming radiation and reflects the remaining 30%. The reflected radiation in the first beam splitter arrived to a *beam analyzer* (BA). Such device (*Ophir, model Beamstar CCD Profiler*) used a charged couple device (CCD) to obtain the beam intensity distribution. It could analyze beams up to 6.2 mm high and 4.6 mm wide, within a spectral range between 320 nm and 1100 nm, and with a detection threshold of 50 nW/cm$^2$. The device acquisition software allowed selecting the type of radiation to be analyzed (continuous or pulsed) and also allowed modifying the gain of the apparatus, as well as the shutter time. Moreover, the image of the beam profile on the screen could be visualized in two or three dimensions. The radiation reflected in the second beam splitter arrived to an *energy meter* (EM). Two different energy meters could be used, depending on the laser pulse energy to be measured. For low energies, a photodiode (*Ophir, model PE10BB*) was used, which allowed detecting laser pulse energies between 10 nJ and 10 µJ. For higher energies, a piroelectric detector (*Ophir, model PE10K*) with an energy range between 10 µJ to 10 mJ was employed. Both energy meters could be branched to a head display (*Ophir, model Nova*) which allowed visualizing the energy value of any laser pulse. Moreover, the head display could communicate to a computer, so that all the measured laser pulse energies could be saved.

It should be noted that, since the laser pulse energy could not be measured in the position where the donor substrate was located due to laser beam focusing, a previous calibration was necessary to determine the relationship between the laser pulse energy measured after the second beam splitter and that measured in

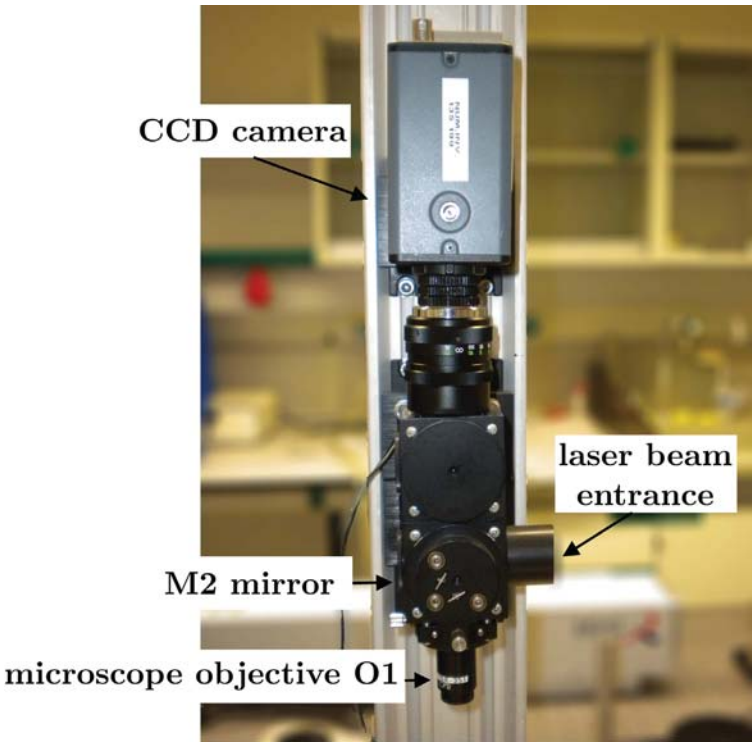


**Fig. 2.7.** Photograph of the focalizing microscope and the CCD camera used to visualize the donor film and to determine the focusing conditions of the experiment.

the donor position. The relationship found for the nanosecond laser was as follows:

$$E_{\substack{\text{focused}\\\text{beam}}} = 1.5\, E_{\substack{\text{measured}\\\text{photodiode}}} \qquad E_{\substack{\text{focused}\\\text{beam}}} = 1.7\, E_{\substack{\text{measured}\\\text{piroelectric}}}$$

For the femtosecond laser the relationship was:

$$E_{\substack{\text{focused}\\\text{beam}}} = 0.47\, E_{\substack{\text{measured}\\\text{piroelectric}}}$$

The radiation transmitted after the beamsplitters was then reflected in the two mirrors that formed the second *beam steering system* (BS2), and guided to the focalizing microscope. The microscope (Fig. 2.7) was composed of a *mirror* (M2), tilted 45° with respect to the beam incidence, which guides the radiation to an *objective lens* (O1). When working with the nanosecond laser, the objective lens (optimized for the 355 nm radiation) had a magnifying power of 15× and a numerical aperture of 0.32, with a focal length of 8.5 mm. In the case of the femtosecond laser, the objective lens (optimized for the 1024 nm radiation) had a magnifying power of 50× and a high numerical aperture of

0.55, with a focal length of 13 mm. It has to be noted that a CCD camera connected to a TV monitor was used to visualize the absorbing layer and the spots generated by the laser pulses on it (Fig. 2.7). The camera position was adjusted so that the laser focus laid on the camera focal plane. Therefore, an object that appeared in focus in the screen connected to the CCD, was actually situated in the laser focus. In this way, the focusing conditions could be easily controlled. All this was possible due to the transparency of the M2 mirror to the visible light, which allowed the arrival of the visible light to the CCD camera, although it acted as a perfect mirror for the UV light.

### 2.1.3 Translation system

The translation system was composed of three motorized micro-translation stages (*Physik Instrumente, model M-126*) to allow the translation of the donor and receptor substrates in the direction of the incident laser beam (vertical direction Z) as well as in the directions perpendicular to it (horizontal directions X and Y), and a stepper motor controller (*Apollo MS85E*). The travel range of each motor stage was 25 mm, with a minimum incremental motion of 0.25 µm and a maximum translation velocity of 15 mm/s.

Such system was connected to a computer so that it could be controlled through a home-made computer program (developed using LabView). The program could be used to position the stages, and once this was done, it allowed 'writing' any micropattern synchronizing laser firing (through the acousto-optic modulator) with the stages motion at a maximum repetition rate of 4 Hz. The program was designed so that a single laser pulse was fired at each position of interest. It should be noted that bitmap files (BMP) or ASCII files could be used to load the desired pattern.

In most experiments, the donor film-receptor substrate distance was kept constant. This was achieved by placing spacers (diverse polymer foils, depending on the desired thickness) between the donor and the receptor substrates. In these cases, the donor-receptor system was positioned on the translation system through the cylinder depicted in Fig. 2.8a. Such cylinder had different channels

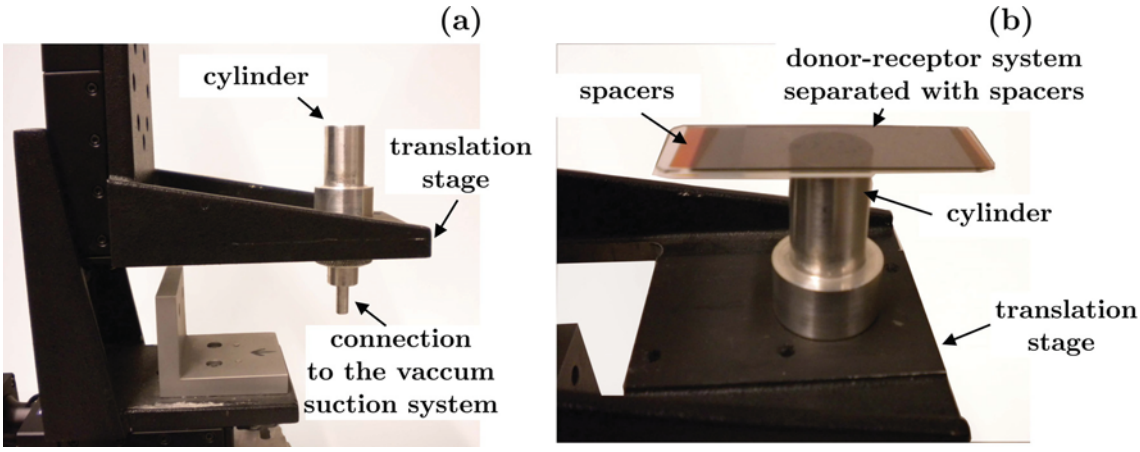


**Fig. 2.8.** a) Photograph of the vertical translation stage with the cylinder used to hold the donor-receptor system. b) Photograph of the donor-receptor system mounted on top of the cylinder.

connected to a vacuum suction system, which allowed holding the receptor by means of the generated vacuum. (Fig. 2.8b).

In order to increase the flexibility of the described system, which only allowed moving the donor and the receptor substrates together, an additional stage was assembled, as it can bee observed in Fig. 2.9a. With this extra stage, the donor and receptor substrates could be situated on independent stages, which moved together in the X and Y directions, but could be independently displaced on the Z direction. Therefore, the donor film-receptor substrate separation could be varied. When the extra stage was used, the donor substrate was supported on it by means of a specially designed aluminum holder (Fig. 2.9b). This extra stage had a manual adjuster screw which allowed setting the position of the donor substrate respect to the receptor substrate. In this configuration, the receptor substrate was placed on the cylinder, as it was before. The only drawback of this setup was the constraint that the aluminum holder imposed on the donor and receptor substrates dimensions. Therefore, the extra stage was not used for the writing of large patterns.

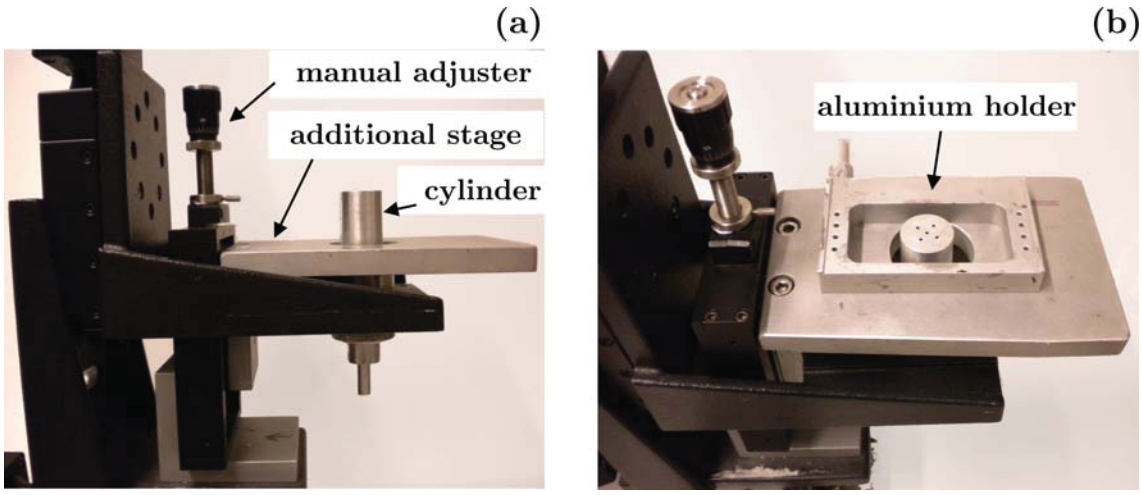


**Fig. 2.9.** a) Photograph of the vertical translation stage with the cylinder and with an additional stage. b) Photograph of the aluminum holder used when working with the additional stage.

## 2.2 Donor-receptor system preparation

### 2.2.1 Donor substrate

The donor system consisted in a liquid film spread on a donor substrate transparent to the laser radiation, which had been previously coated with an absorbing layer.

The printing experiments were carried out using four different liquid solutions:

-Water + glycerol + sodium dodecyl sulphate (SDS) solution

This biomolecule-free solution was a mixture of distilled water and glycerol, both at a concentration of 50 % (v/v), plus the surfactant SDS dissolved at a concentration of 2.0 mg/mL. Such solution was a model solution with a rheology similar to that of biomolecule-containing solutions used for microarrays preparation. The presence of glycerol, moreover, reduced the evaporation rate of the solution.

-Immunoglobulin G (IgG) solution

This biomolecule-containing solution was prepared mixing IgG powder (*Sigma 56834*) with a solution of phosphate buffered saline (PBS, 0.01 M, pH 7.4) with glycerol (40 % v/v), obtaining a solution with a concentration of 0.05 mg/mL.

-Bovine serum albumin (BSA) solution

The preparation of this biomolecule-containing solution was carried out mixing BSA powder (*Sigma A1470*) with distilled water plus glycerol, both at a concentration of 50 % (v/v). The obtained solution had a concentration of 10 mg/mL.

- Deoxyribonucleic acid (DNA) solution

Two different DNA solutions were prepared, each one containing a single human cDNA clone insert amplified by PCR in a buffer solution. The buffer solution consisted of 50 % (v/v) glycerol, 25 %(v/v) dimethyl sulfoxide (*Merck*), and 25 % (v/v) TrisEDTA (*Amreso*). The first cDNA corresponds to the mitogen-activated protein kinase 3 gene (MAPK3, 525 base pairs long, from the IMAGE clone 809939). The second cDNA was the v-ets avian erythroblastosis virus E26 oncogene homolog 2 (ETS2, 2205 base pairs long, from the IMAGE clone 260303).

The transparent holder was a standard microscope glass slide coated with a titanium layer that acted as an absorber of the laser radiation (necessary due to the transparency of the previous solutions to the laser radiation). The choice of titanium seemed appropriate since this element is biologically inert, absorbs the laser radiation at 355 nm, and also presents a good adhesion with glass. The titanium coatings were deposited using thermal evaporation, and had thicknesses ranging between 50 and 70 nm.

The liquid film preparation was carried out using two different techniques. In most cases, a blade coater (*Sheen Instruments, model S210892*) was used to spread the liquid solution onto the titanium coating (Fig. 2.10a). Between 10 and 20 µL of the solution to be used were deposited on the titanium coating, and then spread to the rest of the titanium surface using the blade of the coater, obtaining a rather uniform liquid film. The separation between the titanium and the blade was controlled using a pair of screws, and it was usually kept at 20 µm, obtaining liquid films with a thickness of that order. The dimensions of the

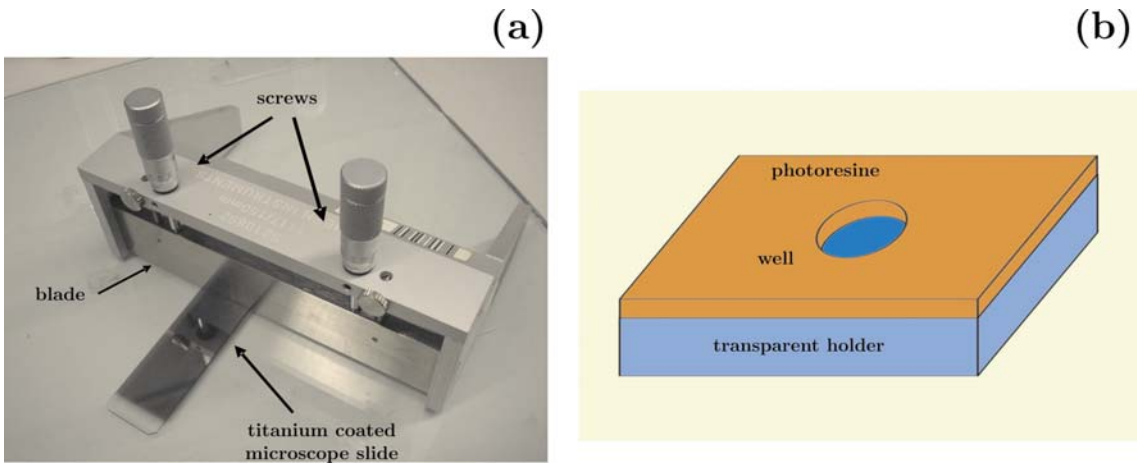


**Fig. 2.10.** a) Image of the blade coater and its elements; b) Scheme of a well prepared with lithography.

liquid films prepared with this technique were large (usually the whole area of the titanium coated slide), and thus it was appropriate for printing large arrays.

The other technique used for the preparation of the liquid films was spin coating. In this case, the titanium coated microscope slides were cut into squares, and then coated with a photoresist layer between 5 and 20 µm thick. After submitting the slides to photolithography, wells were obtained with a diameter of about 1 cm (Fig. 2.10b). The wells were then filled with the solution of interest and then submitted to spin coating in order to obtain a rather uniform liquid film. The liquid films prepared with this technique had a much smaller area that those obtained with the blade coater, and thus were not adequate for large arrays printing. However, this technique allowed preparing liquid films with a thickness below 5 µm.

The thickness of the obtained liquid films, in any of the two described methods, was estimated through weight measurement. That is, known the surface (S) of the liquid film and the density (ρ) of the solution, measuring the mass (m) of the liquid can be used to estimate the film thickness through the relationship:

$$thickness = \frac{m}{\rho S}$$

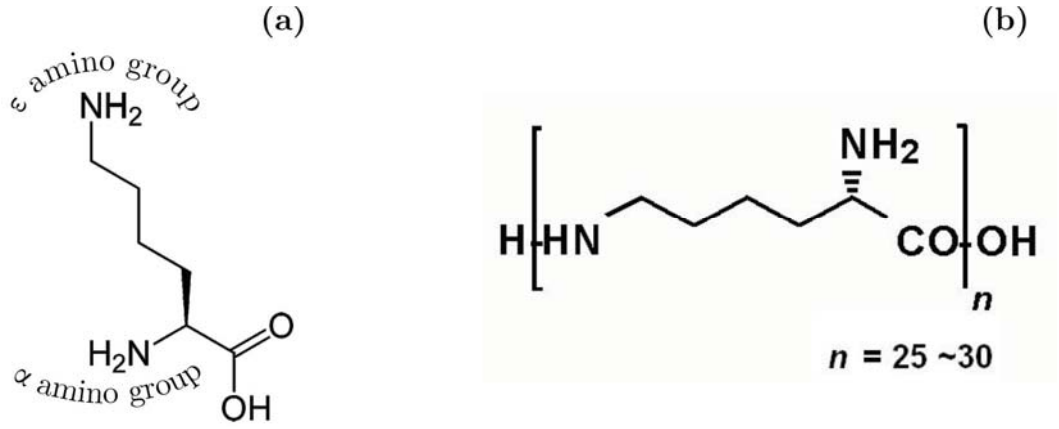


**Fig. 2.11.** a) Representation of the lysine amino acid; b) Representation of a poly-L-lysine molecule, where the lysine amino acids are molecularly linked by the ε amino group and the carboxyl group.

### 2.2.2 Receptor substrate

The present work is mainly focused on the study of the laser printing process of biomolecule-containing solutions. For this reason, substrates which provided a surface on which the biomolecules could be easily attached were required. The receptor substrates used were commercial poly-L-lysine coated glass slides (*Menzel Glaser, Polysine*), commonly employed for biomolecule microarrays preparation. In addition, poly-L-lysine substrates were slightly hydrophobic, and thus allowed a higher printing density than simple glass slides. The poly-L-lysine molecule is composed of a chain of lysines, a type of amino acid with the particularity to have a free amino group ($NH_2$), called the ε-amino group (Fig. 2.11). When the substrates were used for protein immobilization, it was necessary to previously activate them, that is, to chemically modify them to promote protein adhesion. This was done by immersing the substrates in a solution of glutaraldehyde (3% v/v) with PBS for 30 minutes. The glutaraldehyde molecules were covalently bonded to the lysine amino groups, generating free carboxyl groups (CHO). These carboxyl groups were then ready to bond to the α-amino groups of the printed proteins (Fig. 2.12). The last step of the activation process was the substrate rinsing with PBS, methanol and water.

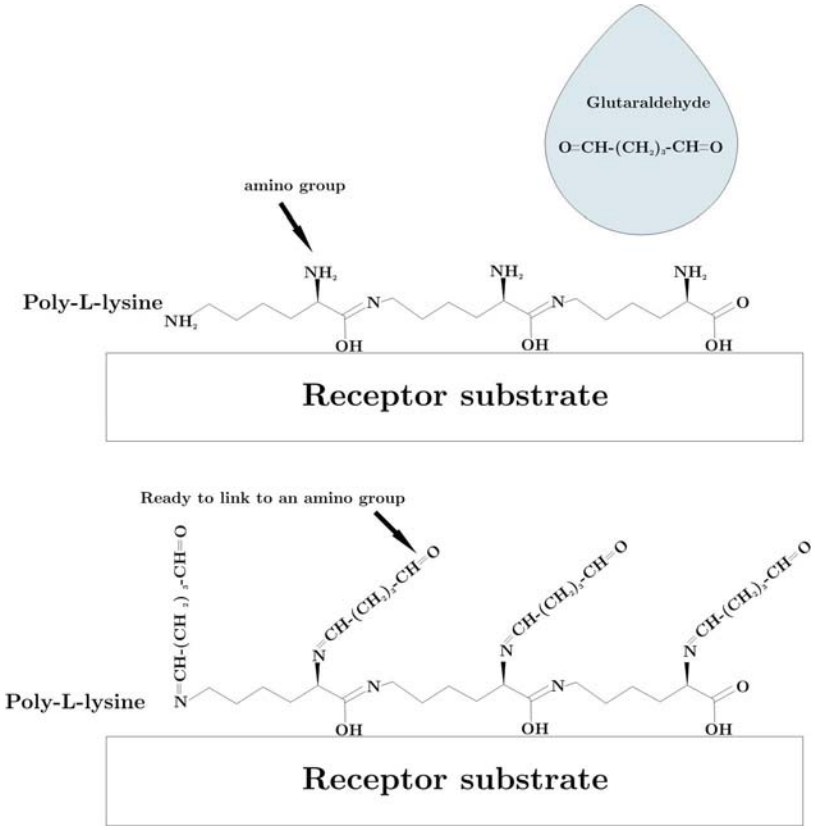


**Fig. 2.12.** Scheme of the poly-L-lysine activation process with glutaraldehyde.

## 2.3 Time-resolved imaging

The dynamics of the studied processes, which are induced by short laser pulses, take place during very short times. Therefore, in order to analyze them in detail, a technique with an extremely high temporal resolution is required. An adequate technique for analyzing such fast processes is time-resolved imaging, and for this reason, it was used to perform the study of the ejection and deposition mechanisms that occur during the LIFT of liquids. Chapter 4 is fully dedicated to the results obtained with such technique.

The imaging system was assembled together with the LIFT setup (Fig. 2.13), so that the previously described transfer system was not modified by the incorporation of this novel element. This was crucial in the attempt to elucidate the LIFT mechanisms, since it assured that the process which generated the

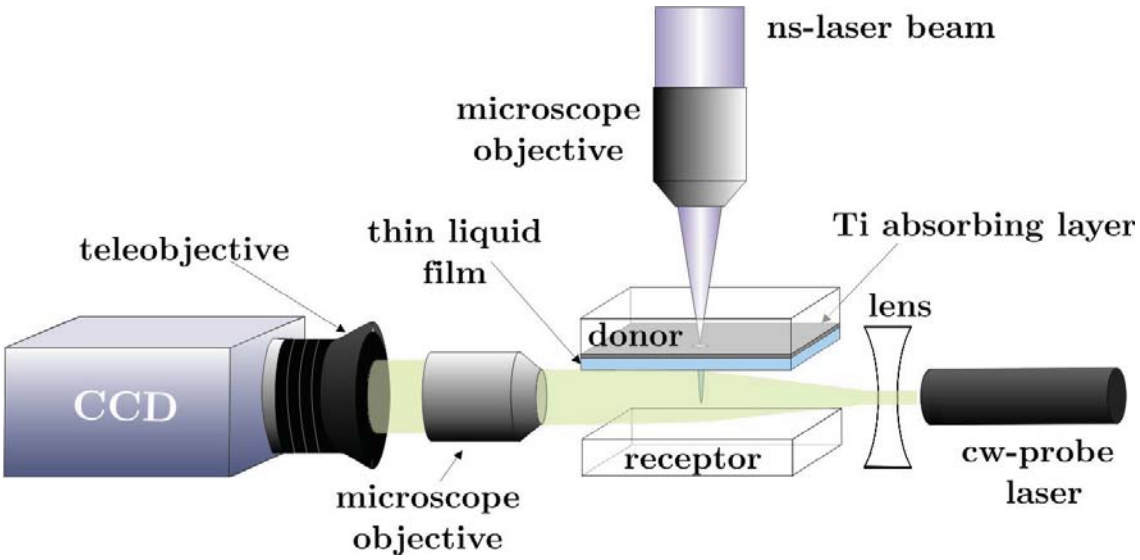


**Fig. 2.13.** Scheme of the time-resolved imaging system with its different elements.

droplets had not been modified. It has to be pointed out that for the study of the ejection mechanisms the receptor substrate was removed from the LIFT setup, whereas it was kept in its location for the study of the deposition mechanisms.

Three different elements constituted the imaging system: an illumination source, an optical system, and a fast-intensified CCD camera (Fig. 2.13). These elements are further described below.

### 2.3.1 Illumination source

A cw Nd:YAG laser was used to illuminate the region of interest. It had a wavelength of 532 nm (green), and a power of 20 mW. The use of such an intense light source was necessary due to the short integration time of the camera of the imaging system. However, the high coherence of the laser light generated a problem: when both donor and receptor substrates were simultaneously illuminated (in order to study the LIFT deposition mechanisms), multiple reflections between these substrates occurred, and thus the illuminated region presented an interference pattern with dark and bright fringes.

### 2.3.2 Optical system

A divergent lens (1 m focal length) was placed after the illuminating source in order to assure a more uniform illumination of the imaged region. After the object to be imaged, a magnification system was assembled. It was composed of a microscope objective with a magnifying power of 15×, a numerical aperture of 0.32 and a focal length of 8.5 mm, plus a teleobjective (*Canon TV Zoom Lens V6x16*, with a focal length of 100 mm).

### 2.3.3 Fast-intensified CCD camera

The previously mentioned teleobjective was assembled to a CCD camera. This camera (*ARP France, model ANIMATER-VI*) had a resolution of 288×385 pixels, with a 8 bits dynamic range, and it was intensified by a microchannel plate (MCP). The MCP could be submitted to voltages ranging from 300 to 900 V. The camera was synchronized with laser firing in the following way (Fig. 2.14):

1) The laser generated an output electrical signal (S1) simultaneously to each laser shot.

2) The signal S1 was then sent to the input of a pulse generator, which was used to trigger two signals: S2, at a controllable time delay after the reception of S1 and with a duration of 100 ns; and S3, simultaneous to S1 and with a duration of 1 µs.

3) The signal S2 was sent to the MCP, which was then intensified during 100 ns.

4) The signal S3 was sent to the acquisition card of the camera, connected to a computer. This signal was necessary since the camera continuously acquired images every 25 ms, but it did not save them. Only when the signal S3 arrived to the acquisition card, that image was saved.

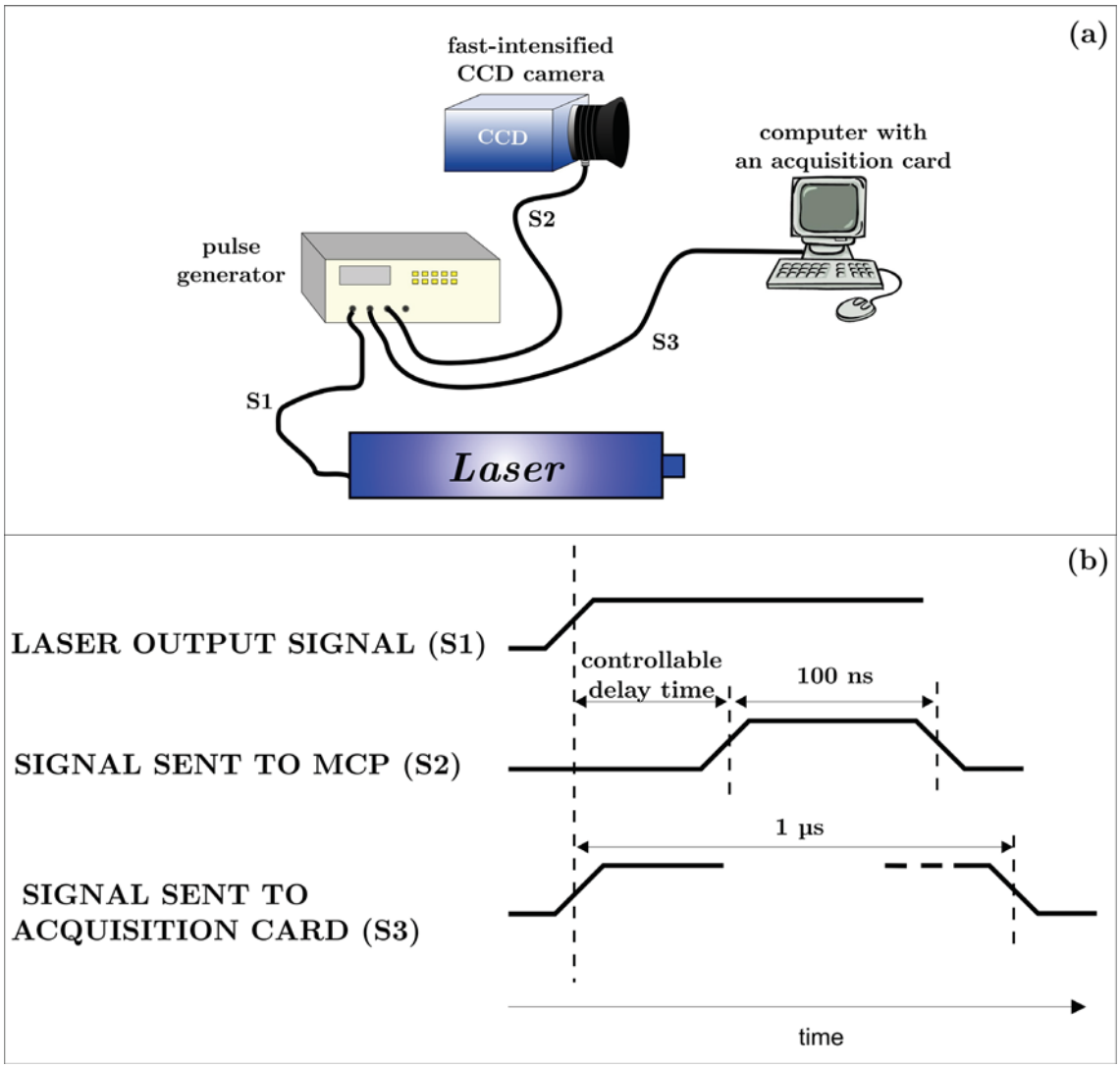


**Fig. 2.14.** a) Scheme of the synchronization setup for the time-resolved imaging; b) Temporal diagram of the different signals involved in the synchronization system.

Therefore, the camera integrated the information received during 25 ms, but the intensification only occurred during S2, and thus S2 sets the effective integration time of the camera (100 ns). On the other hand, the time delay between the moment in which the laser was fired and that in which the image was acquired was controlled through S2. However, there exists a fixed delay of 80 ns (due to the response time of the pulse generator) which could not be avoided, and which fixed the minimum acquisition delay of the system. A single image frame was taken for each laser pulse, and varying the time delay between the laser pulse and the MCP allowed reconstructing a stop-action movie of the transfer process.

## 2.4 Characterization techniques

The morphological analysis of the printed microarrays was carried out using two different characterization techniques, which are described below: optical microscopy and optical profilometry.

Additionally, the biological activity of the printed biomolecules was tested using a fluorescence immunoassay for the protein solutions (IgG and BSA), and a hybridization test for the DNA solution.

### 2.4.1 Optical microscopy

The main analysis of the transferred material was performed using an optical microscope (*Zeiss, model AX10*) with a CCD camera (*Jenoptik, model Progress C10 plus*) connected to a computer, in order to save the obtained images. The microscope had a rotary revolver which contained 5 objectives of the following magnifications: 5×, 10×, 20×, 50×, and 100×. The microscope allowed working with both reflected and transmitted light modes.

### 2.4.2 Optical profilometry

The three-dimensional profiles of the deposited material were obtained using an optical profiler (*Veeco, model NT1100*). In the case in which circular droplets were deposited, the droplet contact angle was also measured from the obtained profiles.

An optical profiler is a device based on the interferences created by two white-light beams: the beam reflected on a fixed reference mirror, and that reflected on the object to be measured (Fig. 2.15). Since the coherence length ($c_\lambda$) of the white light is very short, interferences are produced only when the optical path difference between the two light beams is less than $c_\lambda$. The path of the beam reflected on the surface is then varied, which is achieved by translating a microscope objective, a method called *vertical scanning interferometry* or *VSI*, while the path of the reference mirror is kept constant. During the translation of

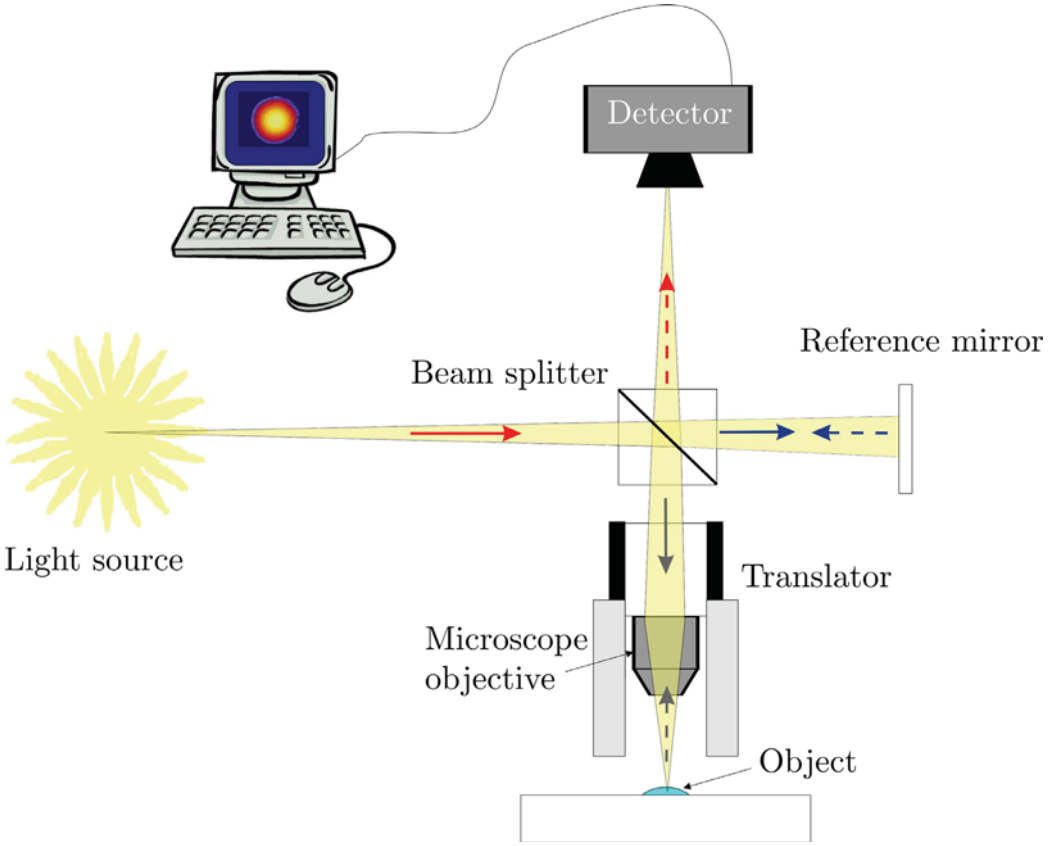


**Fig. 2.15.** Scheme of the principle of operation of an optical profiler.

the microscope objective, interferences are only produced at the parts of the object that result in a reflected beam with a path difference with respect to that of the reference mirror of about $c_\lambda$. Recording simultaneously the parts of the object that result in interferences and the position of the microscope objective, it is possible to reconstruct the two and three dimensional profiles of that object (Fig. 2.16).

The vertical resolution of the optical profiler employed was 3 nm, whereas the horizontal resolution depended on the objective used. In the presented experiments a 50× objective with a resolution of 0.5 µm was employed, which allowed obtaining the profiles of droplets with diameters between 20 and 100 µm. For droplets smaller than 20 µm, the device did not provide enough information to extract their detailed profiles, whereas droplets larger than 100 µm did not fit in the field of view of the objective.

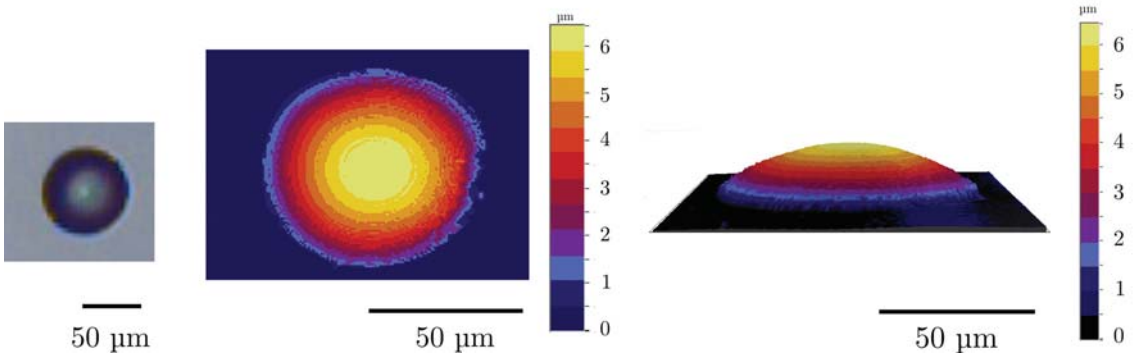


**Fig. 2.16.** Optical microscopy image of a sessile droplet and its corresponding two and three-dimensional profiles obtained with the optical profiler.

### 2.4.3 Bioactivity test

The bioactivity of the printed biomolecules was analyzed using a fluorescence immunoassay when the printed specimens were proteins, and a hybridization test for the case of DNA. Both tests are based on the specificity of the active biomolecules to bond to their prefect complementaries[4] tagged with fluorescent substances. Using a fluorescence detector (such as a fluorescence scanner) it is possible to check whether the biomolecules have preserved their bioactivity or not: the apparatus will only detect a signal where the deposited biomolecules have bond to their tagged complementaries, and such bonding is only possible if the biomolecules are active.

Once the biomolecules were printed through LIFT on the activated substrates (when required), and left to dry (overnight at room temperature for the proteins, and 2 hours at 80°C in an oven for DNA), the fluorescence test was carried out. It consists of the following protocols:

#### Protein protocol

1) Washing stage

The excess proteins were washed away with a PBS-T20 solution, so that the only remaining proteins were those bonded to the glutaraldehyde.

[4] The complementary of a given biomolecule is another biomolecule which has a high affinity to bond to it, such as an antigen is complementary to its antibody.

2) Blocking stage

This step consisted in blocking the glutaraldehyde molecules which were not bonded to the printed biomolecules in order to avoid any possible bonding of any other biomolecule (such as the tagged complementaries) to the glutaraldehyde. For the IgG experiments, the blocking agent was BSA. When BSA was printed, the blocking agent was ovalbumin diluted with PBS at a concentration of 10 mg/mL.

3) Complementary conjugation stage

After blocking, the substrate was immersed in a solution containing the complementaries of the printed proteins. In the case in which IgG was printed, the complementary used was anti-IgG, tagged to a cyanine molecule (Cy5, a fluorochrome which emits red light at 670 nm under excitation).

For the BSA experiments, BSA was not directly bonded to its tagged complementary, but an intermediate amplification process was carried out. The BSA was bonded to a non-specific complementary (IgG). Then, the IgG was bonded to its tagged complementary, anti-IgG with Cy5. Since each BSA molecule involved in the process can bond to several IgG molecules at the same time, this method produces an amplification of the fluorescence signal (each BSA molecule will result in much more fluorescent molecules than in the case of BSA directly bonded with tagged anti-BSA). Therefore, this method produced a clear sensibility increase.

### DNA protocol

1) Fixation stage

The DNA microarrays were cross-linked to the poly-L-lysine molecules of the receptor substrate using UV radiation in a Stratalinker at 130 mJ for 1 minute.

2) Blocking stage

The poly-L-lysine molecules which were not bonded to DNA molecules were blocked using a solution which consisted in a mixture of 17 mL of sodium borate (0.2 M, pH 8.0) and 150 mL of n-methyl-pyrollidone with 3 g of succinic anhydride previously dissolved in it.

3) Hybridization stage

The two DNA solutions were then submitted to a hybridization stage in order to bond them to their corresponding complementaries strands tagged with fluorochromes. A detailed description of this stage can be found in Colina 2006. It has to be pointed out that the complementary strand of MAPK3 was tagged with Cy5 (it emits red light with a wavelength of 670 nm under excitation), whereas the complementary of ETS2 was tagged with Cy3 (it emits green light with a wavelength of 570 nm under excitation). The concentration of the solutions containing the complementaries was 10 ng/µL.

After the described protocols, the substrates were left dry and then analyzed through the fluorescence scanner (*AxonInstruments*, *GenePix 4000*). This device uses light providing from a laser source to excite the fluorochromes. Two different laser sources could be used in order to excite Cy5 or Cy3 fluorochromes. For the first one, the laser source employed had a power of 10 mW, and emitted at a wavelength of 635 nm. The second laser source had a power of 17 mW and the emitted light had a wavelength of 543 nm. Both laser sources could be employed separately or simultaneously. The fluorescence signal was amplified using photomultiplier tubes and converted into an electrical signal, which was sent to a computer with the adequate software (*GenePix Pro 3.0*) to process the signal. The name scanner comes from the method used to analyze the sample, consisting in employing the laser source to scan all the desired area (the maximum scanned area is 22×72 $mm^2$). The maximum resolution of the technique was 5 µm, and the digital resolution was 16 bits.

## 2.5 Particular measuring methods

### 2.5.1 Beam dimensions characterization

In order to carry out a quantitative study of the transfer process, it is important to characterize the cross-sectional dimensions of the laser beam in the plane in which the radiation is absorbed, that is, at the titanium layer. This could have been done by simply placing the beam analyzer at the position where the titanium layer is situated. However, the laser beam energy density at that point was so high that it would have damaged the analyzer. Therefore, an alternative method was necessary. This was achieved through an indirect measurement, only valid for Gaussian beams, as it is described below.

The first step of this method consisted in the analysis, using the beam analyzer, of the laser beam intensity distribution (laser beam energy density) before the focalizing microscope (section 2.1, *optical system*). It was found that the beam energy density distribution corresponded to an elliptical Gaussian beam, which mathematical expression is:

$$F(x,y) = \frac{2E}{\pi\omega_x\omega_y} e^{-2\left(\frac{x^2}{\omega_x^2}+\frac{y^2}{\omega_y^2}\right)} \tag{2.1}$$

where $E$ is the laser beam energy, $\omega_x$ and $\omega_y$ are the major and minor beam radii, and $x$ and $y$ are the Cartesian coordinates along the major an minor axis, respectively. Then, a titanium coated microscope slide was placed at the position where the beam dimensions had to be determined (where the donor substrate would be further on situated), and a single laser shot was fired at different positions obtaining an array of ablated spots. Different laser pulse energies were used (always with an energy density higher than that corresponding to the ablation threshold of the titanium film), so that spots of different dimensions were obtained (Fig. 2.17a). The energy of each laser pulse was measured, and so were the dimensions of the spots. Since a Gaussian beam is still Gaussian after passing through any optical system (in our case, the

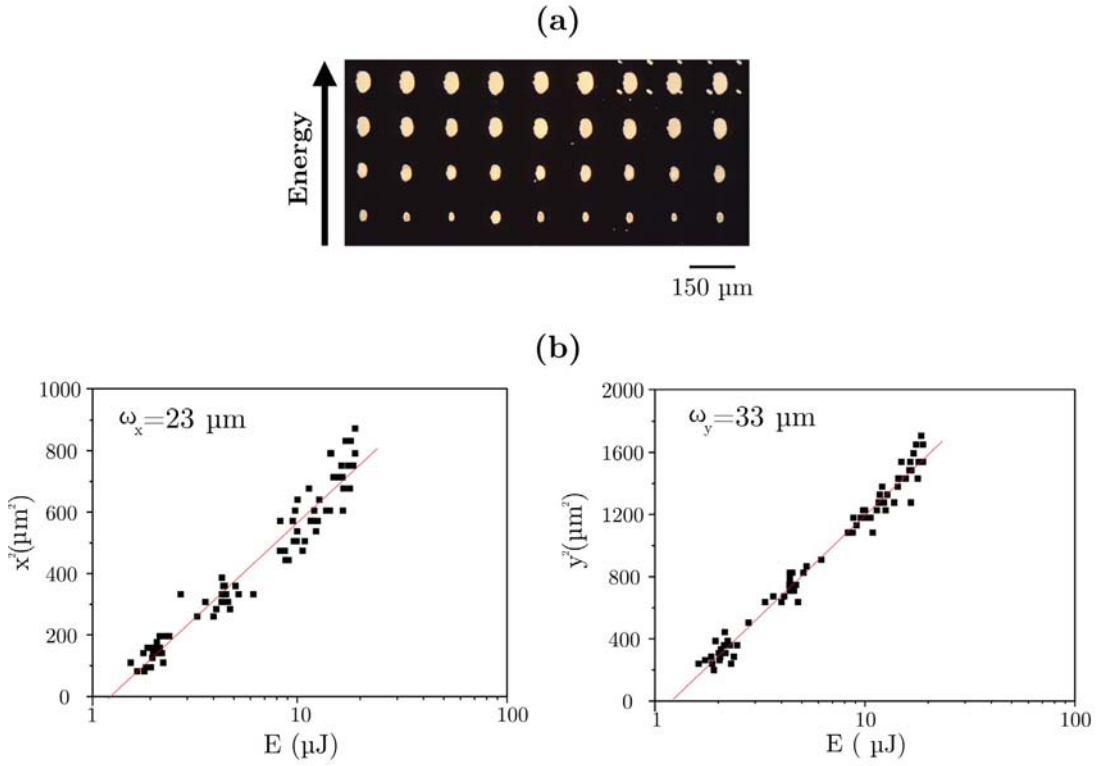


**Fig. 2.17.** a) Optical microscopy image of the ablated spots on the titanium film obtained at different laser pulse energies and fixed beam dimensions; b) Plot of the square of the x and y axis of the elliptical spots versus the laser pulse energy, which allowed obtaining the beam dimensions.

focusing objective), then it was possible to relate the spot dimensions with the laser pulse energy that ablated such spot, using the relationship:

$$x_j^2 = \frac{\omega_j^2}{2}\left(\ln E - \ln\left(\pi\omega_x\omega_y\frac{F_{th}}{2}\right)\right) \qquad (2.2)$$

where j can represent the $x$ or $y$ axis, and $F_{th}$ is the ablation energy density threshold of the titanium layer. Then, measuring the axis dimensions of the elliptical ablated spots, and plotting the squared values versus the logarithm of the laser pulse energy, it was possible to obtain the laser beam dimensions (Fig. 2.17b).

At this stage, an additional comment is required. Although the laser pulse energy is a basic parameter for the characterization of the laser beam, and it is

directly measured, it has an important inconvenient: it does not provide by itself any information about the laser beam effects on a determined material. That is, the capacity to ablate or produce any change to a material using a laser pulse depends on two factors: the laser pulse energy and the laser focusing conditions. Therefore, the parameter which is usually used to characterize a laser pulse is the so-called *laser fluence* ($F$), which relates these two factors: it corresponds to the laser pulse energy per unit cross-sectional area. Such definition, however, is controversial, since it is not always clear what stands for the cross-sectional area of a beam, and how to determine it. A common procedure consists in ablating a material with a laser and measuring the laser spots. Then, the laser spot is considered as a measure of the laser beam dimensions. However, this procedure is incorrect, since it depends strongly on the properties of the irradiated material. In the case of a Gaussian beam, though, it is possible to obtain the complete profile of the beam energy density from the laser spots obtained when ablating a particular material, as it has been described above. The access to the whole beam energy density profile allows the unambiguous determination of parameters related with the ideal concept of fluence. Then, an *average fluence* can be defined as:

$$F = \frac{E}{\pi \omega_x \omega_y}, \tag{2.3}$$

where $E$ is the laser pulse energy, and $\omega_x$ and $\omega_y$ are the major and minor beam semiaxis, respectively, of the elliptical beam. This procedure is correct, since it results in a universal parameter lack of ambiguities.

Another similar parameter that could also be used to characterize a Gaussian beam, instead of the average fluence, is the *peak energy density* ($F_P$). Such parameter corresponds to the peak of the Gaussian intensity (or energy density) profile, and is related to the average fluence as follows:

$$F_P = 2F, \tag{2.4}$$

and thus it is related to the laser pulse energy and beam dimensions,

$$F_P = \frac{2E}{\pi\omega_x\omega_y} \tag{2.5}$$

Therefore, for the different experiments reported in this work both *laser pulse energy* and *peak energy density* were usually provided. The first one as the parameter which was directly measured and the latter as the parameter which provided more information about the effects that the laser beam caused on the interacting material. It should be pointed out that in some parts of the thesis the term *fluence* was also employed to refer to *average fluence.*

### 2.5.2 Determination of the droplet volume

The droplet diameter is a parameter easy to measure through optical microscopy, and provides valuable technological information of the deposited droplets. Moreover, it also determines the resolution of the technique. However, this parameter depends on the wettability of the receptor substrate. On the other hand, the volume is independent of the nature of the receptor substrate, and thus it is a more adequate parameter in order to infer general laws on the transfer process.

The calculus of the droplet volume was carried out using two different methods. The first one (only used in the first four sections of chapter 3) consisted in the following steps:

1. Grazing-incidence microscopy images of some LIFT deposited circular droplets revealed that they presented a spherical cap shape with a fixed contact angle.
2. Circular and well-defined droplets printed at any irradiation condition were assumed to be spherical caps with the same contact angle $\theta$.
3. The volume of a spherical cap with a certain contact angle $\theta$ can be calculated provided its diameter $d$, through the relationship:

$$V = \frac{\pi d^3\left(2 - 3\cos\theta + \cos^3\theta\right)}{24\sin^3\theta} \tag{2.6}$$

4. The determination of the diameter of the printed droplets was measured using a graphics editor.

The second method to determine the volume of the printed droplets consisted in using optical profilometry to obtain the three-dimensional profiles of all the droplets. Using an appropriate software, the diameter and the contact angle of the droplets could be measured from these profiles. Then, the volume of the droplets was calculated using equation 2.6. This second method provided an accurate measurement of the droplet volume, only limited by the resolution of the optical profiler. On the contrary, the first method was based on the strong assumption that all droplets had the same contact angle, which limited its applicability. In fact, it was found that that assumption was only valid in a certain laser pulse energy range (section 3.5).

## Chapter 3

# Study of the influence of the LIFT process parameters on the morphology of the printed droplets

In this chapter, a detailed analysis of some of the main experimental parameters which affect the LIFT process is carried out. Although the effects of some parameters on the printed droplets have already been described [Serra *et al.* 2004a, 2004b, Colina *et al.* 2006], the series of experiments presented next uses that background to complete and extend those results, so that a more general picture of the LIFT of liquids is obtained. Moreover, this study is important from a technological point of view, since it provides information which allows the optimization of the technique.

This chapter is divided into eight sections, being the first three focused on the analysis of a different experimental parameter each: laser pulse energy, laser focusing conditions, and liquid film thickness. These parameters are varied systematically and the consequences of these variations on the deposited droplets are reported. The study is carried out both for biomolecule-free solutions and biomolecule-containing solutions. In the fourth section, an interpretation of the results obtained in the previous sections is provided, as well as a model to describe the LIFT process. The fifth section presents a study of the effects that the laser peak energy density has on the contact angle of the deposited droplets. The sixth section analyses another experimental parameter: the liquid film-receptor substrate distance. The seventh section uses the results of the other sections to obtain the smallest droplets ever printed with the present experimental setup, as a proof of concept achievable thanks to this

study. Finally, the eighth section tests the feasibility of the technique to print biomolecules without significant damage.

## 3.1 Influence of the laser peak energy density on the printed droplets

In a previous experiment (section 1.3.3), the effects of the laser pulse energy and the laser beam dimensions on the droplets printed through LIFT were analyzed. In that case, the liquid solution used was a biomolecule-free solution. Although the results of that study could be possibly extrapolated to biomolecule-containing solutions, an additional confirmation is convenient, since biomolecules can change the rheological properties of a solution.

In the present experiment, a study of the laser pulse energy effects on the LIFT printed droplets of an immunoglobulin G (IgG) solution was carried out (section 2.2.1). The choice of such protein was due to the fact that IgG is the most common antibody, and it has the capability to adapt and recognize different antigens, which makes it useful in many clinical applications, such as medical diagnostic or disease therapy.

The experiment consisted in the preparation of a microarray of 10 rows per 20 columns varying the laser pulse energy from row to row. The liquid film thickness was about 5 µm, and the liquid film-receptor substrate separation was 50 µm. The dimensions of the laser beam on the titanium layer were $\omega_x$=27 µm and $\omega_y$=19 µm.

An optical microscopy image of the printed microarray is presented in Fig. 3.1. It can be observed that droplets with a circular and well-defined contour were deposited at all positions where the laser was fired, except in the rows corresponding to the lowest three energies where some voids appear. The minimum energy to eject a droplet, $E_{min}$ (section 1.3.3), has a value of 1.6 µJ. The voids correspond to laser pulses with an energy lower than $E_{min}$, resulting from common laser fluctuations.

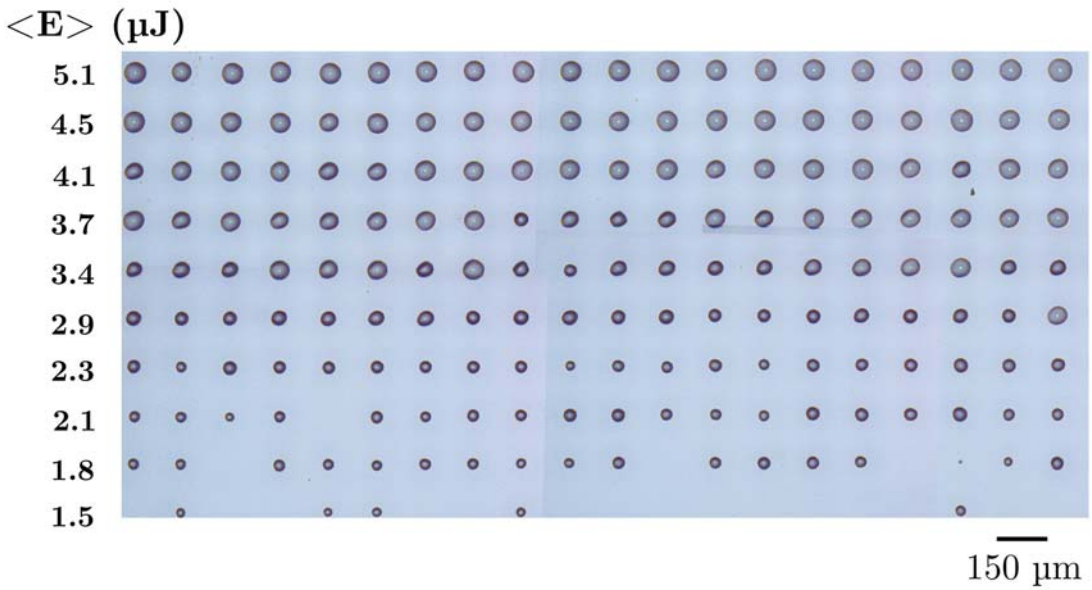


**Fig. 3.1.** Optical microscopy image of the IgG microarray. The values on the left correspond to the average laser pulse energy per row.

Another relevant aspect in the present experiment is the droplet diameter increase with the laser pulse energy. The smallest droplets are obtained at energies slightly above $E_{min}$, which constitutes the maximum resolution of the technique for the given laser beam dimensions. In this case, droplets with a diameter of 25 µm were printed, a value similar to that obtained with other biological solutions on identical substrates [Fernández-Pradas *et al.* 2004, Colina *et al.* 2005], and considerably smaller than the minimum ones obtained with commercial arrayers [Barron *et al.* 2005a]. The value of $E_{min}$ can be related to a peak energy density, $F_1$, through the equation 2.5. This last parameter constitutes the energy density threshold for the deposition process (table 3.1).

In order to provide a quantitative analysis of the present results, the droplet

**Table 3.1.** Major ($\omega_x$) and minor ($\omega_y$) beam radii, minimum laser pulse energy necessary to deposit a droplet ($E_{min}$), corresponding peak energy density ($F_1$), and fitting parameters ($C$ and $F_0$) for the microarray of Fig. 3.1.

| $\omega_x$ $(\mu m)$ | $\omega_y$ $(\mu m)$ | $E_{min}$ $(\mu J)$ | $F_1$ $(J/cm^2)$ | $C$ $(pLcm^2/J)$ | $F_0$ $(J/cm^2)$ |
|---|---|---|---|---|---|
| 27 | 19 | 1.6 | 0.19 | 17 | 0.15 |

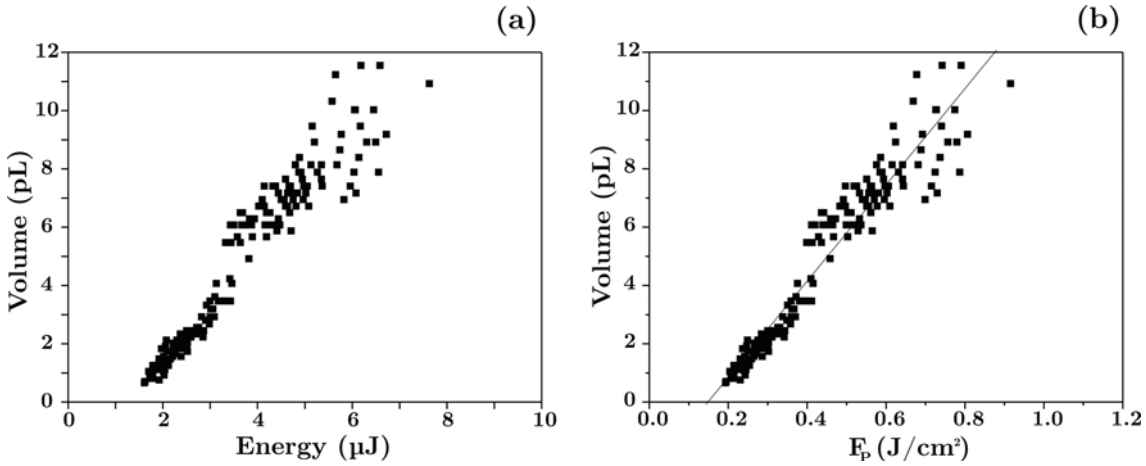


**Fig. 3.2.** Plot of the deposited droplet volume versus a) the laser pulse energy, and b) the laser pulse peak energy density. The solid line corresponds to the linear fit.

volumes were calculated and plotted versus the laser pulse energy $E$ (Fig. 3.2a). In this occasion, the volume was calculated using the first method described in section 2.5.2, in which all droplets were assumed to be spherical caps with the same contact angle. As it can be observed, the points present an upward trend, with a linear dependence between droplet volume and laser pulse energy. Such results are in good agreement with those obtained for a biomolecule-free solution [Colina *et al.* 2006], in which a linear relationship between droplet volume and laser pulse energy was also found. However, in the present case two clearly differentiated regions can be observed: for laser pulse energies up to 4 µJ all points are quite well aligned, with little dispersion, while for higher laser pulse energies, a significant and sudden increase in the dispersion of the droplet volumes is produced, as well as a slight shift towards upper volumes. Such change, which could be attributed to the activation of a different deposition mechanism at high energies, will be discussed in the next sections. In fact, in chapter 4 a time-resolved analysis of the deposition process will allow elucidating the different mechanism responsible for the observed transition.

The plot of the droplet volume versus the peak energy density ($F_p$) presented in Fig. 3.2b also reveals a linear relationship between these two parameters, otherwise obvious, since $F_p$ and $E$ are proportional (section 2.5.1). Such linear dependence can be characterized through the simple fit:

$$V = C(F_P - F_0)\,, \tag{3.1}$$

where $V$ is the droplet volume, $F_P$ is the laser peak energy density, and $C$ and $F_0$ are the fitting parameters. The values of these parameters are presented in table 3.1.

The interpretation of equation 3.1 suggests that $F_0$ is the energy density threshold which must be overcome in order to deposit a droplet. However, as it has been previously stated, a droplet is only deposited if the energy density surpasses a certain value $F_1$, higher than $F_0$ (see table 3.1). The parameter $F_0$ can be then considered the threshold which sets the initiation of the transfer process, that is, a primary threshold that must be surpassed in order to originate an impulsion in the liquid film. However, only if the laser energy density overcomes $F_1$ the impulsion is energetic enough to cause material release. In chapter 4, it will be shown that this impulsion is due to the generation of a cavitation vapor bubble inside the liquid film.

In a previous experiment using a biomolecule-free solution [Colina *et al.* 2006], the finding of the parameter $F_0$ led to establishing a model which provided an oversimple description of the transfer process. According to that model, the amount of transferred material would be given by the volume of the cylinder which base corresponds to the points where the threshold is overcome (energy density $F>F_0$), and which height corresponds to the liquid film thickness ($d$), as indicated in Fig. 1.7.

In order to test the validity of that model for the present solution, the droplet volume was plotted versus the volume of the mentioned cylinders (Fig. 3.3). The cylinder volumes were calculated as $\pi x_0 y_0 d$, where $x_0$ and $y_0$ are respectively the maximum and minimum radii of the elliptical intersection of the Gaussian distribution and $F_0$ (Fig. 1.7). As it can be observed in Fig. 3.3, for cylinder volumes up to 4 pL all the points lie close to (and slightly below) the unit-slope line, which means that the model describes rather correctly the transfer process in this situation, which corresponds to the low-energy (or low peak energy density) range. However, for higher energies (or peak energy densities), the

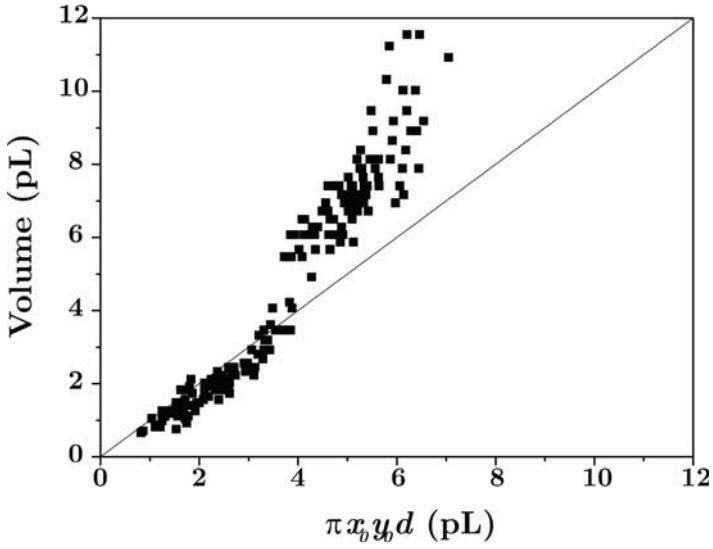


**Fig. 3.3.** Plot of the droplet volume versus the volume of the cylinders of the model. The solid line represents the unit slope line.

volume of the transferred droplets is shifted clearly above the unit-slope line, which means that the cylinder model cannot be successfully applied in this energy range. This could be attributed to two different effects:

1. At high laser peak energy densities, border effects could become relevant. For instance, liquid drag from the borders of the area delimited by $F_0$ could result in an additional contribution of material which is not considered in the cylinder model.

2. The possible activation of a different deposition mechanism at high peak energy densities could also account for such increase in the amount of transferred material. In fact, the values which do not fit to the cylinder model correspond to the high energy region found in Fig. 3.2.

In conclusion, it has been observed that circular and well defined droplets of an IgG solution were successfully printed through LIFT, with a volume that increases linearly with the laser peak energy density. The process is activated by two thresholds: $F_0$ which must be surpassed in order to produce an impulsion on the liquid which initiates the transfer process, and $F_1$, higher than $F_0$, which

must be overcome in order to produce the deposition of a droplet. It has also been found that the previously proposed cylinder model correctly describes the transfer process at low energies but not at high energies. All this allows stating that the effects of the laser pulse energy on the printed droplets for the present biomolecule-containing solution do not seem to significantly differ from those previously obtained with a biomolecule-free solution.

## 3.2 Influence of the focusing conditions on the printed droplets

In the previous section, the effects of the laser pulse energy on the deposited droplets for given beam dimensions were analyzed. However, the effects of varying the laser focusing conditions on the deposited droplets for a biomolecule-containing solution have not yet been studied.

In this section, such study is presented. A protein solution was also used, but in this case it was a bovine serum albumin (BSA) solution (section 2.2.1). The choice of BSA was mainly carried out for two reasons: it is widely used in numerous biochemical applications, such as Enzyme-Linked Immunosorbent Assay (ELISAs), and it is a biomolecule-containing solution different from that used in section 3.1, which allows increasing the number of solutions deposited through LIFT and thus testing the general validity of the obtained results.

This experiment consisted in the preparation of two microarrays of 8 rows per 26 columns at different laser focusing conditions, each one varying the laser pulse energy from row to row. The liquid film had a thickness of 8 µm, and the liquid film-receptor substrate separation was 50 µm. The dimensions of the laser beam on the titanium layer were $\omega_x$=8 µm and $\omega_y$=6 µm for the first microarray, and $\omega_x$=34 µm and $\omega_y$=23 µm for the second one. It has to be noted that the first microarray was prepared at stronger focusing conditions than those used in preceding works. This was done since it is known [Colina *et al.* 2006] that the smaller the beam dimensions the smaller the diameter of the printed droplets.

An optical microscopy image of a portion of the first microarray is presented in Fig. 3.4a. It can be clearly observed that the deposited droplets have in all cases a circular contour, with a diameter that increases with the laser pulse energy. In this experiment, the value of $E_{min}$ is 0.3 µJ, and the corresponding peak energy density $F_1$ is 0.4 µJ/cm$^2$ (table 3.2).

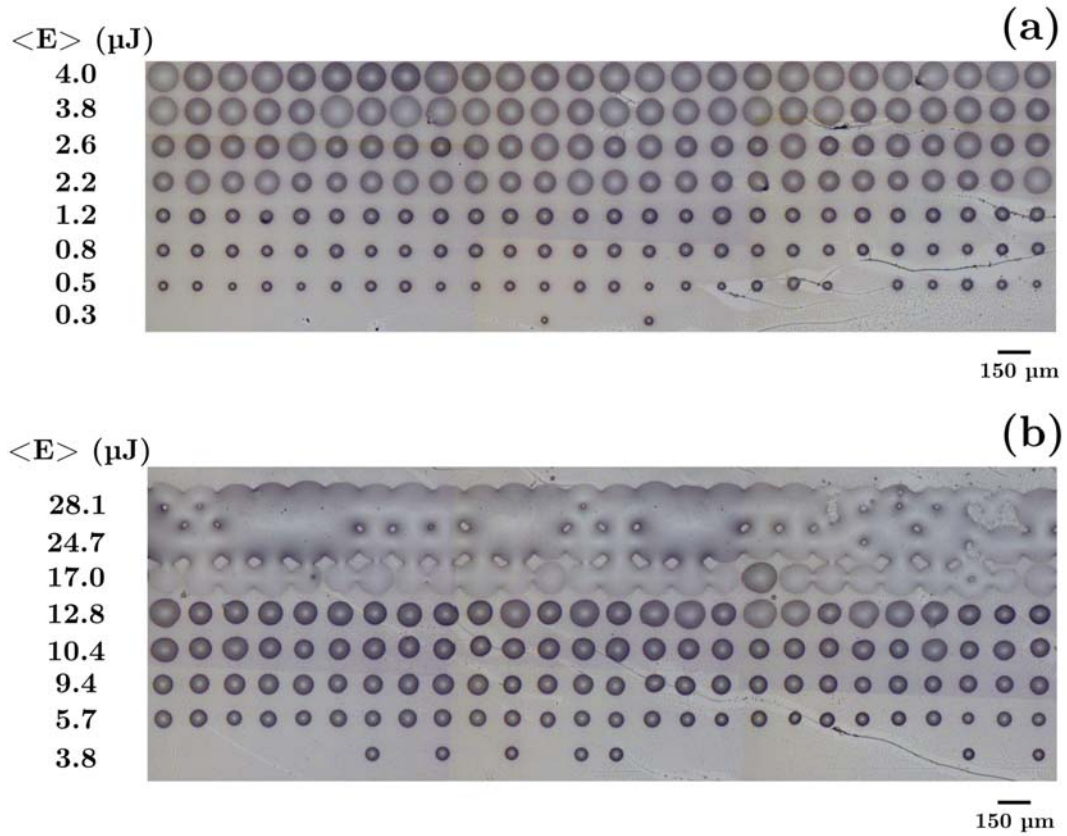


**Fig. 3.4.** Optical microscopy images of the BSA droplets deposited at two different beam dimensions: (a) $\omega_x$=8 $\mu m$, $\omega_y$=6 $\mu m$, (b) $\omega_x$=34 $\mu m$, $\omega_y$=23 $\mu m$. The values represented on the left of each row correspond to the average energy at which the droplets in that row were transferred.

A quantification of these results was also carried out by calculating the volume of each droplet, as it was done in the previous section, and plotting it versus the laser pulse energy and the corresponding laser peak energy density ($F_P$) (Fig. 3.5). The experimental data present two different linear behaviors: for low energies (or low peak energy densities), the points are well aligned, with little

**Table 3.2.** Major ($\omega_x$) and minor ($\omega_y$) beam radii, minimum laser pulse energy necessary to deposit a droplet ($E_{min}$), corresponding peak energy density ($F_1$), and fitting parameters ($C$ and $F_0$) for the two microarrays of the BSA solution prepared at different focusing conditions.

| $\omega_x$ ($\mu m$) | $\omega_y$ ($\mu m$) | $E_{min}$ ($\mu J$) | $F_1$ ($J/cm^2$) | $C$ ($pLcm^2/J$) | $F_0$ ($J/cm^2$) |
|---|---|---|---|---|---|
| 8 | 6 | 0.3 | 0.4 | 2.3 | 0.24 |
| 34 | 23 | 4 | 0.3 | 22 | 0.26 |

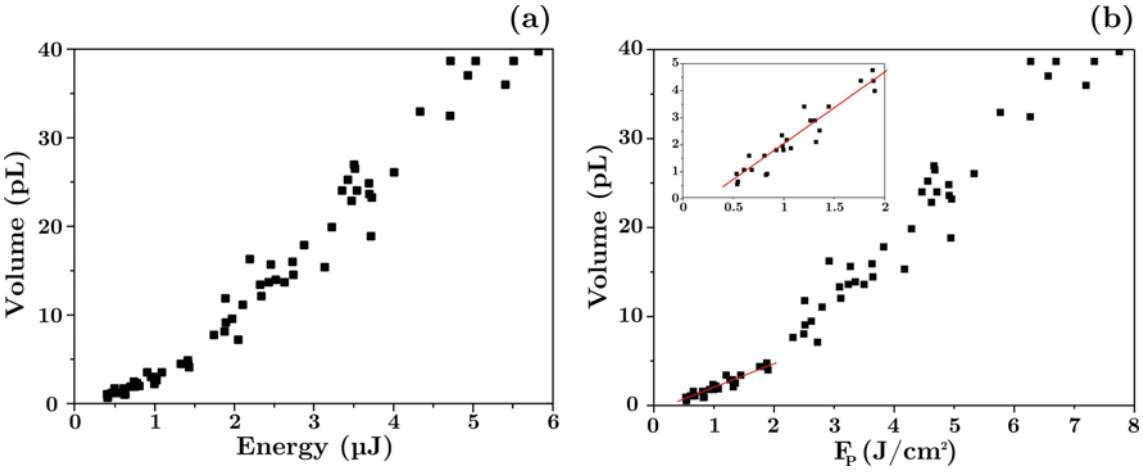


**Fig. 3.5.** Plot of the deposited droplet volume versus a) the laser pulse energy, and b) the laser peak energy density, for a beam which dimensions were $\omega_x$=8 $\mu m$, $\omega_y$=6 $\mu m$. The inset shows a magnification of the points corresponding to the low peak energy densities, and the solid line is the linear fit.

dispersion; for energies higher than 1.5 µJ (or peak energy densities higher than 2 J/cm$^2$) there is an increase in the slope, as well as an increase in the points dispersion. The increase in the slope will be demonstrated to be due to an inadequacy of the method used to calculate the volume, which will be clarified in section 3.5. The increase in the points dispersion could again be attributed to the activation of a different transfer mechanism, as will be reported in chapter 4. A simple linear fit to equation 3.1 of the points in the low-energy density range allows obtaining the values of $C$ and $F_0$ (table 3.2) for the present experiment. It can be observed that the parameter $F_0$ is of the same order as in the previous experiments. This agrees with the interpretation of this parameter, since the energy density required to originate a bubble in the liquid film must be similar for two aqueous solutions, provided that a similar absorbing layer is used. The parameter $F_0$ must be therefore independent of the liquid film thickness and the laser beam dimensions.

The cylinder model, which relates the amount of deposited liquid to the parameter $F_0$, was also tested for the present experiment. In Fig. 3.6 the plot of the droplet volume versus the volume of the corresponding elliptical cylinder is presented. The volume of such cylinder was calculated as $\pi x_0 y_0 d$ (section 3.1). It can be observed that all the points lie well above the unit slope line, which means that the amount of transferred material is in general significantly higher

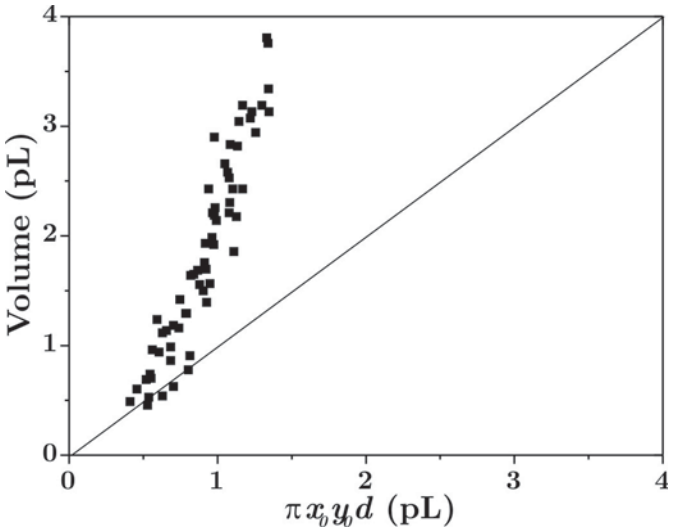


**Fig. 3.6.** Plot of the droplet volume versus the volume of the cylinders of the model, for a beam with dimensions: $\omega_x$=6 $\mu m$, $\omega_y$=8 $\mu m$. The solid line represents the unit slope line.

than the volume of the considered cylinder and that, therefore, the model does not describe the present situation correctly. This clearly contrasts with the results obtained with both a biomolecule-free solution (section 1.3.3), and the previous biomolecule-containing solution (section 3.1). The differences observed with those experiments could be attributed to two effects: the use of a solution different from the previous ones, which does not seem likely since it has been observed that the behavior of different aqueous solutions is similar; or the fact that the present experiment was performed under much stronger focusing conditions than ever in the past. Actually, in the previous cases (section 1.3.3 and 3.1) the beam dimensions were considerably larger than the liquid film thickness, whereas in the present situation they are similar (Fig. 3.7). In order to test whether the beam dimensions were the parameter that really played a key role in the failure of the model, and thus verify its possible influence on the degree of validity of the model, the second microarray was prepared at larger beam dimensions placing the titanium layer 300 µm above the focal plane.

The droplets obtained in this second microarray (Fig. 3.4b) also present an increase in its diameter with the laser pulse energy. In this case, the minimum deposition energy ($E_{min}$) is about 4 µJ, much higher than at strong focusing conditions, as is the minimum droplet diameter, but the corresponding threshold

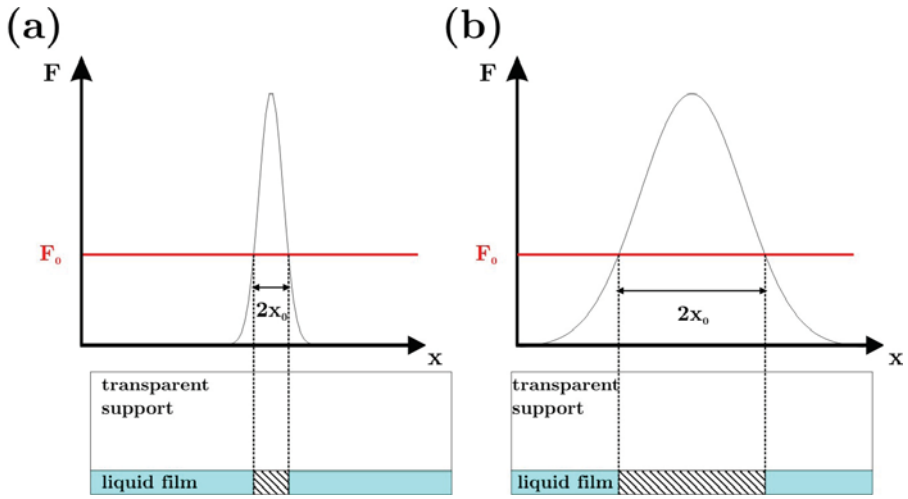


**Fig. 3.7.** Scheme of the cylinder model showing the energy density distribution for (a) $\omega_x$=8 $\mu m$, $\omega_y$=6 $\mu m$, (b) $\omega_x$=34 $\mu m$, $\omega_y$=23 $\mu m$. The striped areas correspond to the cylinder of the model and, therefore, to the transferred material which the model predicts.

$F_1$ is 0.3 J/cm$^2$, similar to that of the previous experiment (table 3.2). In order to compare this experiment with the previous one, the droplet volume of this second microarray was also measured and plotted versus the laser pulse energy and the laser peak energy density (Fig. 3.8). A linear dependence is found again, and two regions can also be distinguished: at low energies, the points have a smaller dispersion than the points obtained at energies higher than 8 µJ. In this case, however, no change in the slope at high energies is appreciated. From the linear fit of equation 3.1 the new values of $C$ and $F_0$ were obtained and depicted

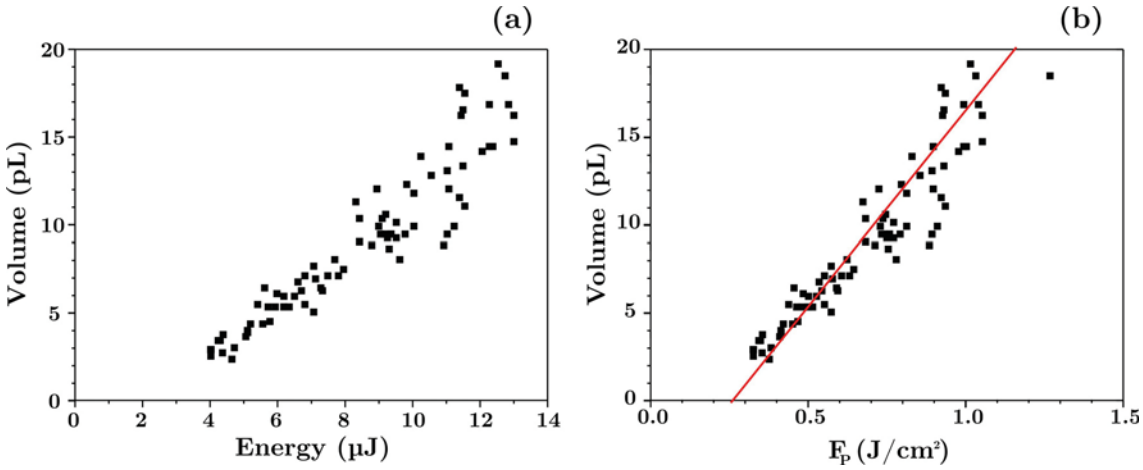


**Fig. 3.8.** Plot of the deposited droplet volumes versus a) the laser pulse energy, and b) the laser peak energy density, for a beam which dimensions were $\omega_x$=34 $\mu m$, $\omega_y$=23 $\mu m$. The solid line corresponds to the linear fit.

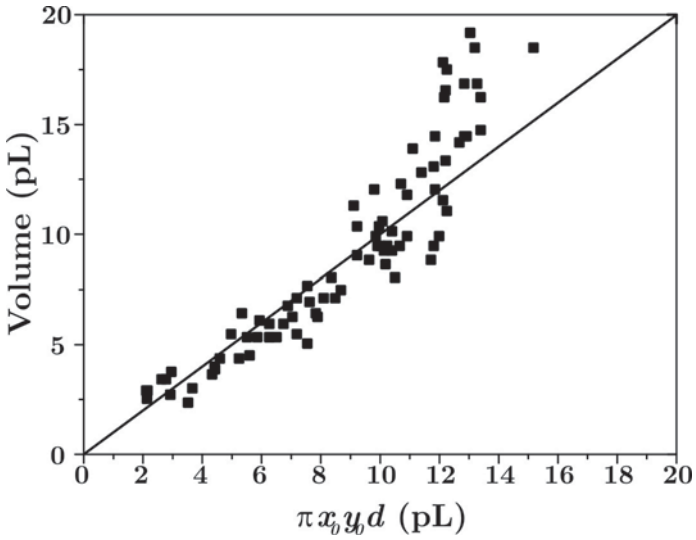


**Fig. 3.9.** Plot of the droplet volume versus the volume of the cylinders of the model, for a beam with dimension: $\omega_x$=34 $\mu m$, $\omega_y$=23 $\mu m$. The solid line represents the unit slope line.

in table 3.2. It has to be noted that $F_0$ has nearly the same value as in the first experiment. This shows that $F_0$ is indeed independent of the laser focusing conditions and that, therefore, it really constitutes a true energy density threshold for the initiation of the transfer process, as it was supposed to be. The droplet volume was then plotted versus the elliptical cylinder of the model (section 3.1) as it had been previously done (Fig. 3.9). It can be observed that most of the points are distributed close to and slightly below the unit slope line, except those corresponding to high energies, a situation that clearly resembles that of Fig. 3.3. All this indicates that the cylinder model describes pretty well the transfer process in situations in which the laser beam dimensions are significantly larger than the liquid film thickness, as it occurred in most of the previous experiments.

Finally, a possible explanation of the adequacy of the cylinder model is provided. The expression corresponding to the volume of the cylinder ($V_{cil}=\pi x_0 y_0 d$, where $x_0$ and $y_0$ are respectively the maximum and minimum radii of the intersection of the Gaussian distribution and $F_0$, and $d$ is the liquid film thickness) will be analyzed, and it will be related to the laser pulse energy $E$.

Considering the energy density distribution *F(x,y)* of an elliptical Gaussian beam with energy $E$ and beam radii $\omega_x$ and $\omega_y$ (equation 2.1):

$$F(x,y) = \frac{2E}{\pi\omega_x\omega_y} e^{-2\left(\frac{x^2}{\omega_x^2}+\frac{y^2}{\omega_y^2}\right)},$$

it is possible to calculate the values of $x_0$ and $y_0$ as:

$$x_0 = \frac{\omega_x}{\sqrt{2}}\sqrt{\ln\left(\frac{2E}{\pi\omega_x\omega_y F_0}\right)} \qquad y_0 = \frac{\omega_y}{\sqrt{2}}\sqrt{\ln\left(\frac{2E}{\pi\omega_x\omega_y F_0}\right)} \tag{3.2}$$

With the results detailed in section 1.3.3, $F_0$ can be related to $E_0$ through the equation[5] $E_0 = \frac{\pi\omega_x\omega_y F_0}{2}$, which allows expressing $x_0$ and $y_0$ as:

$$x_0 = \frac{\omega_x}{\sqrt{2}}\sqrt{\ln\left(\frac{E}{E_0}\right)} \qquad y_0 = \frac{\omega_y}{\sqrt{2}}\sqrt{\ln\left(\frac{E}{E_0}\right)} \tag{3.3}$$

Therefore, the volume of the cylinder ($V_{cil}$) can be related to the laser pulse energy as follows:

$$V_{cil} = \pi x_0 y_0 d = \frac{\pi\omega_x\omega_y d}{2}\ln\left(\frac{E}{E_0}\right) \tag{3.4}$$

According to the cylinder model, the above equation must be equivalent to that which relates the deposited volume $V$ with the laser pulse energy, $V = K(E - E_0)$ (equation 1.1). It is evident that the two equations do not coincide, and therefore, it is clear that the model cannot provide a complete description of the transfer process for the entire space of experiments. However, under some conditions the droplet volume can be indeed rather well approximated by the volume of the cylinder model, as it has been experimentally demonstrated.

Actually, it is possible to give a qualitative interpretation of why the cylinder model only describes correctly the transfer process when the dimensions of the laser beam are larger than the liquid film thickness. As it was mentioned above, the cylinder base would correspond to the area of the cavitation vapor bubble produced in the liquid. Then, this bubble can be considered to expand acting as

[5] $E_0$ is the energy of a Gaussian beam of radii $\omega_x$ and $\omega_y$ and peak energy density $F_0$.

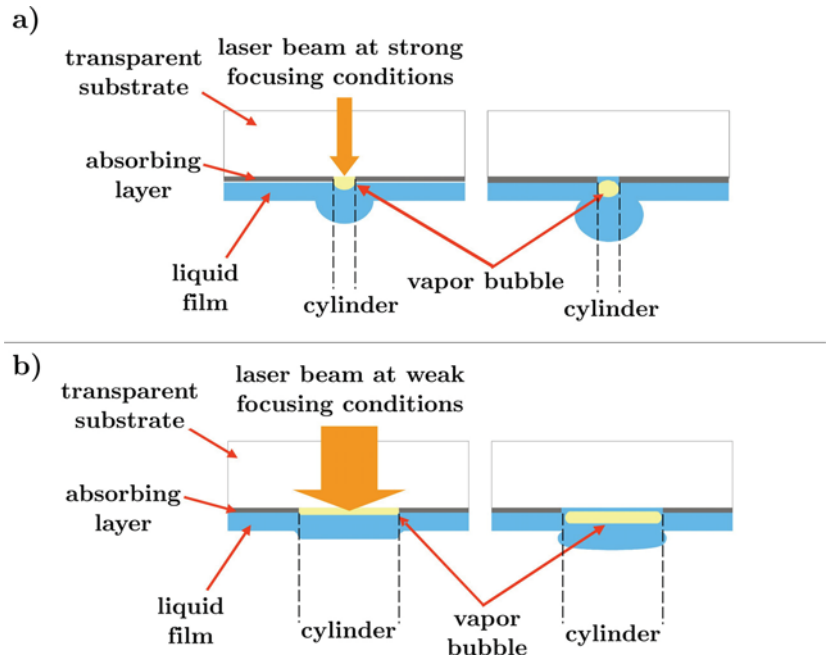


**Fig. 3.10.** Scheme of the proposed transfer process: a) beam dimensions similar or smaller than the liquid film thickness (point impelling force); b) beam dimensions larger than the liquid film thickness (piston effect)

a piston that pushes the liquid that lies below it. It would be expected then that only when the piston dimensions are much larger than the liquid film thickness the ejected material will in fact correspond to the disc that lies below this piston. If the bubble area is equal to or smaller than the liquid film thickness, the bubble effect would be expected to be closer to that of a point impelling force, removing an amount of material which will be higher than that corresponding to the cylinder defined by the area of the initial bubble (Fig. 3.10). Further discussion about this issue is presented in chapter 4 after the acquisition of time-resolved images of the process at different focusing conditions.

In conclusion, it has been observed that smaller droplet diameters were obtained for smaller beam dimensions. Again, a linear relationship between droplet volume and peak energy density was found for the two focusing conditions analyzed, which also present the same value for the threshold $F_0$. However, when the beam dimensions are similar or smaller than the liquid film thickness, the cylinder model does not describe well the transfer process.

## 3.3 Influence of the liquid film thickness on the printed droplets

The other main parameter which could affect the characteristics of the printed droplets and which effect has not yet been studied is the liquid film thickness. In the previous experiments, films of different thicknesses have been used, but a systematic study has not been carried out. Therefore, it has not yet been possible to obtain a clear correlation between this parameter and the morphology of the printed droplets. In the present experiments, it was attempted to fill this void: different microarrays were prepared using liquid films of different thicknesses, and the morphology of the printed droplets was analyzed. The solution used in these experiments was the BSA solution described in section 2.2.1.

In a first experiment, three microarrays of the BSA solution were prepared at fixed laser beam dimensions and varying the laser pulse energy from row to row. Each of these three microarrays was obtained using donor substrates with liquid films of different thicknesses. The preparation of the liquid films was achieved using spin coating. Controlling the angular speed of the spinning, three different films with a thickness of 5 µm, 7 µm and 10 µm were obtained (the thickness was estimated through the film weight). The liquid film-receptor substrate separation was 50 µm, and the dimensions of the laser beam on the titanium layer were again the smallest possible ($\omega_x$=8 µm and $\omega_y$=6 µm).

In Fig. 3.11 an optical microscopy image of each microarray is presented. It can be observed that the droplet diameter increases with the laser pulse energy, as it occurred in the previous experiments, and also that it increases with film thicknesses for fixed irradiation conditions. Therefore, it exists a direct correlation between the liquid film thickness and the amount of deposited material. In order to quantify this, the droplet volume was calculated and plotted versus the laser pulse energy (Fig. 3.12a). It can be observed that all the points corresponding to the different microarrays present a linear dependence, as

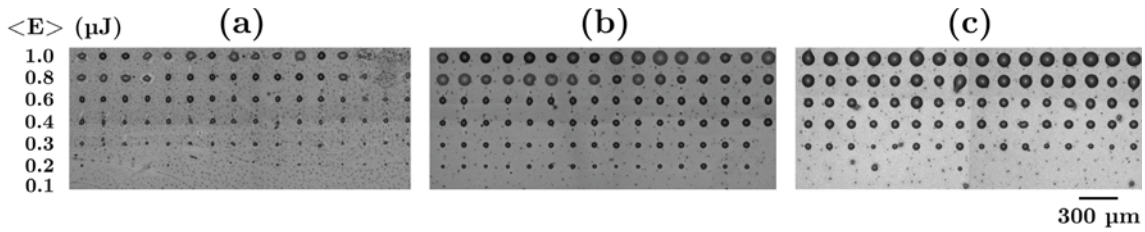


**Fig. 3.11.** Optical microscopy images of the three prepared microarrays varying the laser pulse energy from row to row (average energy values indicated on the left). The thickness of the liquid films used were: (a) 5 µm, (b) 7 µm, and (c) 10 µm.

it was found in the experiments of the previous sections, with a slope increasing as the film thickness is increased. The minimum laser pulse energy required to deposit a droplet ($E_{min}$) also increases with the liquid film thickness (table 3.3).

The plot of the volume versus the laser peak energy density ($F_P$) reveals the same behavior (Fig. 3.12b), since the three microarrays were prepared using the same laser beam dimensions, and thus in the three cases $E$ and $F_P$ are proportional, with the same factor of proportionality. The points can be then fitted to equation 3.1. The values of the fitting parameters are presented in table 3.3. The parameter $C$ can be regarded as the process efficiency (it is proportional to $K$ with the same factor of proportionality). Thus, the process efficiency increases significantly with the film thickness. This can be clearly

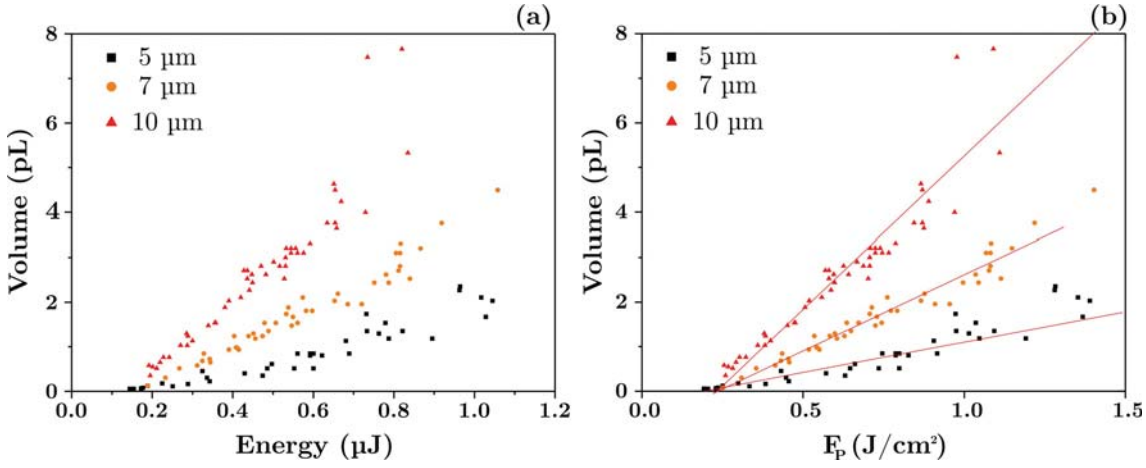


**Fig. 3.12.** Plot of the droplet volume versus a) the laser pulse energy; and b) the laser peak energy density ($F_P$), for each of the liquid films employed (thicknesses indicated in the figure legend). The solid lines are the respective linear fits.

**Table 3.3.** Liquid film thickness, major ($\omega_x$) and minor ($\omega_y$) beam radii, minimum laser pulse energy necessary to deposit a droplet ($E_{min}$), corresponding energy density threshold ($F_1$), and fitting parameters ($C$ and $F_0$).

| *Film thickness* ($\mu m$) | $\omega_x$ ($\mu m$) | $\omega_y$ ($\mu m$) | $E_{min}$ ($\mu J$) | $F_1$ ($J/cm^2$) | $C$ ($pLcm^2/J$) | $F_0$ ($J/cm^2$) |
|---|---|---|---|---|---|---|
| 5 | 8 | 6 | 0.15 | 0.20 | 1.1 | 0.17 |
| 7 | 8 | 6 | 0.17 | 0.22 | 3.4 | 0.22 |
| 11 | 8 | 6 | 0.19 | 0.25 | 6.9 | 0.21 |

observed in the plot of the $C$ parameter versus the liquid film thickness (Fig. 3.13). Actually, there seems to exist a quite linear relationship between these two parameters[6]. On the other hand, $F_0$ presents a similar value for the three microarrays analyzed (especially for the thicknesses of 7 and 10 µm), a value which is in addition close to that found in previous experiments [Colina *et al.* 2006]. This is consistent with the interpretation of $F_0$ as the threshold to initiate the transfer process: it must depend on the absorption of the laser radiation in the titanium layer and on the liquid properties (such as the boiling temperature), but not on the liquid film thickness, which should not play any role at this point. Finally, the parameter $F_1$ (minimum energy density required to deposit a droplet) increases with the liquid film thickness: the thicker the liquid film the higher the energy required to overcome the forces opposed to liquid ejection.

In conclusion, it has been observed that the droplet diameter increases with the film thickness for given irradiation conditions. Moreover, the amount of deposited material per laser pulse energy (process efficiency), as well as the minimum energy density required to eject a droplet ($F_1$), increase when

[6] Such statement cannot be considered concluding, since the inference has been carried out from only three experimental points. However, the excellent alignment between them makes the comment worth mentioning.

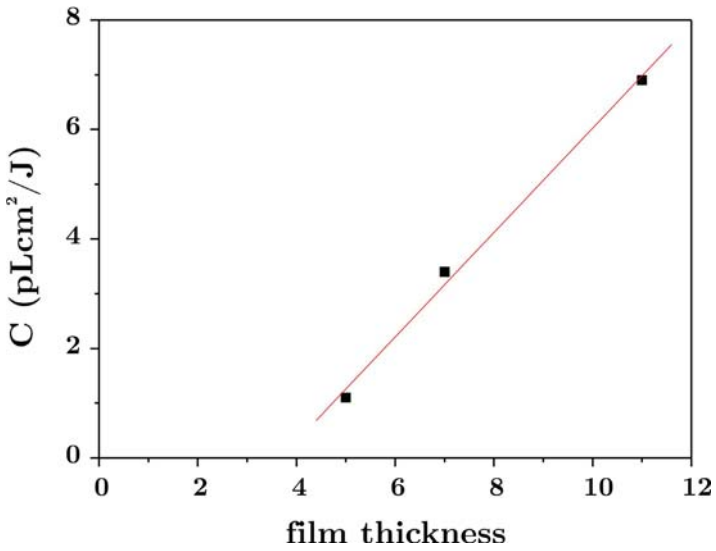


**Fig. 3.13.** Plot of the C parameter (representing the process efficiency) versus the liquid film thickness.

increasing the liquid film thickness. These results are also in good agreement with the interpretation of the threshold $F_0$ described above.

## 3.4 Interpretation of the relationship between droplet volume and laser pulse energy

Although in the previous sections some results have been found which allow a better understanding of the LIFT process (for instance the finding of the energy density threshold $F_0$) there are still several aspects which have not yet been interpreted. Therefore, it has been considered convenient to add a section to discuss them. In this section, no new experimental results are presented, but the previous ones are examined and interpreted in more detail.

All the discussions presented next arose when trying to answer the following question: which is the physical meaning of $E$-$E_0$? Before answering it, some results previously found should be recalled. The volume of the printed droplets presents a linear relationship with the laser peak energy density through the equation $V = C(F_P - F_0)$, in which $F_0$ has been proved to be an energy density threshold which initiates the transfer process. In terms of energy, the same equation can be rewritten as $V = K(E - E_0)$, in which $E_0$ is the total energy of a Gaussian beam with a peak energy density equal to $F_0$ (section 1.3.3). According to this, $E$-$E_0$ would correspond to the grey area depicted in Fig. 3.14a[7]. Thus, the volume of the printed droplets is proportional to this colored area. However, this does not seem consistent with the idea of $F_0$ as a threshold: zones in the absorbing layer beyond that delimited by $F_0$ seem to contribute to liquid ejection (the grey area extends beyond the $2x_0$ long zone delimited by $F_0$). A further analysis of $E$-$E_0$ (appendix) allows relating this expression to the value $E_A$, corresponding to the colored area of Fig. 3.14b; in fact, it turns out that $E - E_0 = E_A$. Therefore, the relation:

$$V = KE_A, \tag{3.5}$$

holds, in which $E_A$ is the fraction of the energy of the incoming laser pulse corresponding to the points with an energy density larger than $F_0$. This new

[7] In fact, to the volume equivalent to the grey area in the three-dimensional plot, since $F$ is a function of both $x$ and $y$. Fig. 3.14 corresponds to a section of the three-dimensional plot along the $y=0$ plane.

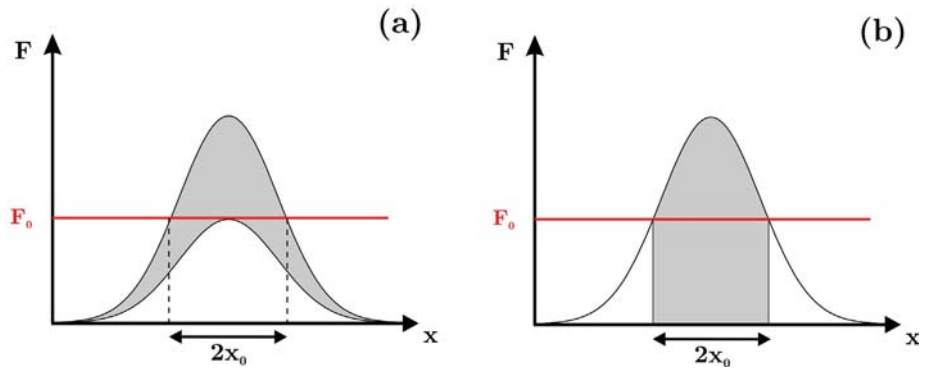


**Fig. 3.14.** Two dimensional representation of the laser pulse energy density distribution ($F$) of the Gaussian beam. The solid horizontal line corresponds to the transfer threshold $F_0$. (a) The grey area is $E$-$E_0$. (b) The grey area is $E_A$.

expression is perfectly consistent with the idea of $F_0$ as a threshold and allows answering the initial question: $E$-$E_0$ is the fraction of the laser pulse energy that directly contributes to liquid ejection.

With this new finding, the results of the previous experiments can be expressed in terms of $E_A$. The droplet volume was plotted versus $E_A$ for each of them, and presented in Fig. 3.15. In all cases the proportionality relation with $E_A$ obviously holds. It is also interesting to remark the behavior of the proportionality constant $K$ (table in Fig. 3.15). In the case of Fig. 3.15a in which the laser beam dimensions were varied, $K$ presents the same value at all the focusing conditions. On the contrary, in the BSA solution experiment (Fig. 3.15c and 3.15d) the $K$ value is higher for smaller beam dimensions. Such differences in the $K$ value could be attributed to the fact that the laser beam size in Fig. 3.15c was comparable to the liquid film thickness, whereas in all the previous cases the laser beam size was much larger than the liquid thickness (section 3.2). Therefore, it seems that the process efficiency (parameter $K$) depends on the relation between *laser beam size* and *liquid film thickness*. In fact, in the experiment in which the liquid film thickness was varied (Fig. 3.15e) at fixed laser beam size, $K$ increases with the thickness, which is also consistent with the mentioned $K$ dependence. In order to reveal this dependence, a plot of the $K$ parameter versus the fraction *laser beam size/liquid thickness* is presented in Fig. 3.16. It can be observed that the $K$ parameter does not present an injective

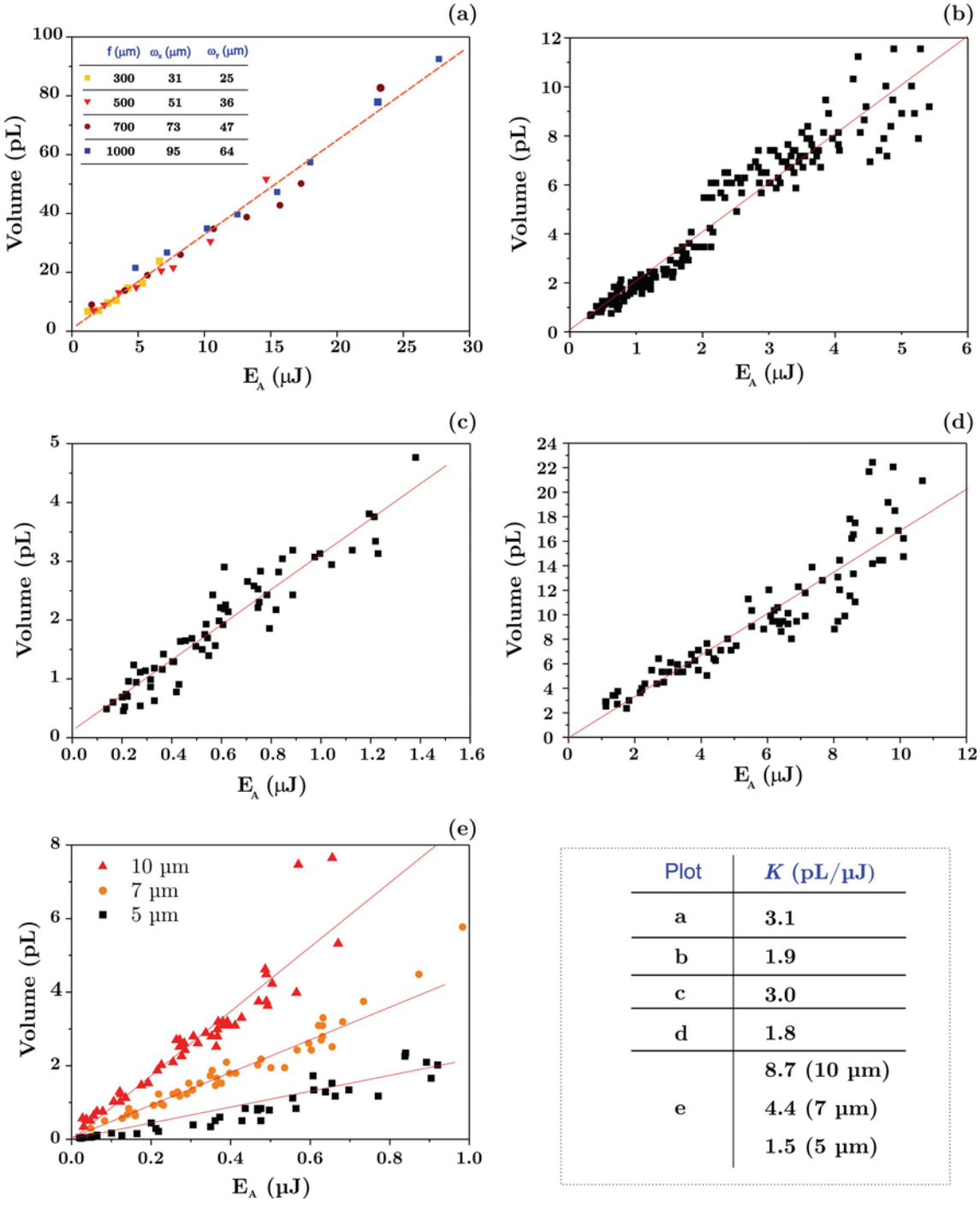


| Plot | $K$ (pL/µJ) |
|---|---|
| a | 3.1 |
| b | 1.9 |
| c | 3.0 |
| d | 1.8 |
| e | 8.7 (10 µm) |
| | 4.4 (7 µm) |
| | 1.5 (5 µm) |

**Fig. 3.15.** Plot of the droplet volume versus $E_A$ for: a) the experiment varying the laser beam dimensions using the water+glycerol+SDS solution (section 1.3.3); b) the experiment using the IgG solution (section 3.1); c) the experiment using the BSA solution (section 3.2) and $\omega_x$=8 *µm*, $\omega_y$=6 *µm*; d) the experiment using the BSA solution (section 3.2) and $\omega_x$=34 *µm*, $\omega_y$=23 *µm*; e) the experiment varying the liquid film thickness (section 3.3). The bottom-right table provides the values of the $K$ parameter of thet different experiments.

relation with the fraction *laser beam size/liquid thickness*. This implies that the $K$ parameter does not exclusively depend on the fraction *laser beam size/liquid*

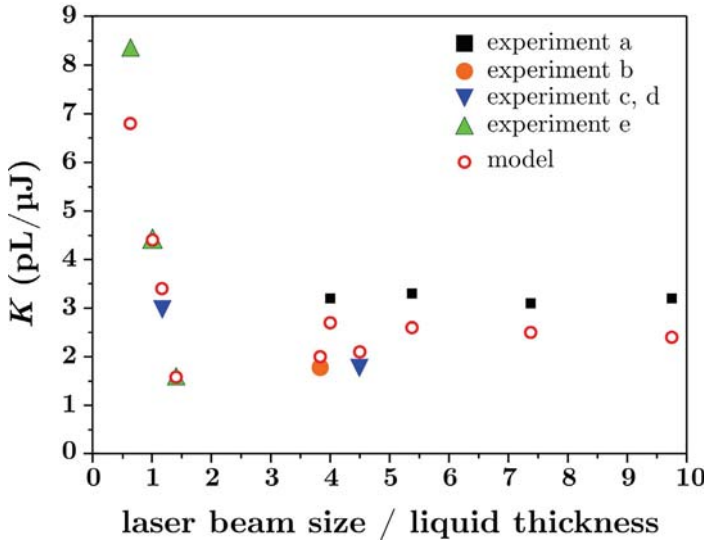


**Fig. 3.16.** Plot of the K parameter (process efficiency) versus the fraction laser beam size / liquid thickness for the experiments represented in Fig. 3.15, as well as for the proposed model.

*thickness* but rather on both members of the fraction separately. However, Fig. 3.16 provides an illustrative image of the behavior of the $K$ parameter: at fraction values smaller than or similar to 1 (*laser beam size* $\leq$ *liquid thickness*), the process efficiency increases strongly when decreasing the fraction; at fraction values larger than 1 (*laser beam size* $>$ *liquid thickness*), $K$ is kept rather constant given a certain beam size. It is important to notice that the two different behaviors of the $K$ parameter coincide well with the observed range of applicability of the cylinder model previously described: only at fraction values larger than 1 the cylinder model can be successfully applied.

Finally, a new model is presented which tries to reproduce the behavior of the $K$ parameter. Although the model is oversimple, the obtained results are quite consistent with the experimental ones, what makes it worth mentioning. This model considers that the bubble generated during the LIFT process expands making work to the surrounding fluid. The model hypothesis assumes that this work will be proportional to the deposited volume.

It will be first considered that after the laser pulse is absorbed a vapor bubble is generated with an energy proportional to $E_A$ (the fraction of the incoming

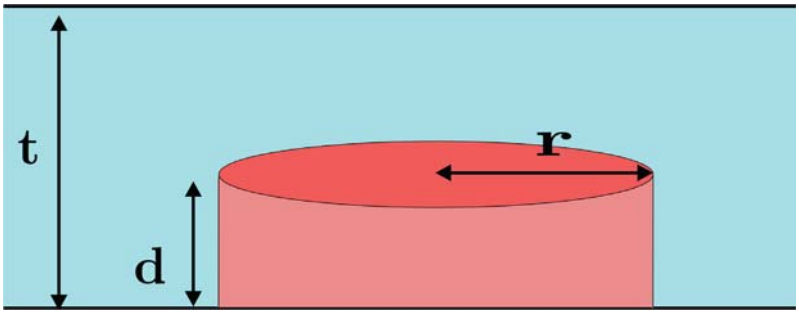


**Fig. 3.17.** Scheme of the proposed model, assuming a cylindrical geometry with: $r$ radius of the cylinder, $d$ height of the cylinder, and $t$ liquid film thickness.

energy above the threshold). Assuming an ideal gas, the initial pressure $p_i$ and volume $V_i$ of the bubble can be related to $E_A$ (internal energy) as $p_i V_i \propto E_A$, and thus $p_i \propto E_A / V_i$. This pressure will produce the expansion of the bubble, in a process in which the bubble will do work ($W$) to the surrounding fluid. It is considered that the expansion is adiabatic (it is expected a very fast expansion). The work done in such adiabatic process can be written as:

$$W \propto p_i V_i \left[ 1 - \left( \frac{V_f}{V_i} \right)^{1-\gamma} \right] \propto E_A \left[ 1 - \left( \frac{V_f}{V_i} \right)^{1-\gamma} \right] \tag{3.6}$$

where γ is the adiabatic constant (7/5 for a diatomic gas, as it will be considered), and $V_f$ the final volume. For simplicity, it is assumed that the generated bubble has a simple geometry, for instance a cyilinder (3.17). The initial bubble volume can be then expressed as:

$$V_{initial} = \pi r^2 d\,, \tag{3.7}$$

where $r$ is the initial bubble radius and $d$ the initial bubble height.

If it is considered that the cylinder expansion occurs at the same speed at both vertical and horizontal directions, and that most of the work is done while the bubble expands from its initial volume until reaching the liquid-air free surface, then the final bubble volume can be expressed as:

$$V_f = \pi (t - d + r)^2 t \tag{3.8}$$

where $t$ is the liquid thickness.

Substituting equations 3.7 and 3.8 into equation 3.6 yields:

$$W \propto E_A\left[1-\left(\frac{(t-d+r)^2 t}{r^2 d}\right)^{-2/5}\right]$$

And considering the model hypothesis:

$$V_{deposited} \propto E_A\left[1-\left(\frac{(t-d+r)^2 t}{r^2 d}\right)^{-2/5}\right] \tag{3.9}$$

In order to test the model, the $K$ parameter is calculated using equation 3.9 as follows:

$$V_{deposited} = D\left[1-\left(\frac{(t-d+r)^2 t}{r^2 d}\right)^{-2/5}\right]E_A \rightarrow K = D\left[1-\left(\frac{(t-d+r)^2 t}{r^2 d}\right)^{-2/5}\right] \tag{3.10}$$

where $D$ is the proportionality constant. This equation can be compared with the values of the previous experiments provided that two additional assumptions are made: the initial bubble height $d$ does not strongly depend on $E$, and the initial bubble radius $r$ is related to the beam dimensions as $r = \sqrt{\omega_x \omega_y}$ .

The two unknown variables of equation 3.10 ($D$ and $d$) were calculated from the results of section 3.3. The obtained values were $D$=10 pL/µJ, and $d$=4.0 µm. This last value of the initial bubble height $d$ is much larger than the estimated value of the depth of liquid affected by a temperature rise after the absorption of the laser pulse in the titanium layer, which has been calculated to be of the order of 1.5 µm [Mézel *et al.* 2009]. Despite this controversial aspect, if the model values of the $K$ parameter are calculated for the different experiments and plotted versus the fraction *laser beam size/liquid thickness* (Fig. 3.16), it can be observed that the general behavior of the $K$ parameter is reasonably well reproduced by the model, with most of its points lying close to the experimental values. In fact, considering the uncertainty in the measurement of the liquid film thickness, all the model points could be considered to fall within the margin of the experimental error. Thus, the model is quite consistent with the experimental results.

In conclusion, it has been found that the deposited volume is directly proportional to the fraction of the laser beam which energy density overcomes the threshold $F_0$, termed $E_A$. Such relationship can be written as $V=KE_A$, where $K$ represents the efficiency of the process. This equation makes the relation $V=K(E-E_0)$ consistent with the existence of the threshold $F_0$. An oversimple model has been introduced which reasonably describes the dependence of $K$ with the different experimental parameters.

## 3.5 Influence of the laser peak energy density on the droplet contact angle

In the first two sections, the analysis of the droplet volume when varying the laser peak energy density revealed that there exists a transition at high energies which seems to indicate a change in the deposition mechanism. Such change is characterized by an increase in the data dispersion (Fig. 3.1 and Fig. 3.2), and by an apparent shift towards upper volumes, especially significant for the case of the BSA solution.

In this section, an attempt to get a deeper understanding of the causes related to such change is carried out. To do so, a solution consisting in a mixture of water and glycerol with SDS is used (section 2.2.1). Such solution is chosen since it would be interesting to analyze whether the mentioned transition at high laser pulse energies is also observed for a biomolecule-free solution.

A 10 rows per 10 columns microarray of the biomolecule-free solution was prepared at fixed laser beam dimensions, and varying the laser pulse energy from row to row. The liquid film had a thickness of 10 µm, and the liquid film-receptor substrate separation was 50 µm. The dimensions of the laser beam on the titanium layer were the smallest possible: $\omega_x$=8 µm and $\omega_y$=6 µm (the titanium layer was situated on the focal plane). Such high focusing conditions were selected since it was observed that, for a different solution (section 3.2), those were the conditions which led to the noticeable appearance of a different region at high laser pulse energies.

An optical microscopy image of the microarray is presented in Fig. 3.18. It can be observed that most droplets are circular with a well-defined contour. In this case there is no row with any void, since the lowest laser pulse energy in this experiment was above the minimum energy that results in droplet deposition ($E_{min}$). In the upper three rows, corresponding to the highest laser pulse energies, the droplets have an irregular contour.

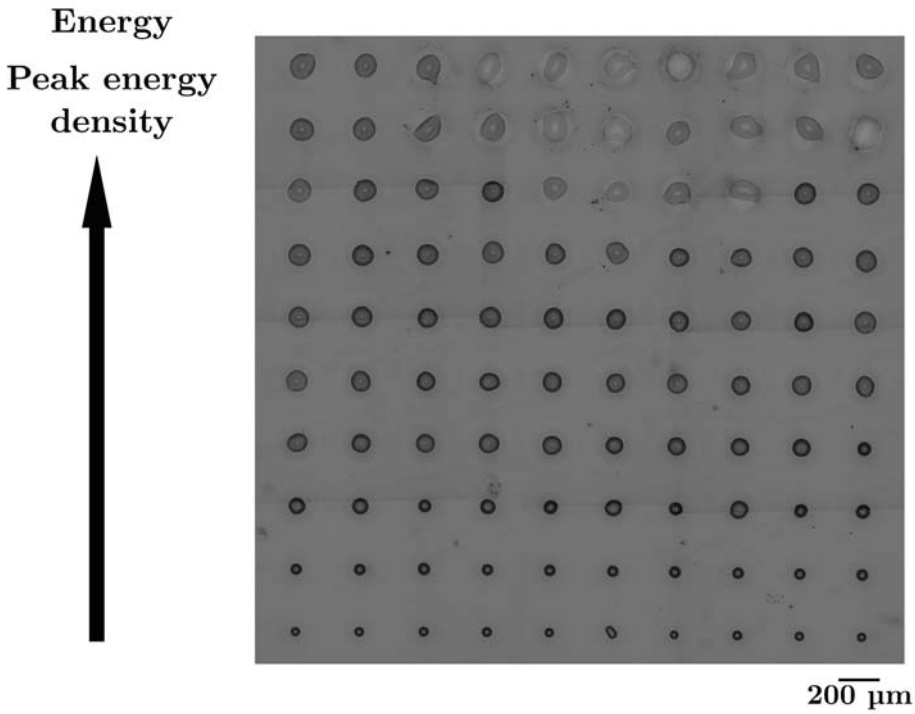


**Fig. 3.18.** Optical microscopy image of the microarray of the water+glycerol+SDS solution prepared varying the laser pulse energy from row to row.

The volume of the printed droplets was calculated from their diameters, assuming a fixed contact angle of 30° for all droplets (first method of section 2.5.2). In Fig. 3.19, the droplet volume was plotted versus its corresponding laser peak energy density. Three different regions can be distinguished: up to 1.5 J/cm$^2$, all points are well aligned; from 1.5 J/cm$^2$ to 2.5 J/cm$^2$, the points are still aligned, but present a higher slope and a higher dispersion; finally, above 2.5 J/cm$^2$ the slope decreases again and the points dispersion becomes even higher.

In order to find a correlation between the three regions observed in the plot and the morphology of the printed droplets of the corresponding regions, Fig. 3.18 was analyzed in more detail. It was found that in the first two rows and in some positions of the third one, corresponding to the low peak energy densities, the droplets appear darker than in the rest of the microarray. This color change suggests differences in the droplet contact angle. Therefore, the contact angle of a representative selection of the printed droplets was accurately measured

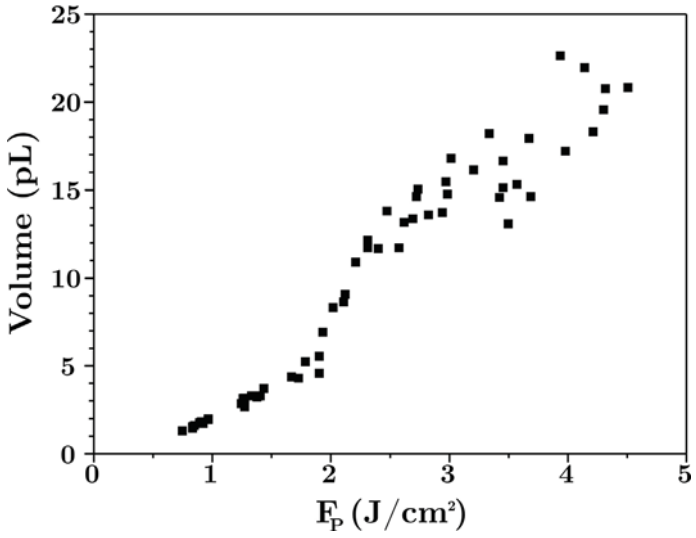


**Fig. 3.19.** Plot of the droplet volume versus the laser peak energy density ($F_P$). The volume has been calculated assuming a fixed contact angle of 30°for all droplets.

through optical profilometry[8] (section 2.5.2). It must be pointed out that in all the previous experiments in which the contact angle was measured this parameter was found to be independent of the irradiation conditions [Colina et al. 2006, Colina 2006]. However, in those cases the color differences of the present experiment were not observed.

A plot of the contact angle versus the peak energy density is presented in Fig. 3.20. It is observed that, in clear contrast to previously mentioned works [Colina et al. 2006, Colina 2006], the contact angle is not constant. Up to three different regions could be distinguished. At low peak energy densities (up to 2 J/cm$^2$) it presents values close to 30°, which is the previously measured value through grazing-incidence microscopy [Colina *et al.* 2006]. At intermediate peak energy densities (from 2 to 2.5 J/cm$^2$), there exists a pronounced transition in which the contact angle is reduced from 30 to 20°. Finally, at higher peak energy densities (above 2.5 J/cm$^2$) the contact angle is kept constant around 20°. These different regions can be directly correlated with those observed in Fig. 3.19. Moreover, the discovery of these three regions also has technological

[8] A selection of the printed droplets was necessary due to the long time required to measure the contact angle of a single droplet through optical profilometry, which made the contact angle measurement of all the printed droplets unfeasible.

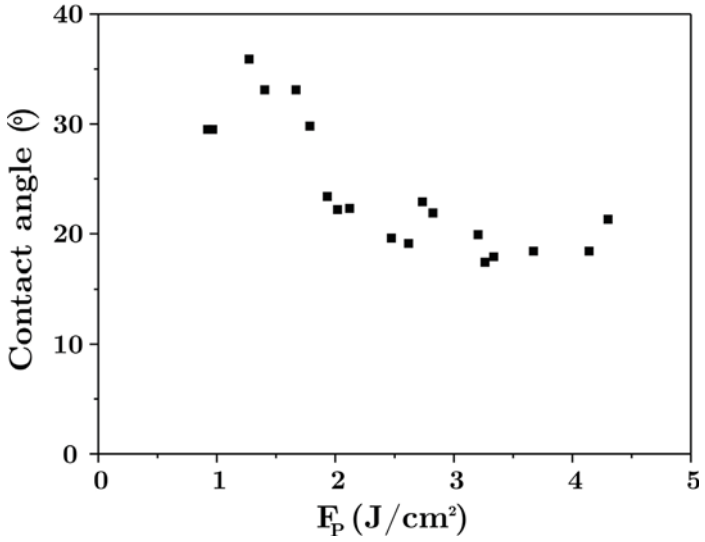


**Fig. 3.20.** Plot of the droplet contact angle versus the laser peak energy density ($F_P$).

implications, since it demonstrates that, in order to print droplets with a small volume and diameter, low peak energy densities must be used.

Using the contact angle values of the printed droplets, the real volume of each droplet was recalculated, and plotted versus its peak energy density (Fig. 3.21). It can be observed that in this case there is a very clear linear relationship between the droplet volume and the peak energy density: all the points are well aligned in the same direction. The recovery of the linear dependence between these two parameters demonstrates that such relationship is a fundamental characteristic of the technique. However, at high peak energy densities (above 2.5 J/cm$^2$) the data still present more dispersion than at low peak energy densities. This last is still another hint of a possible change in the deposition mechanism, which can only be elucidated through time-resolved imaging of the process, as it will be done in chapter 4.

The points were then fitted to equation 3.1 in order to compare the present results with those of sections 3.1 and 3.2. The fitting parameters obtained are depicted in table 3.4. It can be observed that the value of $F_0$ is of the same order as in the previous experiments, since it may not be significantly affected

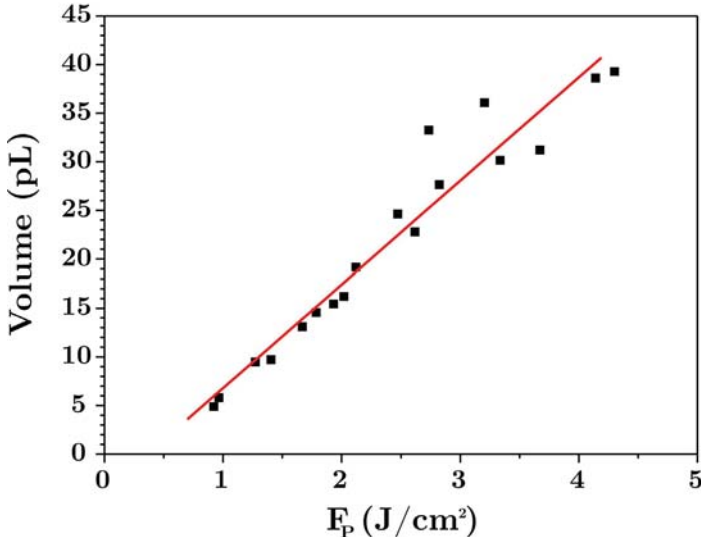


**Fig. 3.21.** Plot of the real droplet volume versus the laser pulse peak energy density ($F_P$). The solid line is the linear fit.

by the rehology of the liquid. On the contrary, the $C$ parameter could depend on the liquid properties, and so it presents a value different from those previously obtained.

In conclusion, it has been observed that the droplet contact angle can depend on the laser peak energy density, presenting a lower value at high energies. The change in the contact angle occurs quite abruptly when a certain value of the laser peak energy density is surpassed, which suggests that the change is due to the activation of a different deposition mechanism. However, the linear relationship between droplet volume and laser peak energy density is preserved even when the contact angle changes.

**Table 3.4.** Major ($\omega_x$) and minor ($\omega_y$) beam radii, and fitting parameters ($C$ and $F_0$) for the water+glycerol+SDS solution.

| $\omega_x$ $(\mu m)$ | $\omega_y$ $(\mu m)$ | $C$ $(pLcm^2/J)$ | $F_0$ $(J/cm^2)$ |
|---|---|---|---|
| 8 | 6 | 10 | 0.30 |

## 3.6 Influence of the liquid film-receptor substrate separation on the printed droplets

Apart from the irradiation conditions, other parameters affect the morphology of the droplets printed through LIFT. One of the most important ones is the liquid film-receptor substrate separation (in the following, the separation distance), which has an especial relevance for technological applications: techniques which require processes in which the different parts must be very close to each other are difficult to be industrially implemented, since any external factor (for instance, vibrations) could seriously affect the process. Therefore, it is important to determine the range of separation distances which lead to the deposition of circular and well-defined droplets for the LIFT technique.

In this section, the analysis of the separation distance influence on the morphology of the deposited droplets was carried out. Two different liquid solutions were used (section 2.2.1): a biomolecule-containing solution (BSA), and a biomolecule-free solution (water+glycerol+SDS).

In a first experiment, three microarrays of 3 rows per 23 columns of a BSA solution were prepared varying the liquid film-receptor substrate separation from row to row. Each one was prepared at a different laser pulse energy. The liquid film thickness was about 5 µm, whereas the dimensions of the laser beam on the titanium layer were $\omega_x$=8 µm and $\omega_y$=6 µm (the titanium layer was placed on the laser focus position).

Optical microscopy images of each of the three microarrays are presented in Fig. 3.22. It can be observed that at low laser pulse energies (170 nJ, Fig. 3.22a) circular and well-defined droplets are printed at separation distances up to 0.6 mm. From 0.7 to 1.3 mm satellite droplets appear, and at higher separations no material is deposited. At intermediate laser pulse energies (360 nJ, Fig. 3.22b), circular droplets are also printed up to separations of 0.6 mm. For separations

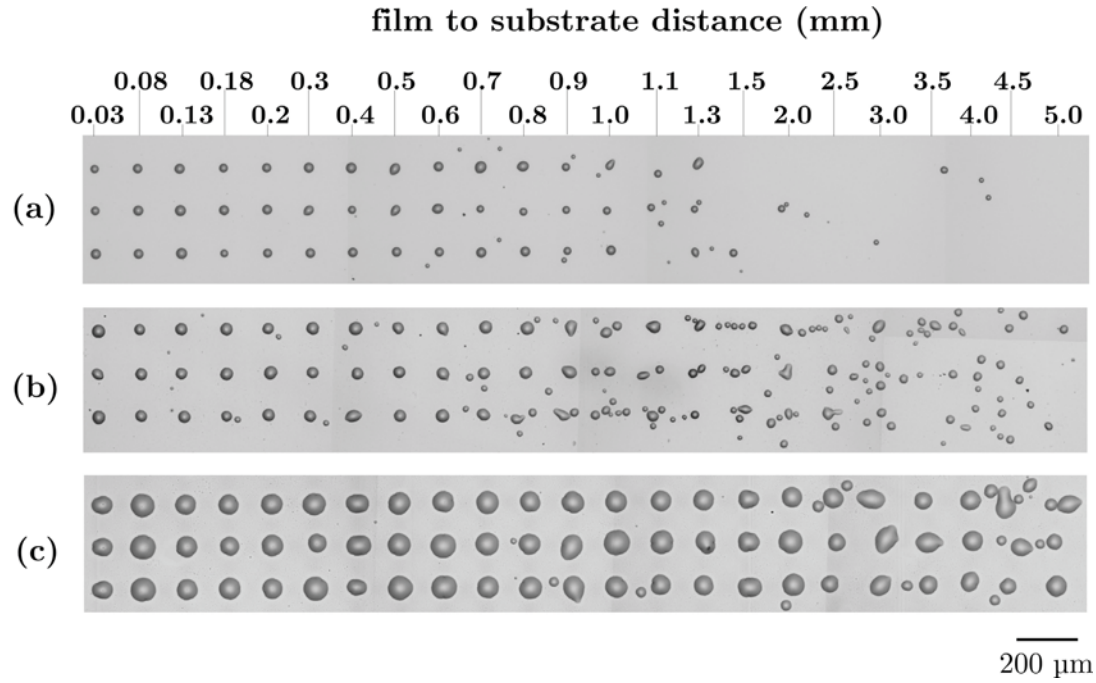


**Fig. 3.22.** Optical microscopy images of the three BSA microarrays obtained varying the separation distance, prepared at three different energies: (a) 170 nJ, (b) 360 nJ, and (c) 630 nJ.

between 0.7 and 1 mm, satellites appear, and the circular shape of the droplets is lost. At even higher separation (1-5 mm), only small random-distributed droplets are present. Finally, at high laser pulse energies (630 nJ, Fig. 3.22c), rather well-defined droplets are printed up to almost 2 mm. When the separation distance is increased above 2 mm, satellite droplets appear, and the shape of the droplets becomes very irregular.

The previous results concerning the printing of well-defined droplets even at large separation distances have shown that the LIFT of aqueous solutions exhibits properties clearly different from those of the LIFT of solid materials [Yamada *et al.* 2002] or pastes [Lewis *et al.* 2006], in which the technique was found to be very sensitive to the donor film-receptor substrate separation. Therefore, it is expected that the transfer process for aqueous solutions is completely different from the previously studied LIFT of solid materials or viscous pastes. Actually, in the present situation two plausible transfer mechanisms could be invoked: the generation of a single droplet that flies until

it reaches the receptor substrate, or the formation of a liquid jet which directly contacts the receptor substrate.

The first one was the most widely accepted mechanism [Colina *et al.* 2006] since it is the responsible for the droplet deposition in ink-jet printing, and it seemed reasonable to attribute the mechanism of inkjet printing to LIFT due to the similarity of the patterns printed with both techniques. However, the last results present some inconsistencies with this assumption. The most obvious one is that at high separation distances and low laser pulse energies there is no deposited material, which cannot be explained considering the formation of a single flying droplet. Furthermore, for intermediate and high energies, and also at high liquid film-receptor substrate distances, the number of multiple small droplets increases significantly and irregular droplets appear. This result could hardly be explained considering the flying droplet mechanism. In this case, the only reason to obtain multiple and irregular droplets once a certain liquid film-receptor substrate distance has been reached, would be that the kinetic energy of the flying droplet when it impacts the receptor substrate produces its disintegration into multiple small droplets [Xu *et al.* 2005]. However, the difference in the kinetic energy between a flying droplet which results in the deposition of a well-defined droplet (separation distance of 0.08 mm, for example) and a flying droplet which results in multiple small droplets (separation of 2.0 mm, for example), is only due to the gravitational force, and it can be calculated using the following relationship:

$$\Delta v = \sqrt{2g}\left(\sqrt{h_2} - \sqrt{h_1}\right) \Rightarrow \Delta v = \sqrt{20}\left(\sqrt{2 \cdot 10^{-3}} - \sqrt{8 \cdot 10^{-5}}\right) = 0.16 \text{ m/s}$$

A difference in the impact velocity of only 0.16 m/s or even less, does not seem sufficient to justify the transition to droplet splashing, specially when considering that a typical velocity of a flying droplet obtained through ink-jet printing is of around 10 m/s [Fillmore 1983].

The second mechanism, in which transfer is driven by the formation of a jet, was considered due to the jets observed in time-resolved studies of the LIFT

process using a viscous solution [Young *et al.* 2002] and also using a protein solution [Barron *et al.* 2005a]. However, those jets were turbulent and irregular for the viscous solution and, for the protein solution, jet breakup into multiple droplets occurred when the jet had a very short length. Therefore, none of the previous situations could account for the deposition of well defined droplets. Despite this fact, the present results seem to point towards the direction of jetting, since this mechanism is consistent with the absence of droplets observed at low energies and high separation distances (attributable to the recoil of the jet before reaching the receptor substrate), as well as with the transition to splashing obtained at intermediate energies and high separation distances (attributable to jet breakup before contact with the receptor substrate). This transfer mechanism, however, is not free from drawbacks: the jet which would generate the deposition of droplets, should be extremely long (more than 1 mm), and thin (at most 50 µm, the average droplet diameter, although possibly much less), which should result in extremely high aspect ratios. Moreover, it should be really straight, uniform, and stable, since droplets are always quite identical in size and shape over a long range of separation distances. However, these characteristics contrast with the previously observed jets in LIFT experiments [Young *et al.* 2002, Barron *et al.* 2005a]. Therefore, in order to clarify which is the dynamics of the LIFT process, and thus elucidate the transfer mechanism, other characterization techniques, such as time-resolved imaging, are necessary. Such study is reported in chapter 4.

In a second experiment, a 16 rows per 10 columns microarray of a water plus glycerol and SDS solution was prepared (section 2.2.1). The separation distance was varied from row to row, while the laser pulse energy was kept constant at 2 µJ. The liquid film thickness in this occasion was 20 µm, and the titanium layer was also placed on the laser focus position, thus the dimensions of the laser beam were $\omega_x$=8 µm and $\omega_y$=6 µm.

An optical microscopy image of this microaray is presented in Fig. 3.23. The behavior observed in the previously obtained BSA microarray at intermediate energies (Fig. 3.22b) is again reproduced: well-defined droplets, very similar in

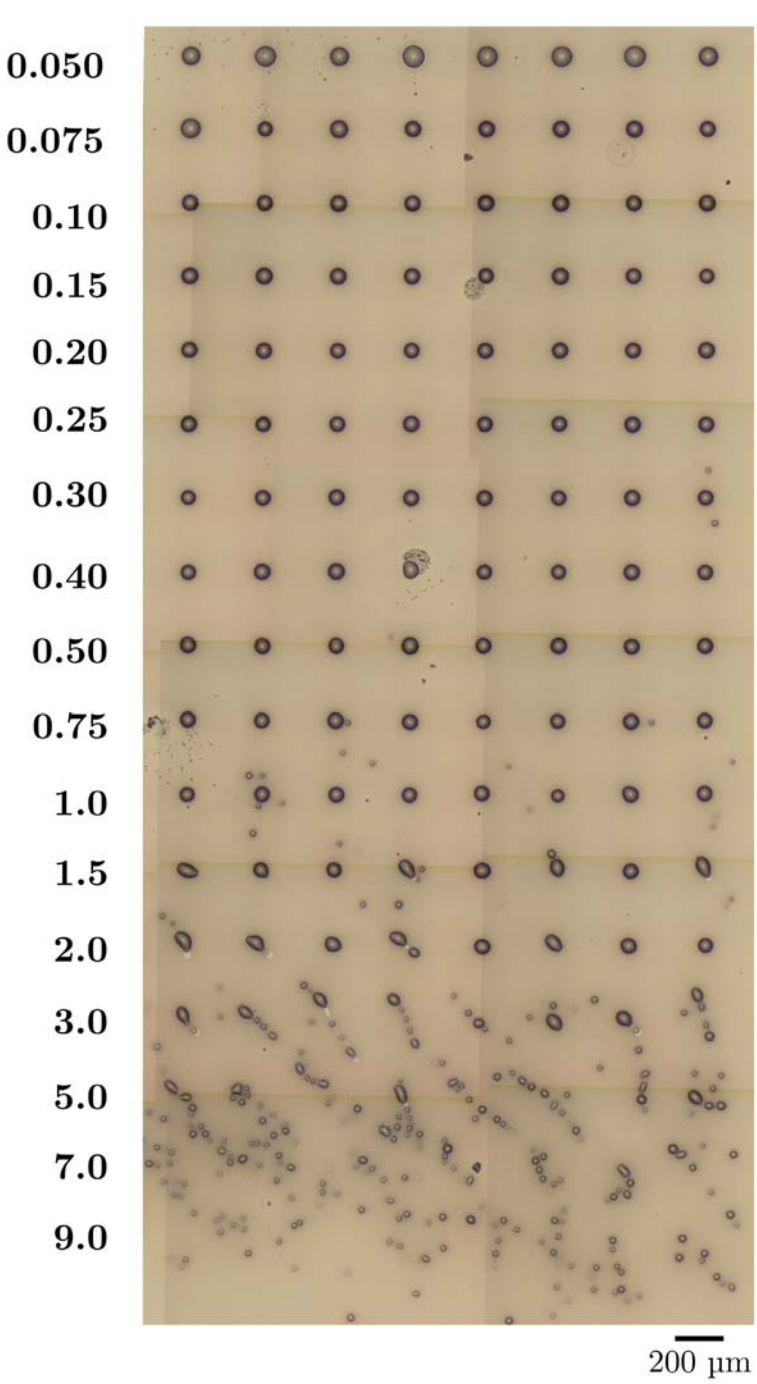


**Fig. 3.23.** Optical microscopy image of the water+glycerol+SDS microarray prepared at a fixed laser pulse energy of 2 µJ, and varying the separation distance from row to row (values indicated on the left side of the image in mm).

size, are deposited up to liquid film-receptor substrate distances of 1 mm; at higher distances, several satellite droplets appear, and when the distance is further increased, only multiple small droplets are printed. The reproduction of the previous behavior indicates that the general trend of the transfer mechanism

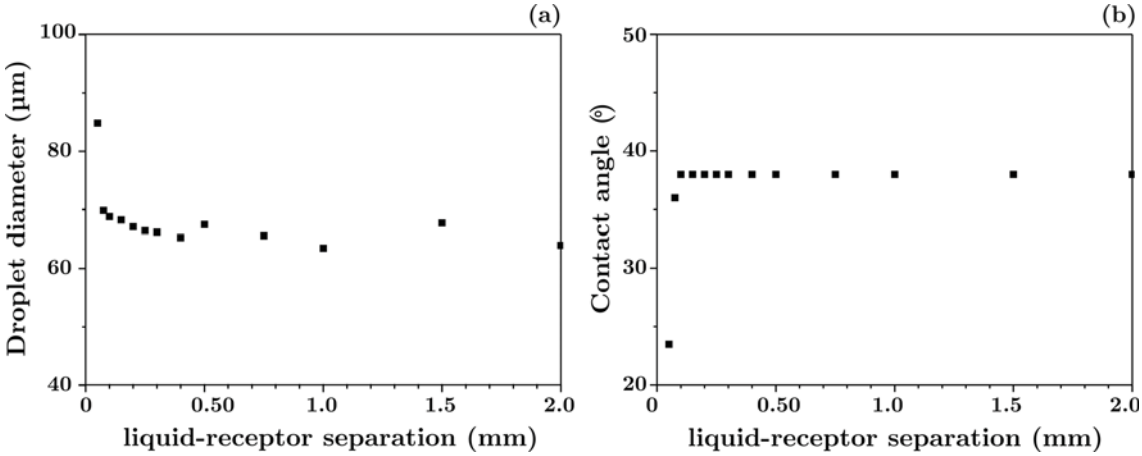


**Fig. 3.24.** a) Average droplet diameter versus the separation distance; b) average contact angle of the deposited droplets versus the separation distance.

is rather independent of the solution used. However, in the present case there is a noticeable difference with respect to the BSA microarray: at the shortest liquid film-receptor substrate distance (50 µm), the droplets appear brighter and with a larger diameter than in the rest of the array (Fig. 3.24a). Such change in the droplets appearance was previously found to be caused by a difference in the contact angle (section 3.5). In order to clarify whether the present transition had the same origin as before, the contact angle of the printed droplets was measured through optical profilometry. Then, the average contact angle of the droplets printed in a row was calculated, and plotted versus the separation distance (Fig. 3.24b). It can be observed that the contact angle for the first row (around 24°) and the second row (around 36°) is smaller than that for the other droplets (38°). The change in contact angle was attributed in section 3.5 to a different transfer mechanism. However, the activation of that different transfer mechanism occurred at high energies. In the present case, the laser pulse energy is kept constant, and the presumed mechanism seems to be activated when approaching the liquid film to the receptor substrate. For all that, it results clear that an interpretation of the origin of such behavior is complicated, evidencing again that the LIFT transfer mechanism is complex, and making necessary an in-depth study of the dynamics of the process.

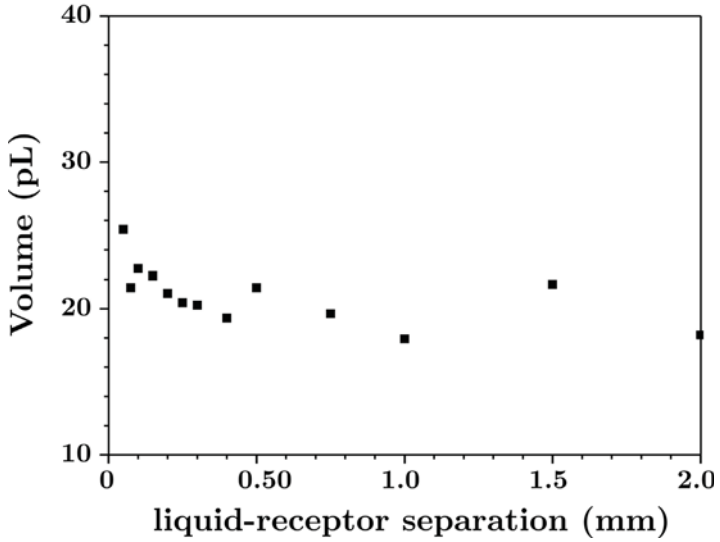


**Fig. 3.25.** Average volume of the printed droplets versus the separation distance.

Finally, the measured contact angles were used to calculate the average volume of the droplets printed per row, and these values were plotted versus the separation distance (Fig. 3.25). Such quantification demonstrates that the volume of the printed droplets does not seem to depend much on this distance. Since the printed droplets also present a wide range of distances in which their diameter remains constant, all this allows stating that LIFT is a technique with quite a high degree of flexibility concerning the separation distances that can be employed, which makes it suitable as a technological process.

In conclusion, it has been demonstrated that circular and well-defined droplets can be printed through LIFT for a wide range of liquid film-receptor substrate distances. This provides the technique with quite a high degree flexibility: there is a wide range of distances where transfer can be carried out without loss of resolution. Moreover, the present results also evidence that time-resolved imaging is necessary to unveil the deposition mechanism, a study that will be presented in chapter 4.

## 3.7 Printing very small droplets through LIFT

In this section, the results previously obtained are used to select the conditions which lead to the deposition of the smallest droplets achieved with the present experimental setup.

A BSA solution microarray was prepared at the optimum conditions for the printing of very small droplets. The BSA solution was chosen due to its rheology, which makes the preparation of a very thin liquid film easier to achieve than with the other solutions described in section 2.2.1. The conditions at which the BSA microarray was prepared are detailed next: laser peak energy density slightly higher than $F_1$ (a first microarray using the same donor film was prepared in order to determine this value, since this parameter depends on the properties of each particular liquid film), strong focusing conditions, short liquid film-receptor substrate separation, and a very thin liquid film obtained through spin coating. The numerical values of these conditions are presented in table 3.5. It should be noted that a small liquid film-receptor substrate separation was used, in order to assure the deposition of droplets (high separations could be problematic, as it was observed in section 3.6).

An optical microscopy image of the microarray is presented in Fig. 3.26. Circular droplets with a diameter ranging between 8 and 11 µm were printed, although the reproducibility was not as good as in the previous experiments.

**Table 3.5.** Liquid film thickness, separation distance, major ($\omega_x$) and minor ($\omega_y$) beam radii, and laser pulse energy for the prepared BSA microarray.

| *Film thickness* ($\mu m$) | *Liquid-receptor separation* ($\mu m$) | $\omega_x$ ($\mu m$) | $\omega_y$ ($\mu m$) | $E$ ($\mu J$) |
|---|---|---|---|---|
| 2 | 30 | 8 | 6 | 0.05 |

This is possibly due to the lack of uniformity of the liquid film. Actually, obtaining uniform and very thin liquid films is very hard. This fact motivated the research of an alternative technique which could dispense with the liquid film preparation, as it is presented in chapter 5. The contact angle of the small droplets could not be measured due to limitations in the resolution of the optical profilometer (section 2.4.2). However, assuming the same contact angle for these droplets as that of bigger ones (about 7°), the volume was estimated to be about 10 fL. This value is around 100 times smaller than the minimum one obtained in previous works [Colina *et al.* 2006], and $10^4$ times smaller than the volume routinely deposited with conventional inkjet printing. This result confirms that LIFT is a competitive alternative for bioprinting applications, due to the high achievable resolution.

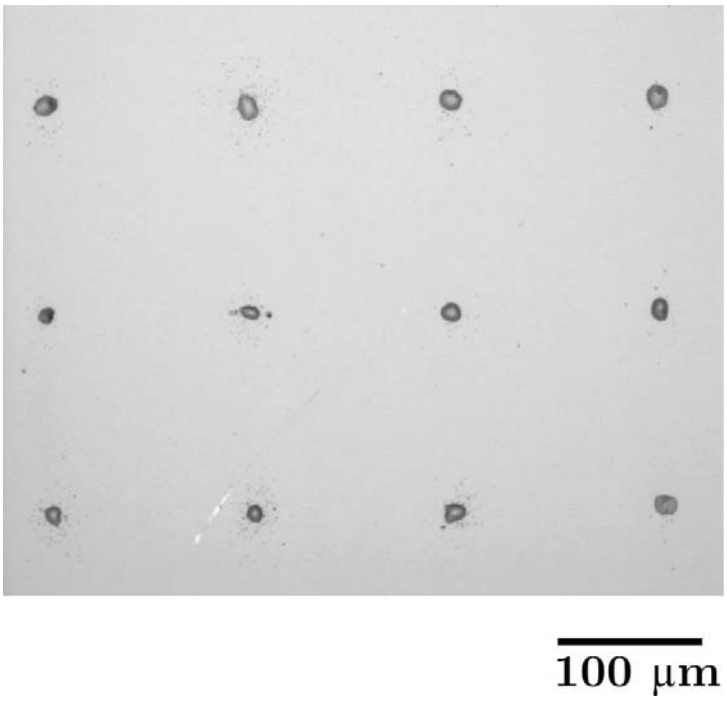


**Fig 3.26.** Optical microscopy image of the BSA microarray with the smallest droplets ever printed using that experimental setup.

## 3.8 Study of the feasibility of LIFT for protein printing

The last section of this chapter is focused on the study of the feasibility of the LIFT technique to print biomolecules, in particular, the proteins IgG and BSA (section 2.2.1). It is evident that any technique suitable for biomolecule printing must assure the conservation of the printed specimens. Actually, the term conservation referred to biomolecules is not lacking of ambiguities, but for the applications pursued by LIFT (biosensing, proteomics, genomics...) it would be enough that the printed specimens preserve their functional properties. That is, if a protein preserves its capacity to specifically bind with a complementary, then it is considered that the printing process has conserved the specimen (even if the protein may have suffered slight changes in its structure).

In the present experiment, two different microarrays were prepared. The first one was a 10 rows per 5 columns microarray of the previously used IgG solution (section 3.1), obtained varying the laser pulse energy from row to row. The liquid film thickness was 10 µm, and the separation distance was 300 µm. The dimensions of the laser beam on the titanium layer were $\omega_x$=47 µm and $\omega_y$=30 µm (the titanium layer was situated 500 µm above the focal plane). An optical microscopy image of this first microarray is presented in Fig. 3.27a. It can be observed that droplets are obtained within all the energy range explored, with their diameter increasing with the laser pulse energy. The droplets are not as regular as those obtained before and present some satellites. Once the microarray was printed, it was submitted to a fluorescence test (section 2.4.3). In this case, the IgG was directly bonded to its complementary (anti-IgG) tagged with the fluorochrome Cy5. An image of the microarray obtained with the fluorescence scanner is presented in Fig. 3.27b. It can be observed that a red signal is detected at the positions in which the droplets were printed, indicating that the biomolecules have preserved their functionality (otherwise no signal would have been detected). The pretty good correspondence between droplets and red spots also evidences that the laser pulse energy does not affect significantly the biomolecule functionality.

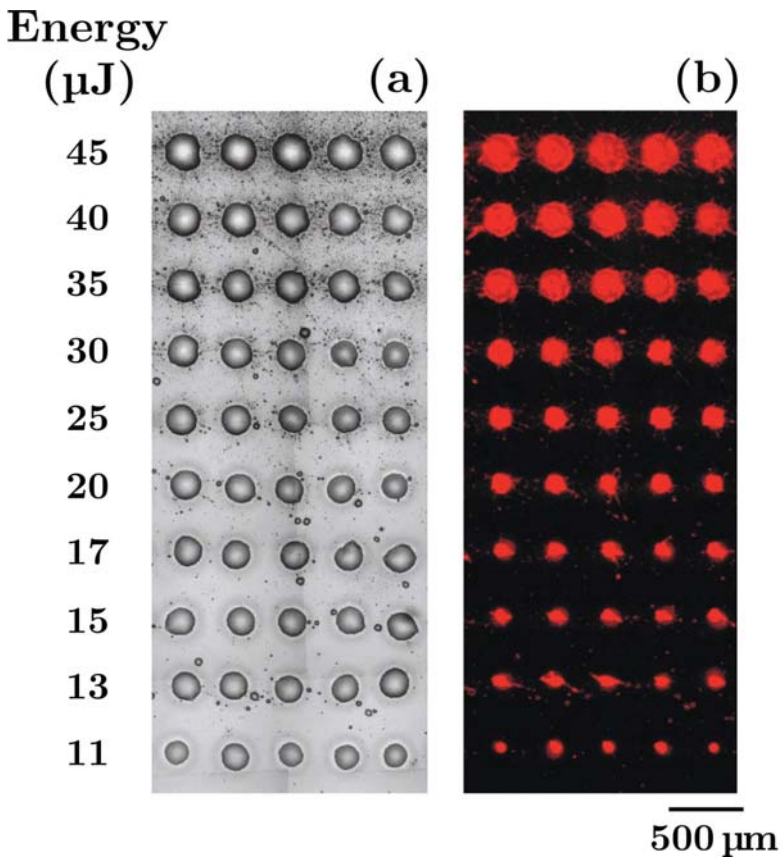


**Fig 3.27.** (a) Optical microscopy image of the IgG microarray. The values on the left side correspond to the row average laser pulse energies. (b) Corresponding fluorescence image after immunoassay with its anti-IgG complementary tagged with Cy5.

The second microarray had 20 rows and 10 columns, and was obtained combining one row of the BSA solution with another of a biomolecule-free solution (water+glycerol+SDS). In this way, the biomolecule-free solution constituted a negative control of the feasibility test. The liquid film thickness for both solutions was 10 µm, and the separation distance was 300 µm. The dimensions of the laser beam on the titanium layer were $\omega_x$=8 µm and $\omega_y$=6 µm (the titanium layer was situated in the focal plane). In this occasion, the laser pulse energy was fixed along the whole printed area. An optical microscopy image of this second microarray is presented in Fig. 3.28a. It can be observed that circular and well-defined droplets of two different colors are obtained. The darker ones correspond to the biomolecule-free solution, whereas the brighter ones to the BSA solution. There are some voids in some rows attributable to laser fluctuations, which in a certain position could not reach the minimum energy to deposit a droplet. After printing this microarray, it was submitted to

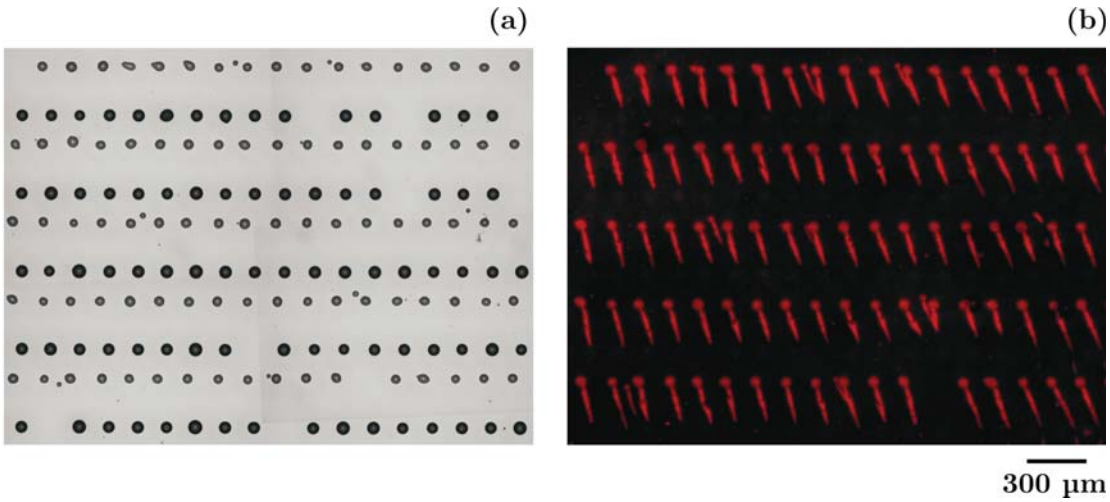


**Fig 3.28.** (a) Optical microscopy image of the microarray prepared to check the feasibility of LIFT to print BSA. The darker droplets correspond to the biomolecule-free solution, whereas the brighter ones to the BSA solution. (b) Corresponding fluorescence image of the microarray after immunoassay.

a fluorescence test, as explained in section 2.4.3 In this occasion, the BSA was not directly bonded to its complementary tagged with a fluorochrome, but an extra amplifying step was carried out. This allowed increasing the sensitivity of the test. An image of the fluorescence scanner is presented in Fig. 3.28b. It can be observed that circular red spots are only present at the positions in which the BSA solution was deposited. On the contrary, at the positions in which the biomolecule-free solution was deposited, no signal is detected. All this allows stating that the technique has a high specificity. As a final remark, it must be pointed out that an incident occurred during the conjugation protocol: the microarray was submitted to the immunoassay before it was completely dry. As a consequence, the printed solution was spread beyond the spot area due to the fluid flows generated in the washing step of the immunoassay protocol, leading to the formation of the red lines observed in the image, called comet tails.

In conclusion, the results presented in this section demonstrate that LIFT is feasible for the preparation of protein arrays which preserve their functionality. Therefore, this technique is suitable for the fabrication of functional devices such as miniaturized immunosensors.

# Chapter 4

# Time-resolved imaging of the LIFT of aqueous solutions

In this chapter, the study of the LIFT dynamics is performed using time-resolved imaging. As it was concluded in the previous chapter, the next step towards a further comprehension of the mechanisms involved in the LIFT process consists in the imaging of liquid ejection and deposition. This is important from a fundamental point of view, since it could allow unveiling the physics governing the process, but it also involves technological aspects, since it could help understanding the role that the diverse experimental parameters have in the LIFT of liquids.

It is important to notice that the LIFT of aqueous solutions can be divided into two different sub-processes: a transfer process, which accounts for the laser pulse interaction with the donor film and the resulting ejection of material towards the receptor substrate; and a deposition process, which includes the transferred material arrival to the receptor substrate and the way it deposits there. Considering these aspects, the chapter has been divided into four sections. The first three are devoted to the study of liquid ejection and transport during LIFT. The first section presents the time-resolved images of the transfer process at conditions in which well-defined droplets are deposited. The dynamics of transfer at different laser fluences is studied in the second section, whereas in the third one time-resolved imaging is carried out to investigate the influence of varying the laser beam dimensions. Finally, the fourth section is dedicated to the study of the mechanisms involved in liquid deposition and droplet formation.

## 4.1 Time-resolved imaging of liquid ejection and transport during LIFT

The first step in the time-resolved study of LIFT is the imaging of the transfer process at the conditions in which well defined droplets are obtained. The material used in the study was the model liquid solution consisting in a mixture of water and glycerol plus SDS (section 2.2.1). As it was observed in chapter 3, the results obtained with this solution were very similar to those obtained with biomolecule-containing solutions.

A microarray was prepared using a liquid film thickness of 20 µm spread on a Ti layer 50 nm thick, and with a liquid film-receptor substrate separation of 130 µm (the receptor substrate was poly-L-lysine). The laser pulse energy was kept constant at a value of around 0.7 µJ. Since the dimensions of the laser beam on the titanium layer were $\omega_x=\omega_y=4$ µm, the fluence was about 2.8 J/cm$^2$. An optical microscopy image of this microarray is presented in Fig. 4.1. It can be observed that circular droplets are obtained, with diameters that vary between 70 and 90 µm (such variations can be attributable to laser fluctuations). Thus, the conditions of interest to analyze the transfer process were set. Immediately after deposition, the receptor substrate was removed, and time-resolved images of the LIFT process from the side view (section 2.3) were acquired using the same liquid film as in the preparation of the previous microarray, and under identical irradiation conditions.

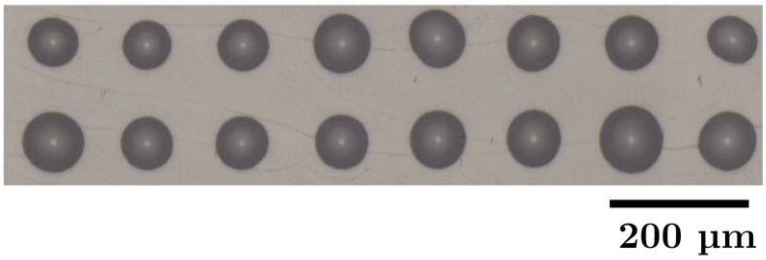


**Fig. 4.1.** Optical microscopy image of the prepared microarray.

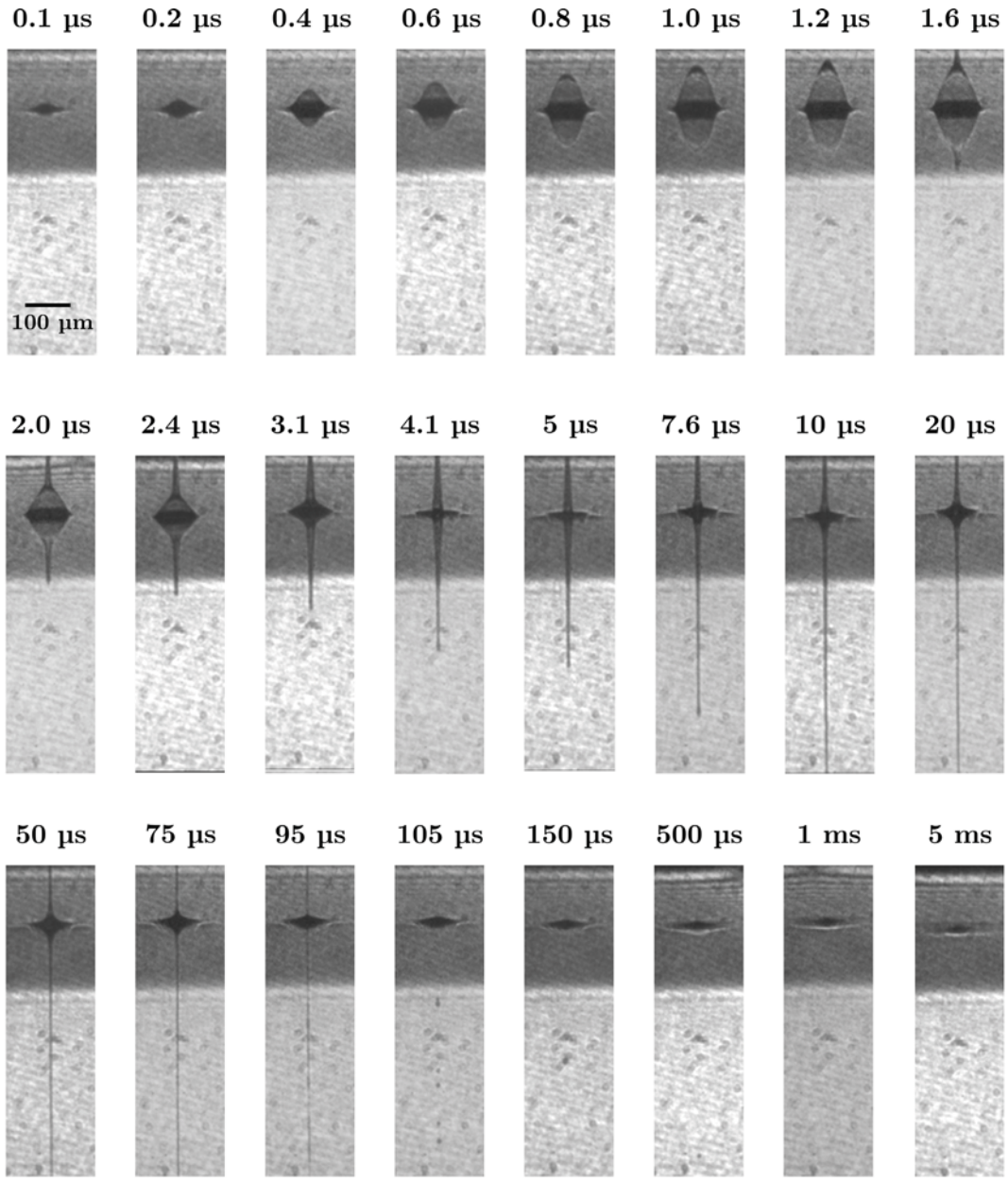


**Fig. 4.2.** Images of the liquid dynamics obtained during LIFT at different delay times with respect to the laser pulse. Integration time for each image is 100 ns.

A series of the acquired images is presented in Fig. 4.2. In these images, the dark grey upper part of the background corresponds to the donor substrate surface, as the CCD optical axis was slightly tilted with respect to the zero grazing angle. Due to the high reflectivity of the Ti layer, two liquid expansion fronts seem to evolve into opposite directions: since the upward front corresponds to the reflected image, only the downward one must be considered

in the interpretation of the results. Four different stages can be distinguished during the transfer process: up to 1.2 µs, a bubble is generated, which expands like an inflating balloon; from 1.2 to 4.0 µs, the bubble gradually collapses from its sides while the central tip maintains its progression, and a jet with a diameter of a few microns develops; from 4.0 to 95 µs, the jet continues advancing and reducing its diameter while preserving its well-defined shape, surpassing the field of vision of the imaging system at about 10 µs; finally, 95 µs after the laser pulse, several "bumps" appear along the jet surface just before it breaks into multiple small droplets, remaining only a protrusion which persists over a long time (up to ms).

The plot of the propelled liquid front position versus time (Fig. 4.3) reveals that two different regions can be distinguished, each one presenting a linear relationship between position and time. The first region (0.1-1.4 µs) corresponds to the balloon-like stage, being the front velocity of around 90 m/s. The second region corresponds to the jet formation and its advancing process until it disappears from the field of view, being the front velocity of about 55 m/s, much lower than that of the initial expansion. It must be pointed out that, despite the high speed of the jet, the liquid flow remains laminar during the whole transfer process. This can be attributed to the small lateral dimensions of both bubble and jet, which counterbalance the effect of a high velocity, and prevent the flow of becoming turbulent. In fact, assuming a characteristic lateral length of about 7 µm (average jet diameter), and a flow speed of about 55 m/s (jet front velocity), the Reynolds number of this flow is estimated to be around 60, a value well below the turbulence threshold (about 2300). The jet forward movement is also accompanied by a decrease in the jet diameter from 9 to 6.5 µm, at an approximately constant rate of 0.03 m/s (Fig. 4.3). If it is assumed that the jet continues advancing at constant speed until breakup, the final length of the jet could be estimated to be of around 5 mm, a value that clearly contrasts with the reduced jet diameter, and that would result in an aspect ratio as high as 800.

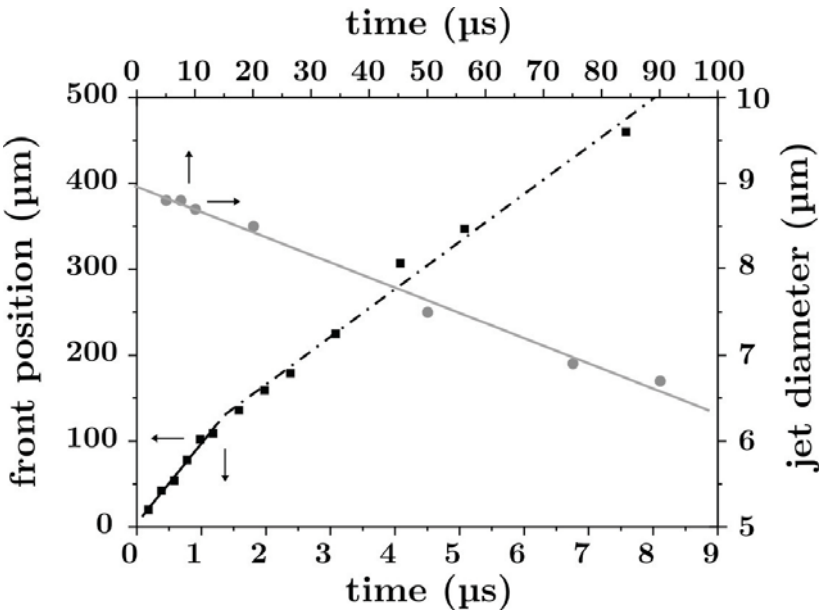


**Fig. 4.3.** Plot of the propelled liquid front position (black squares) and jet diameter (grey circles) versus time. Lines correspond to linear fits.

From Fig. 4.2, the volume of the generated feature[9] can also be calculated assuming revolution symmetry. A plot of this volume versus time is presented in Fig. 4.4. Again, three different behaviors can be distinguished. During the expansion process, the feature increases in volume, reaching its maximum 2 µs after the laser pulse. From 2 µs to 4 µs, during the bubble collapse, its volume suffers an important reduction. Since during these stages bubble expansion and collapse take place, it must be stated that most of the computed volume corresponds to the expanding and compressing vapor. Finally, for times longer than 4 µs the most relevant issue of this figure is revealed: the jet, completely developed, propagates without significant change in its volume. Jet elongation and thinning proceed in such a way that the volume remains constant. It should also be pointed out that this jet volume approximately corresponds to the volume of the sessile droplet printed at these conditions.

[9] The feature corresponds to both bubble and jet. Therefore, in the calculus of the feature volume both gas and liquid phases are considred.

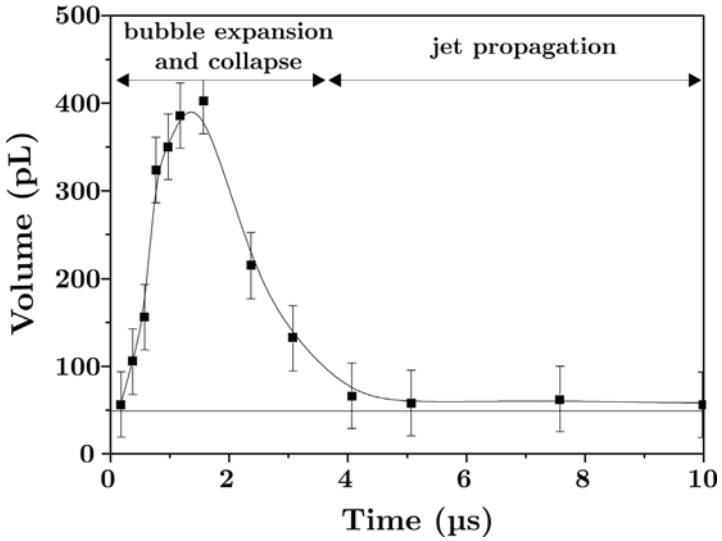


**Fig. 4.4.** Plot of the feature volume versus time. The horizontal straight line corresponds to the volume of the sessile droplet printed at those conditions. The vertical lines are the error bars.

An additional experiment was performed in which time-resolved images of the process from the top view were acquired at similar irradiation conditions as before (fluence of 3 J/cm$^2$) but this time with the receptor substrate in place (Fig. 4.5a). In this occasion, a continuous white lamp (150 W power) was used as illuminating source, situated below the receptor substrate. This high power lamp provided enough light to visualize the printing process through the Ti coating: the coating was thin enough to allow passing a small fraction of the incoming light though it. In this experiment, it was possible to simultaneously visualize both liquid film and receptor substrate, since the short liquid film-receptor substrate separation was within the depth of field of the microscope objective of the imaging setup. In the upper part of each image, an array of droplets deposited on the receptor substrate can be distinguished. This array was prepared previously to the imaging experiment, in order to demonstrate that the irradiation conditions were adequate for well-defined droplet printing. All images show in the central part a dark circle with a lighter spot and a halo. This circle corresponds to the vapor bubble generated in the donor film, as it was observed in the side view images, that will further result in the deposition of a droplet (such droplet can be observed in the posterior frames, situated in the left side of the halo). Actually, the behavior of the bubble, with the diameter initially increasing (80 – 580 ns) until reaching a maximum diameter

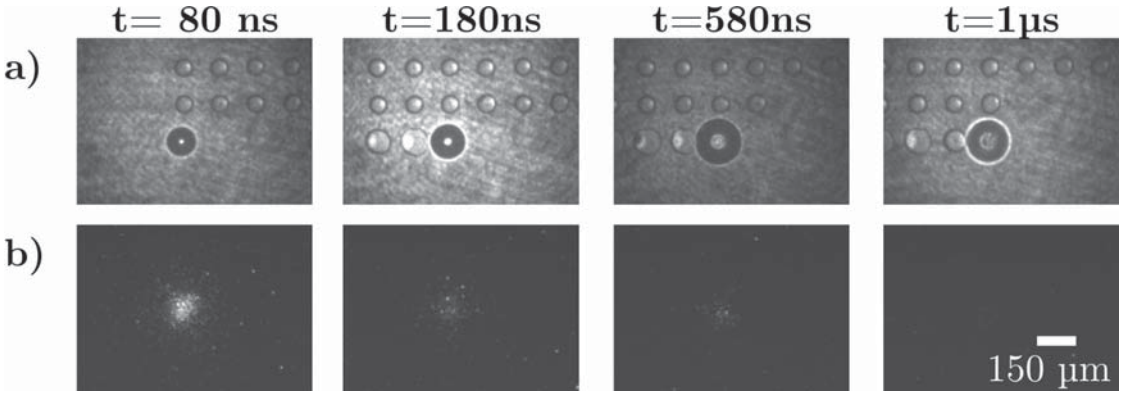


**Fig. 4.5.** Top view images of the transfer process using a) an illuminating source, which allows visualizing the vapor bubble generated; and b) no illuminating source, which allows detecting the presence of a plasma. The bright points in the background of this last series are due to the high intensification of the MCP, which produces a low signal-to-noise ratio.

of around 100 µm which then remains constant (580 ns – 1 µs), is consistent with the side view images (Fig. 4.2). The top view images also demonstrate that the bubble presents revolution symmetry around the axis of the laser beam. Therefore, it is clear that all the bubbles and jets observed in the side view images of the process (Fig. 4.2) also have such revolution symmetry, validating the previous assumption made in the calculations of the feature volume. A second series of images was acquired at the same conditions as the first one, but without any illumination source (Fig. 4.5b). In this case, the MCP was intensified at its maximum in order to detect any signal. It can be observed that a spark of light is initially generated, which progressively fades away until it completely disappears at about 1 µs. This spark is an evidence of plasma formation, a plasma which is generated due to the ablation of the Ti film. In fact, the presence of spots on the Ti film (not shown) at all analyzed fluences, even at those not leading to droplet deposition, confirms the ablation of the absorbing coating.

The dynamics observed in this experiment, in which very long and stable jets are developed, had never been reported before. Actually, in previous time-resolved LIFT experiments liquid ejection proceeded in a different way [Young *et al.* 2001, 2002, Barron *et al.* 2005a]. Images of the LIFT process in the case of a barium-zirconium titanate/terpineol (BZT) suspension [Young *et al.* 2001,

2002], a viscous paste with a rheology clearly different from that of the present experiment, showed the development of a relatively short, irregular and turbulent jet which fragmented into multiple droplets short after its formation. It should be pointed out that, for such a suspension and irradiation conditions, material deposition did not take place in the form of a single droplet on the receptor substrate, but rather as a set of multiple droplets. On the other hand, and also under different conditions from those of the present experiment, images of the process using a bovine serum albumin (BSA) solution [Barron *et al.* 2005a] showed the formation of a thin and blurred jet which broke into multiple droplets after traveling only 200 µm. In that case, though, the time-resolved images were obtained at different conditions from those of the deposits. Therefore, a direct correlation between time-resolved images and deposited material could not be carried out. Contrary to those previous works, the present experiment shows for the first time the dynamics of the LIFT of aqueous solutions at conditions truly leading to the deposition of well-defined droplets (as Fig. 4.1 witnesses). And the consequences of such finding are very relevant from a physical point of view, since the deposition mechanism in LIFT can be now unveiled: the formation of the long and stable jet indicates that the deposition mechanism must be due to the contact of such jet with the receptor substrate. This definitely overthrows the general assumed idea according to which the deposition mechanism in LIFT was mediated by the formation of a single flying droplet [Barron *et al.* 2005a, Colina *et al.* 2006].

The singular dynamics observed in the LIFT of liquids is initiated when the laser pulse is absorbed in the Ti film, producing the ablation of a fraction of that coating. Such ablation induces a plasma, as it was found above, which expands inside the liquid in a well-known process which leads to the generation of a cavitation bubble [Schaffer *et al.* 2002, Vogel *et al.* 1996a, Brujan *et al.* 2006]. Therefore, liquid ejection is initially mediated by the formation of a cavitation bubble. The dynamics of a cavitation bubble generated into a liquid and near its free surface has been previously studied [Blake *et al.* 1981]. Actually, if the cavitation bubble is generated close enough to the free surface, the bubble expansion can result in the formation of needle-like jets [Pearson *et*

*al.* 2004, Brennen 1995, Brujan *et al.* 2001, Frank *et al.* 2004]. Such situation is similar to that of the present LIFT experiment, although it is not exactly the same: the cavitation bubble generated in LIFT is not a free standing bubble, contrary to those obtained in the reported cavitation experiments, due to the presence of the donor support; in addition, the aspect-ratio of the jets generated in LIFT is also much higher. Despite these differences, those cavitation experiments can help understanding the dynamics of the LIFT process, as it is presented next.

The initial expansion of the LIFT generated bubble is due to a force balance: while the force exerted by the bubble internal pressure surpasses that due to the outward pressure plus the surface tension force, the expansion proceeds. However, such expansion is not isotropic. The relative ease with which the bubble displaces the liquid-air interface (free surface), which contrasts with the difficulty in displacing the surrounding liquid, produces the creation of a pressure gradient in the fluid surrounding the bubble (with the lowest pressure situated in the pole). This can be appreciated in Fig. 4.6a, which presents theoretical calculations using the boundary integral method to solve the motion of a cavitation bubble near a free surface [Pearson *et al.* 2004]: the pressure beneath the bubble is higher (white color) than that of the bubble pole (black color). As a result of this pressure gradient, the bubble becomes elongated and liquid flows along the liquid sheet displaced by the vapor and coming from the unperturbed liquid meet in the pole (Fig. 4.6b). This turns the pole to a high pressure region (white color). The process has been illustrated in the first two frames of Fig. 4.7 for LIFT. This is a typical situation which leads to the development of needle-like jets [Brujan *et al.* 2001]. Actually, two needle-like jets flowing in opposite directions are usually produced [Brujan *et al.* 2001, Frank *et al.* 2004]: one away the free surface, as it is observed in Fig. 4.2, and another within the bubble (called counterjet), which cannot be appreciated in the time-resolved images (but illustrated in the last frames of Fig. 4.7). The formation of such jets can be understood considering that the high pressure region generated in the bubble pole (white color in Fig. 4.6c and 4.6d) forces the

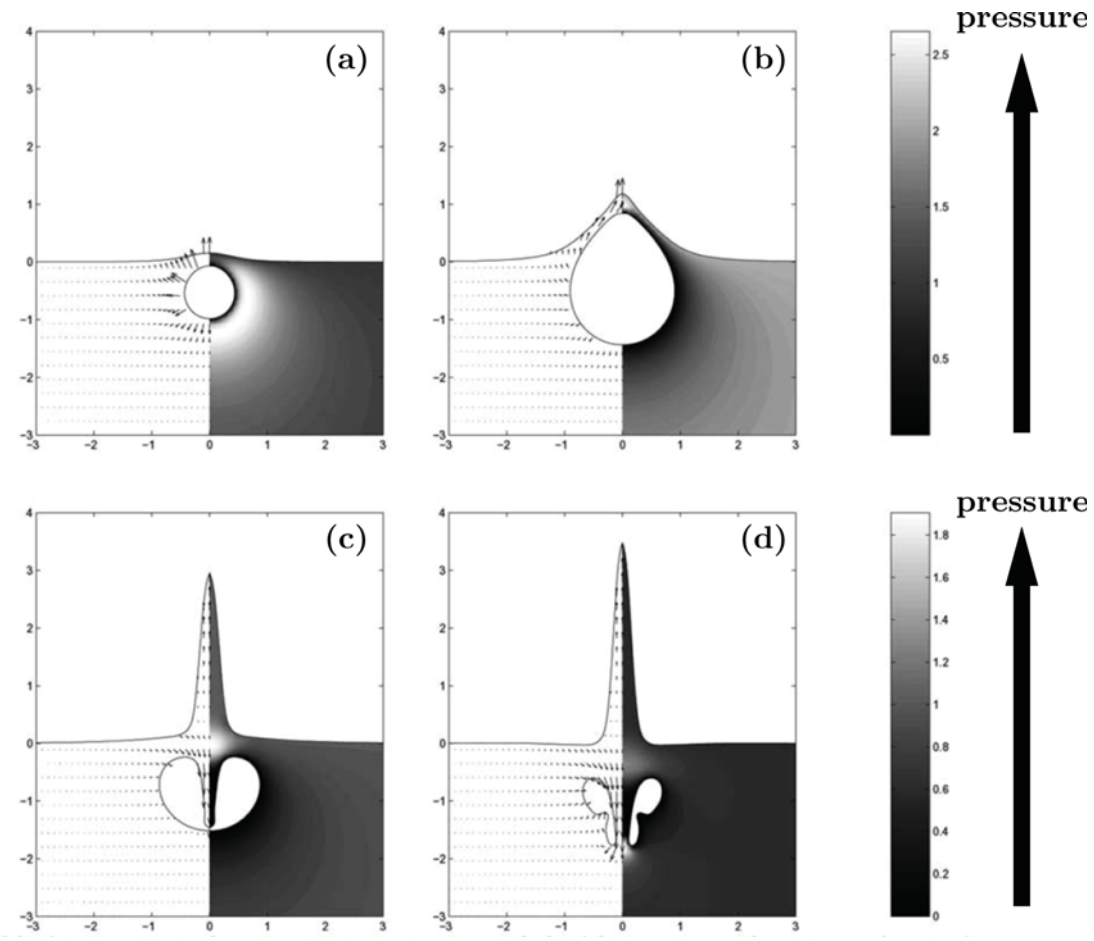


**Fig 4.6.** Calculated velocity and pressure maps corresponding to the motion of a vapor bubble near a free surface at different times. The arrows indicate the velocity vectors, whereas the grey tonalities correspond to the pressure contours. Time evolution from left to right and from top to bottom. From Pearson *et al.* 2004.

fluid towards those regions in which the pressure is lower: the free surface (jet) and the inside of the bubble (counterjet) [Frank *et al.* 2004]. It should also be pointed out that the bubble internal pressure decreases as the bubble expands [Brennen 1995], and thus there exists a moment from which the balance between internal and external forces is favorable to the last ones, which leads to bubble collapse, as it can be observed in Fig. 4.2.

If the jet inertia is high enough to surpass the recoiling force exerted by the surface tension, the jet maintains its progression, while becoming thinner as it advances (Fig. 4.2). As it has been mentioned above, such dynamics has also been observed in cavitation experiments near a free surface [Blake *et al.* 1981].

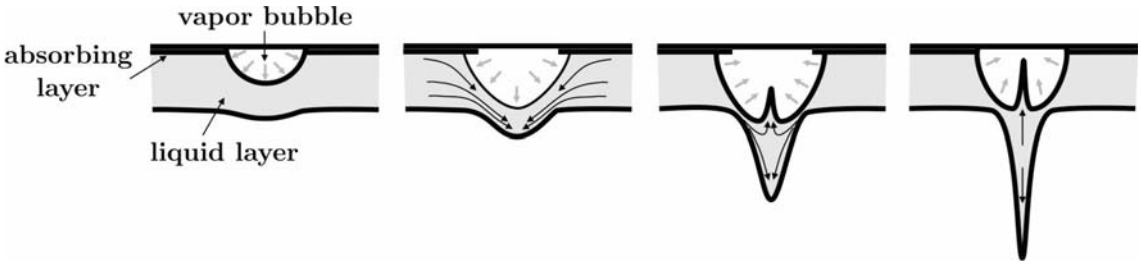


**Fig. 4.7.** Scheme of both bubble evolution and jet formation (from left to right). The black arrows indicate liquid flow, and the grey arrows vapor bubble expansion and recoil.

Actually, the calculations of such experiments [Pearson *et al.* 2004] have evidenced that the evolution of the free-surface position above the bubble is very similar to that of the present experiment (Fig. 4.3). It should be pointed out that the results of those calculations are parameterized respect to the so called standoff distance $\gamma$, which is the distance between the bubble and the free-surface ($d$) scaled with respect to the maximum bubble radius ($R_{max}$), as illustrated in Fig. 4.8a. The $\gamma$ parameter has always a negative value, since $d$ is always considered negative. For any $\gamma$ parameter, the calculation shows that the front position of the raised free-surface initially advances at a high and quite constant speed during bubble expansion, but then it slows down at bubble collapse, continuing advancing at a lower constant speed in the form of a jet (Fig. 4.8b). These two different behaviors, one concerning bubble expansion and the other concerning jet advance at constant speed, are in good agreement with the results of the present experiment. The jet advance does not last forever, but when the jet has reached a long length it becomes unstable and finally breaks (Fig. 4.2) due to surface tension effects in the so called Plateau-Rayleigh instability, as is common in thin liquid streams [Eggers 1997].

In conclusion, time-resolved images of the transfer process during the LIFT of liquids have shown the formation of a regular and uniform jet with a diameter of a few microns and a high-aspect ratio, which develops after the collapse of a laser-generated cavitation bubble. The origin of such bubble has been found to be the plasma generated after laser ablation of the absorbing layer. Once the jet is formed, it advances at a constant velocity of several tens of meters per second

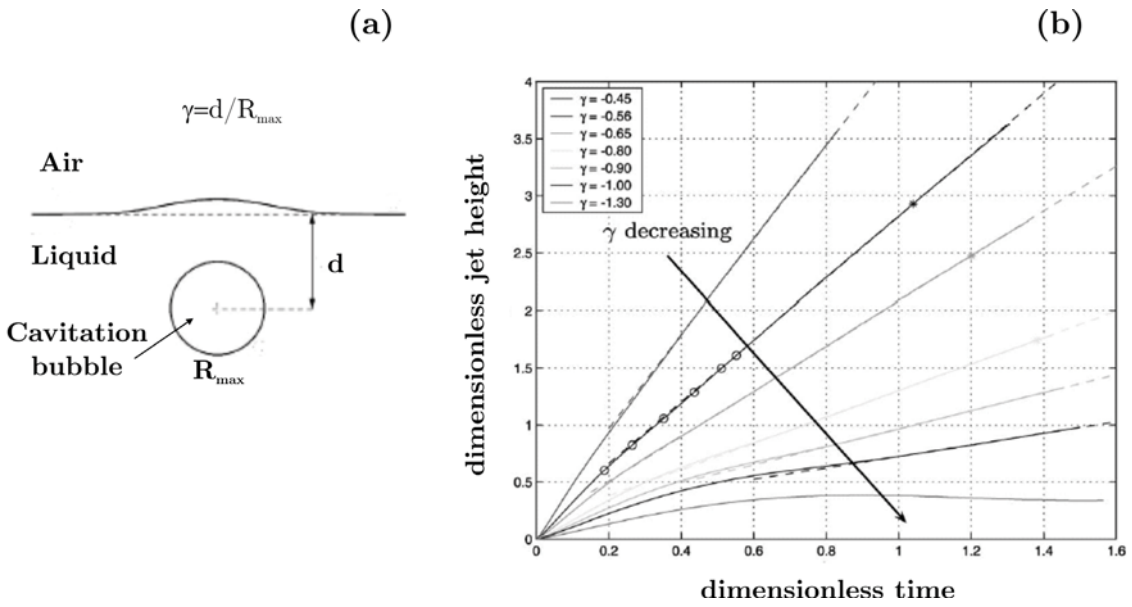


**Fig. 4.8.** a) Scheme of a bubble in a liquid and near its free surface, with the representation of the γ parameter. The γ parameter is always considered negative. b) Calculated evolution of the dimensionless jet height versus the dimensionless time for different γ parameters [Pearson *et al.* 2004].

while its diameter decreases in turn, until it finally becomes unstable and breaks into multiple microdroplets. The formation of such long, regular and stable jets had never been reported before in LIFT experiments. This dynamics is similar to that observed in cavitation bubbles generated close to a free surface, and theoretical calculations of the expansion of such a cavitation bubble predict a behavior which is in good agreement with that observed in the present results. Moreover, this dynamics demonstrates that the process of droplet deposition through LIFT must take place through contact of the liquid jet with the receptor substrate, instead of by free droplet ejection, as it was previously assumed.

## 4.2 Influence of laser fluence in the liquid transfer dynamics

In the previous section, it was observed that the transfer process at conditions which lead to well-defined droplet deposition is mediated through jetting. However, it would be convenient to analyze the transfer process at the different fluence ranges which lead to material deposition with different morphologies.

In this section, a detailed study of the transfer dynamics at different laser fluences is carried out. Moreover, the observed transfer mechanisms are correlated with the morphology of the material deposited at those conditions. Again, the analysis is carried out using the same aqueous solution as in the previous section.

Firstly, a microarray was prepared varying the laser pulse energy from row to row. The liquid film used had a thickness of 20 µm, spread on a Ti coating 50 nm thick, and the liquid-receptor substrate separation was 300 µm (the receptor substrate used was poly-L-lysine). The titanium coating was placed in the focus position, where the laser beam dimensions were $\omega_x=\omega_y=4$ µm. Once the microarray was prepared, the receptor substrate was removed from the LIFT apparatus and analyzed through optical microscopy (Fig. 4.9). It can be observed that there exists a fluence range in which circular and well-defined droplets are obtained. However, at fluences out of this range different situations occur: at high fluences irregular droplets are deposited, and at even higher fluences only splashing is observed; on the other hand, at low fluences no material is transferred. Therefore, the conditions of technological interest, in which a controlled and precise deposition of liquids is required, will be limited to the intermediate fluence range.

Concerning this range, which in this case corresponds to fluences between 1.9 J/cm$^2$ and about 7.0 J/cm$^2$, it can be observed an increase in the droplet dimensions as the laser fluence increases. The droplet volume was measured through optical profilometry and plotted versus the laser fluence (Fig. 4.10).

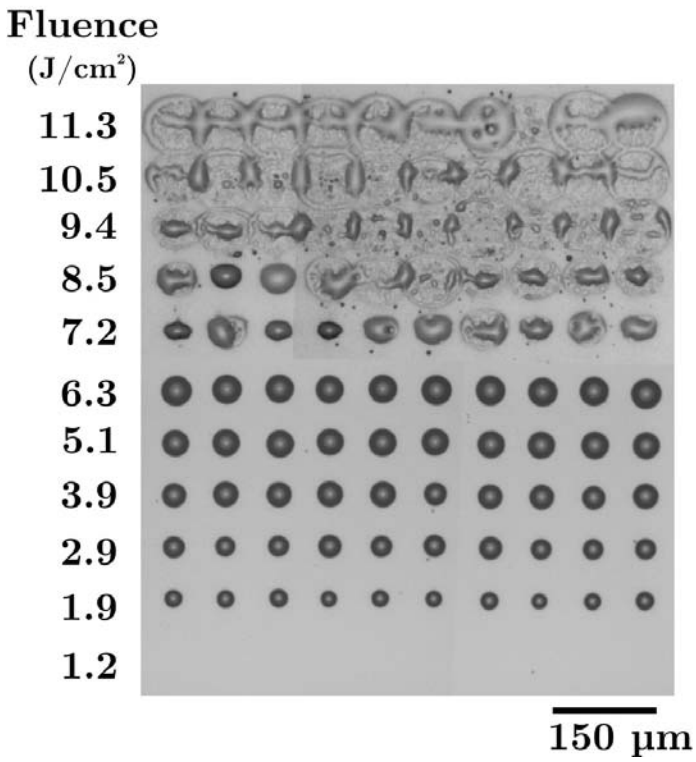


**Fig. 4.9.** Optical microscopy image of the microarray obtained at different laser fluences.

The points present an upward trend with a clear linear increase, as it has also been observed and analyzed previously (chapter 3).

After removal of the receptor substrate (while preserving the donor substrate in its original location), four series of images of the transfer process were acquired in the fluence range of the deposition experiment. Each of these series corresponds to a different laser fluence. The four fluences were chosen to be representative of the different deposition situations that could occur: 1.2 J/cm$^2$ (Fig. 4.11a), in which no material is deposited; 2.4 J/cm$^2$ (Fig. 4.11b) and 5.6 J/cm$^2$ (Fig. 4.11c), which correspond to the regime in which well defined droplets are obtained; and finally 10 J/cm$^2$ (Fig. 4.11d), in which irregular droplets with splashing appear.

In all the images of Fig. 4.11 the laser pulse was incident from above. The background is composed of two clearly differentiated regions, each one with a different grey tonality. The upper dark-grey part corresponds to the donor

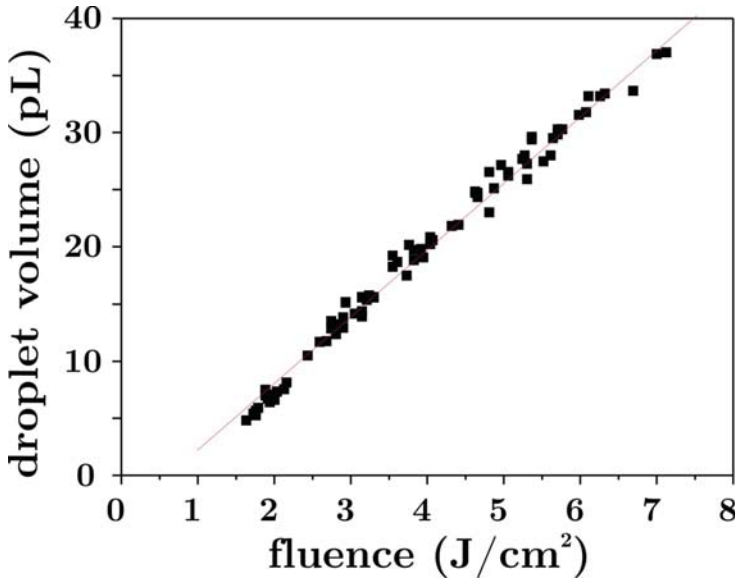


**Fig. 4.10.** Plot of the droplet volume versus laser fluence.

substrate, as the CCD was slightly tilted with respect to the zero grazing angle, and the brightest lower part corresponds to the free space. As described in section 4.1, two different fronts evolving into opposite directions can be distinguished. The upward front is the reflection of the downward one due to the presence of the Ti coating, which acts as a mirror. Therefore, only the downward front should be considered in the analysis.

The initial dynamics of the LIFT process at the different analyzed fluences is mediated by the formation of a cavitation bubble, as it occurred in section 4.1. However, depending on the laser fluence the further evolution is different. In Fig. 4.11a, corresponding to the lowest laser fluence, the bubble expands during the first 1.4 µs, after which it starts suffering a gradual collapse from its sides while the central tip maintains its progression, leading to the formation of a small jet. At 4.1 µs the jet is fully developed, but it does not keep on growing. In fact, in the following frames it can be observed how the jet moves back to the liquid film, noting that recoil is much slower than expansion. Finally, at 100 µs the jet has become a very small protrusion which continues relaxing over a long time (images not shown).

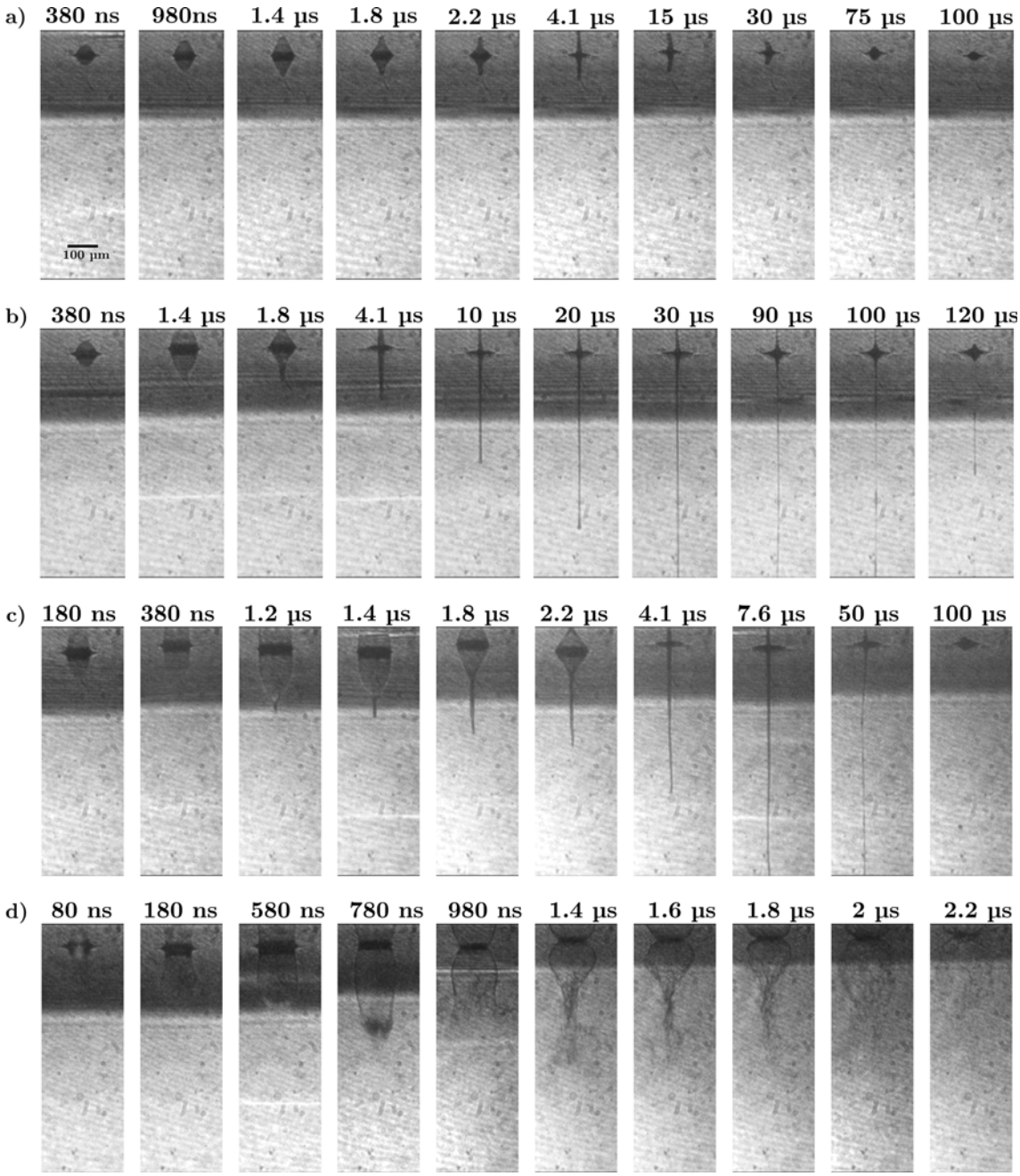


**Fig. 4.11.** Selected images of the time-resolved study of the LIFT process at different laser fluences: a) 1.2, b) 2.4, c) 5.6, and d) 10 J/cm$^2$.

At the fluences in which well-defined droplets are obtained, liquid transfer follows the same singular dynamics as described in section 4.1: the initial expansion process is also similar to that shown in Fig. 4.11a; even the time at which the jet is fully developed is similar for the three series of images (around 4 µs). Yet, it is interesting to notice that expansion is much more significant as the laser fluence increases, that is, the maximum volume of the bubble increases

gradually with fluence. After bubble collapse and once the jet is formed, however, the differences between the dynamics presented in Fig. 4.11a, and those in Figs. 4.11b and 4.11c become relevant: in the latter two cases, once the jet is fully formed it keeps on advancing while maintaining its needle-like shape during the whole progression; the jet thickness decreases as its length increases, leading the jet to achieve a very high aspect-ratio. After the advancing front surpasses the field of view of the camera, it can only be appreciated that thinning proceeds, until the jet finally breaks into multiple parts. The breakup time depends on laser fluence: it occurs between 100 and 120 µs at 2.4 J/cm$^2$ (Fig. 4.11b), while at 5.6 J/cm$^2$ (Fig. 4.11c) it takes place at around 50 µs. After the jet breakup, only a protrusion on the liquid film remains, which persists over several milliseconds (images not shown).

Concerning the transfer dynamics at the highest fluences, a situation different from the previously described ones occurs (Fig. 4.11d). In this case, a bubble is also formed, which expands during the first hundreds of nanoseconds in a similar way as described above. However, at about 780 ns the bubble tip becomes blurred, indicating bubble burst. At 980 ns, burst is evident, and in the following frames the evolution of the broken bubble reveals that it collapses from the sides, reducing its size, with evidence of turbulent flow in the central part. Finally, at 2.2 µs the bubble seems to be almost completely disintegrated.

The analysis of the front position versus time for the four series of images reflects the already described characteristics of the respective dynamics (Fig. 4.12). The initial bubble-expansion process can be easily identified in the four plots, showing a good alignment of the experimental points. The front velocity in this stage notably increases with laser fluence: 25 m/s at 1.2 J/cm$^2$; 90 m/s at 2.4 J/cm$^2$; 150 m/s at 5.6 J/cm$^2$; and finally, 300 m/s at 10 J/cm$^2$. At the lowest fluence (Fig. 4.12a), when bubble collapse and jet formation start, the front position slows down until the jet is fully developed. Then, the jet front undergoes the slow recoiling process described above which corresponds to a quasi exponential decay. At higher fluences (Figs. 4.12b and 4.12c), once the jet

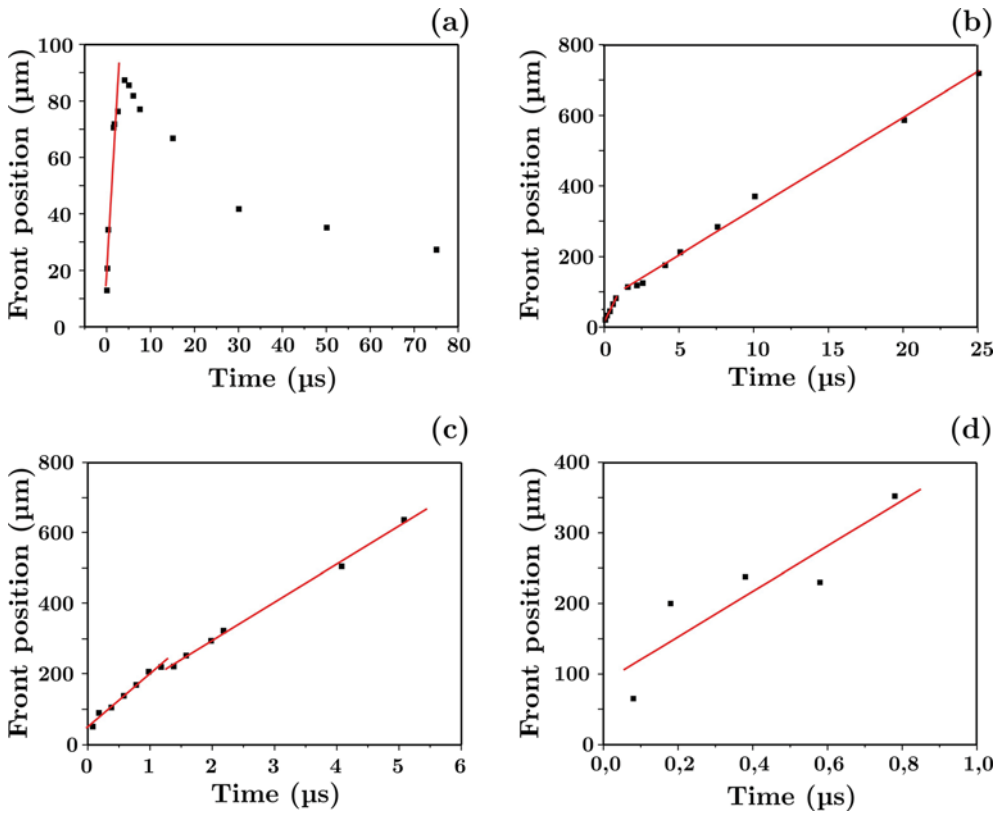


**Fig. 4.12.** Plot of the liquid front position versus time at different laser fluences: a) 1.2, b) 2.4, c) 5.6, and d) 10 J/cm$^2$. The straight lines correspond to the linear fits.

is fully developed, it goes on advancing at constant velocity (25 m/s and 110 m/s respectively) until it disappears from the field of view of the camera. This velocity is always lower than that of the corresponding initial bubble expansion. Finally, at the highest fluences (Fig. 4.12d), since bubble bursting occurs, it is not possible to evaluate the front position after 780 ns.

In order to interpret the present results, it must be pointed out that all the described dynamics have in common the formation of a cavitation vapor bubble which expands (this has already been described in detail in the previous section). However, following bubble expansion three different situations can occur depending on the laser fluence: bubble collapse and formation of a jet which recoils (Fig. 4.11a), bubble collapse and formation of a progressive jet (Fig. 4.11b and 4.11c), and bubble bursting (Fig. 4.11d).

The process of jet formation was already described in section 4.1: during the vapor bubble expansion a pressure gradient is generated in the fluid surrounding the bubble, which leads to fluid flows directed towards the bubble upper pole. When the flows meet in the pole, they generate a high pressure region which produces the formation of a jet. At low laser fluences, once the jet is formed it does not have enough inertia to overcome the force created by surface tension. Therefore, the jet recoils to its initial position (Fig. 4.11a). In this case, since the maximum jet length is shorter than the donor film-receptor substrate distance, the jet cannot reach the receptor substrate and thus, no material is deposited. However, the reduction of this distance could lead to material deposition, as has already been experimentally demonstrated using a different solution (section 3.6).

For higher laser fluences, the jet inertia is high enough to surpass the recoiling force exerted by the surface tension (as it occurred in the previous section). This allows the jet to continuously grow, while becoming thinner as it advances. Such dynamics has been related to that of cavitation experiments near a free surface (section 4.1). Actually, the evolution with fluence of the results presented in Fig. 4.11b and 4.11c is in good agreement with calculations of the motion of a cavitation bubble near a free surface [Pearson *et al.* 2004]. At a fixed depth, as the maximum radius of the bubble increases ($\gamma$ parameter increasing[10]), those calculations show that the initial front speed increases, and the posterior speed reduction (when the jet develops) is less significant (Fig. 4.8b). In the present experiments, we observe the same evolution with the fluence increase: at 2.4 J/cm$^2$ the initial expansion speed is 90 m/s, which is reduced to 25 m/s after jet development; on the other hand, at 5.6 J/cm$^2$, the initial speed is 150 m/s, much higher than in the previous case, and the speed after jet formation is 110 m/s, a much less significant reduction than before (Fig. 4.13). An increase in fluence corresponds to an increase in the maximum radius that the bubble attains during its expansion (Fig. 4.11), while the bubble depth is always the same and corresponds to the liquid film thickness, since the bubble is generated

[10] The absolute value of the $\gamma$ parameter would decrease, but $\gamma$ is always negative.

in the liquid-holder interface. This implies that an increase in fluence produces an increase of the $\gamma$ parameter, and thus indicates that the behavior predicted in Pearson *et al.* 2004 also describes well the evolution in fluence found in the experiments.

In the last stages of jet progression, surface tension effects become relevant and jet breakup finally occurs. The correlation of this dynamics with the droplets deposited at these conditions (Fig. 4.9), allows stating that the conclusion inferred in the previous section is not a singular case, but the deposition of well-defined droplets is in all cases mediated through the formation of long and stable jets, and must proceed by means of the contact of the jet with the receptor substrate.

A very different dynamics occurs at the highest laser fluence. In this case, instead of bubble collapse and jet formation, the bubble bursts. This is due to the high bubble pressure resulting from such energetic laser pulses, which can exert a force on the liquid surface strong enough to overcome the force due to surface tension, leading to the burst of the liquid sheet surrounding the bubble [Pearson *et al.* 2004]. Such dynamics can be related to the deposits of the upper rows in Fig. 4.9 which correspond to these fluences: when the laser fluence surpasses a certain threshold, bubble bursting is the responsible for the splashing obtained on the receptor substrate. Actually, the deposited material at high fluences presents a circular contour, with a diameter comparable to the lateral dimensions of the vapor bubble observed in the initial frames of Fig. 4.11d. This suggests that the bubble initially reaches the receptor substrate leaving a circular mark, and afterwards it bursts producing splashing. The described behavior clearly indicates that the surface tension of the liquid solution is a key parameter which sets the fluence resulting in splashing. Moreover, since the recoiling of the jet is also due to surface tension effects, it can be concluded that this parameter determines the range of fluences resulting in regular and well defined droplet deposition: a low surface tension would result in bubble bursting at low energies and consequent splashing on the receptor

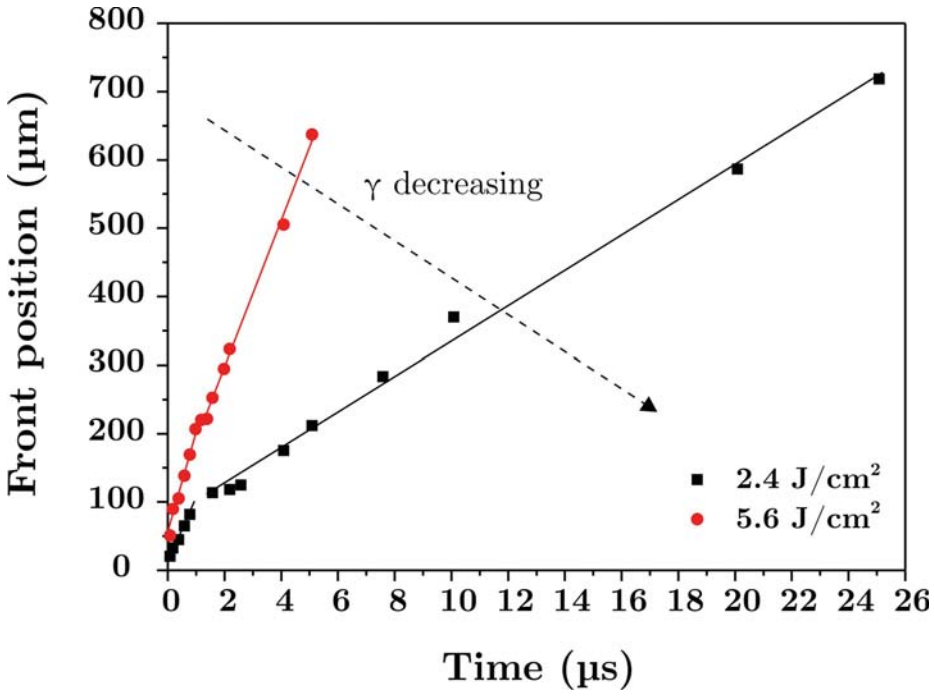


**Fig. 4.13.** Plot of the front position versus time at the two intermediate laser fluences. The solid lines correspond to linear fits. Compare this plot with that of Fig. 4.8b.

substrate, whereas a high surface tension would require high energies to avoid the recoiling of the jet front and thus produce material deposition.

In conclusion, high-speed images of the transfer process dynamics from the side view have shown that initially, and at all the analyzed fluences, a vapor bubble is generated. Once the vapor bubble is formed, it suffers a high-speed expansion process, which can evolve into three different situations, depending on the laser fluence. 1) At low fluences, during the expansion process a needle-like jet is developed due to the high pressure region generated in the bubble pole. Such high pressure is created by the liquid flows towards the bubble pole during bubble expansion. However, the jet is not energetic enough to advance overcoming surface tension forces, and it starts a recoiling process until it finally disappears. Consequently, if the liquid film-receptor substrate separation is higher than the jet length, the jet does not contact the receptor substrate and thus no material is deposited on it. 2) At intermediate fluences, the initial bubble expansion and jet formation is analogous to the previous situation. However, in this case the jet has enough inertia to continue advancing at

constant velocity while progressively thinning. Finally, when the jet has reached a very long length, it becomes unstable due to surface tension effects and breakup occurs. At these conditions, deposition of well-defined circular droplets is achieved. Such dynamics is analogous to that described in section 4.1. 3) At high fluences, the bubble expansion is so violent that it overcomes surface tension resulting in bubble bursting. This situation generates splashing on the receptor substrate.

## 4.3 Influence of the laser beam dimensions on the liquid transfer dynamics

A parameter which plays a key role in the LIFT process is the laser beam dimensions on the titanium layer, as it has been demonstrated in section 3.2. Actually, those results showed that the validity of the previously proposed cylinder model depended on that parameter. Therefore, differences in the transfer mechanism could be expected depending on the laser beam dimensions.

In this section, time-resolved images of the transfer process at focusing conditions different from the ones previously used are presented. In the previous sections, the titanium coating was placed where the laser beam had the smallest beam dimensions. In this occasion, the titanium layer was displaced 300 µm towards the objective, thus increasing the beam dimensions. In order to directly compare these results with the previous ones, the water+glycerol+SDS solution was used (section 2.2.1).

A microarray was prepared varying the laser pulse energy from row to row. The liquid film thickness was 20 µm, spread on a Ti coating 50 nm thick, and the liquid-receptor substrate separation was 300 µm (the receptor substrate was a poly-L-lysine coated slide). The dimensions of the laser beam on the titanium coating were: $\omega_x$=30 µm and $\omega_y$=21 µm. An optical microscopy image of this microarray is presented in Fig. 4.14. It can be observed that well-defined and circular droplets are printed, which diameter increases with the laser pulse energy. The information obtained with this microarray was used to select the laser pulse energy with which the time-resolved imaging experiment was performed. In this case, a laser pulse energy of 5 µJ was selected, which corresponds to an average laser fluence of 0.3 J/cm$^2$, in which circular and regular droplets are deposited with a diameter of about 80 µm. Droplets with the same characteristics were obtained in the previous section using a fluence of 5.1 J/cm$^2$ (Fig. 4.9).

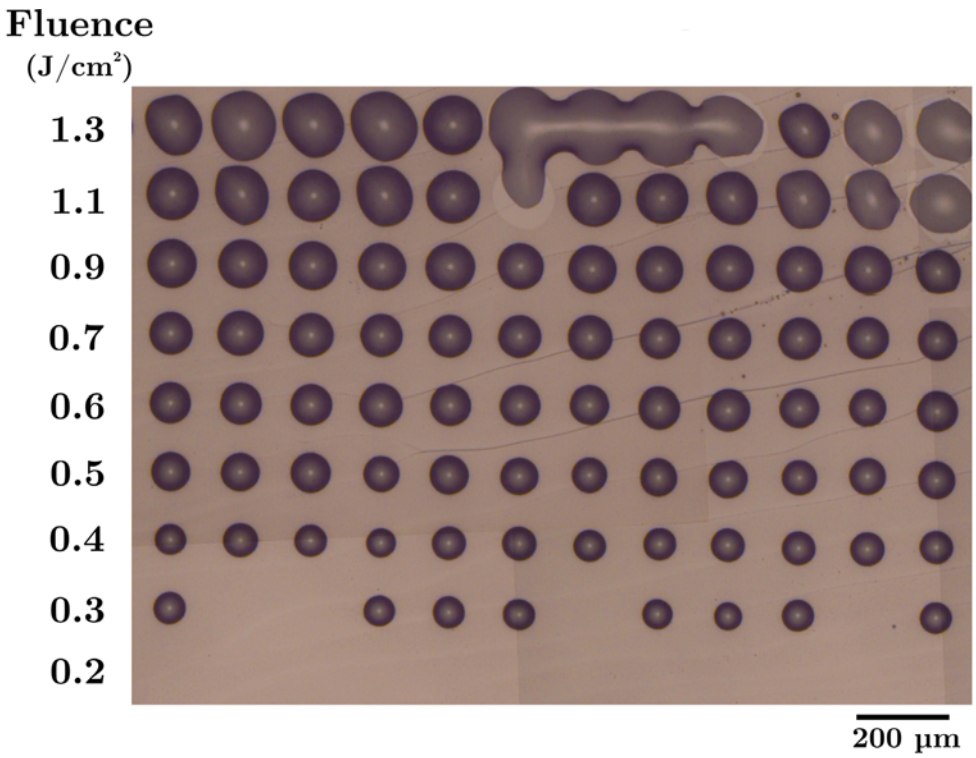


**Fig. 4.14** Optical microscopy image of the LIFT prepared microarray at different laser fluences and at low focusing conditions ($\omega_x$=30 µm and $\omega_y$=21 µm).

The corresponding series of time-resolved images is presented in Fig. 4.15. It can be observed that the main features described for the transfer process of tightly focused beams (sections 4.1 and 4.2) are again reproduced: a vapor bubble initially expands up to about 1.6 µs; then bubble collapses and jet formation occur; once the jet is fully developed at 3.1 µs, it continues advancing while becoming thinner until it reaches a long length and it breaks into different parts. There exist, however, noticeable differences with respect to the previously described cases. In this occasion the jet is formed as a result of the bubble deflation from its sides. This contrasts with the previous results, in which the jet started its development from the bubble tip (Fig. 4.11c, at 1.4 µs). It must also be noted that a much thicker jet than in the previous experiments is developed (around 15 µm at breakup). The jet tip also presents some deviations with respect to the vertical direction (see image at 15 µs), that had already been observed (Fig. 4.10c), but not with such clarity. This last, though, could be due to air flows during the performance of the experiment.

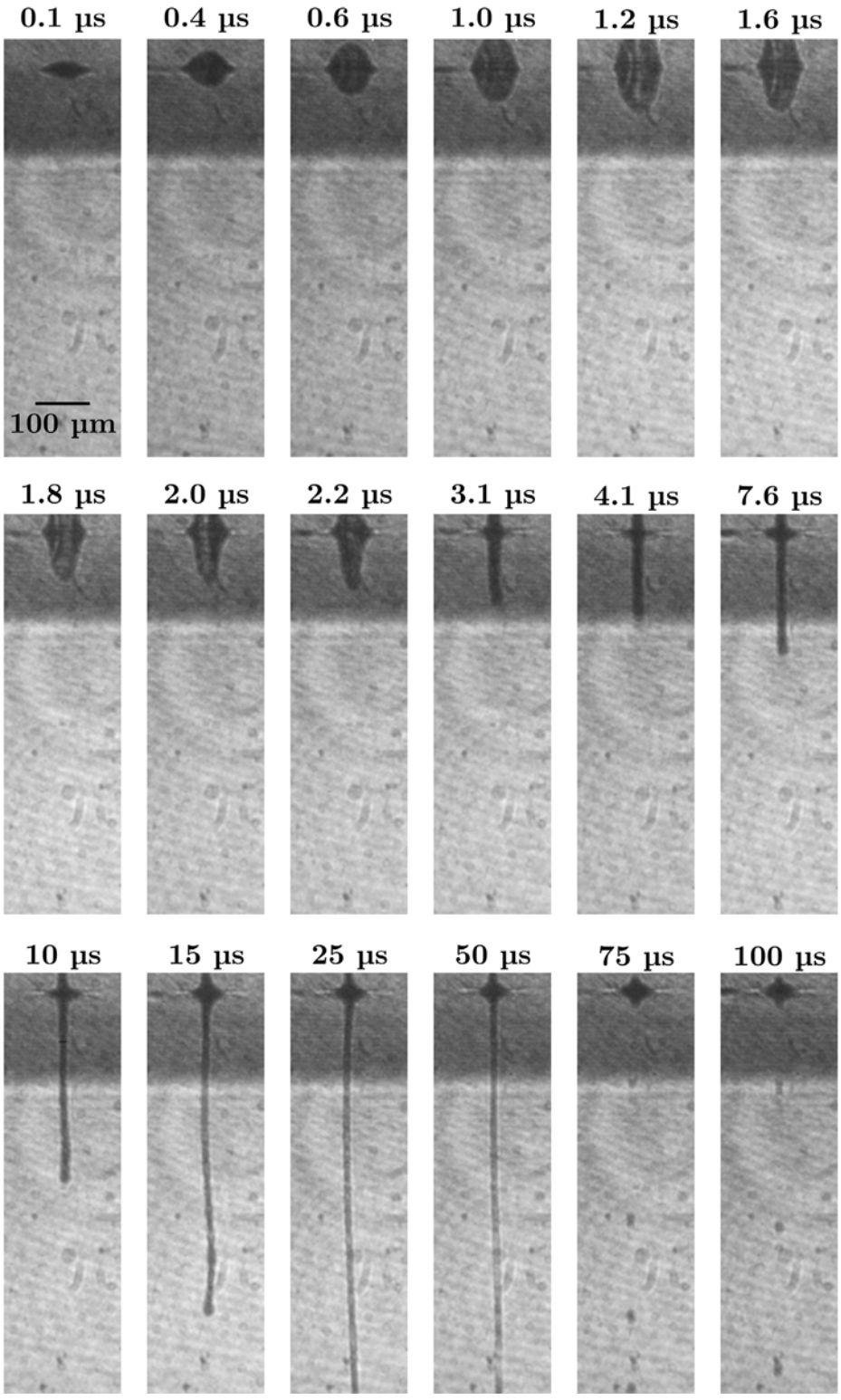


**Fig. 4.15.** Images of liquid dynamics during LIFT using low focused laser beams ($\omega_x$=30 µm and $\omega_y$=21 µm), obtained at different delay times with respect to the laser pulse. Integration time is 100 ns.

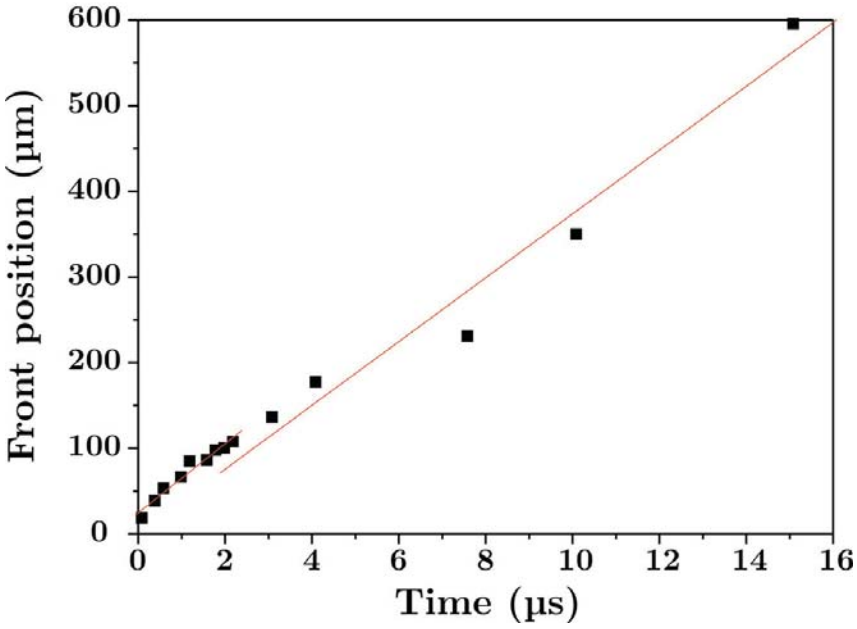


**Fig. 4.16.** Plot of the front position versus time. The solid lines correspond to the linear fits.

The analysis of the front position versus time for low focusing conditions is presented in Fig. 4.16. Again, and despite the differences commented above, the behavior observed in the previous sections is reproduced: during the initial expansion stage (up to 2 µs), the front advances at a higher velocity (40 m/s) than the velocity of the jet when is fully developed (35 m/s). In this occasion, though, the observed velocity difference between the two stages is smaller than that found at focusing conditions (sections 4.1 and 4.2).

The volume of the generated feature can also be calculated from Fig. 4.15, as it was done in section 4.1. The plot of this volume versus time (Fig. 4.17) reveals that after an initial stage in which the volume is significantly increased and further reduced, corresponding to the bubble expansion and its posterior collapse, once the jet is fully developed (4 µs) it advances maintaining its volume approximately constant. This jet behavior has already been observed for tightly focused beams (section 4.1).

The dynamics of the LIFT process for low focused laser beams can be interpreted considering that the initially generated cavitation bubble has a lower pressure than that corresponding for tightly focused beams. Actually, the

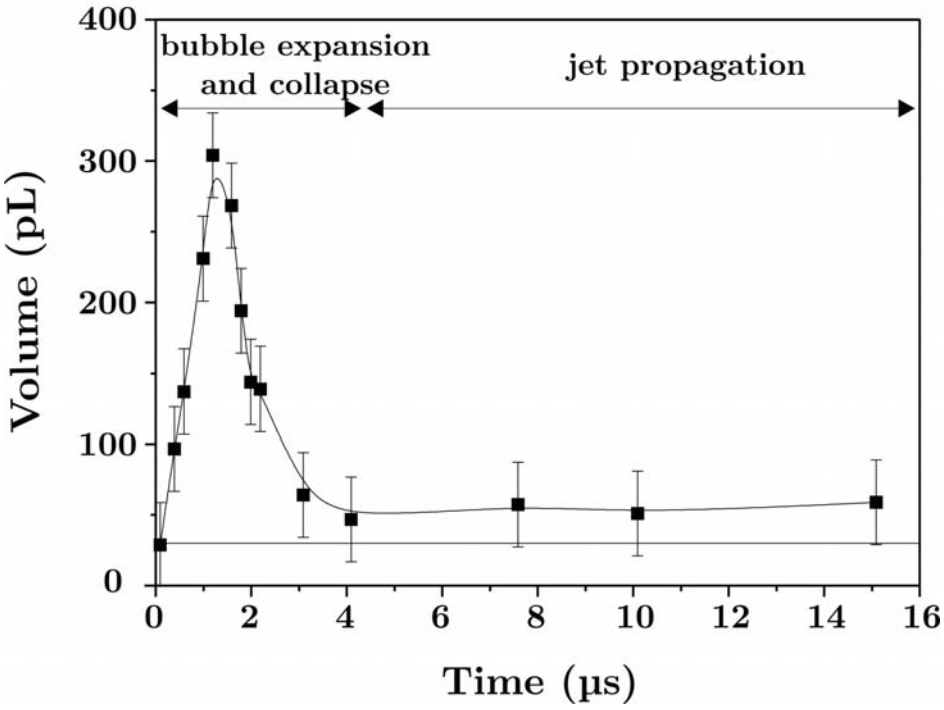


**Fig. 4.17.** Plot of the feature volume versus time. The solid straight horizontal line corresponds to the volume of the sessile droplet deposited at those conditions. The vertical lines are the error bars.

fluences used to print well defined droplets of similar characteristics are much lower at low focusing conditions (Fig. 4.14) than at tightly focusing ones (Fig. 4.9). Such fluence differences are expected to result in differences in the pressure values of the generated cavitation bubble.

In the case of low focused laser beams, once the cavitation bubble is formed it expands, pushing the liquid that surrounds it. Due to the asymmetric environment of the bubble (there is more liquid in the laterals of the bubble than above it), bubble expansion is more prominent algon the vertical direction, producing the displacement of the liquid situated above it towards the free surface (Fig. 4.18a-1 and 4.18a-2). Moreover, and contrary to the case of tighlty focused beams, the bubble lateral pushing force is much weaker (due to the lower bubble internal pressure), which results in a low pressure in the fluid surrounding the bubble laterals. (Fig. 4.18a-2). Therefore, the pressure gradient that appeared at focusing conditions (Fig. 4.18b-1) is practically inexistent (or is very weak). The liquid displaced by the bubble upper hemisphere continues its motion away the free surface, generating the protrusion observed in Fig. 4.15.

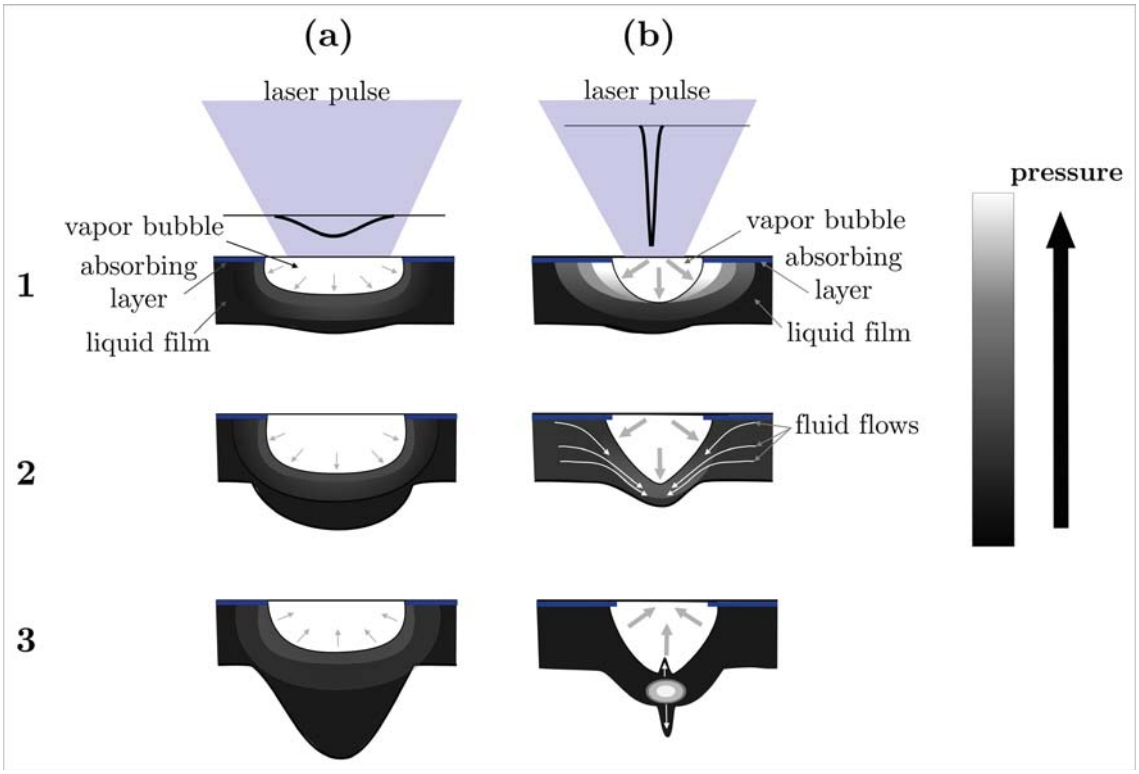


**Fig. 4.18.** Scheme of the LIFT process for: a) low focused beams; b) tightly focused beams. The grey tonalities correspond to the pressure contours. The grey arrows indicate the bubble internal pressure.

Since the bubble internal pressure decreases while it expands [Brennen 1995], there is a certain instance at which the forces oposed to liquid motion (due to the outward pressure and the surface tension) overcome the bubble pushing force. This leads to bubble collapse. Due to the high inertia of the protrusion tip, the liquid from that point continues advancing despite the collapse. On the contrary, the rest of the protrusion points initiate a receding motion (Fig. 4.18a-3). In this way, the jet develops through squeezing and continues propagating (Fig. 4.15, from 3.1 to 50 µs) until breakup occurs due to Plateu-Rayleigh instabilities (Fig. 4.15 at 75 µs).

The previous dynamics contrasts with that occuring at tight focusing conditions (sections 4.1 and 4.2). In that case, and due to the initial high pressure of the cavitation bubble, a pressure gradient in the liquid surrounding the bubble is formed (Fig. 4.18b-1). This produces the appearance of fluid flows towards the bubble pole providing from the unperturbed liquid (Fig. 4.18b-2). The flows

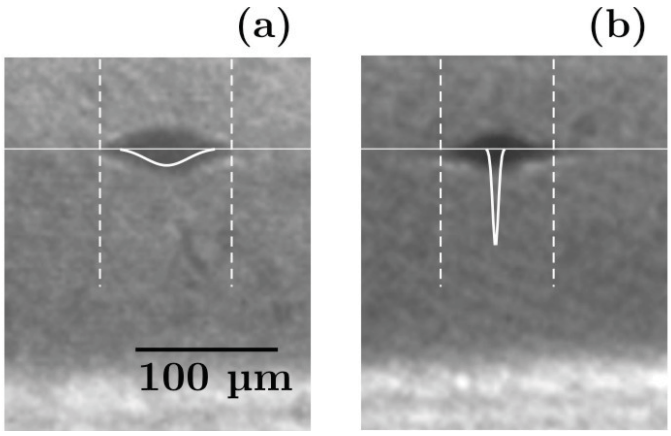


**Fig. 4.19.** Dimensions of the initial protrusion generated in the LIFT process for: a) low focused beam; b) tightly focused beam. The thick white line is the part of the Gaussian beam which overcomes $F_0$. The dashed line indicates the limits of the lateral dimensions of the protrusion.

meet in the pole generating there a high pressure region, which drives the formation of a jet and a counterjet (Fig. 4.18b-3). Therefore, the jet develops from the protrusion tip, and not due to the lateral bubble collapse as it occured in the previous case.

The LIFT process for low focused laser beams can also help understanding the success of the previously proposed cylinder model (section 3.2) at these conditions. Due to the absence of the mentioned pressure gradient, the only liquid displaced at low focusing conditions is that situated above the bubble. Thus, it can be considered that the bubble acts as a piston pushing only the liquid above it, as the cylinder model assumes. In fact, the dimensions of the generated protrusion are similar to those of the base considered in the cylinder model (Fig. 4.19a). Another assumption made in the cylinder model is that the whole displaced liquid is deposited as a sessile droplet. The plot in Fig. 4.17 seems to support this behavior, since the volume of the deposited droplet is similar (within the margin of error) to that of the liquid jet. On the contrary, for tight focused laser beams the cylinder model cannot be correctly applied (section 3.2). This can be related to the dynamics at these conditions: the pressure gradient that appears in the fluid surrounding the bubble produces the appearance of fluid flows from the unperturbed liquid that contribute, in

addition to the liquid initially displaced by bubble expansion, to the jet formation. Thus, in this case not only the liquid situated above the bubble is displaced, but also that providing from the laterals. Since the cylinder model assumption does not consider this additional contribution of liquid from the laterals, it is expected that it will not be possible to successfully apply it. In fact, the dimensions of the initially generated protrusion clearly surpass the dimensions of the base considered by the cylinder model (Fig. 4.19b), which is in agreement with the cylinder model failure.

In conclusion, it has been observed that the transfer dynamics for the LIFT of liquids at low focusing conditions is to some extent similar to that observed at strong focusing conditions. There exist, however, differences between the two processes, being the most important one the fact that, for low focused beams, the jet formation does not occur in the bubble tip but as a result of bubble deflation. This has been interpreted considering that, for low focused beams, the initially generated vapor bubble has a lower pressure which does not result in a significant pressure gradient in the surrounding fluid. In this case, only the liquid above the bubble is displaced during bubble expansion, and when bubble collapse occurs only the liquid from the protrusion tip has enough inertia to continue advancing (the rest of the liquid starts a receding motion). As a result, a jet develops. These results can also help understanding the success of the cylinder model at low focusing conditions.

## 4.4 Time-resolved imaging of droplet deposition during LIFT

In the previous sections, the analysis of LIFT through time-resolved imaging has demonstrated that the transfer process of well defined droplets is mediated by the formation of very stable jets with a very high aspect ratio. The observed jet dynamics allowed concluding that droplet deposition should proceed through contact of the jet with the receptor substrate. However, several aspects concerning the deposition process still remain unknown, including the impact of a high speed jet on the receptor substrate, the posterior jet evolution, or the growth of the sessile droplet, in an overall process gentle enough to allow the deposition of regular and uniform droplets without splashing.

In this section, the dynamics of the LIFT process at real deposition conditions, that is, with the receptor substrate in place, is studied through time-resolved imaging. This allows obtaining a complete picture of the process, and specially the particular dynamics undergone by the growing sessile droplet. In the present experiments, the titanium coating (50 nm thick) was placed in the objective focal plane (the dimensions of the laser beam on the titanium layer were $\omega_x=\omega_y=4$ µm), and the liquid solution employed was the mixture of water and glycerol and SDS previously used (section 2.2.1). The thickness of the liquid film was 20 µm.

Initially, an experiment was carried out in order to determine which is the most appropriate liquid film-receptor substrate separation to be set for the study of the deposition process. This experiment consisted in the preparation of a microarray of droplets through LIFT at diverse liquid film-receptor substrate separations, as shown in Fig. 4.20: every column corresponds to a different distance, from 50 µm to 2 mm. The laser pulse energy was kept constant, at a value of 3.6 µJ, which leads to an average fluence of 4.6 J/cm$^2$. It can be observed that well-defined circular and uniform microdroplets are deposited at distances up to 2 mm. The printing of droplets at distances of the order of the

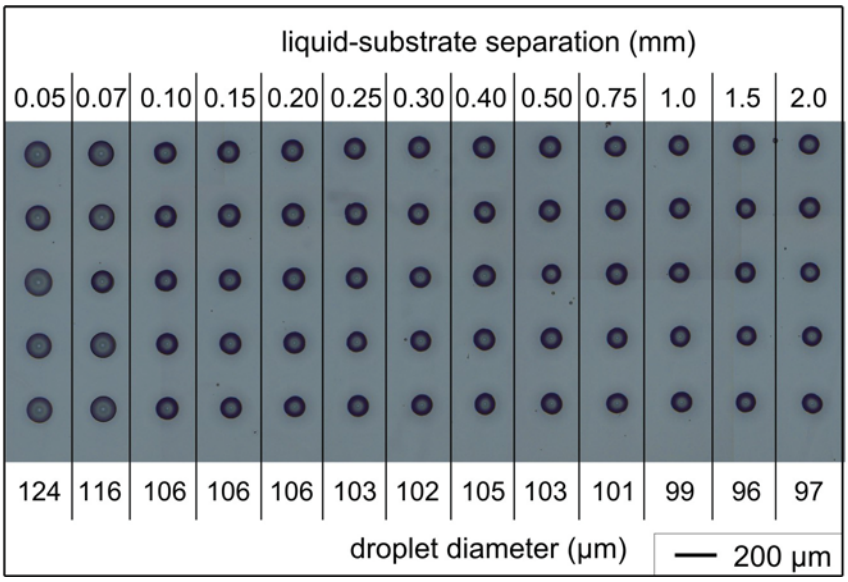


**Fig. 4.20.** Microarray prepared varying the liquid film-substrate separation at an average fluence of 4.6 J/cm$^2$.

mm had already been obtained in section 3.6. Most of the sessile droplets in Fig. 4.20 (from 0.1 to 2 mm) present approximately the same diameter at all distances, with only a slight trend to decrease with that parameter (from 106 μm to 96 μm). This suggests that the deposition mechanism is the same for all the distances within this range, which covers the distances used in practically all LIFT experiments, and thus are the conditions of interest in the present analysis. However, at very short liquid film-receptor substrate distances (50 and 70 μm) the droplets present a larger diameter than at the rest of the distances, and also they have a different grey tonality, being brighter than the other droplets. Such difference in color had already been described in section 3.5, and it was found to be caused by a difference in the droplet contact angle: the brightest droplets presented a smaller contact angle. Moreover, in that section it was also pointed out that the origin of such difference in the droplets morphology could be due to the activation of a different deposition mechanism. Therefore, it could be expected that a different deposition mechanism occurs at separations smaller than 100 μm.

A time-resolved imaging study of the deposition process is presented next. Moreover, that study is complemented with the analysis of the dynamics that

occur at very short liquid film-receptor substrate separations, in order to unveil the different deposition mechanism that could occur at those conditions.

### 4.4.1 Liquid film-receptor substrate separation of 500 µm

The first series of images were acquired at a liquid film-receptor substrate separation of 500 µm, since this gap fits well in the image field of the imaging system and at this distance circular and uniform droplet are obtained (Fig. 4.21). It must be noted that the horizontal fringes which appear in the images correspond to interferences due to the multiple reflections suffered by the illuminating laser beam between the donor and receptor substrates. Moreover, the receptor substrate acts as a mirror for the jet and also for the droplet that grows on its surface; thus, the specular image in the lower part of the figure must not be considered in the analysis.

Liquid ejection and further propagation in the air gap between donor film and receptor substrate proceeds in the same way as it has been reported in imaging experiments with no receptor substrate (sections 4.1 and 4.2): firstly, a bubble is generated in the liquid film which expands like an inflating balloon and produces the formation of a jet; after about 3 µs, the bubble starts a gradual collapse from its sides while the central jet maintains its progression, propagating perpendicularly to the liquid film surface; finally, the jet reaches the receptor surface at about 10 µs after the laser pulse. A detailed explanation of the liquid ejection process is provided in section 4.1.

The plot of the front position versus time (Fig. 4.22) reveals that the jet advances at a constant velocity of almost 50 m/s before it contacts the receptor substrate. Once the jet reaches the receptor substrate, it starts accumulating liquid in the impact position while preserving its stable and well defined shape. In this way, droplet deposition proceeds. The jet gently feeds the growing

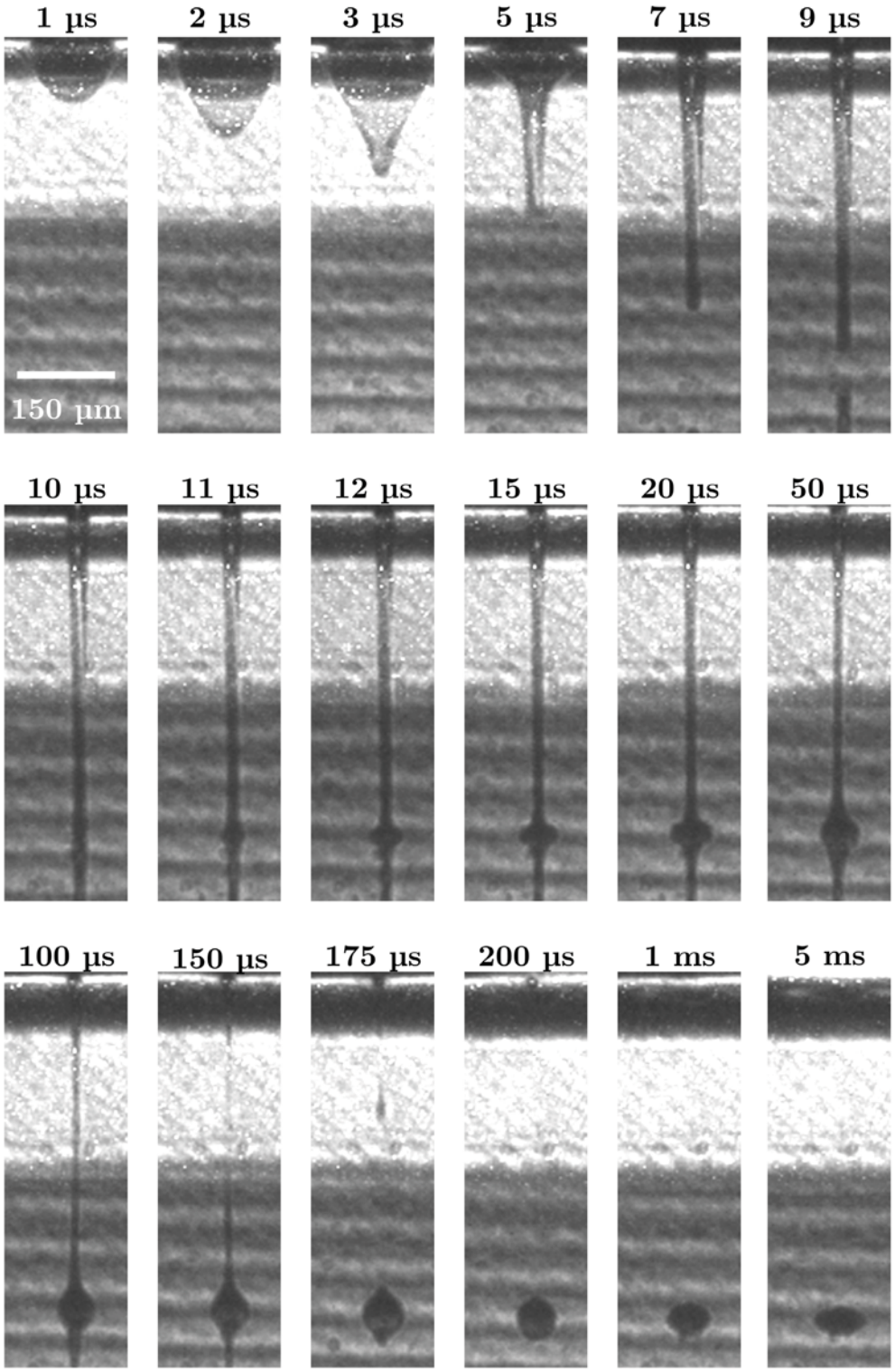


**Fig. 4.21.** Time-resolved images of liquid ejection and sessile droplet formation through LIFT, at different delay times with respect to the laser pulse. The liquid film-receptor substrate separation was 500 µm.

droplet, which volume increases while the jet diameter decreases, a process that lasts about 165 µs (up to 175 µs after the laser pulse), after which jet breakup

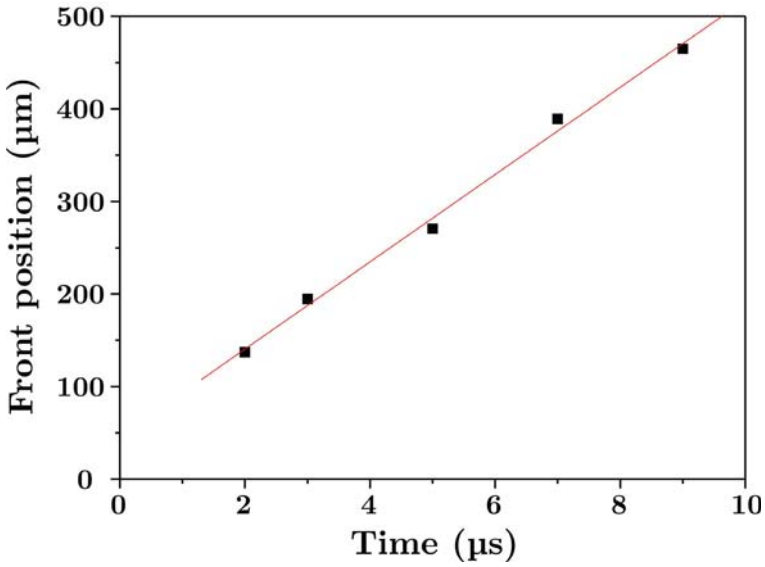


**Fig. 4.22.** Plot of the front position versus time before contact of the jet with the receptor substrate. The solid line corresponds to the linear fit.

occurs. From this instant, the deposited sessile droplet, presenting a spherical cap shape, starts a relaxation stage which leads to the slow increase of the droplet diameter without further liquid contribution; 10 ms after the laser pulse (the maximum delay time of the imaging system) relaxation is still taking place.

A plot of the diameter of the accumulated liquid versus time (Fig. 4.23) reveals three well defined stages during the droplet formation process. In the first one, which starts when the jet tip contacts the receptor substrate and only lasts 10 µs, the diameter of the accumulated liquid increases rapidly from about 30 µm (the jet tip diameter) to almost 70 µm (increase rate of about 4 m/s). During the second stage, which lasts for about 150 µs, the accumulated liquid volume increases at constant diameter. Finally, in the third stage, and after jet breakup, the droplet diameter slowly increases at constant volume (increase rate of about 3 mm/s); this stage corresponds to droplet relaxation after deposition.

The developed jet advances towards the receptor substrate until it impinges on its surface. The impact of liquid jets onto solid surfaces has already been reported [Lesser 1995, Kennedy *et al.* 2000]. However, those studies were focused on thick jets (fractions of mm) at high speed, which acted as a hammer when

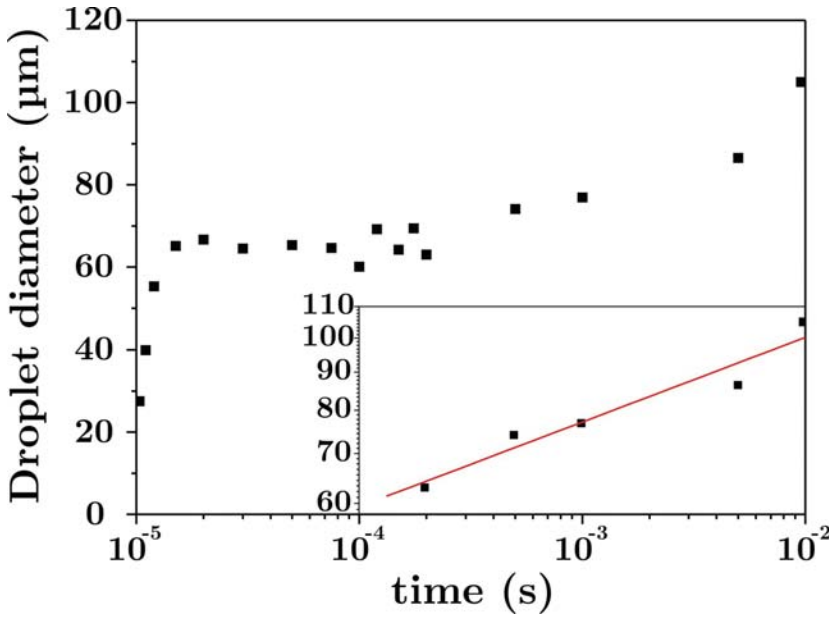


**Fig. 4.23.** Semi-log plot of the growing droplet diameter versus time. The liquid film-receptor substrate separation was 500 µm. The inset presents a log-log plot of the points corresponding to the relaxation phase after jet breakup and their fitting line.

they reached the solid surface, thus damaging it. Contrary to that violent process, the dynamics of the LIFT of liquids is gentle enough to allow the deposition of well-defined droplets without splashing. Therefore, in the analysis of the present results it is more adequate to recall different model instances which, although not corresponding exactly to liquid jets, can help describing the gentle deposition process in the case of LIFT. They consist in the impact of a falling drop onto a solid surface at moderate speed [Rioboo *et al.* 2002, Roux *et al.* 2004], and also in the continuous drop growth through controlled liquid feeding [Kwok *et al.* 1997].

Just after the arrival of the liquid jet onto the receptor substrate, the liquid which has contacted the solid surface suffers a spreading process, as it can be appreciated in the initial increment of the plot in Fig. 4.23. This behavior is also observed in the early stages of a droplet which impacts onto a dry surface at a speed in which splashing is avoided [Rioboo *et al.* 2002, Roux *et al.* 2004]. In that situation, the landed droplet initially takes the form of a truncated sphere which expands preserving its shape, until a lamella is ejected from the droplet

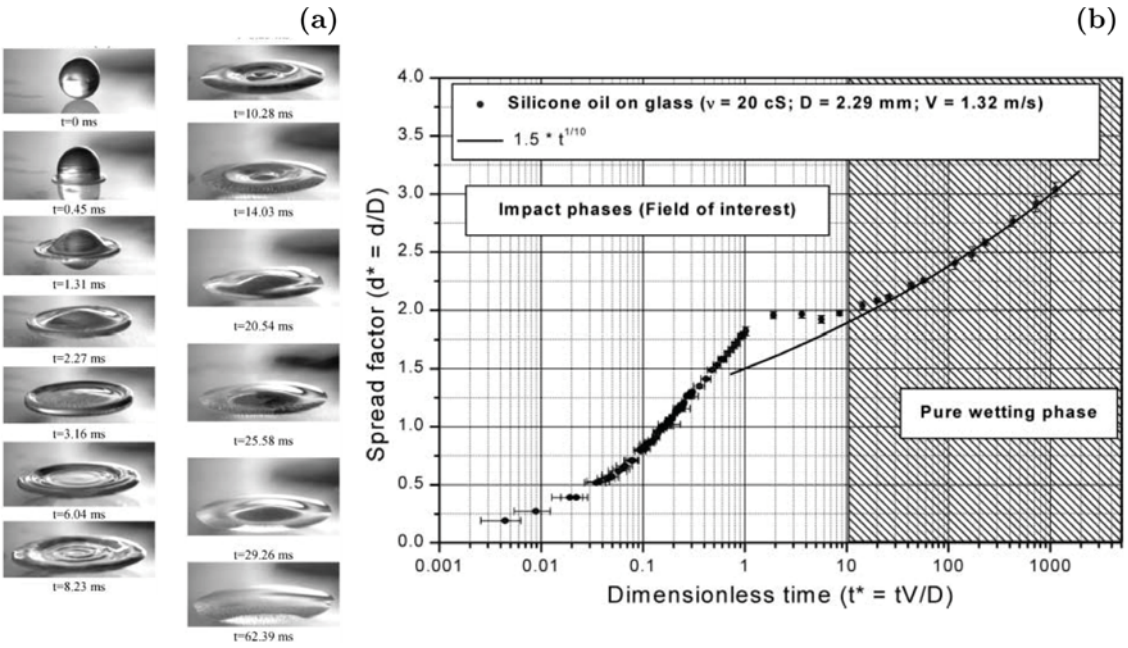


**Fig. 4.24.** a) Time-resolved images of a water droplet impacting on a glass surface; b) Plot of the spread factor (sessile droplet diameter divided by the initial spherical drop diameter) versus the dimensionless time (time multiplied by the impact velocity and divided by the initial spherical drop diameter) for a wettable substrate (from Rioboo *et al.* 2002).

base continuing the spreading process. Such dynamics is accompanied by the flattening of the droplet. In fact, the slightly flat shape of the deposited feature in the images of Fig. 4.21 corresponding to 12-20 µs resembles that observed during the spreading stage of a water droplet impacting on a glass surface (Fig. 4.24a). This initial process stops when a certain diameter is reached, which results from the competition between the liquid inertia, given by the initial impact conditions, and the fluid friction due to liquid viscosity.

After the spreading stage, the diameter of the deposited liquid remains constant although the jet continues feeding the growing droplet. This situation resembles that found in low-rate dynamic contact angle experiments, in which liquid is progressively added to a sessile droplet [Kwok *et al.* 1997]. In some of those cases, for instance when a water droplet is deposited onto a polymeric surface, it is also observed a growth in the sessile droplet volume at constant diameter, which is accompanied by an increase in the contact angle. The reason of such behavior is that the sessile droplet is in a metastable state, and in order to

produce the increase of the sessile droplet diameter a certain energy of activation (which depends on the liquid/vapor interface area) must be provided [Gao *et al.* 2006]. When feeding the droplet, the liquid/vapor interface area will increase maintaining the droplet diameter constant until enough energy of activation is reached to produce the contact line advance. For quasi-static experiments, such as the low-rate dynamic contact angle ones described above, the energy of activation required to initiate the droplet motion is reached when the sessile droplet presents a certain contact angle, the so-called advancing contact angle. In the present experiment, however, the jet feeding is clearly a dynamic process. In these situations it has been observed that the advancing contact angle can be surpassed without producing the droplet advance [Sikalo *et al.* 2005]. This would account for the high contact angle that can be observed for the droplet at 200 µs. The jet feeding process ends up with the jet breakup into multiple parts. This is due to the Plateau-Rayleight instability [Eggers 1997], as it occurs in time resolved imaging without any receptor substrate (sections 4.1 and 4.2).

The final stage of droplet formation takes place after the jet breakup. At this instance, the formed sessile droplet starts a slow relaxation process which is manifested through an increase in the droplet diameter and a decrease in the droplet contact angle. This stage is driven by the wettability of the substrate with the liquid: the droplet tends to spread in order to diminish its contact angle so that it can reach the contact angle observed in static conditions[11]. For good liquid-substrate wettability, the droplet diameter increase with time is proportional to $t^{1/10}$ [Rioboo *et al.* 2002]. The final stage of Fig. 4.24b illustrates this behavior for a water droplet impacting on a glass substrate. The alignment of the experimental points in the log-log plot of the inset in Fig. 4.23 reveals such a potential dependence with time, and the fit provides with an exponent of 0.11, in good agreement with the predicted behavior.

[11] For non-perfect surfaces, the static contact angle presents hysteresis, that is, it can have any value comprised between two extreme values: the advancing contact angle $\theta_A$ and the receding contact angle $\theta_R$ [Gao *et al.* 2006].

Some additional considerations concerning the relation between the jet dynamics and the deposited material are still convenient. When the jet contacts the receptor substrate surface, the force due to surface tension, which initially tended to brake jet progression (even stopping it at low laser fluences, as shown in section 4.2), now pulls it down, promoting liquid feeding of the forming droplet. Furthermore, this pulling effect can contribute to maintain the stability of the jet during droplet formation. However, such effect does not seem to result in additional liquid collection from the liquid film, as the preservation of the droplet volume when varying the donor film-receptor substrate distance seems to indicate. In fact, the jet evolves keeping its volume constant, and the volume of the deposited material corresponds approximately to that of the fully developed jet. Certainly, the preservation of the jet volume during its propagation has already been described (section 4.1). Considering Fig. 4.4, which presents a plot of the protrusion and jet volume versus time, it can be observed that after 4 µs it maintains a constant volume of 60±10 pL all along its progression. Thus, the jet presents an "elastic-like" behavior, in the sense that during propagation it becomes progressively thinner by elongation, without further liquid collection from the film. On the other hand, the volume of the sessile droplet deposited on a receptor substrate at identical irradiation conditions is around 50 pL. Moreover, the jet breakup process always occurs so that only a short thread remains attached to the donor, as it can be observed in time-resolved images of the LIFT process with receptor substrate (Fig. 4.21), and without it (Fig. 4.2 and Fig. 4.11). Estimations of the volume of the thread indicate that it is considerably smaller (about 1 pL) than the total jet volume. This, in addition to the approximate correspondence (within the experimental error) between the volume of the jet and that of the droplet, indicates that the sessile droplet is formed from practically all the jet with no additional collection of liquid from the film. Thus, the "elastic-like" character observed in a free evolving jet would not be altered by the presence of the receptor substrate. Hence, surface tension can possibly modify the jet dynamics when this contacts the receptor substrate, but it does not seem to significantly affect the final amount of deposited material.

### 4.4.2 Liquid film-receptor substrate separation of 250 µm

In order to find out which is the deposition mechanism that occurs at very short liquid film-receptor substrate separations, and which leads to the differences in the morphology of the sessile droplets observed in Fig. 4.20, a time-resolved imaging study of the deposition process at those conditions was intended. However, the donor film-receptor substrate system at the extremely short separations in which the different deposition mechanism was presumably activated (50 or 70 µm) could not be visualized with the present experimental setup: the amount of light that passes through such a short separation is not enough to obtain a clear image even with the maximum intensification of the MCP. In spite of this inconvenient, the results of section 3.6 showed that the possible activation of the different deposition mechanism could also occur at higher donor film-receptor substrate separations using high laser pulse energies (Fig. 3.20). Therefore, in order to unveil the origin of this different deposition mechanism the time-resolved analysis was performed at the shortest donor film-receptor substrate separation that allowed the acquisition of images (250 µm), and at a laser pulse energy high enough so that the droplets printed in this way presented the morphological characteristics of those obtained when the different deposition mechanism was activated. In the present case, such energy was found to be 4.5 µJ (average fluence of 5.9 J/cm$^2$).

This second series of images is presented in Fig. 4.25. First of all, it must be pointed out that the high laser pulse energies used in this experiment were close to the conditions that produce bubble bursting. Therefore, any inhomogeneity of the liquid film could easily result in splashing on the receptor substrate. This made difficult the acquisition of a large series of images. In Fig. 4.25 it can be observed that, after the laser pulse absorption at the Ti coating, a vapor bubble is generated which expands. As a result of the high laser pulse energy employed, the dimensions of the vapor bubble are considerably large. In fact, during its expansion the bubble reaches the receptor substrate (at about 0.5 µs). This process is completely different from the one observed in the previous case, in which the vapor bubble collapsed into a jet, and it was the jet which contacted

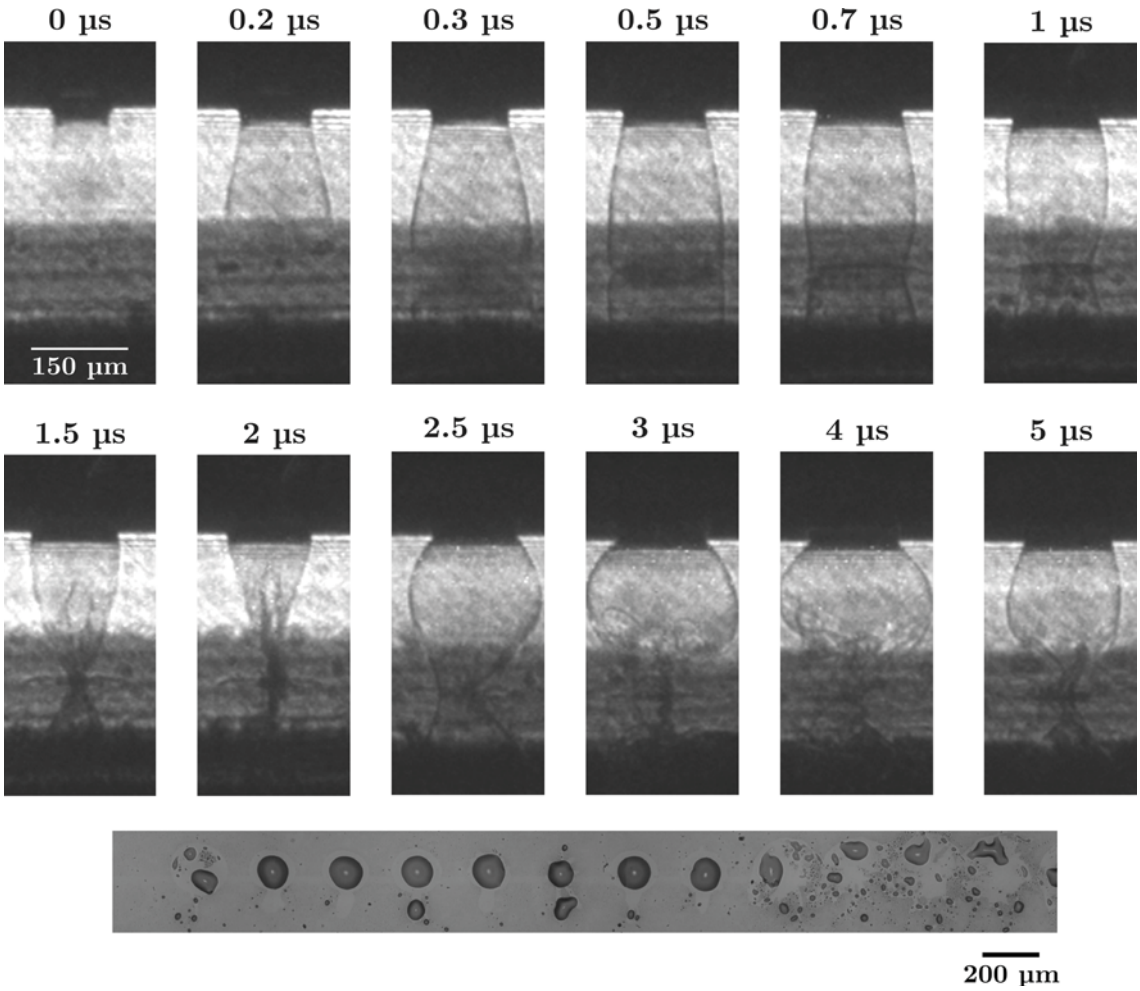


**Fig. 4.25.** Time-resolved images of the LIFT process at different delay times with respect to the laser pulse, and at a liquid film-receptor substrate separation of about 250 µm. The optical microscopy image in the bottom directly corresponds to the droplets printed during the time-resolved imaging experiment.

the receptor substrate. After the bubble impact, the bubble collapses from its tip (in contact with the receptor substrate) and it seems to evolve into a jet at 2 µs. At further times, however, the evolution changes drastically: the bubble presents a turbulent aspect which indicates bubble bursting. This abrupt change denotes that the images obtained from 2.5 to 5 µs were acquired at different conditions from the previous images: probably the donor film did not present a uniform thickness over all the irradiated area. Such difference, and due to the mentioned extreme conditions of the experiment, would have produced the change in the dynamics observed. In fact, the morphology of deposited droplets from 2.5 to 5 µs evidence splashing, contrary to the previously obtained ones (Fig. 4.25), which is in agreement with this assumption. Therefore, the images

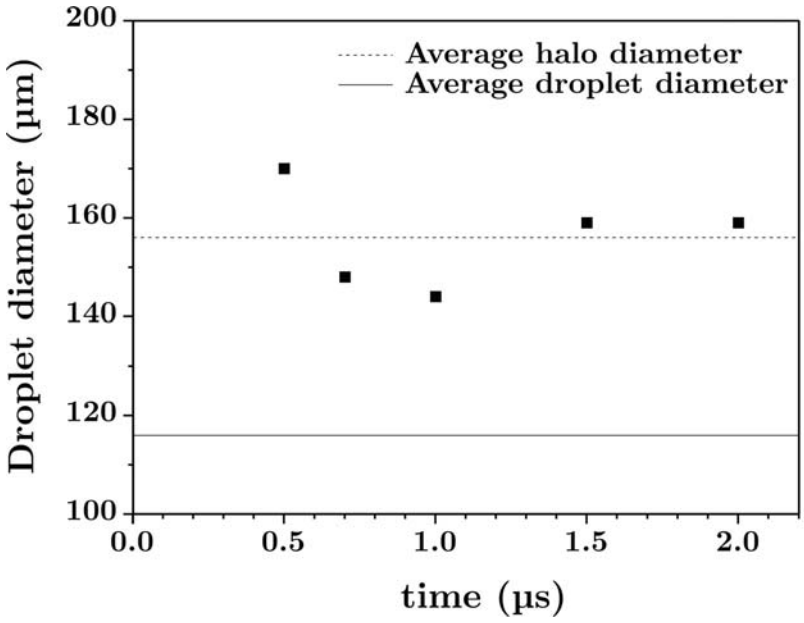


**Fig. 4.26.** Plot of the growing droplet diameter versus time, with a liquid film-receptor substrate separation of 250 µm. Both halo and droplet diameter were determined from the optical microscopy images in Fig. 4.27.

at times longer than 2 µs are out of the regime that pretends to be analyzed, and will not be further considered. However, the situation found at 2 µs, in which the bubble seems to evolve into a jet, suggests that the dynamics at longer times will be similar to that previously found: a jet will be formed which will continue feeding the forming droplet until jet breakup occurs.

The plot of the accumulated liquid versus time (Fig. 4.26) clearly differs from that obtained when the jet contacts the receptor substrate (Fig. 4.23). In the present situation, the initial size of the forming droplet corresponds to the bubble contact area with the receptor substrate, which is about 170 µm, much larger than in the case of jet contact. When the bubble collapses, the forming droplet maintains its diameter rather constant, at a value which closely corresponds to the initial contact area. At longer times, no more images are available for quantifying the droplet diameter, as it was previously mentioned. Despite this fact, the optical microscopy images of the sessile droplets deposited at these conditions can be used to track the evolution of the forming droplet. From the magnified images of some of the printed droplets (Fig. 4.27) it can be

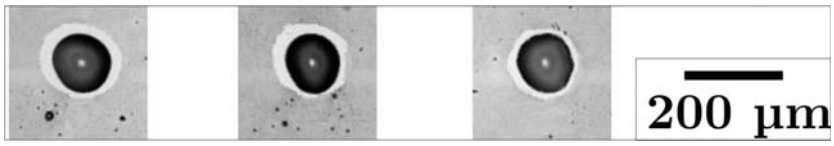


**Fig. 4.27.** Magnified images of some of the droplets printed in Fig. 4.25.

clearly observed that the sessile droplets present a diameter of about 115 µm, and that they are surrounded by a halo with a diameter of about 155 µm. Both quantities have been represented in Fig. 4.26. It can be observed that the final droplet diameter is clearly inferior to that observed during the initial stage of the droplet formation process. Therefore, it is expected that the droplet diameter will suffer a receding process. On the other hand, the halo has approximately the dimensions of the initial bubble contact area, and thus this halo is a vestige of this initial impact. A further discussion of the dynamics of this process is presented next.

When the bubble impacts on the receptor substrate it wets a large area of it, thus producing an initial droplet with a large diameter (Fig. 4.25 and 4.26). The droplet diameter is expected to remain constant during the posterior jet feeding process. This has already been observed in the previous experiment, and the plot of Fig. 4.26 seems to indicate this trend. After the jet breakup, the droplet would suffer a relaxation process. This stage, as it was mentioned in the previous experiment, is driven by the liquid-receptor substrate wettability. In the present case, the droplet relaxation produces a receding of the droplet diameter (as it is deduced from fig. 4.26) which must be accompanied by an increase in the contact angle. An evidence of the droplet recoil would also be the halo that surrounds the droplet in Fig. 4.27. The recoil process would be caused by the fact that the droplet diameter at the beginning of the relaxation process has a larger diameter with a smaller contact angle than that found for a droplet of the same volume in equilibrium at static conditions (the bubble impact forces a non-equilibrium situation). Therefore, the droplet will recede increasing its contact angle until reaching the static contact angle. Since the receptor substrate surface is not perfect, there will be contact angle hysteresis [Gao *et al.*

2006]: the static contact angle could have any value within a range determined by the advancing contact angle $\theta_A$ (characteristic of an advancing droplet) and the receding contact angle $\theta_R$ (characteristic of a receding droplet), being $\theta_A > \theta_R$. This hysteresis would be responsible for the differences observed between the sessile droplets obtained in the present case and those corresponding to the contact of the jet with the receptor substrate (section 4.4.1). In the first case, the static value of the contact angle is reached after a receding process. Therefore, it is expected that the droplet deposited at this conditions will stop its motion when reaching a contact angle value close to $\theta_R$. On the other hand, for the second case the static value of the contact angle is reached after an advancing process. Thus, this contact angle is expected to be close to $\theta_A$. Moreover, if it is assumed that the volume deposited in both cases is the same, the droplets of the first case must have a larger diameter than the second one (Fig. 4.28). The advancing and receding processes are not the reverse of one another [Gao *et al.* 2006], and this could also account for differences between the diameter dispersion of droplets obtained after one process or the other, as it was observed in chapter 3 (sections 3.1, 3.2 and 3.5).

In order to check that the previous interpretation is consistent with the obtained results, the values of $\theta_A$ and $\theta_R$ for the used solution were determined. This was performed by acquiring a picture of a large droplet of the solution sliding on the inclined surface of the receptor substrate. The droplet was deposited using a micropipette, and the picture was taken with a conventional digital camera. The obtained image is presented in Fig. 4.29. From this image, the value of $\theta_A$ is found to be 40°, whereas $\theta_R$ has a value of 11°. The results found in sections 3.5 and 3.6 in which differences in the contact angle of the deposited droplets were obtained are presented again in Fig. 4.30. In the plots, the values of the advancing and receding contact angles have been added. It can be observed that the higher values of the contact angle are close to $\theta_A$, whereas the lower values are close to $\theta_R$. Therefore, this result is in good agreement with the interpretation described above.

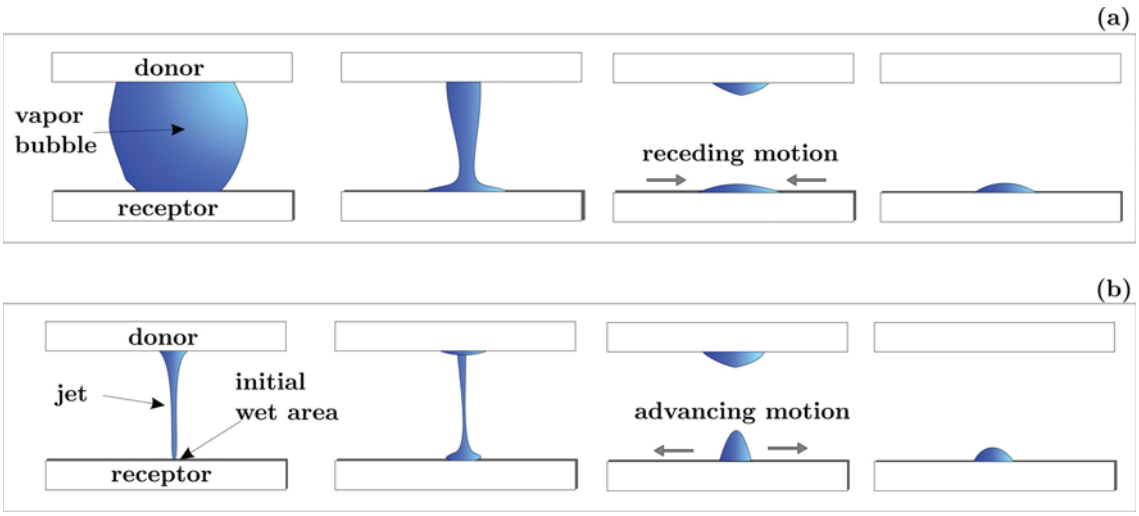


**Fig. 4.28.** Scheme of the droplet deposition process at a) when the bubble contacts the receptor substrate, and b) when the jet contacts the receptor substrate.

With the results obtained in this section, the different deposition mechanism presumed in chapter 3 and which was activated at short liquid film-receptor substrate separations or at high laser pulse energies has been unveiled. In fact, rather than a different deposition mechanism it has been found to be a different deposition regime, characterized by the direct impact of the laser-generated vapor bubble on the receptor substrate, before it can collapse into a jet. This regime could be called *bubble regime*, in order to differentiate it from the LIFT deposition process mediated by a jet, which could be referred to as *jetting regime*. The standard LIFT deposition conditions occur within the *jetting regime*. However, if the receptor substrate is placed close enough to the liquid film, or the laser pulse energy used is high enough to generate a very large

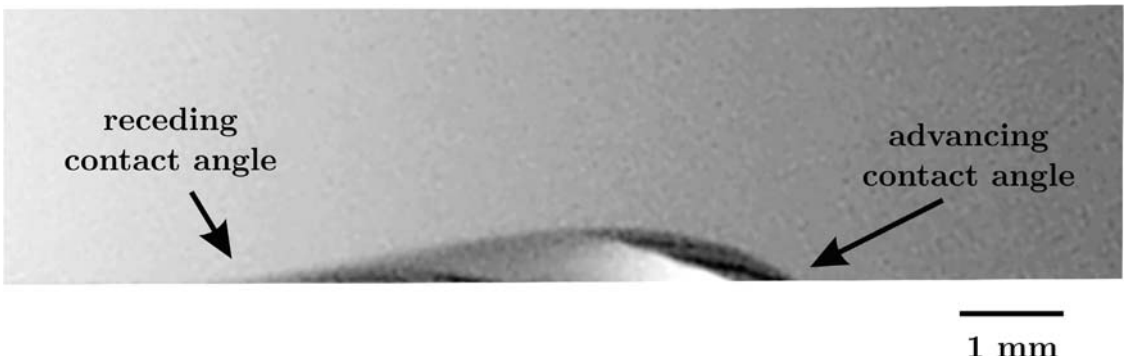


**Fig. 4.29.** Image of a droplet advancing on a tilted substrate which was used to determine the values of both advancing and receding contact angles.

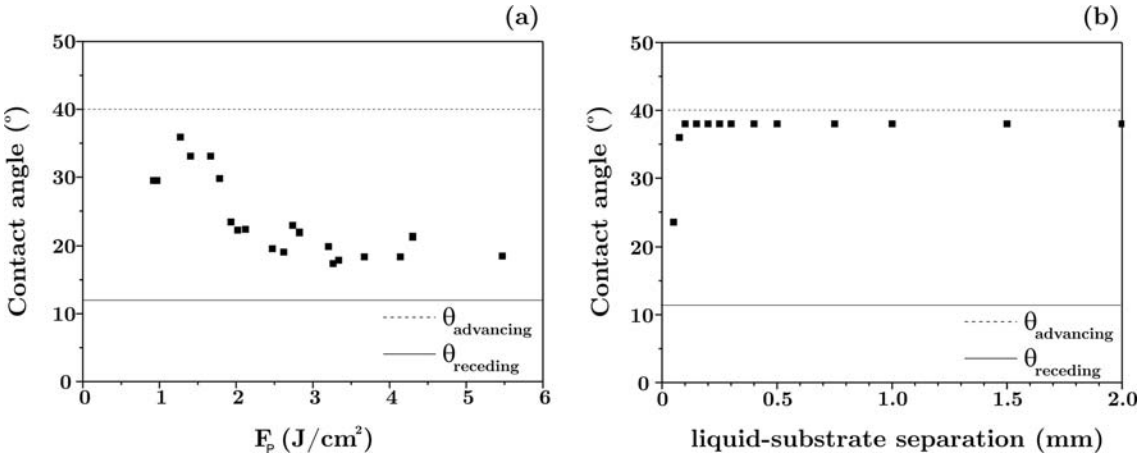


**Fig. 4.30.** Plot of the contact angle verus: a) the laser fluence (section 3.5); and b) the liquid-substrate separation (section 3.6). The values of both advancing and receding contact angles have been represented in the plots.

vapor bubble, the bubble may reach the receptor substrate before collapsing leading to the *bubble regime*.

As a final remark, this section will end up with an explanation of the effects that varying the liquid film-receptor substrate separation have on the printed droplets, according to the previous results. For this purpose, the microarray prepared at an energy of 2 µJ (fluence of 2.6 J/cm$^2$) and varying the liquid film-receptor substrate separation from 50 µm to 9 mm (Fig. 3.23) will be considered (section 3.6). Apart from the droplets deposited at very short separation distances, which present a larger diameter due to the different deposition regime described (*bubble regime*), three additional different regions can be distinguished: up to 750 µm, circular and well-defined droplets are deposited without satellites; from 1 to 3 mm, a central droplet can still be appreciated, which shape becomes more irregular as the distance increases, and also some satellite droplets appear with their amount increasing with distance; from 5 to 9 mm, only small and randomly distributed droplets are present. These three different regions can be interpreted considering the observed dynamics of the deposition process. The first region corresponds to the *jetting regime*. In this case, the liquid film-receptor substrate distance is short enough to assure that all the multiple parts fall down on the same position as the sessile droplet was formed, and thus no satellites are present. As the liquid film-receptor substrate

distance is increased (second described region), the same process occurs, but with a significant difference: the multiple parts resulting from the jet breakup cannot reach the same impact position as the jet, which produces the appearance of satellite droplets. It would not be surprising since, despite its high stability, for very high donor-receptor substrate distances the jet can be deflected from the vertical direction, as it is sometimes observed in time-resolved images acquired without any receptor substrate (Fig. 4.11). Two actions can contribute to this: air flows, which effect is more prominent at high separations, and the reduction in the jet diameter as its length increases, which makes it more sensitive to any perturbation. Such jet deviation results in the clear directionality of both droplet shape and satellites distribution, which is clearly observed at a separation of 3 mm in Fig. 3.23. Finally, at very high separation distances (third region), the jet breaks into multiple parts before it reaches the receptor substrate, and thus no central droplet is presented, but only the mentioned broken parts randomly distributed.

In conclusion, time resolved imaging of the LIFT of liquids has proved that the sessile droplet deposition process is in general due to the contact of an emitted liquid jet with the receptor solid substrate, the so-called *jetting regime*. When the jet reaches the receptor substrate it gently accumulates liquid in the impact position while preserving its stable and well defined shape, and thus initiates the formation of a sessile droplet. In the first stage of this process the diameter of the forming droplet rapidly increases up to a certain value. In the second stage, with the jet still feeding the droplet, the droplet volume increases while maintaining constant its diameter, which leads to the increase of the contact angle. In the third stage, jet breakup occurs due to Plateau-Rayleigh instability. The sessile droplet starts then a slow relaxation process in which its contact angle diminishes and its diameter increases. During its progression, the jet becomes thinner by elongation, while preserving its volume constant. This jet volume corresponds to the final sessile droplet volume, which indicates that only the liquid contained in the jet is deposited on the receptor substrate; that is, no

additional liquid collection from the liquid film occurs during the jet feeding of the growing droplet.

A different deposition regime has been found to occur when the donor film - receptor substrate separation is short enough, or when the vapor bubble is high enough, so that the bubble impacts on the receptor substrate before collapsing. In this regime, referred to as *bubble regime*, the bubble collapses into a jet after reaching the receptor substrate, and the jet continues feeding the forming droplet until jet breakup occurs. Then, the droplet starts a relaxation process in which its diameter recedes and its contact angle increases. As a consequence of the contact angle hysteresis, the final stage that the droplet reaches is different from that obtained in the *jetting regime*: the droplet has a larger diameter and a smaller contact angle.

The liquid film-receptor substrate distance is not a critical parameter in the LIFT process, since it is possible to print well-defined droplets up to separations above 1 mm without significant changes in their morphology and volume. At slightly larger distances, the jet still reaches the receptor substrate, but the multiple parts resulting from the jet breakup do not fall down at the jet impact position, rather they are deposited as satellite droplets. Finally, at even larger liquid film-receptor substrate distances, the jet breaks before reaching the substrate and only randomly distributed small droplets are deposited.

# Chapter 5

# Development and test of a novel laser-direct printing technique

In this chapter, a novel laser-direct printing technique is presented. This original idea was developed at the group of Capes Fines i Enginyeria de Superfícies from the Universitat de Barcelona in order to overcome the main inconvenient of the LIFT technique, that is, the preparation of the liquid film. The technique consists in the focalization of ultrashort laser pulses underneath the free surface of a liquid contained in a reservoir: absorption of the laser pulses produces the ejection of material towards a substrate, which is situated close to the liquid surface, in a process which results in the deposition of droplets. The technique allows two different configurations, the so-called *backward* configuration and the *forward* configuration.

This chapter is divided into four sections. The first one is devoted to the motivations that led to the development of the novel technique, as well as to the advantages that it presents with respect to LIFT. The second section is focused on the *backward* configuration, particularly on its description and on the characterization of the first arrays prepared with it. In the third section the *forward* configuration is presented, as well as the first results obtained using this configuration. Finally, in the fourth section different experiments were performed in order to test the feasibility of the technique to print biomolecules in any of the two configurations.

## 5.1 Why a novel laser-based technique?

The previous two chapters have been focused on the LIFT technique. The different experiments described in those sections have allowed a better understanding of the LIFT process. However, they have also demonstrated that the technique faces a serious drawback: the preparation of the liquid film. In fact, obtaining uniform liquid films with a controlled thickness is difficult, especially when the liquid is spread over large areas: local inhomogeneities appear which result in inhomogeneous arrays. This can be clearly observed in Fig. 5.1, which presents a large BSA microarray prepared through LIFT in which the laser pulse energy was increased from row to row (from bottom to top). The differences between the left and right side of the array are evident: the droplets have a much larger diameter on the right and central side than on the left one. Moreover, the bottom row of droplets does not present any void on the left area, whereas the presence of droplets becomes sporadic as moving right. Thus, higher laser pulse energies are required to eject a droplet on the right side. All this allows concluding that the right side is probably thicker than the left side, and therefore, the liquid film used to print that array did not present a uniform thickness.

Another example that illustrates the difficulties of preparing a uniform film is presented in Fig. 5.2. In this case, a large microarray of a water+glycerol+SDS solution was prepared at fixed irradiation conditions and fixed donor film-receptor substrate distance. The laser source used in this experiment was a compact Nd:YAG laser (532 nm wavelength, 5 ns pulse duration, 100 Hz repetition rate) with a very high stability. It can be observed that well-defined droplets with diameters of about 20 µm were printed. However, the array is not

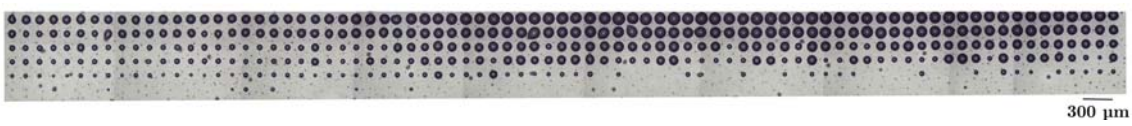


**Fig. 5.1.** Optical microscopy image of the entire BSA microarray prepared with an average thickness of 10 µm, varying the laser pulse energy from row to row (increasing the energy from bottom to top). The lack of uniformity of the liquid film can be appreciated in the differences in morphology of the droplets.

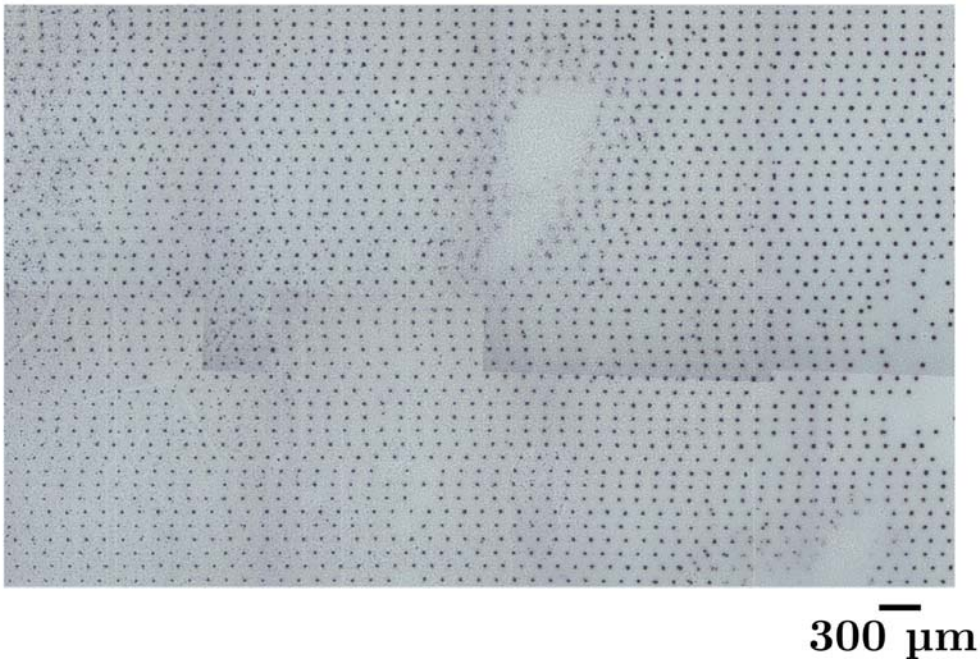


**Fig. 5.2.** Optical microscopy image of a large water+glycerol+SDS microarray prepared with an average thickness of 5 µm and at a fixed laser pulse energy. Different regions with no droplets can be clearly appreciated, attributable to the lack of uniformity of the liquid film.

uniform all over the printed area: on the left side droplets present satellites or some splashing, and on the center of the array as well as on the bottom right corner no droplets were printed. These differences can only be attributed to the presence of local areas with different thickness in the donor film, since this was the only experimental parameter that was not controlled from shot to shot. Therefore, it is evident that the inhomogeneity of the liquid film seriously compromises the LIFT technique when large arrays are prepared.

Several reasons account for the difficulties of obtaining reproducible thin films with good thickness uniformity and stability, as are detailed in the next list:

1- Liquid films are energetically unfavorable. Their large surface to thickness ratio provides them with a large surface energy, which surface tension tends to minimize shrinking the surface. The effect can be appreciated even for low surface tension liquids.

2- Evaporation is critical for liquid films. The loss of material caused by evaporation produces a decrease in the liquid film thickness, which thus modifies the properties of the liquid film[12]. This could be solved through the addition of low vapor pressure liquids, such as glycerol. However, these liquids are not compatible with certain fragile biomolecules.

3- The wettability of the substrate on which the liquid is spread is another limiting factor. Only hydrophilic substrates can be used to support liquid films, and they must be perfectly clean, which usually requires several cleaning steps. In order to improve wettability, surfactants are usually added to the solution to be spread. However, this is detrimental to the deposition of droplets with very small diameters.

4- The film preparation constitutes an additional step in the printing process, which increases the risk of sample contamination. This is a serious drawback when working with biological solutions, since their fragility makes them vulnerable to contamination agents.

Considering the above difficulties, it would be really advantageous to be able to dispense with the preparation of the liquid film. With this premise, it was initiated the development of a novel technique capable of depositing liquids which were not necessarily in a film form. The main idea that was pursued for such technique consisted in directly focusing a laser pulse underneath the free surface of a liquid contained in a reservoir. If laser absorption could be localized just some micrometers underneath the free surface, then it could be expected the liquid layer between the free surface and the focal volume to play the same role as the liquid film in the LIFT technique (Fig. 5.3). It should be pointed out that, in order to achieve such localized absorption, this novel technique would

[12] This is especially problematic for LIFT, since the deposited droplets size strongly depends on the liquid film thickness.

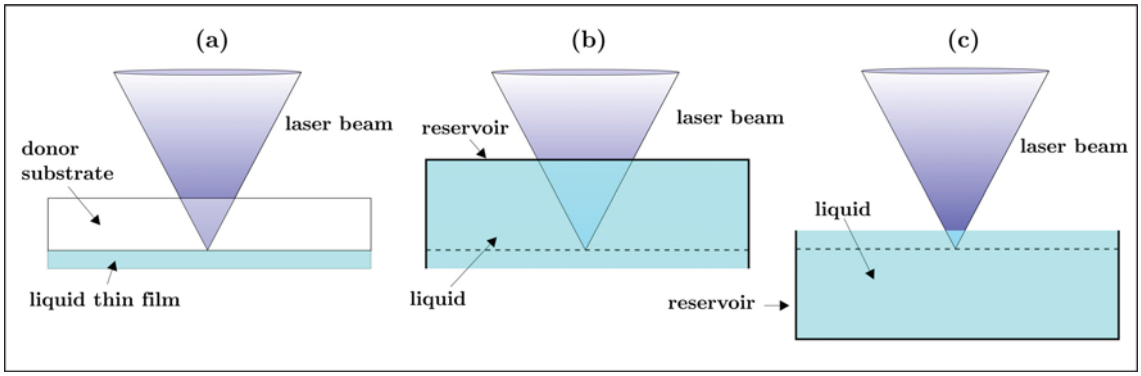


**Fig. 5.3.** a) Scheme of the LIFT technique. b) and c) Scheme of the underlying idea pursued by the novel technique: the focal volume is focused underneath the free surface of a liquid contained in a reservoir, so that the liquid layer between the focal volume and the free surface (delimited by a dashed line) plays the same role as the liquid thin film in LIFT.

require the liquid solution to be transparent or weakly absorbing of the laser radiation employed.

The first assays using the mentioned configuration were performed in 2006 through the use of nanosecond laser pulses (section 2.1) and a microscope objective of 15×. Those first results were unsatisfactory: no material was deposited at any of the conditions analyzed, even at very high laser pulse energies. Two different hypotheses were then considered to explain this failure. The first one was based on the idea that the presence of a liquid/holder interface was required in order to favor the ejection of liquid away the free surface. That is, the holder surface was considered a necessary element to break the symmetry of a vapor bubble generated close to the liquid/holder interface: the vapor bubble could expand towards the liquid but not towards the holder. As a result of this anisotropy, the bubble expansion would be clearly directional towards the liquid, impelling a fraction of the liquid away the free surface. Without the holder surface, the bubble expansion would be more isotropic and the previous directionality would be lost, as well as the capacity to eject material. The second hypothesis considered that the intensity threshold required to produce liquid ejection could not be achieved with the present experimental setup: nanosecond laser pulses and a microscope objective with a moderate magnification would not produce the localized absorption underneath the free surface necessary to eject any liquid. Since this novel technique did not provide

the expected results, and any of the two hypotheses suggested a solution of the encountered problems, the testing of this technique was abandoned.

It was not until 2008 that two factors came into play, which opened new possibilities to perform more experiments with the novel technique. The first one was related to the results of the LIFT transfer and deposition process that had been recently obtained (chapter 4). The jetting based mechanism found was not only particular of the LIFT technique, but similar configurations, for instance the generation of a vapor bubble close to a liquid free surface, could also lead to the formation of jets even in the absence of any close solid surface [Blake *et al.* 1982, Pearson *et al.* 2004]. This ruled out the first hypothesis of the novel technique failure: it was certainly possible to produce jets without the presence of any liquid/holder interface (although such jets had never been used before to deposit droplets). The second factor was the acquisition of a new femtosecond laser. For such laser beam, a microscope objective with a high magnification (50×) was also acquired. This new system would significantly increase the localized absorption of the laser pulses just underneath the free surface, since in this situation highly confined absorption in the focal volume could be expected due to the nonlinear absorption conditions of a highly focused femtosecond laser beam.

In the following sections, the first experiments performed with the novel technique are presented. It has to be pointed out that the technique had two possible configurations: the so-called *forward* configuration or the *backward* configuration, which will be further described in detail.

## 5.2 Backward configuration

In this section, one of the two possible configurations of the novel technique is presented: the backward configuration. A detailed description of this configuration and of the first arrays printed with it are presented, a description which is completed with an explanation of the physics of the process.

The backward configuration was the first one tested. This configuration consists in focusing a laser pulse underneath the free surface of a liquid (transparent to the laser radiation) in the way schematized in Fig. 5.4: laser pulses pass through a substrate (placed above the liquid free surface) and are then focused in the liquid. A fraction of the liquid is then projected in the opposite direction of the incident laser pulse (backwards) and deposited on the substrate. As it can be deduced from Fig. 5.4, this configuration requires the substrate to be

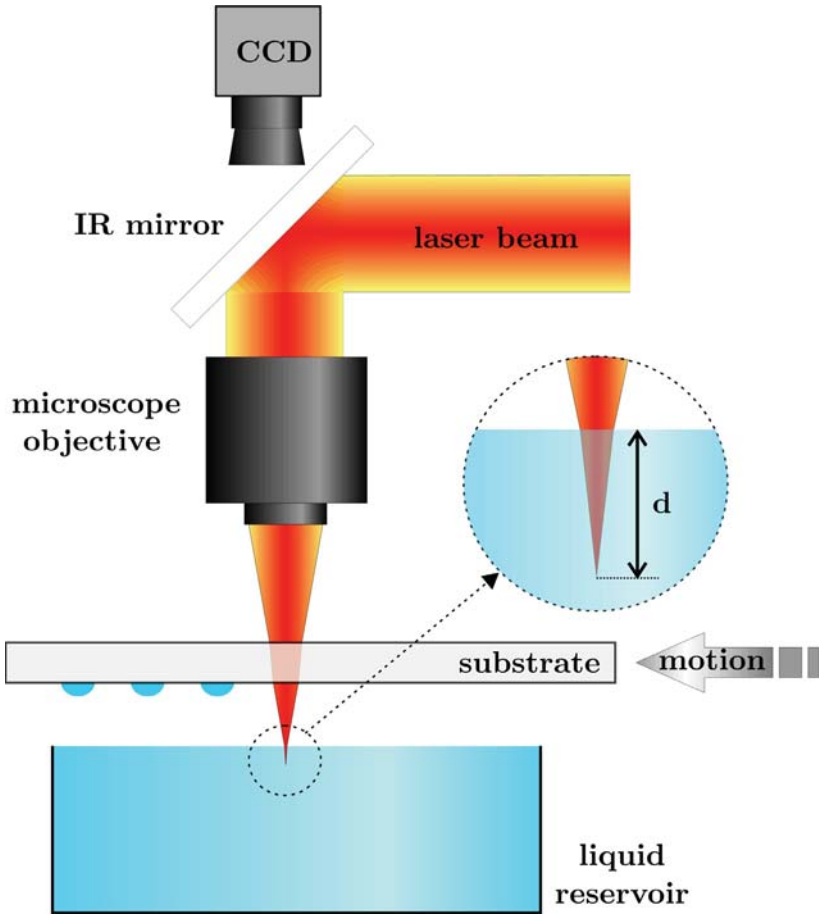


**Fig. 5.4.** Scheme of the backward configuration.

transparent to the laser radiation. Despite this fact, it must be pointed out that this is not a problem for most biological applications, since in those cases transparent substrates are normally used. Such configuration had already been used to deposit absorbing solids [Hon *et al.* 2006]. However, it must be stressed that although the geometrical configuration is the same as in the presented technique, the underlying concept is completely different: in the case of deposition from solid materials, radiation is absorbed in the material surface, a process which will occur quite irrespectively of the laser focusing conditions, while in the present case achieving the right focusing conditions for subsurface absorption to take place is crucial.

The key issue of the technique is to achieve, only in a tiny focal volume situated underneath the free surface, an absorption (absorbed radiation power per unit volume) high enough to produce the generation of a cavitation bubble in that position. Such cavitation bubble is expected to produce the transfer of material to the substrate. In order to clarify how to attain this localized absorption, it must be pointed out that the radiation absorption can be expressed as $\alpha I$, where $\alpha$ is the absorption coefficient and $I$ the laser pulse intensity ($I = E/A\tau$, where $E$ is the laser pulse energy, $A$ is the beam cross-sectional area, and $\tau$ is the pulse duration). For transparent or weakly absorbing materials, the value of $\alpha$ is always small. When the laser beam is strongly focused inside those materials, the value of $I$ increases quickly in depth, since the beam section decreases as it approaches the beam waist. Thus, the value of $\alpha I$ will be maximum in the focal volume, whereas it will be much smaller in the rest of the material points traversed by the laser beam. In this way, radiation absorption will be mainly localized, and thus the cavitation bubble will be generated there, making possible to control its exact location inside the material. Moreover, for nonlinear radiation absorption the value of $\alpha$ increases with $I$. In those cases, the selective absorption in the focal volume is greatly enhanced (there is less relative absorption in the rest of the points within the material). Therefore, the use of femtosecond lasers is convenient, since for transparent or weakly absorbing materials the predominant absorption mechanism of femtosecond laser radiation is nonlinear. It should be pointed out that nonlinear absorption

can also occur for nanosecond laser pulses. However, in those cases such absorption is nondeterministic [Schaffer *et al.* 2001], and therefore not controllable.

The experiments reported in this section were carried out using the femtosecond laser described in section 2.1.1, with a high numerical aperture objective in order to achieve the desired sub-surface radiation absorption. The liquid reservoir employed was a cubic plastic container with a capacity of 6 mL (lateral dimensions of 3.5 cm and height of 0.5 cm), as is presented in Fig. 5.5a. Such reservoir was used since its big capacity allowed printing large amounts of droplets, making it adequate for the preparation of large arrays in order to find the optimal printing conditions. The plastic container was completely filled using a pipette, and the solution used was a mixture of distilled water and glycerol at 20 % (v/v). In this occasion, since the liquid was not prepared in thin film form, the addition of surfactants was not necessary, in contrast with the LIFT solutions (section 2.2.1). The reservoir was held in a manual translation stage, which allowed translating the reservoir in the z direction (Fig. 5.5b), so that the separation between reservoir and substrate could be manually controlled. On the other hand, the substrate (a poly-L-lysine coated glass slide)

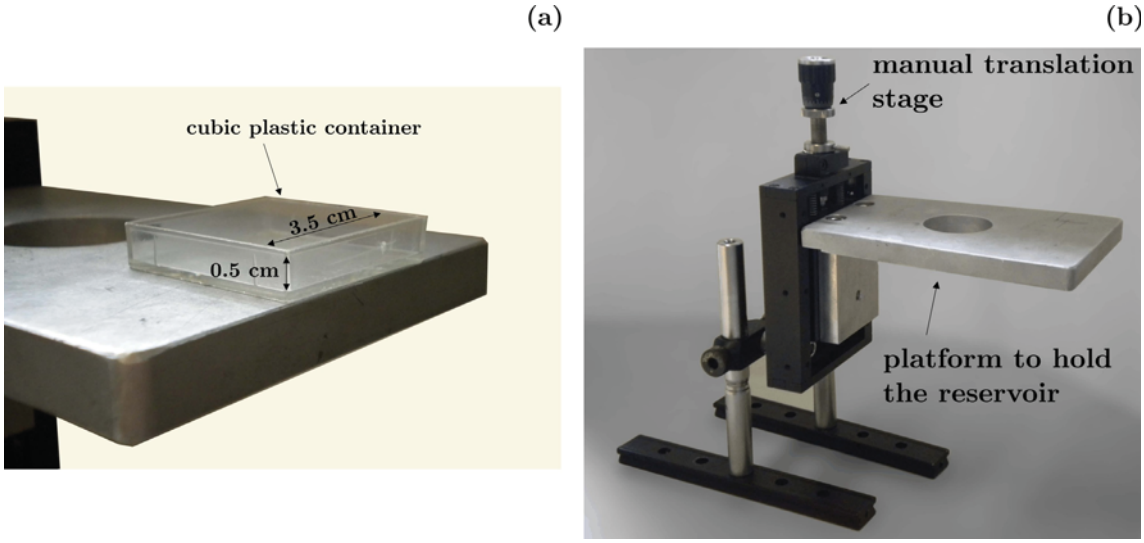


**Fig. 5.5.** a) Image of the plastic container used as a reservoir in the backward transfer experiments. b) Image of the manual z translation stage which held the plastic container.

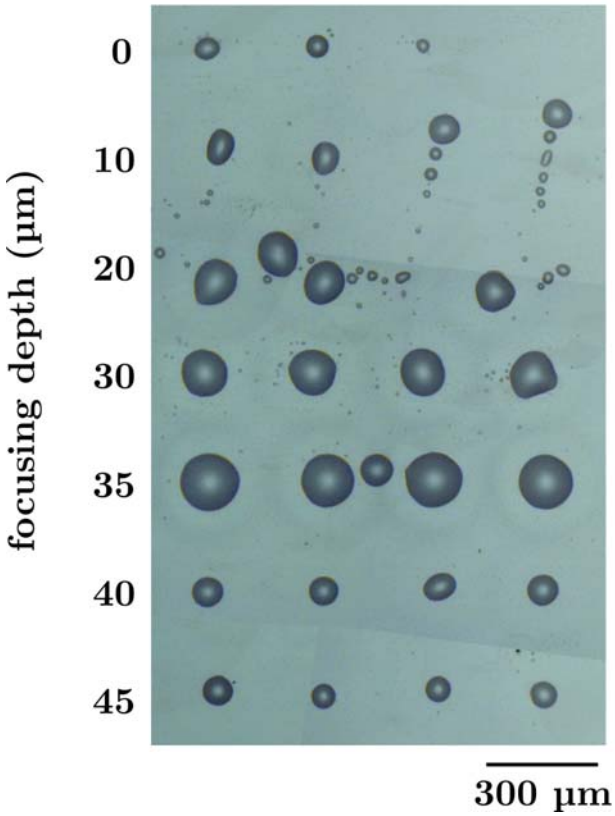


**Fig. 5.6.** Array of the water + glycerol solution prepared varying the laser focusing depth inside the liquid reservoir. The values on the left are expressed with respect to the free surface.

was placed on the XYZ translation stages described in section 2.1.3. The separation between the liquid free surface and the substrate in the present experiments was around 500 µm. The laser pulses were synchronized with the translation of the substrate using a home-made computer program, so that the stages were translated after each laser pulse, while the reservoir remained stationary during the whole process.

A first microarray was prepared at a fixed laser pulse energy of 2 µJ and varying the focusing depth inside the liquid through the upward translation of the reservoir[13] (Fig. 5.6). The diameter of the laser beam waist in the objective focus was of about 1.2 µm, which resulted in an intensity of about $10^{14}$ W/cm$^2$.

[13] Due to the difference in the index of refraction between the air and the liquid, the laser beam focal position is displaced when it enters the liquid. This produces a mismatch between the distance the reservoir is translated and the translation of the focal position inside the liquid. This has been considered and appropriately corrected in the values displayed in Fig. 5.6.

Each row of the microarray corresponds to a different depth, and each deposited feature was obtained with a single laser shot. It can be observed that there is liquid deposition only in a limited range of focusing depths. Printing droplets of this transparent solution using femtosecond laser pulses is a situation completely different from that of the LIFT process, in which a titanium coating was required in order to linearly absorb the nanosecond laser pulses. Therefore, this new instance deserves a further description, as it is presented next.

For the water and glycerol solution used in this experiment, there is no linear absorption of the incoming laser radiation due to the transparency of the solution (the solution is a dielectric with an energy band gap larger than the energy of the incoming laser photons). However, the deposition of material with the femtosecond laser pulses indicates that nonlinear absorption must take place. For the present conditions, such nonlinear absorption process occurs through three different mechanisms (Fig. 5.7): multiphoton ionization (MPI), free-carrier absorption, and impact ionization [Schaffer *et al.* 2001].

**Multiphoton ionization**

This mechanism consists in the simultaneous absorption of several photons by an electron from the valence band, so that the electron receives enough energy to be promoted to the conduction band (a single photon did not have enough energy to produce such transition). This is illustrated in Fig. 5.7a. It must be noted that this process requires an extraordinary high photon flux in order to occur, which is achieved by the use of femtosecond laser pulses.

**Free-carrier absorption**

Once the electron has already been promoted to the conduction band of the material it absorbs several laser photons sequentially, moving to higher energy states in the conduction band (Fig. 5.7b).

**Impact ionization**

This process occurs when an electron of the conduction band has been promoted through free-carrier absorption to such a high energy level that its energy excess

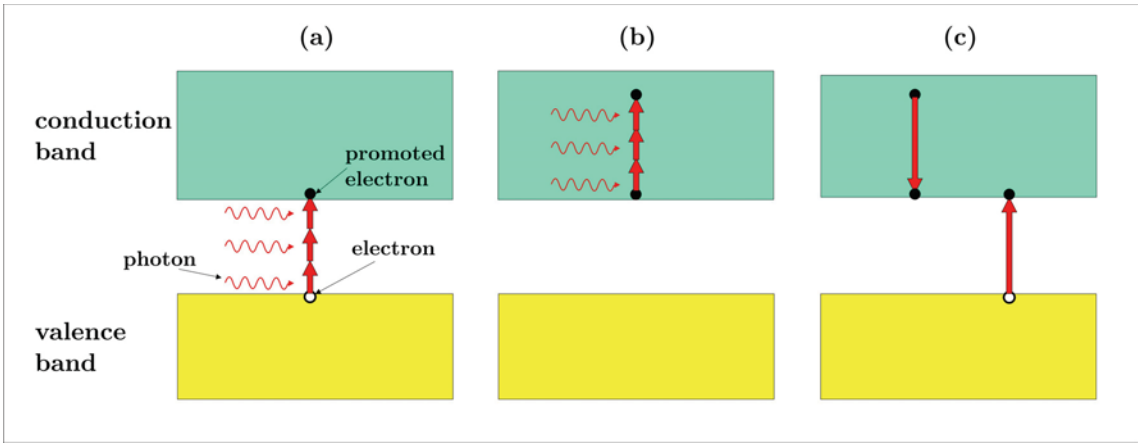


**Fig. 5.7.** Scheme of the three mechanisms of the nonlinear absorption process at the present experimental conditions: a) multiphoton absorption; b) free-carrier absorption; c) impact ionization.

surpasses the band-gap energy. In this case, the electron can collisionally promote another electron from the valence band (Fig. 5.7c), resulting in two electrons near the bottom of the conduction band. These two electrons can again absorb energy through free-carrier absorption, and sequentially collide with additional valence band electrons, in an avalanche process that results in a very fast growth of the conduction band electron density (also called free-electron density).

When a free-electron density of around $10^{18} cm^{-3}$ is exceeded [Vogel *et al.* 1996b], the formation of a highly excited and confined plasma occurs, a process which is called *optical breakdown*. The threshold for optical breakdown in water has been found to be slightly above $3{\cdot}10^{12}$ W/cm$^2$, for 340 fs pulses of 1040 nm laser radiation [Vogel *et al.* 2008]. In the present experiment such intensity was clearly surpassed (it was of about $10^{14}$ W/cm$^2$), and thus the formation of the described plasma is expected. It has to be noted that for sub-picosecond pulses there is practically no conduction of heat to the surroundings of the interaction region, since the deposition of energy occurs in a time scale much shorter than the thermal diffusion time. This represents an additional advantage of using ultrashort laser pulses for manipulating materials such fragile as biomolecules. After its generation, the plasma expands, originating a cavitation bubble inside

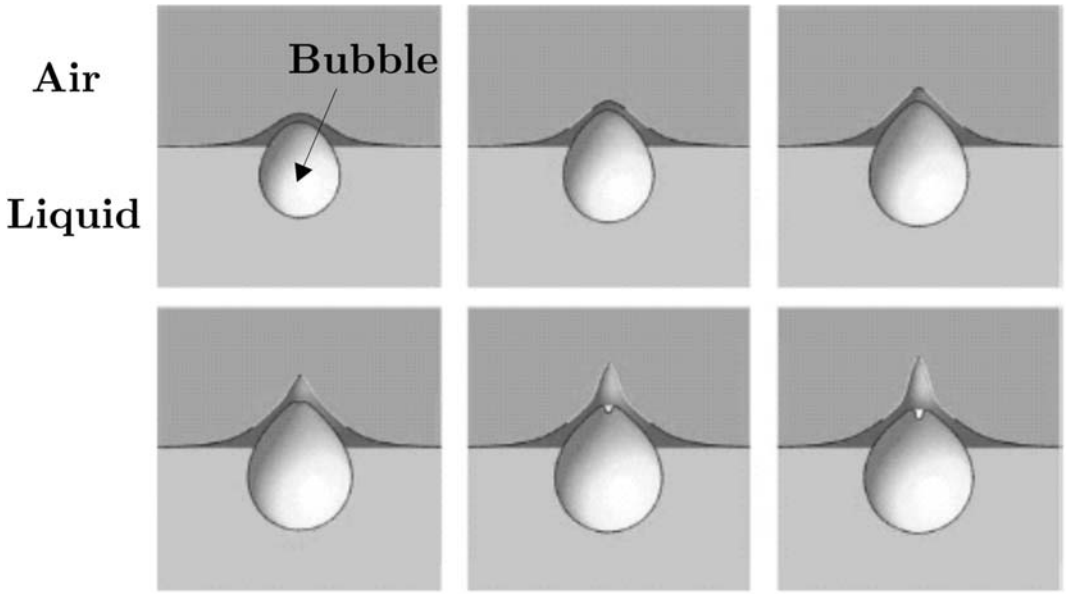


**Fig 5.8.** Computer generated bubble and surface showing the initiation of the free surface jet generated by the cavitation bubble motion near an infinite free surface (time evolves from left to right and from top to bottom) [Pearson *et al.* 2004].

the liquid [Schaffer *et al.* 2002], which further expansion displaces some material beyond the free surface. At this point, the situation is identical to that described in Pearson *et al.* 2004 for cavitation bubbles generated near a free surface (Fig. 5.8). Therefore, it is expected that the cavitation bubble will expand producing an overpressure in the bubble pole situated close to the free surface. This overpressure and the posterior bubble collapse would result in the generation of a needle-like jet, as it occurred in the LIFT experiments reported in chapter 4: the long, uniform and stable jet should then lead to the droplet deposition when contacting the substrate.

Returning to the results presented in Fig. 5.6, it must be pointed out that there exist significant differences in the amount and morphology of deposited material depending on the relative position of the focal volume with respect to the liquid free surface. For the shallowest positions, where the focal volume partially intersects the free surface, absorption will increase as the laser beam waist penetrates inside the solution. This accounts for the up-to-bottom increase in the dimensions of the deposited droplets in the first rows of Fig. 5.6.

Furthermore, the random irregular shape of these droplets, in addition to their misalignment and the presence of satellites, indicate that liquid ejection took place in a turbulent way, possibly through bursting and/or formation of unstable irregular jets. Once the focal volume is completely immersed in the liquid, energy absorption will be nearly independent of the focusing depth. Then, the amount of deposited material will be determined by the balance between two competing issues: the availability of liquid to be displaced (liquid amount above the bubble), and the resistance of this liquid to being displaced. Thus, while availability dominates over resistance, the dimensions of the deposits keep on increasing, but there exists a focusing depth (about 35 µm) beyond which this trend is reversed. The most relevant feature observed in this region is the deposition of well-defined, uniform, and satellite-free droplets, an issue which is achieved within a depth range of about 10 µm, and which constitutes the proof of feasibility of the technique. The obtaining of such regular droplets can be attributed to liquid ejection in the form of the stable and regular jets above described. It has to be finally noted that for deeper laser focusing there is no material deposition: more liquid needs to be displaced, and it has not enough energy to reach the substrate.

The reproducibility of the technique in droplet printing was demonstrated through the preparation of a large microarray (15 rows per 50 columns) at the above conditions, which lead to well-defined droplet deposition (Fig. 5.9). All the droplets are uniform, with a well-defined circular contour, and present a diameter of around 40 µm. Such high reproducibility demonstrates that the technique allows overcoming the drawbacks associated with the lack of uniformity and stability of the liquid film inherent to LIFT. Moreover, the in-situ control of the deposition process through the CCD camera (Fig. 5.4) facilitates finding the adequate printing conditions through the simultaneous adjustment of both pulse energy and focusing depth. This allows obtaining very small droplets in an easy way, as is illustrated in Fig. 5.10, where droplets with diameters as small as 5 µm are presented (the extremely small features in the background correspond to the poly-L-lysine coating of the slide); achieving the same result through LIFT would require the preparation of a very thin liquid

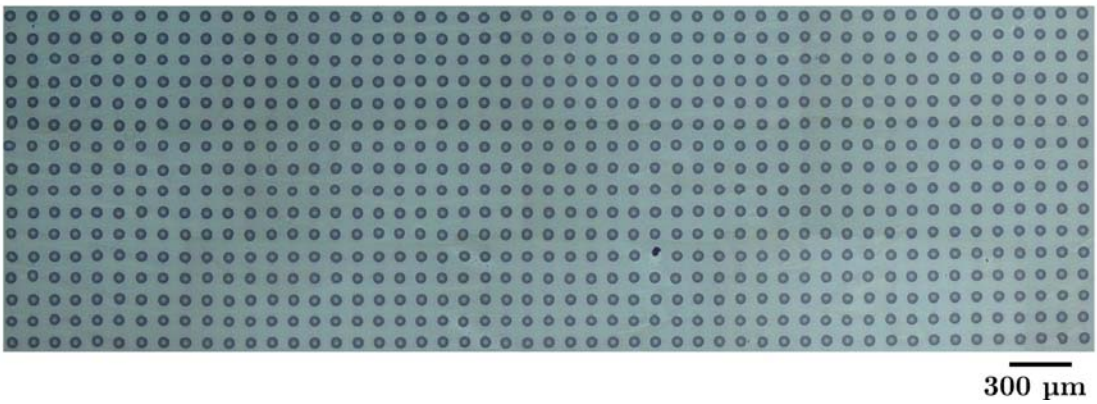


**Fig. 5.9.** Large microarray prepared with the backward configuration, using the water + glycerol solution.

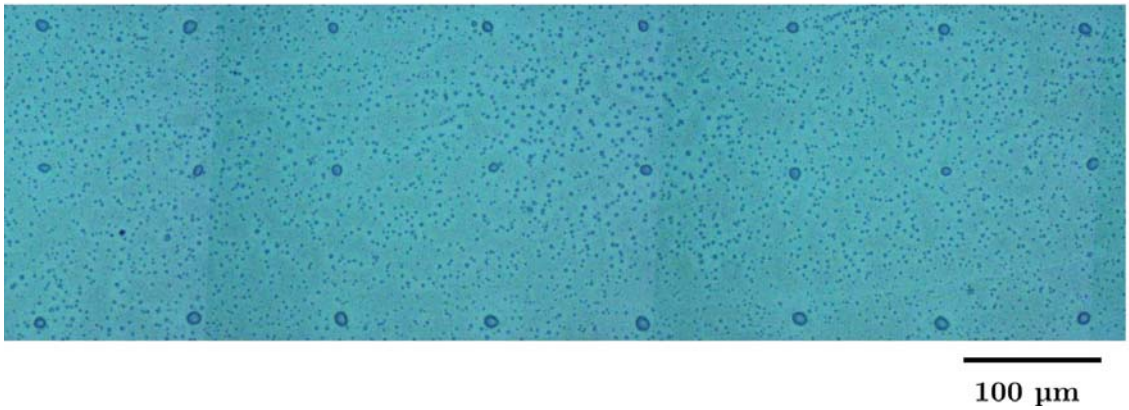


**Fig. 5.10.** Small microdroplets printed with the backward configuration using the water + glycerol solution.

film, which is always problematic. These results demonstrate that this new printing technique indeed makes possible printing droplets with high resolution and reproducibility in a really user-friendly way, making unnecessary the use of printing heads or the previous preparation of the liquid in thin-film form. In fact, liquids can be spotted from practically any container, like the wells of a microtiter plate, which in addition minimizes the risk of contamination.

In conclusion, it has been proved the feasibility of the novel technique for printing liquids. The backward configuration allows printing transparent liquids on transparent substrates avoiding the constraints imposed by the preparation of a liquid-film: the liquid is directly deposited from the reservoir which contains it through subsurface absorption of a strongly focused femtosecond laser beam.

Moreover, it has been shown that for a given laser pulse energy there exists a range of focusing depths inside the liquid which leads to the deposition of circular microdroplets. The technique allows printing uniform, well-defined microdroplets in a very reproducible and friendly way, which makes it adequate for micropatterning applications. In addition, very high resolutions can be attained.

## 5.3 Forward configuration

Despite the success of the backward configuration, it presents a limitation that would be convenient to overcome: the requirement of working with transparent substrates. This is not a problematic issue in many biological applications, since substrates are usually glass slides or glass plates. However, for many other applications, for instance the printing of organic electronics, or for printing biological solutions on certain electrodes for the fabrication of biosensors, the substrates are absorbent to a broad spectrum of wavelengths, which would make unfeasible the use of the backward configuration. In order to avoid this restriction the position between the liquid reservoir and the substrate was switched, resulting in a similar configuration to that of LIFT that will be referred to as *forward configuration* (Fig. 5.11). With this configuration, the restriction of using a transparent substrate is avoided, since the laser radiation never passes through the substrate, but is directly focused on the liquid and then forward ejected towards the substrate. Despite this change, the ejection and deposition mechanisms are expected to be essentially the same as in the previous configuration.

In this section, a detailed description of the forward configuration is presented, as well as the first experiments concerning the feasibility of the technique to print well defined circular droplets.

The experiments reported in this section were carried out using mainly the setup described in the previous section, but in this occasion the liquid reservoir was a cylindrical well supported in a polymethyl methacrylate (PMMA) slide, with a capacity of 60 µL (Fig. 5.12). This well was completely filled using a micropipette, and then it was turned upside down and placed in the independent z stage (Fig. 5.5b). The substrate used in these experiments was a poly-L-lysine coated glass slide placed on the XYZ translation stage (section 2.1.3), and the separation between the liquid free surface and the substrate was around 500 µm. Patterns were obtained through the translation of the substrate

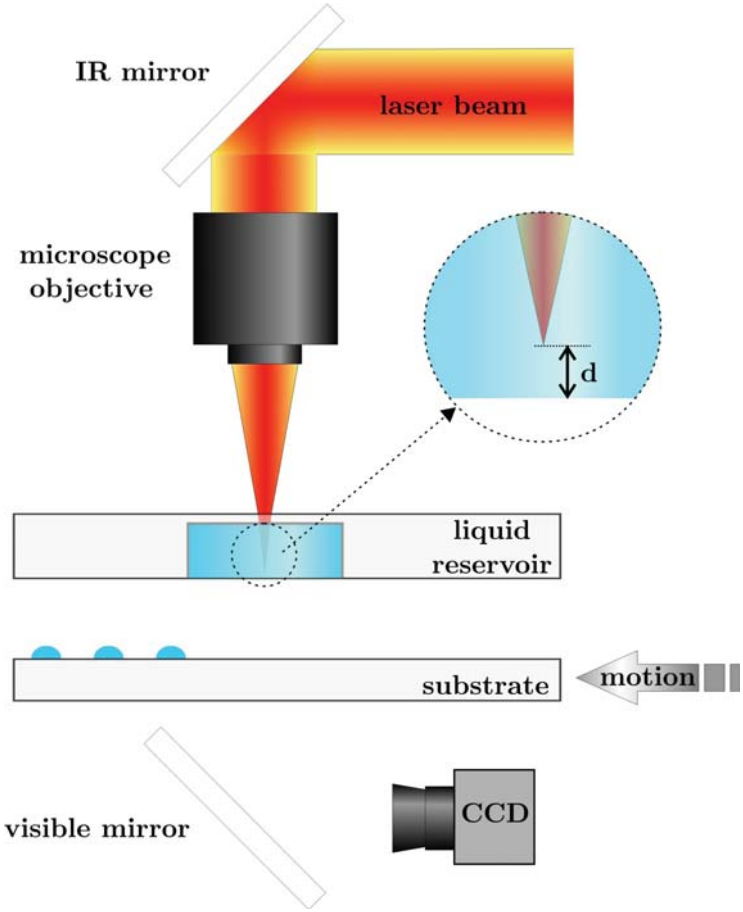


**Fig. 5.11.** Scheme of the forward configuration.

with respect to the laser pulse, while the cylindrical well remained stationary during the printing process.

It should be noted that with the present experimental setup[14] there exists a limitation in the size of the reservoir, since surface tension is the only force that compensates the pulling effect of gravity: increasing the reservoir size may cause the liquid to fall down. Such constraint in the reservoir size made the technical implementation of this configuration more difficult than the backward configuration. For instance, the reservoir lateral size had to be large enough to allow the beam to completely enter the reservoir (due to the high NA of the microscope objective such beam dimensions were large), but small enough to avoid the liquid to fall down. The adopted compromise was to design a reservoir

[14] The reservoir is placed upside down.

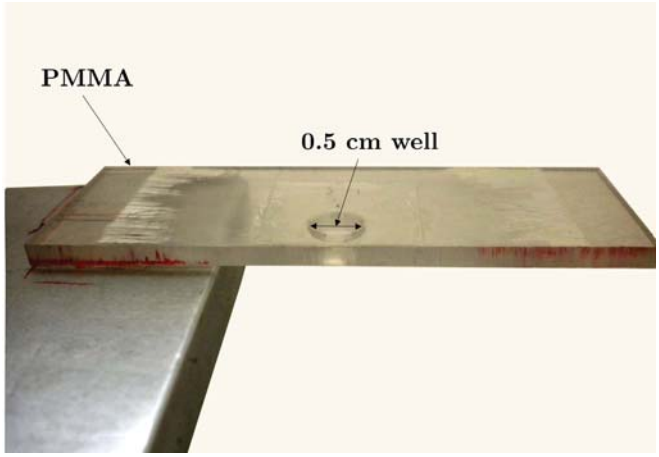


**Fig. 5.12.** Image of the well used as reservoir for the experiments in the forward configuration.

which had approximately the same lateral size as that of the beam at its entrance. However, this forced a very careful alignment of the reservoir with the laser beam, which was not easy. These sort of problems were not present in the backward configuration, since in that case a large reservoir could be used. This is why that configuration was initially tested. It has to be pointed out that the encountered problems of the forward configuration are technical problems which are not intrinsic to the technique. That is, reversing the laser system by placing the microscope objective under the plastic container (so that the liquid reservoir does not have to be turned) could be enough to overcome the described drawbacks.

Initially, the adequate conditions to print well-defined droplets were determined. In a first experiment, the laser focusing depth inside the liquid was varied, and the deposited material was observed in situ through the CCD camera placed under the substrate (Fig. 5.11). Such camera allowed visualizing the deposited material because in this case the substrate was transparent to the visible light. For opaque substrates, a different imaging system would have been necessary. When well-defined droplets were obtained (at a focusing depth of about 40 μm), an additional array was prepared varying the laser pulse energy from row to row (Fig. 5.13). With the forward configuration, the mechanisms that lead to the ejection and deposition of material are essentially the same as described in the

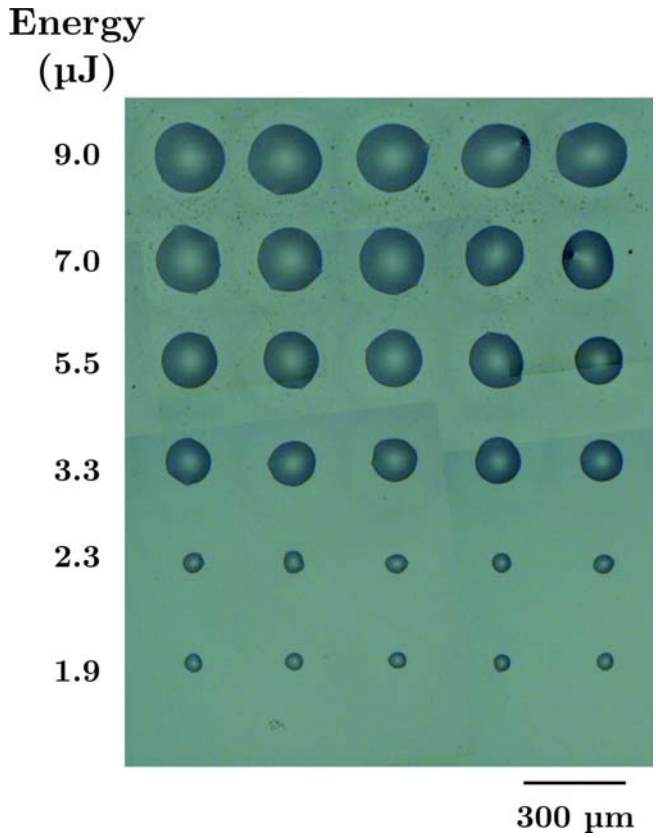


**Fig. 5.13.** Microarray of the water + glycerol solution prepared varying the laser pulse energy from row to row at a fixed focusing depth of around 40 µm.

previous section: the nonlinear absorption process produces the formation of a cavitation bubble which further evolves into a jet. The impact of the jet on the substrate initiates then the formation of a sessile droplet. In fact, the energy range of the array in Fig. 5.13 corresponds to laser intensities between $10^{14}$ and $10^{15}$ W/cm$^2$, all of them well above the threshold necessary to produce a cavitation bubble in water (section 5.2). Two clearly different regions can be distinguished in the array according to the droplet size: the two lowest rows have a much smaller diameter than the others. The transition from one region to the other is abrupt. In order to quantify this, the droplet diameter was plotted versus the laser pulse energy (Fig. 5.14a). The above mentioned two regions can be appreciated, with the abrupt transition situated around 3 µJ. It is also noticeable the linear dependence between the droplet diameter and the laser pulse energy at the high energy region. The droplet volume was also plotted (assuming a contact angle of 30° for all droplets, as described in section 2.5.2) versus the laser pulse energy (Fig. 5.14b). Again, the two regions are

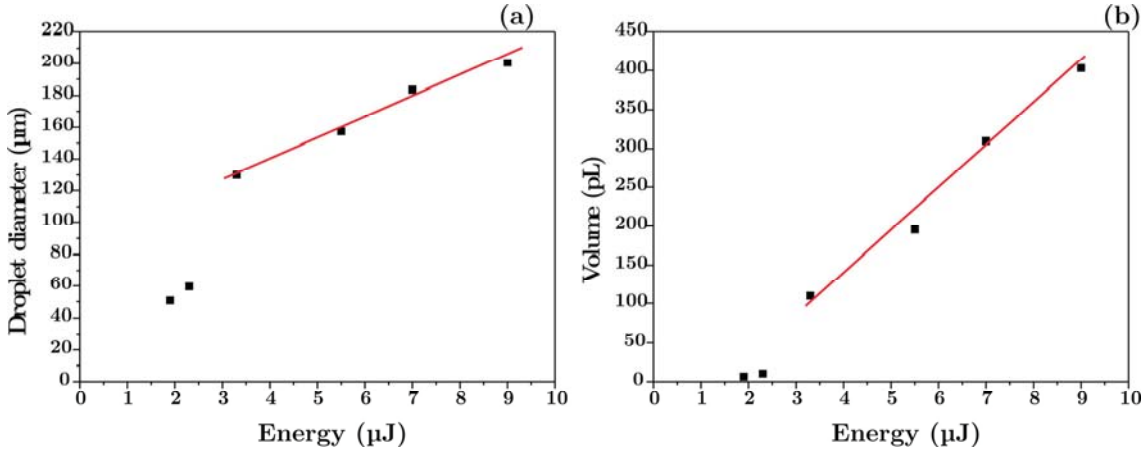


**Fig. 5.14** a) Plot of the droplet diameter versus the laser pulse energy; b) Plot of the droplet volume versus the laser pulse energy. The solid lines correspond to linear fits.

clearly differentiated, and the high-energy region also presents a linear volume-energy dependence. It should be pointed out that more data points would be required in order to clarify whether it is the droplet diameter or the droplet volume which has a linear dependence with the energy. The present transition at high energies resembles that found in section 3.5 which was due to the change in the deposition mechanism, from the *jetting regime* to the *bubble regime*. (section 4.4). However, that transition was not so abrupt and was accompanied by a change in the color of the deposited droplets (due to a contact angle change), which is not observed in the present situation. Therefore, the origin of the present transition is probably different, maybe attributable to nonlinear absorption effects, although additional experiments would be required in order to understand it. Anyway, the array of Fig. 5.13 clearly shows that the most appropriate energies for the preparation of microarrays are around 2 µJ, in which well-defined circular droplets with a relatively small diameter can be obtained.

A large microarray (13 rows per 42 columns) was prepared at 2 µJ in order to check the reproducibility of the technique, as it is presented in Fig. 5.15. It can be observed that droplets are printed at almost all positions, with diameters ranging from 40 to 60 µm, a smaller value than those routinely obtained with conventional microprinting techniques [Barron *et al.* 2005a]. The uniformity of

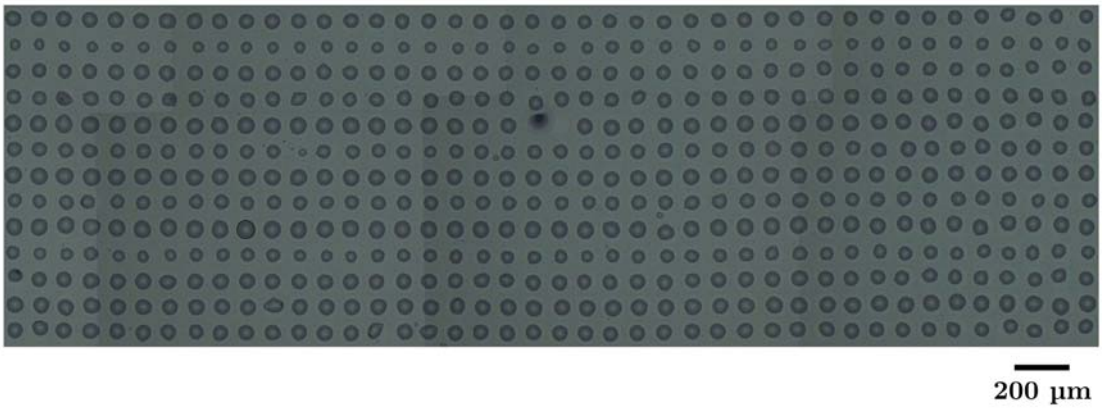


**Fig. 5.15.** Large microarray of the water + glycerol solution prepared with the forward configuration.

these droplets is better than that attainable with the LIFT technique for such large microarray. However, the large array obtained with the backward configuration (Fig. 5.9) was more uniform than the present one, which shows variations of the droplet diameters between different rows. A possible explanation of the difference in the uniformity of the printed droplets between the backward and the forward configuration could be attributed to spherical aberration [Hnatovsky *et al.* 2005]. Such aberration occurs when the laser pulse encounters materials with different indexes of refraction in the optical path (as it occurs in the present experiment between air and the liquid solution), and it produces a distortion of the focal volume which is more pronounced as the beam path within the second material is longer (in the present case, the liquid). Thus, since in the forward configuration such beam path in the liquid is longer than in the backward configuration, it is expected a larger spherical aberration and a larger distortion of the focal volume. This could in turn affect the morphology of the generated cavitation bubbles and jets, and therefore the uniformity of the deposited droplets. However, a further investigation of the process mechanisms should be carried out in order to clarify this behavior.

In conclusion, it has been demonstrated that the forward configuration is an adequate technique for printing transparent or weakly absorbing liquids without any restriction concerning the transparency of the substrates. This technique also overcomes the restrictions imposed by the preparation of a liquid film that

occurred in the LIFT technique. The deposited droplets morphology depends on the laser pulse energy: at low energies, droplets with a small diameter are obtained, whereas at higher energies the droplets diameter suffers an abrupt transition towards larger diameters.

Finally, it should be pointed out that the development of this original novel technique, with both forward and backward configurations, has led to the filing of a patent application (P. Serra, M. Duocastella, J.M. Fernández-Pradas, J.L. Morenza, *Aparato y método para la impression directa con laser*. Patent Application ES 200901669, filed July 22, 2009).

## 5.4 Study of the feasibility of the novel technique for biomolecule printing

The previous sections have demonstrated that both configurations of the novel technique, backward and forward, are feasible for printing arrays of droplets. However, it would be convenient to test whether the technique can be used for patterning functional materials preserving their desired properties after transfer. In order to test this, in the present section different biomolecule containing solutions were printed with the technique and their activity (capacity to bind to its complementary) was analyzed after deposition. This section is divided into three different parts, each one corresponding to a different experiment performed to test the technique feasibility for biomolecule printing.

### 5.4.1 DNA microarray (backward configuration)

A first experiment was performed using the backward configuration and the two different DNA solutions described in section 2.2.1, each one containing a single human cDNA clone insert (MAPK3 and ETS2). Two microarrays of 3 rows per 9 columns were printed on poly-L-lysine substrates using a laser pulse energy of 2 µJ (intensity of about $10^{14}$ W/cm$^2$), each one with the different cDNA. The printed droplets had a diameter of 30 µm in each microarray. After printing, they were submitted to a standard hybridization protocol with a solution that contained the complementary strands of the Cy5-conjugated MAPK3 cDNA and the Cy3-conjugated ETS2 cDNA (section 2.4.3). The fluorescence image of each of the arrays after hybridization is presented in Fig. 5.16. It can be observed that, although both arrays were submitted to a solution that contained different fluorochromes, only red signal is observed in the case of MAPK3, while the signal is green for ETS2. This reveals that the deposited specimens have preserved their specificity to bind to their perfect complementaries. Therefore, the backward configuration is suitable for DNA printing.

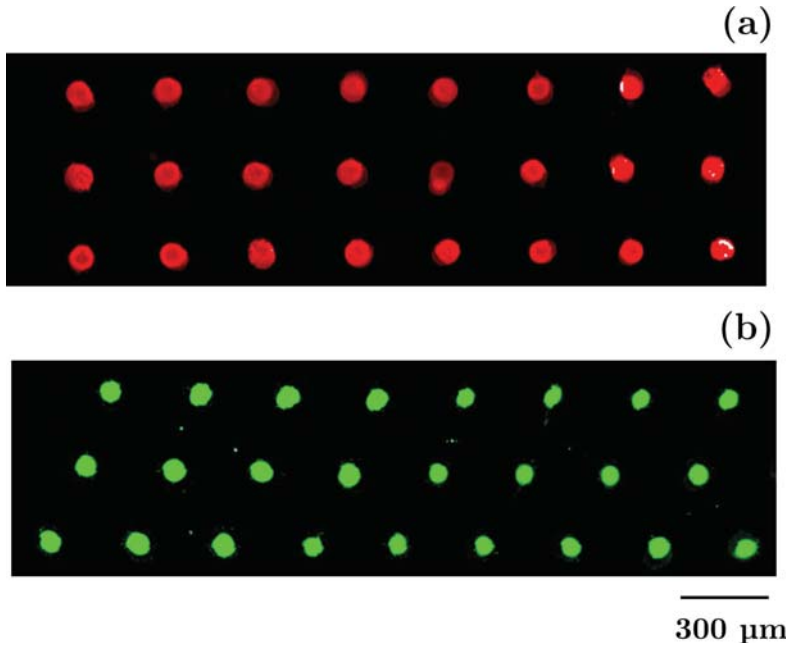


**Fig. 5.16.** Fluorescence image of the two printed cDNA corresponding to a) the MAPK2 human gene, and b) the ETS2 human gene, after hybridization with a solution that contained both Cy5-conjugated MAPK3 cDNA and Cy3-conjugated ETS2 cDNA.

### 5.4.2 IgG microarray (forward configuration)

In a second experiment, two IgG microarrays (section 2.2.1) were prepared, each one only containing a single type of antigen (rabbit IgG and mouse IgG). The forward configuration was used to print these arrays on poly-L-lysine activated substrates (section 2.2.2). An energy of 2 µJ (laser intensity of about $10^{14}$ W/cm$^2$) was used in the printing process. Optical microscopy images of the arrays are presented in Fig. 5.17a and Fig. 5.18a for mouse and rabbit IgG solutions, respectively. In both arrays circular droplets with a diameter of about 30 µm can be observed. After printing, the arrays were submitted to an immunoassay with Cy5-conjugated mouse anti-IgG and Cy3-conjugated rabbit anti-IgG (section 2.4.3). The fluorescence images of the microarrays are presented in Fig. 5.17b for the mouse IgG solution, and in Fig. 5.18b for the rabbit IgG solution. It can be observed that there exists a very good correspondence between the deposited droplets and the fluorescence spots. Moreover, only red signal is detected in the mouse IgG array, whereas the signal is green for the rabbit IgG array. This proves the preservation of the selectivity

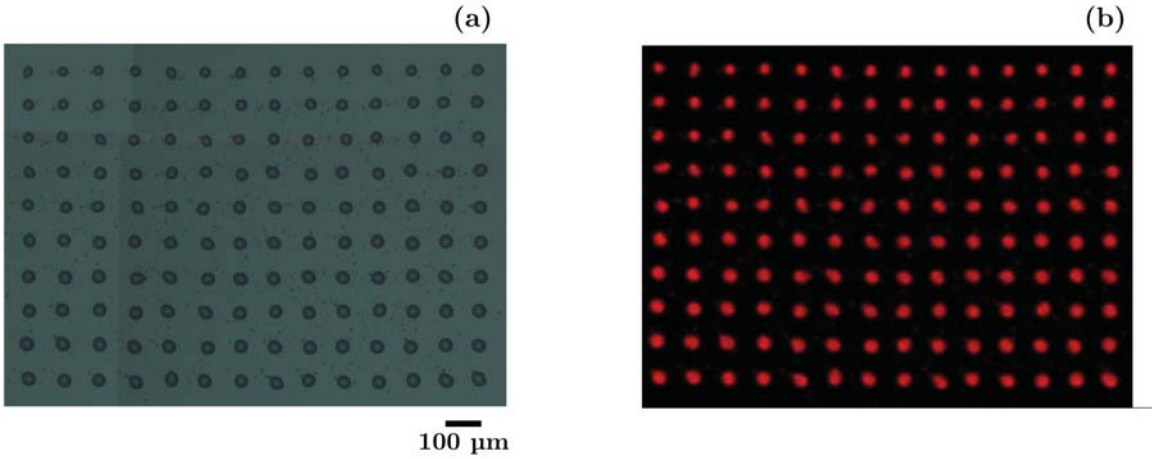


**Fig. 5.17.** a) Optical microscopy image of the mouse IgG microarray; b) Fluorescence image of the array after conjugation with Cy5-conjugated mouse anti-IgG.

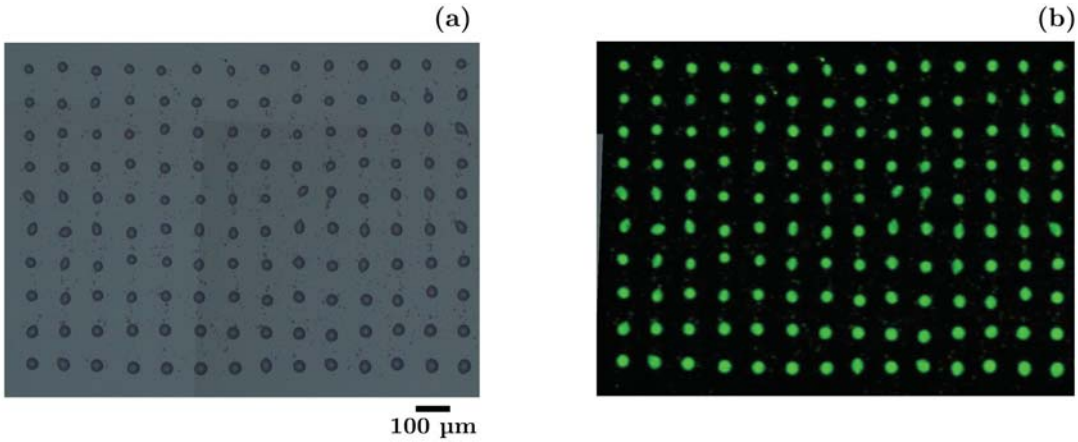


**Fig. 5.18.** a) Optical microscopy image of the rabbit IgG microarray; b) Fluorescence image of the array after conjugation with Cy3-conjugated rabbit anti-IgG.

of the deposited proteins after deposition, making the forward configuration feasible for protein printing.

### 5.4.3 IgG functional immunosensor (backward configuration)

Finally, a functional immunosensor[15] combining two different antigens in the same array (mouse and rabbit IgG) was prepared using the backward configuration. In this case, the two IgG solutions (section 2.2.1) were used to

[15] An immunosensor is a biosensor in which the detection element is an antigen (such as IgG) which binds to an antibody through an antigen-antibody reaction. Such reaction produces a physical signal that is measured.

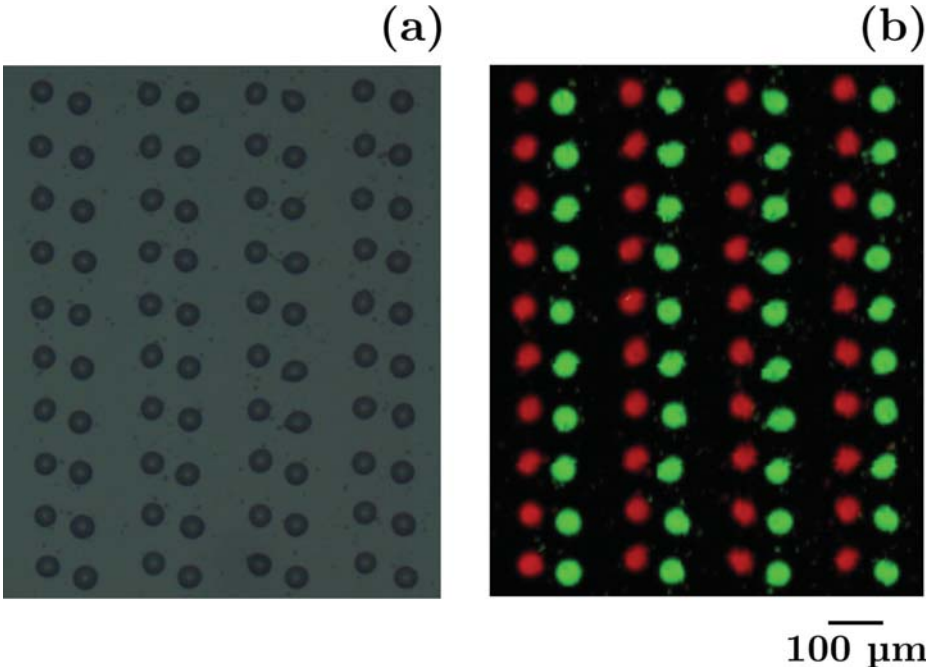


**Fig. 5.19.** a) Optical microscopy image of the microarray prepared with mouse IgG and rabbit IgG; b) Fluorescence image of the microarray after conjugation with a solution containing Cy5-conjugated mouse anti-IgG and Cy3-conjugated rabbit anti-IgG. The red spots correspond to the mouse IgG and the red ones to the rabbit IgG.

spot a microarray of 10 rows per 8 columns, in which alternating columns corresponded to a different solution: from left to right, odd columns corresponded to mouse IgG, and even columns to rabbit IgG (Fig. 5.19a). Again, the laser pulse energy intensity used in the printing process was 2 µJ (intensity of about $10^{14}$ W/cm$^2$). The fluorescence image presented in Fig. 5.19b of the same microarray obtained after the immunoassay (section 2.4.3) reveals the specific binding of each tagged anti-IgG to its complementary, with an intensity level that can be detected with a conventional scanner. Moreover, there exists a perfect correspondence between the deposited droplet and the fluorescence spot. Thus, it can be stated that the proteins have preserved their functionality after the printing process.

In conclusion, it has been proved that the novel technique is feasible for biomolecule printing in any of its two configurations. DNA and protein microarrays have been deposited through this technique, and the deposited

specimens have preserved their capacity to bind to their respective complementaries. Moreover, a functional immunosensor has been prepared, which constitutes the proof-of-concept of the technique for the preparation of devices with functional elements.

# Conclusions

The following conclusions can be deduced from the study of the laser-induced forward transfer technique of aqueous solutions.

*The systematic variation of different process parameters and the corresponding morphological characterization of the deposited material have revealed that:*

1) There exists a laser peak energy density range in which well-defined and circular microdroplets can be printed. Within this range, the volume of the deposited droplets presents a linear relationship with the laser peak energy density. Therefore, controlling the irradiation conditions allows obtaining droplets of different size. On the other hand, below this range no material is deposited, whereas above this range only irregular droplets with satellites or splashing are obtained.

2) There exists an energy density threshold $F_0$ which must be overcome in order to initiate the transfer process. Surpassing this threshold results in the generation of a vapor bubble in the liquid. However, material is only deposited if a minimum peak energy density $F_1$, higher than $F_0$, is overcome, which sets the deposition threshold of the technique. Only in this case the bubble is energetic enough to allow the transfer of liquid to the receptor substrate.

3) The predictions of the previously proposed cylinder model [Colina *et al.* 2006], consisting in relating the amount of deposited material with $F_0$, are in good agreement with the obtained results when the laser beam dimensions are larger than the liquid film thickness. On the contrary, for laser beam dimensions similar of smaller than the liquid film thickness, the model does not reproduce well the experimental results.

4) The droplet diameter increases with the film thickness for given irradiation conditions. The amount of deposited material per laser pulse energy, as well as the minimum laser peak energy density required to deposit a droplet ($F_1$), also increase with the film thickness.

5) The volume of the deposited droplet is proportional to the fraction of the initial laser pulse energy delimited by the points which overcome the threshold $F_0$, named $E_A$, through the relation $V = KE_A$. According to this expression, $K$ represent the efficiency of the process. This parameter $K$ depends on both the laser beam size and the liquid thickness. The finding of this equation makes the previously found linear relation between the droplet volume and the laser pulse energy $V = K(E - E_0)$ consistent with the existence of the threshold $F_0$.

6) It is possible to print well-defined and circular droplets up to liquid film-receptor substrate distances of the order of the millimeter. Above those distances, only irregular droplets with satellites can be obtained.

7) The fluorescence tests performed with LIFT prepared microarrays of immunoglobulin G (IgG) and bovine serum albumin (BSA) have proved the feasibility of the technique for protein printing. Moreover, it has also been found that LIFT has the required sensitivity for biosensor preparation.

*The time-resolved imaging study of the LIFT process has allowed unveiling which are the mechanisms that lead to the different morphologies of the deposits. In this way, such study has revealed that:*

8) The ejection mechanism in the LIFT of aqueous solutions is driven by the formation of a cavitation bubble generated due to the plasma formed after laser ablation of the absorbing layer. Once created, the bubble suffers a further expansion process.

*The bubble expansion process can result into three different situations depending on the laser fluence:*

9) At low fluences, during the expansion process a needlelike jet is developed due to the high pressure region generated in the bubble pole. However, the jet is not energetic enough to advance overcoming surface tension forces, and it starts a recoiling process until it finally disappears. Consequently, if the liquid film-receptor substrate separation is higher than the maximum jet length, the jet does not contact the receptor and thus no material is deposited on it.

10) At intermediate fluences, the initial bubble expansion and posterior jet formation is analogous to the previous situation. However, in this case the jet has enough inertia to continue advancing at constant velocity while progressively thinning. Such dynamics is very similar to that observed in cavitation bubbles generated close to the free surface of a liquid, and theoretical calculations of the expansion of such a cavitation bubble predict a behavior which is in good agreement with that observed in the present results. Finally, when the jet has reached a very long length, it becomes unstable due to the Plateau-Rayleigh instability and breakup occurs. At these conditions, deposition of well-defined circular droplets can be achieved.

11) At high fluences, the bubble expansion is so violent that it overcomes surface tension, resulting in bubble bursting, a situation which generates splashing on the receptor substrate.

12) The contact of the emitted liquid jet with the receptor solid substrate can result in the formation of well-defined and circular droplets (jetting regime). This deposition process can be divided into three stages. Initially, just after the jet impact on the receptor, the forming droplet suffers a fast spreading process. Then, with the jet still feeding the droplet, the droplet grows while maintaining constant its diameter. Finally, jet breakup occurs and the sessile droplet starts a slow relaxation process. Once the jet is fully developed, its volume remains

constant during progression, and fairly corresponds to the final sessile droplet volume, with no additional liquid collection from the liquid film. This mechanism leads to circular sessile droplets up to liquid film-receptor substrate separations of the order of the mm. At higher separations, the jet still reaches the receptor substrate, but the multiple parts resulting from the jet breakup do not fall down at the jet impact position; rather they are deposited as satellite droplets. At even larger separations, the jet breaks before reaching the substrate and only randomly distributed small droplets are deposited.

13) A different deposition mechanism (bubble regime) based on the contact of the initial cavitation bubble with the receptor substrate can occur at short liquid film-receptor substrate distances and/or high laser pulse energies. After reaching the receptor, the bubble collapses into a jet, which continues feeding the sessile droplet until jet breakup occurs. This mechanism results in droplets with a smaller contact angle than those obtained with the jetting mechanism. Moreover, the droplets reproducibility is also worsen respect to the previous case.

*The implementation of a femtosecond laser in the direct-writing setup has allowed demonstrating that:*

14) It is possible to print transparent or weakly absorbing liquids directly from a liquid contained in the reservoir by strongly focusing a laser beam underneath the free surface of the liquid. This has resulted in the development of a new and original technique which allows overcoming the main drawback of the LIFT of liquids, the preparation of the liquid in thin film form.

15) The new printing method can operate in two different configurations: the so-called *backward configuration*, which requires the substrate to be transparent to the laser radiation; and the *forward configuration*, which does not impose any restriction on the transparency of the substrate. Both configurations allow the preparation of large arrays with uniform and circular droplets in a versatile way.

16) It has been found that the position of the focal point under the free surface of the liquid is a critical parameter to obtain well-defined microdroplets. Furthermore, the volume of the printed droplets depends linearly on the laser pulse energy, with an abrupt transition to high volumes when the laser pulse energy reaches a certain value. Resolutions significantly higher than those characteristic of the LIFT technique can be attained with the new printing technique.

17) The hybridization test of a DNA microarray and the immunoassay of an IgG microarray, both prepared with the novel technique, have proved that the technique is feasible for biomolecule printing in its two configurations. The preservation of the selectivity of the deposited specimens, in addition to the small size of the printed spots, also demonstrates that the technique is suitable for the preparation of miniaturized biosensors.

## Appendix

# Determination of the relationship between $E$-$E_0$ and $E_A$

The calculus of the relationship between the expression $E$-$E_0$ (section 3.4) and the value $E_A$, the fraction of the incoming laser pulse energy that overcomes the threshold $F_0$, is presented next.

Considering that $F(x,y)$ is the elliptical Gaussian distribution of the laser beam (equation 1.2), $\omega_x$ and $\omega_y$ the laser beam dimensions, and $x_0$ and $y_0$ the intersection points between $F_0$ and $F(x,y)$, then the value of $E_A$ can be calculated as follows:

$$E_A = \int_{\forall x,y;\frac{x^2}{x_0^2}+\frac{y^2}{y_0^2}\le 1} F(x,y)dxdy = \int_{\forall x,y;\frac{x^2}{x_0^2}+\frac{y^2}{y_0^2}\le 1} \frac{2E}{\pi\omega_x\omega_y} e^{-\left(\frac{2x^2}{\omega_x^2}+\frac{2y^2}{\omega_y^2}\right)}dxdy$$

Where $F_0 = F(x_0,0) \rightarrow x_0^2 = \frac{\omega_x^2}{2}\ln\frac{2E}{\pi\omega_x^2\omega_y^2F_0}$ and

$$F_0 = F(0,y_0) \rightarrow y_0^2 = \frac{\omega_y^2}{2}\ln\frac{2E}{\pi\omega_x^2\omega_y^2F_0}$$

Using the change of variables:

$$x' = \frac{x}{\omega_x}$$

$$y' = \frac{y}{\omega_y}$$

Then, $E_A = \int_{\forall x',y';x'^2+y'^2\le R} \frac{2E}{\pi} e^{-2\left(x'^2+y'^2\right)}dx'dy'$

and thus with this change of variables the elliptical beam becomes circular, with a radius $R$.

In cylindrical coordinates, the above expression is:

$$E_A = \int_0^{2\pi} d\theta \int_0^R r \frac{2E}{\pi} e^{-2r^2} dr = \frac{4\pi E}{\pi} \int_0^R r e^{-2r^2} dr$$

where $x'^2 + y'^2 = r^2$

The solution of this integral is:

$$E_A = E\left|e^{-2r^2}\right|_R^0 = E\left[1 - e^{-2R^2}\right] \tag{A.1}$$

Considering that $F_0 = \frac{2E}{\pi\omega_x\omega_y} e^{-2\left(\frac{x_0^2}{\omega_x^2}+\frac{y_0^2}{\omega_y^2}\right)} = \frac{2E}{\pi\omega_x\omega_y} e^{-2R^2}$ (for a Gaussian beam with energy $E$) and that $E_0 = \frac{\pi\omega_x\omega_y F_0}{2} \rightarrow F_0 = \frac{2E_0}{\pi\omega_x\omega_y}$ (section 1.3.3), then it is found that:

$\frac{2E_0}{\pi\omega_x\omega_y} = \frac{2E}{\pi\omega_x\omega_y} e^{-2R^2}$ and thus $E_0 = Ee^{-2R^2}$

Therfore, returning to equation A.1,

$$E_A = E - Ee^{-2R^2} = E - E_0$$

And thus the value of $E_A$ is equivalent to that of $E$-$E_0$.

# References


Adrian F.J., Bohandy J., Kim B.F., Jette A.N., Thompson P., *A study of the mechanism of metal deposition by the laser-induced forward transfer process*, J. Vac. Sci. Technol. B **5** (1987) 1490

Arnold C.B., Wartena R.C., Swider-Lyons K.E., Piqué A., *Direct-write planar microultracapacitors by laser engineering*, J. Electrochem. Soc. **150** (2003) A571

Arnold C.B., Sutto T., Kim H., Piqué A., *Direct-write laser processing creates tiny electrochemical systems*, Laser Focus World **40** (2004a) S9

Arnold C.B., Kim H., Piqué A., *Laser direct write of planar alkaline microbatteries*, Appl. Phys. A. **79** (2004b) 417

Arnold C.B., Serra P., Piqué A., *Laser direct write of complex materials*, MRS Bull. **32** (2007) 23

Banks D.P., Grivas C., Mills J.D., Eason R.W., Zergioti I., *Nanodroplets deposited in microarrays by femtosecond Ti:sapphire laser-induced forward transfer*, Appl Phys. Lett. **89** (2006) 193107

Barron J.A., Wu P., Ladouceur H.D., Ringeisen B.R., *Biological laser printing: a novel technique for creating heterogeneous 3-dimensional cell patterns*, Biomed. Microdevices **6** (2004a) 139

Barron J.A., Rosen R., Jones-Meehan J., Spargo B.J., Belkin S., Ringeisen B.R., *Biological laser printing of genetically modified Escherichia coli for biosensor applications*, Biosens. Bioelectron. **20** (2004b) 246

Barron J.A., Ringeisen B.R., Kim H., Spargo B.J., Chrisey D.B., *Application of laser printing to mammalian cells*, Thin Solid Films **453-454** (2004c) 383

Barron J.A., Spargo B.J., Ringeisen B.R., *Biological laser printing of three dimensional cellular structures,* Appl. Phys. A **79** (2004d) 1027

Barron J.A., Young H.D., Dlott D.D., Darfler M.M., Krizman D.B., Ringeisen B.R., *Printing of protein microarrays via a capillary-free fluid jetting mechanisms*, Proteomics **5** (2005a) 4138

Barron J.A., Krizman D.B., Ringeisen B.R., *Laser printing of single cells: statistical analysis, cell viability, and stress*, Ann. Biomed. Eng. **33** (2005b) 121

Baseman R.J., Froberg N.M., Andreshak J.C., Schlesinger Z., *Minimum fluence for laser blow-off of thin gold films at 248 and 532 nm*, Appl. Phys. Lett. **56** (1990) 1412

Blake J.R., Gibson D.C., J. Fluid. Mech., *Growth and collapse of a vapour cavity near a free surface*, **111** (1981) 123

Bohandy J., Kim B.F., Adrian F.J., *Metal deposition from a supported metal film using an excimer laser*, J. Appl. Phys. **60** (1986) 1538

Bohandy J., Kim B.F., Adrian F.J., Jette A.N., *Metal deposition at 532 nm using a laser transfer technique*, J. Appl. Phys. **63** (1988) 1158

Boland T., Xu T., Damon B., Cui X., *Application of inkjet printing to tissue engineering*, Biotechnol. J. **1** (2006) 910

Boutopoulos C., Tsouti V., Goustouridis D., Chatzandroulis S., Zergioti I., *Liquid phase direct laser printing of polymers for chemical sensing applications*, Appl. Phys. Lett. **93** (2008a) 191109

Boutopoulos C., Andreakou P., Kafetzopoulos D., Chatzandroulis S., Zergioti I., *Direct laser printing of biotin microarrays on low temperature oxide on Si substrates*, Phys. Stat. Sol. (a) **205** (2008b) 2505

Bratton D., Yang D., Dai J., Ober C.K., *Recent progress in high resolution lithography*, Polym. Adv. Technol. **17** (2006) 94

Brennen C.E., *Cavitation and Bubble Dynamics*, Oxford University Press, New York, 1995, p. 79

Brisbane A.D., *Pattern deposit by laser*, U.S. Patent 3,560.258, Feb. 2 1971

Brujan E.A., Nahen K., Schmidt P., Vogel A., *Dynamics of laser-induced cavitation bubbles near an elastic boundary*, J. Fluid. Mech. **433** (2001) 251

Brujan E.A., Vogel A., *Stress wave emission and cavitation bubble dynamics by nanosecond optical breakdown in a tissue phantom*, J. Fluid. Mech. **558** (2006) 281

Calvert P*., Inkjet printing for materials and devices,* Chem. Mat. **13** (2001) 3299

Cerami L.R., Mazur E., Nolte S., Schaffer C.B., 'Femtosecond laser micromachining'. In *Ultrafast Optics*, edited by Trebino R. and Squier J. (2007)

Chakraborty S., Sakata H., Yokoyama E., Wakaki M., Chakravorty D., *Laser-induced forward transfer technique for maskless patterning of amorphous V2O5 thin film,* Appl. Surf. Sci. **254** (2007) 638

Chen C.Y., Barron J.A., Ringeisen B.R., *Cell patterning without chemical surface modification: cell-cell interactions between printed bovine aortic endothelial cells (BAEC) on a homogeneous cell-adherent hydrogel*, Appl. Surf. Sci. **252** (2006) 8641

Chrisey D.B., A. Piqué, Fitz-Gerald J., Auyeung R.C.Y., McGill R.A., Wu H.D., M. Duignan, *New approach to laser direct writing active and passive mesoscopic circuit elements*, Appl. Surf. Sci. **154-155** (2000) 593

Chrisey D.B., Piqué A., 'Introduction to direct-write technologies for rapid prototyping'. In *Direct-write technologies for rapid prototyping applications*, edited by Piqué A. and Chrisey D.B. (Academic Press San Diego, 2002), p. 1

Chrisey D.B., Piqué A., McGill R.A., Horwitz J.S., Ringeisen B.R., Bubb D.M., Wu P.K., *Laser deposition of polymer and biomaterial films*, Chem. Rev. **103** (2003) 553

Colina M., Serra P., Fernández-Pradas J.M., Sevilla L., Morenza J.L., *DNA deposition through laser induced forward transfer*, Biosens. Bioelectron. **20** (2005) 1638

Colina M., Duocastella M., Fernández-Pradas J.M., Serra P., Morenza J.L., *Laser-induced forward transfer of liquids: study of the droplet ejection process,* J. Appl. Phys. **99** (2006) 084909

Colina M., *Transferencia inducida por láser para la elaboración de microarrays de biomoléculas,* PhD Thesis 2006

Craighead, *Nanoelectromechanical systems*, Science **24** (2000) 879

Dinca V., Kasotakis E., Catherine J., Mourka A., Mitraki A., Popescu A., Dinescu M., Farsari M., Fotakis C., *Development of peptide-based patterns by laser transfer*, Appl. Surf. Sci. **254** (2007a) 1160

Dinca V., Ranella A., Popescu A., Dinescu M., Farsari M., Fotakis C., *Parameters optimization for biological molecules patterning using 248-nm ultrafast lasers*, Appl. Surf. Sci. **254** (2007b) 1154

Dinca V., Ranilla A., Farsari M., Kafetzopoulos D., Dinescu M., Popescu A., Fotakis C., *Quantification of the activity of biomolecules in microarrays obtained by direct laser transfer*, Biomed. Microdevices **10** (2008a) 719

Dinca V., Farsari M., Kafetzopoulos D., Popescu A., Dinescu M., Fotakis C., *Patterning parameters for biomolecules microarrays constructed with nanosecond and femtosecond UV lasers*, Thin Solid Films **516** (2008b) 6504

Dinca V., Kasotakis E., Mourka A., Ranella A., Farsari M., Mitraki A., Fotakis C., *Fabrication of amyloid peptide micro-arrays using laser-induced forward transfer and avidin-biotin mediated assembly*, Phys. Stat. Sol. (c) **5** (2008c) 3576

Dinu C.Z., Dinca V., Howard J., Chrisey D.B., *Printing technologies for fabrication of bioactive and regular microarrays of streptavidin*, Appl. Surf. Sci. **253** (2007) 8119

Doraiswamy A., Narayan R.J., Lippert T., Urech L., Wokaun A., Nagel M., Hopp B., Dinescu M., Modi R., Auyeung R.C.Y., Chrisey D.B., *Excimer laser forward transfer of mammalian cells using a novel triazene absorbing layer*, Appl. Surf. Sci. **252** (2006) 4743

Ducasse A., Rullière C., Couillard B., 'Methods for the generation of ultrashort laser pulses: modelocking'. In *Femtosecond laser pulses, principles and experiments*, edited by Rullière C. (Springer Science, New York, 2004), p. 57

Eggers J., *Nonlinear dynamics and breakup of free-surface flows*, Rev. Mod. Phys. **69** (2007) 865

Fardel R., Nagel M., Nüesch F., Lippert T., Wokaun, A., *Fabrication of organic light-emitting diode pixels by laser-assisted forward transfer*, Appl. Phys. Lett. **91** (2007) 061103

Fernández-Pradas J.M., Colina M., Serra P., Domínguez J., Morenza J.L., *Printing biological solutions through laser-induced forward transfer*, Thin Solid Films **453-454** (2004) 27

Fillmore G.L., *Drop velocity from an ink-jet nozzle*, IEEE T. Ind. Appl. **19** (1983) 1098

Fitz-Gerald J.M., Piqué A., Chrisey D.B., Rack P.D., Zeleznik M., Auyeung R.C Y., Lakeou S., *Laser direct writing of phosphor screens for high-definition displays,* Appl. Phys. Lett. **76** (2000) 1386

Fogarassy E., Fuchs C., Kerherve F., Hauchecorne G., Perriere J., *Laser-induced forward transfer of high-Tc YBaCuO and BiSrCaCuO superconducting thin films,* J. Appl. Phys. **86** (1989) 457

Frank J.P., Michel J.M., *Fundamentals of cavitation*, Kluwer Academic Publishers, Dordrecht, 2004, p. 57

Gao L., McCarthy T.J., *Contact angle hysteresis explained*, Langmuir **22** (2006) 6234

Greer J.A., Parker T.E., *Laser-induced forward transfer of metal oxides to trim the frequency of surface acoustic wave resonator devices,* SPIE Proc. **998** (1988) 113

Guillemot F., Souquet A., Catros S., Guillotin B., Lopez J., Faucon M., Pippenger B., Bareille R., Remy M., Bellance S., Chabassier P., Fricain J.C., Amedee J, *High-throughput laser printing of cells and biomaterials for tissue engineering*, Acta Biomaterialia (2009) doi:10.1016/j.actbio.2009.09.029

Hon K.K.B., Li L., Hutchings I.M., *Direct writing technology- advances and developments*, CIRP Ann.-Manuf. Techn. **57** (2008) 601

Hopp B., Smausz T., Antal Z., Kresz N., Bor Z., Chrisey D., *Absorbing film assisted laser induced forward transfer of fungi (Trichoderma conidia)*, J. Appl. Phys. **96** (2004) 3478

Hopp B., Smausz T., Kresz N., Barna N., Bor Z., Kolozsvári L., Chrisey D.B., Szabó A., Nógrádi A., *Survival and proliferative ability of various living cell types after laser-induced forward transfer*, Tissue Eng. **11** (2005) 1817

Hnatovsky C., Taylor R.S., Simova E., Bhardwaj R., Rayner D.M., Corkum P.B., *High resolution study of photoinduced modification in fused silica produced by a tightly focused femtosecond laser beam in the presence of aberrations*, J. Appl. Phys. **98** (2005) 013517

Ion J.C., *Laser processing of engineering materials*, Oxford (UK): Elsevier Butterworth-Heinemann (2005) p. 188

Janasek D., Franzke J., Manz A., *Scaling and the design of miniaturized chemical-analysis systems*, Nature **442** (2006) 374

Kántor Z., Tóth Z., Szörényi T., *Laser induced forward transfer: the effect of support-film interface and film-to-substrate distance on transfer*, Appl Phys. A **54** (1992) 170

Kántor Z., Tóth Z., Szörényi T., Tóth A.L., *Deposition of micrometer-sized tungsten patterns by laser transfer technique*, Appl. Phys. Lett. **64** (1994) 3506

Kántor Z., Tóth Z., Szörényi T., *Metal pattern deposition by laser-induced forward transfer*, Appl. Surf. Sci. **86** (1995a) 196

Kántor Z., Szörényi T., *Dynamics of long-pulse laser transfer of micrometer-sized metal patterns as followed by time-resolved measurements of reflectivity and transmittance,* J. Appl. Phys. **78** (1995b) 2775

Kattamis N.T., Purnick P.E., Weiss R., Arnold C.B., *Thick film laser induced forward transfer for deposition of thermally and mechanically sensitive materials*, Appl. Phys. Lett. **91** (2007) 171120

Kattamis N.T., McDaniel N.D., Bernhard S., Arnold C.B., *Laser direct write printing of sensitive and robust light emitting organic molecules,* Appl. Phys. Lett. **94** (2009) 103306

Kaur K.S., Fardel R., May-Smith T.C., Nagel M., Banks D.P., Grivas C., Lippert T., Eason R.W., *Shadowgraphic studies of triazene assisted laser-induced forward transfer of ceramic thin films*, J. Appl. Phys. **105** (2009) 113119

Kennedy C.F., Field J.E., *Damage threshold velocities for liquid impact*, J. Mater. Sci. **35** (2000) 5331

Kim H., Kushto G.P., Arnold C.B., Kafafi Z.H., Piqué A., *Laser processing of nanocrystalline TiO2 films for dye-sensitized solar cells,* Appl. Phys. Lett. **85** (2004) 464

Kim H., Auyeung R.C.Y., Ollinger M., Kushto G.P., Kafafi Z.H., Piqué A., *Laser-sintered mesoporous TiO2 electrodes for dye-sensitized solar cells,* Appl. Phys. A **83** (2006) 73

Kim H., Auyeung R.C.Y., Piqué A., *Laser-printed thick-film electrodes for solid-state rechargeable Li-ion microbatteries,* J. Power Sources **165** (2007) 413

Kim H., Auyeung R.C.Y., Lee S.H., Huston A.L., Piqué A., *Laser forward transfer of silver electrodes for organic thin-film transistors*, Appl. Phys. A **96** (2009) 441

Kim H., Auyeung R.C.Y., Lee S.H., Huston A.L., Piqué A., *Laser-printed interdigitated Ag electrodes for organic thin film transistors*, J. Phys. D: Appl. Phys. **43** (2010) 085101

Ko S.H., Pan H., Ryu S.G., Misra N., Grigoropoulos C.P., Park H.K., *Nanomaterial enabled laser transfer for organic light emitting material direct writing*, Appl. Phys. Lett. **93** (2008) 151110

Kwok D.Y., Gietzelt T., Grundke K., Jacobasch H.J., Neumann A.W., *Contact angle measurements and contact angle interpretation. 1. Contact angle measurements by axisymmetric drop shape analysis and a goniometer sessile drop technique*, Langumir **13** (1997) 2880

Lesser M., *Thirty years of liquid impact research: a tutorial review*, Wear **186-187** (1995) 28

Levene M.L., Scott R.D., Siryj B.W., *Material transfer recording*, Appl. Optics **9** (1970) 2260

Lewis B.R., Kinzel E.C., Laurendeau N.M., Lucht R.P., Xu X., *Planar laser imaging and modeling of matrix-assisted pulsed-laser evaporation direct write in the bubble regime*, J. Appl. Phys. **100** (2006) 033107

Lin Y., Huang Y., Chirsey D.B., *Droplet formation in matrix-assisted pulsed-laser evaporation direct writing of glycerol-water solution*, J. Appl. Phys. **105** (2009) 093111

Loo Y.L., McCulloch I., *Progress and Challenges in Commercialization of Organic Electronics,* MRS Bull. **33** 653 (2008)

Maiman Th., *Stimulated optical radiation in ruby*, Nature **187** (1960) 493

Mézel C., Hallo L., Souquet A., Breil J., Hébert D., Guillemot F., *Self-consistent modeling of jet formation process in the nanosecond laser pulse regime*, Phys. Plasmas **16** (2009) 123112

Modi R., Wu H.D., Auyeung R.C.Y., Gilmore C.M., Chrisey D.B*., Direct writing of polymer thick film resistors using a novel laser transfer technique*, J. Mater. Res. **16** (2001) 3214

Nagel D.J., 'Technologies for micrometer and nanometer pattern and material transfer'. In *Direct-write technologies for rapid prototyping applications*, edited by Piqué A. and Chrisey D.B. (Academic Press, San Diego, 2002), p. 558

Nakata Y., Okada T., Maeda M., *Microscopic and spectroscopic imaging of laser-induced forward transfer and its application to material transfer*, Proc. SPIE **5399** (2004) 156

Narazaki A., Sato T., Kurosaki R., Kawaguchi Y., Niino H., *Nano-and microdot array formation of FeSi2 by nanosecond excimer laser-induced forward transfer*, Appl. Phys. Express **1** (2008) 057001

Othon C.M., Wu X., Anders J.J., Ringeisen B.R., *Single-cell printing to form three-dimensional lines of olfactory ensheathing cells*, Biomed. Mater. **3** (2008) 034101/1

Papakonstantinou P., Vainos N.A., Fotakis C., *Microfabrication by UV femtosecond laser ablation of Pt, Cr and indium oxide thin films*, Appl. Surf. Sci. **151** (1999) 159

Park J.U., Hardy M., Kang S.J., Barton K., Adair K., Mukhopadhyay D., Lee C.Y., Strano M.S., Alleyne A.G., Georgiadis J.G., Ferreira P.M., Rogers J.A., *High-resolution electrohydrodynamic jet printing*, Nature Mat. **6** (2007) 782

Pearson A., Cox E., Blake J.R., Otto S.R., *Bubble interactions near a free surface*, Eng. Anal. Bound. Elem. **28** (2004) 295

Piqué A., Chrisey D.B., Auyeung R.C.Y., Fitz-Gerald J., Wu H.D., McGill R.A., Lakeou S., Wu P.K., Nguyen V., Duignan M., *A novel laser transfer process for direct writing of electronic and sensor materials*, Appl. Phys. A **69** (1999) S279

Piqué A., Auyeung R.C.Y., Stepnowski J.L., Weir D.W., Arnold C.B., McGill R.A., Chrisey D.B., *Laser processing of polymer thin films for chemical sensor applications*, Surf. Coat. Techn. **163-164** (2003) 293

Piqué A., Arnold C.B., Kim H., Ollinger M., Sutto T., *Rapid prototyping of micropower sources by laser direct-write*, Appl. Phys. A **79** (2004) 783

Rapp L., Diallo A.K., Alloncle A.P., Videlot-Ackermann C., Fages F., Delaporte P., *Pulsed-laser printing of organic thin-film transistors*, Appl. Phys. Lett. **95** (2009a) 171109

Rapp L., Cibert C., Alloncle A.P., Delaporte P., *Characterization of organic material micro-structures transferred by laser in nanosecond and picosecond regimes*, Appl. Surf. Sci. **255** (2009b) 5439

Ringeisen B.R., Chrisey D.B., Piqué A., Young H.D., Modi R., Bucaro M., Jones-Meeham J., Spargo B.J., *Generation of mesoscopic patterns of viable Escherichia coli by ambient laser transfer*, Biomaterials **23** (2002a) 161

Ringeisen B.R., Wu P.K., Kim H., Piqué A., Auyeung R.Y.C., Young H.D., Chrisey D.B., *Picoliter-scale protein microarrays by laser direct write*, Biotechnol. Prog. **18** (2002b) 1126

Ringeisen B.R., Othon C.M., Barron J.A., Young D., Spargo B.J., *Jet-based methods to print living cells*, Biotechnol. J. **1** (2006) 930

Rioboo R., Marengo M., Tropea C., *Time evolution of liquid drop impact onto solid, dry surfaces*, Exp. Fluids **33** (2002) 112

Roux D.C.D., Cooper-White J.J., *Dynamics of water spreading on a glass surface*, J. Colloid Interf. Sci. **424** (2004) 277

Sano T., Yamada H., Nakayama T., Miyamoto I., *Experimental investigation of laser induced forward transfer process of metal thin films*, Appl Surf. Sci. **186** (2002) 221

Serra P., Fernández-Pradas J.M., Berthet F.X., Colina M., Elvira J., Morenza J.L., *Laser direct writing of biomolecule microarrays*, Appl. Phys. A **79** (2004a) 949

Serra P., Colina M., Fernández-Pradas J.M., Sevilla L., Morenza J.L., *Preparation of functional DNA microarrays through laser-induced forward transfer*, Appl. Phys. Lett. **82** (2004b) 1639

Schiele N.R., Koppes R.A., Corr D.T., Ellison K.S., Thompson D.M., Ligon L.A., Lippert T.K.M., Chrisey D.B., *Laser direct writing of combinatorial libraries of idealized cellular constructs: biomedical applications*, Appl. Surf. Sci. **255** (2008) 5444

Schaffer C.B., Brodeur A., Mazur E., *Laser-induced breakdown and damage in bulk transparent materials induced by tightly-focused femtosecond laser pulses*, Meas. Sci. Technol. **12** (2001) 1784

Schaffer C.B., Nishimura N., Glezer E.N., Kim A.T., Mazur E., *Dynamics of femtosecond laser-induced breakdown in water from femtoseconds to microseconds*, Opt. Express **10** (2002) 196

Schultze V., Wagner M., *Laser-induced forward transfer of aluminium*, Appl. Surf. Sci. **52** (1991) 303

Sikalo Š., Wilhelm H.D., Roisman I.V., Jakirlić S., Tropea C., *Dynamic contact angle of spreading droplets: experiments and simulations*, Phys. Fluids **17** (2005) 062103/1-13

Sirringhaus H., Shimoda T., *Inkjet printing of functional materials*, MRS Bull. **28**, (2003) 802

Thomas B., Alloncle A.P., Delaporte P., Sentis M., Sanaur S., Barret M., Collot P., *Experimental investigations of laser-induced forward transfer process of organic thin films*, Appl. Surf. Sci. **254** (2007) 1206

Tolbert W.A., Lee I.Y.S., Doxtader M.M., Foley D.M., Arnold D.R., Ellis E.W., *High-speed color imaging by laser-ablation transfer with a dynamic release layer: fundamental mechanisms*, J. Imaging Sci. Tech. **37** (1993a) 411

Tolbert W.A., Lee I.Y.S., Wen X., Dlott D.D., Doxtader M.M., Ellis E.W., *Laser-ablation transfer imaging using picosecond optical pulses: ultra-high speed, lower threshold and higher resolution*, J. Imaging Sci. Tech. **37** (1993b) 485

Tóth Z., Szörényi T., Tóth A.L., Ar+ *laser-induced forward transfer (LIFT): a novel method for micrometer-size surface patterning*, Appl. Surf. Sci. **69** (1993) 317

Veiko V.P., Shakhno E.A., Smirnov V.N., Miaskovski A.M., Nikishin G.D., *Laser-induced film deposition by LIFT: physical mechanisms and applications*, Laser Part. Beams **24** (2006) 203

Vogel A., Busch S., Parlitz U., *Shock wave emission and cavitation bubble generation by picosecond and nanosecond optical breakdown in water*, J. Acoust. Soc. Am. **100** (1996a) 148

Vogel A., Nahen K., Theisen D., Noack J., *Plasma formation in water by picosecond and nanosecond Nd:YAG laser pulses—part I: optical breakdown at threshold and superthreshold irradiance*, IEEE J. Sel. Top. Quantum Electron. **2** (1996b) 847

Vogel A., Linz N., Freidank S., Paltauf G., *Femtosecond laser induced nanocavitation in water: implication for optical breakdown threshold and cell surgery*, Phys. Rev. Lett. **28** (2008) 295

Voldman J.L., Gray M.L., Schmidt M.A., *Microfabrication in biology and medicine*, Annu. Rev. Biomed. Eng. **1** (1999) 401

Wartena R., Curtright A.E., Arnold C.B., Piqué A., Swider-Lyons K.E., *Li-ion microbatteries generated by a laser direct-write method*, J. Power Sources **126** (2004) 193

Willis D.A., Grosu V., *Microdroplet deposition by laser-induced forward transfer*, Appl. Phys. Lett. **86** (2005) 244103

Wu P.K., Ringeisen B.R., Callahan J., Brooks M., Bubb D.M., Wu H.D., Piqué A., Spargo B., McGill R.A., Chrisey D.B., *The deposition, structure, pattern deposition, and activity of biomaterial thin-films by matrix-assisted pulsed laser evaporation (MAPLE) and MAPLE direct write*, Thin Solid films **398-399** (2001) 607

Wu P.K., Ringeisen B.R., Krizman D.B., Frondoza C.G., Brooks M., Bubb D.M., Auyeung R.C.Y., Piqué A., Spargo B., McGill R.A., Chrisey D.B., *Laser transfer of biomaterials: matrix-assisted pulsed laser evaporation (MAPLE) and MAPLE direct write*, Rev. Sci. Instrum. **74** (2003) 2546

Xu L., Zhang W.W., Nagel S.R., *Drop splashing on a dry smooth surface,* Phys. Rev. Lett. **94** (2005) 184505

Yamada H., Sano T., Nakayama T., Miyamoto I., *Optimization of laser-induced forward transfer process of metal thin films,* Appl. Surf. Sci. **197-198** (2002) 411

Yang L., Wang C., Ni X., Wang Z., Jia W., Chai L., *Microdroplet deposition of copper film by femtosecond laser-induced forward transfer*, Appl. Phys. Lett. **89** (2006) 161110

Young D., Auyeung R.C.Y., Piqué A., Chrisey D.B., Dlott D., *Time-resolved optical microscopy of a laser-based forward transfer process*, Appl. Phys. Lett. **78** (2001) 3169

Young D., Auyeung R.C.Y., Piqué A., Chrisey D.B., Dlott D., *Plume and jetting regimes in a laser based forward transfer process as observed by time-resolved optical microscopy,* Appl. Surf. Sci. **197-198** (2002) 181

Zergioti I., Mailis S., Vainos N.A., Papakonstantinou P., Kalpouzos C.,. Grigoropoulos C.P, Fotakis C., *Microdeposition of metal and oxide structures using ultrashort laser pulses*, Appl. Phys. A **66** (1998) 579

Zergioti I., Papazoglou D.G., Karaiskou A., Vainos N.A., Fotakis C., *Laser microprinting of InOx active optical structures and time resolved imaging of the transfer process*, Appl. Surf. Sci. **197-198** (2002) 868

Zergioti I., Papazoglou D.G., Karaiskou A., Fotakis C., Gamaly E., Rode A., *A comparative schlieren imaging study between ns and sub-ps laser forward transfer of Cr*, Appl. Surf. Sci. **208-209** (2003) 177

Zergioti I., Karaiskou A., Papazoglou D.G., Fotakis C., Kapstetaki M., Kafetzopoulos D., *Femtosecond laser microprinting of biomaterials*, Appl. Phys. Lett. **86** (2005) 163902

# Publications

The present thesis has resulted in the following publications:

### Journal papers

M. Duocastella, J.M. Fernández-Pradas, J.L. Morenza, P. Serra, *Sessile droplet formation in the laser-induced forward transfer of liquids: a time-resolved imaging study*, Thin Solid Films (accepted)

M. Duocastella, J.M. Fernández-Pradas, J.L. Morenza, D. Zafra, P. Serra, *Novel laser printing technique for miniaturized biosensors preparation*, Sens. Actuators B **145** (2010) 596

M. Duocastella, J.M. Fernández-Pradas, J.L. Morenza, P. Serra, *Time resolved imaging of the laser forward transfer of liquids*, J. Appl. Phys. **106** (2009) 084907

M. Duocastella, J.M. Fernández-Pradas, P. Serra, J.L. Morenza, *Printing biological solutions through laser-induced forward transfer*, Appl. Phys. A **93** (2008) 941

M. Duocastella, J.M. Fernández-Pradas, P. Serra, J.L. Morenza, *Jet formation in the laser forward transfer of liquids*, Appl. Phys. A **93** (2008) 453

J.M. Martín-Durán, M. Duocastella, P. Serra, R. Romero, *A new method to deliver exogenous material into developing planarian embryos*, J. Exp. Zool. (Mol. Dev. Evol.) **310B** (2008) 668

P. Serra, M. Duocastella, J.M. Fernández-Pradas, J.L. Morenza, *Liquids microprinting through laser-induced forward transfer*, Appl. Surf. Sci. **255** (2008) 5342

M. Duocastella, M. Colina, J.M. Fernández-Pradas, P. Serra, and J.L. Morenza, *Study of the laser-induced forward transfer of liquids for laser bioprinting,* Appl. Surf. Sci. **253** (2007) 7855

M. Duocastella, J.M. Fernández-Pradas, P. Serra, J.L. Morenza, *Laser-induced forward transfer of liquids for miniaturized biosensors preparation,* JLMN-Journal of Laser Micro/Nanoengineering **3** (2007) 1

J.M. Fernández-Pradas, M. Duocastella, P. Serra, J.L. Morenza, *Production of miniaturized biosensors through laser-induced forward transfer,* Proc. SPIE **6592** (2007) 65920R

P. Serra, J.M. Fernández-Pradas, M. Colina, M. Duocastella, J. Domínguez, J.L. Morenza. *Laser induced forward transfer: a direct writing technique for biosensors preparation*, Journal of Laser Micro/Nanoengineering **1** (2006) 236

M.Colina, M.Duocastella, J.M. Fernández-Pradas, P.Serra, and J.L. Morenza, *Laser-induced forward transfer of liquids: study of the droplet ejection process*, J. Appl. Phys. **99** (2006) 74

## Book chapters

P. Serra, M. Duocastella, J.M. Fernández-Pradas, J.L. Morenza, 'Laser-induced forward transfer: a laser-based technique for biomolecules printing'. In *Cell and organ printing,* edited by B.R. Ringeisen, B.J. Spargo, P. Wu, Springer Verlag, Berlin, Germany (in press)

P. Serra, M. Duocastella, J.M. Fernández-Pradas, J.L. Morenza, 'Laser-induced forward transfer: a versatile technique for microprinting'. In *Advances in laser materials processing technology, research and applications*, edited by J. Lawrence, J. Pou, D.K. Low, E. Toyserkani, CRCPress & Woodhead Publishing Ltd.(2009), Cambridge, UK

## Patent

P. Serra, M. Duocastella, J.M. Fernández-Pradas, J.L. Morenza, *Aparato y método para la impresión directa con láser*. Patent application ES 200901669 (2009)

# Resum en català

Els làsers són unes eines úniques, la radiació de les quals presenta característiques tan notòries com una llarga longitud de coherència, poca divergència o una alta monocromaticitat. També cal destacar que els làsers permeten dipositar de manera controlada quantitats d'energia sobre una gran varietat d'objectes. Aquest darrer aspecte els fa adequats pel processament de materials: irradiar un material amb un làser pot resultar en modificacions permanents a la superfície o volum del material. Aquest aspecte s'ha utilitzat en aplicacions industrials tals com soldar, tallar o perforar. A més a més, és possible utilitzar sistemes òptics per tal de focalitzar la radiació làser en volums molt petits, permetent traslladar les operacions prèviament citades al món microscòpic, en el que es coneix com a microfabricació.

La tècnica de microfabricació làser més emprada és l'ablació làser, consistent en el disseny de motius tot arrencant selectivament material d'un substrat. No obstant, també és possible la utilització d'un làser per a afegir material, aconseguint d'aquesta manera la impressió dels motius desitjats sobre un substrat. Cal destacar aquest últim punt, ja que la capacitat de dipositar controladament i amb una alta resolució diferents tipus de materials (incloent-hi materials sensibles o fràgils) sobre una gran varietat de substrats, suposaria un gran avenç en diverses àrees. Per exemple, podria permetre la fabricació de dispositius miniaturitzats, com biosensors, o fins i tot la construcció d'òrgans artificials tot combinant el dipòsit de cèl·lules i biomaterials.

La present tesi es centra en l'estudi d'una d'aquestes tècniques d'addició de material mitjançant làser: la transferència induïda per làser o LIFT (de l'anglès, laser-induced forward transfer). La LIFT consisteix en la utilització d'impulsos làser per tal de transferir material des d'un substrat emissor a un substrat receptor. El substrat emissor està constituït per un suport transparent a la

radiació làser recobert per una capa del material que es vol dipositar. El substrat receptor es troba situat paral·lel i a poca distància del substrat emissor, fent front al material a dipositar. Quan un impuls làser arriba al substrat emissor, travessa el suport transparent fins que arriba a la capa de material, on és absorbit, provocant l'ejecció d'una fracció d'aquesta que acaba dipositant-se sobre el substrat receptor.

Els materials dipositats en aquesta tesi han estat sempre solucions aquoses[15]. En el cas de la LIFT de líquids és important destacar que el material pot ser dipositat en forma de microgotes al substrat receptor mantenint les seves propietats. Així, és possible la impressió de materials funcionals tals com biomolècules en solució, amb una gran resolució, fet que té un especial interès en aplicacions com la realització de biosensors miniaturitzats.

L'objectiu d'aquesta tesi és l'estudi complet de la LIFT de líquids per tal d'aconseguir un millor coneixement d'aquesta tècnica i de trobar les condicions òptimes d'impressió. Aquest estudi comprèn l'anàlisi dels efectes que alguns del paràmetres experimentals tenen en les gotes impreses, així com l'anàlisi dels mecanismes involucrats en l'ejecció i el dipòsit de material a través de la LIFT. Per tal d'efectuar aquest estudi s'ha procedit a la caracterització morfològica de les gotes impreses i a la adquisició ràpida d'imatges del procés de la LIFT. El treball que es presenta ha permès trobar les condicions adequades per la impressió de gotes, així com descobrir els mecanismes responsables de la generació d'aquestes gotes. A més a més, s'ha trobat que el punt dèbil de la tècnica és la preparació de la capa prima líquida. Aquest darrer aspecte ha motivat la recerca d'una nova tècnica capaç d'evitar la preparació de la capa líquida. Aquesta nova i original tècnica s'ha dissenyat, desenvolupat i provat en el Grup de Capes Fines i Enginyeria de Superfícies de la Universitat de Barcelona, i també es presenta en aquesta tesi.

[15] Les solucions aquoses solen ser transparents a la longitud d'ona de la majoria de làsers. Aquest fet es soluciona intercalant una capa metàl·lica absorbent entre la capa líquida i el suport transparent.

## Estudi de la influència dels paràmetres del procés de la LIFT en la morfologia de les gotes impreses

La primera part d'aquesta tesi es centra en l'estudi que alguns dels principals paràmetres experimentals tenen en la morfologia de les gotes impreses. Aquests paràmetres s'han variat sistemàticament, i s'han descrit les conseqüències d'aquestes variacions en el material dipositat mitjançant tècniques de caracterització com la microscòpia òptica o la perfilometria òptica. Els paràmetres estudiats han estat: fluència de l'impuls làser, condicions de focalització del làser, gruix de la capa líquida i distància de separació entre la capa líquida i el substrat receptor. A més a més, s'ha comprovat la viabilitat de la LIFT per a la impressió de proteïnes mitjançant un assaig de fluorescència. En tota aquesta primera sèrie d'experiments s'ha emprat un làser polsat, els polsos del qual tenien una durada d'uns quants nanosegons.

Els experiments variant la fluència han permès determinar l'existència d'un rang intermedi de fluències el qual és possible dipositar gotes ben definides i amb un contorn circular (condicions òptimes de dipòsit). Per sota d'aquest rang, no és possible dipositar res, mentre que per sobre només s'observen gotes irregulars i amb esquitxades. Dintre del rang de fluències intermèdies, el volum de les gotes dipositades augmenta linealment amb la fluència.

Les condicions de focalització (o dimensions del feix làser), també afecten les gotes dipositades: com més focalitzat un feix, l'energia necessària per dipositar una gota és més baixa, i és possible obtenir gotes de diàmetre més petit. A més a més, s'observa l'existència d'una densitat d'energia llindar ($F_0$), la qual s'ha de superar per tal de generar una bombolla de vapor en el líquid que inicia el procés de transferència. Per dipositar una gota, però, cal superar una segona densitat d'energia $F_1$, major que $F_0$. Només en aquest cas la bombolla és suficientment energètica per permetre la transferència de líquid cap al substrat receptor.

És possible relacionar les dimensions de les gotes obtingudes amb el paràmetre $F_0$ a través d'un model senzill[16]. Aquest model es pot aplicar correctament quan les dimensions del feix són superiors al gruix de la capa líquida. En cas contrari, el model falla.

Un altre paràmetre important és el gruix de la capa líquida. Com més prima és una capa, més petites són les gotes que es poden obtenir. La quantitat de material dipositat per energia de l'impuls làser, així com la densitat d'energia mínima necessària per dipositar una gota ($F_1$), augmenten amb el gruix de la capa líquida.

Les gotes dipositades no depenen en excés de la distància entre els substrats emissor i receptor: és possible obtenir gotes ben definides fins a distàncies de l'ordre del mil·límetre. Si es supera aquesta distància màxima, les gotes presenten satèl·lits, i per a distàncies encara més grans, només s'obtenen múltiples gotes distribuïdes aleatòriament.

Finalment, s'ha demostrat la viabilitat de la LIFT per al dipòsit de proteïnes mitjançant la preparació d'un microarray d'una solució que contenia la proteïna immonoglobulina G (IgG), i d'un segon microarray d'una solució d'albúmina bovina (BSA). Després de la seva impressió, els microarrays van ser sotmesos a un test de fluorescència, que ha revelat que les proteïnes preserven la seva funcionalitat un cop dipositades.

[16] El model considera que el volum del material dipositat consisteix en el volum d'un cilindre l'alçada del qual és el gruix de la capa líquida, i la base està formada pels punts del feix amb una densitat d'energia superior a $F_0$ [Colina *et al.* 2006].

## Adquisició ràpida d'imatges del procés de la LIFT de solucions aquoses

Els experiments anteriors han permès determinar les condicions òptimes de dipòsit mitjançant LIFT. No obstant, per tal d'aconseguir una millor comprensió dels processos físics que donen lloc a la formació de les gotes ben definides, és necessari una tècnica capaç d'analitzar la dinàmica de la LIFT en detall: l'adquisició ràpida d'imatges. La segona part de la tesi es centra en l'estudi de la dinàmica de la LIFT mitjançant aquesta tècnica. Cal destacar que el procés de la LIFT es pot dividir en dos sub-processos: l'ejecció i transport de material cap al substrat receptor, i el dipòsit de material sobre el substrat receptor. En aquesta segona part els experiments també s'han realitzat amb el mateix làser de nanosegons que en la primera.

### Mecanismes d'ejecció i transport

Quan l'impuls làser arriba al substrat emissor, és absorbit a la capa metàl·lica. Això provoca la formació d'un plasma, el qual acaba generant una bombolla de cavitació que s'expandeix. Depenent de la fluència de l'impuls làser, pot donar lloc a tres situacions diferents: creació d'un jet que retrocedeix (fluències baixes); formació d'un jet que continua avançant (fluències intermèdies); o trencament de la bombolla (fluències altes).

La generació d'un jet a fluències baixes i intermèdies es pot interpretar de la mateixa manera: quan la bombolla s'expandeix provoca un flux de líquid cap al pol d'aquesta, el qual a la vegada genera una sobrepressió en aquest punt. Durant aquest procés la pressió interna de la bombolla decreix, fet que condueix al seu col·lapse. La sobrepressió generada al pol de la bombolla força el fluid a desplaçar-se a través de l'eix de simetria, cap on la pressió és més baixa: cap a l'exterior del líquid, tot formant un jet perpendicular a la capa líquida; i cap a l'interior de la bombolla, generant el que s'anomena contra-jet.

Per a fluències baixes, la inèrcia del jet generat no és suficient per vèncer la tensió superficial del líquid, i el jet s'acaba frenant i retrocedint cap a la capa líquida. En aquesta situació, si la longitud màxima del jet és menor que la distància de separació entre els substrats emissor i receptor, no es diposita material sobre el receptor. En cas contrari, el jet impacta sobre el substrat receptor tot dipositant una gota.

Per a fluències intermèdies, el jet té suficient inèrcia per continuar avançant. Quan ha assolit una longitud de l'ordre del mil·límetre, es trenca en múltiples parts degut a la inestabilitat de Plateau-Rayleigh. Si el jet impacta sobre el substrat receptor abans de trencar-se, s'obtenen gotes circulars i ben definides.

Per a fluències altes, la força generada per la pressió interna de la bombolla és molt gran, de manera que pot vèncer la força deguda a la tensió superficial, fet que provoca l'explosió de la bombolla. En aquesta situació, el material es diposita sobre el receptor en forma de gotes irregulars o d'esquitxades.

**Mecanismes de dipòsit**

Com s'ha comentat anteriorment, l'impacte d'un jet amb el substrat receptor permet la formació de gotes ben definides Un estudi més detallat del procés de dipòsit, però, ha permès caracteritzar-lo.

Quan el jet arriba al substrat receptor, es comença a acumular líquid a la zona d'impacte, tot iniciant la formació d'una gota. Aquesta primera etapa es caracteritza per un creixement molt ràpid del diàmetre de la gota que es forma. Seguidament, el jet continua alimentant la gota, que augmenta de volum però manté el seu diàmetre constant, és a dir, augmenta l'angle de contacte. Finalment, el jet es trenca degut a la inestabilitat de Plateau-Rayleigh, tot acabant amb l'etapa d'alimentació. S'inicia, en aquest moment, un procés de relaxació de la gota, on el diàmetre de la gota augmenta i l'angle de contacte disminueix.

Cal destacar, però, que existeix un mecanisme de dipòsit diferent. Té lloc quan la separació entre substrat emissor i receptor és prou petita com perquè la bombolla que es forma inicialment contacti el substrat receptor abans que es pugui formar un jet. En aquest cas, la bombolla arriba al receptor tot formant una gota d'un gran diàmetre. Seguidament, la bombolla col·lapsa convertint-se en un jet, que continua alimentant el líquid acumulat. Finalment, el jet es trenca degut a inestabilitats, s'interromp l'alimentació de la gota, i s'inicia un procés de relaxació on la gota disminueix el seu diàmetre. Aquest mecanisme resulta en gotes amb un angle de contacte menor que les obtingudes en el cas de l'impacte del jet, així com en una pèrdua de reproductibilitat de les gotes impreses.

## Desenvolupament i test d'una nova tècnica d'impressió làser

Els experiments amb la tècnica LIFT han permès posar de manifest el major inconvenient que aquesta tècnica té: la preparació de capes primes líquides. De fet, obtenir capes uniformes amb gran control és una etapa àrdua que imposa restriccions pel que fa als líquids que es poden utilitzar, ja que per poder estendre una capa líquida la mullabilitat líquid-substrat emissor ha de ser bona. Per millorar la mullabilitat, es poden usar tensoactius, però això va en detriment d'obtenir gotes amb una gran resolució. A més a més, les capes líquides tendeixen a encongir-se i a evaporar-se, i també cal tenir en compte que la preparació de la capa és una etapa que consumeix temps i augmenta el risc de contaminació. Tot això ens ha portat a la creació i al desenvolupament d'una tècnica nova i original, que evita la utilització de capes líquides, i que s'ha traduït en la sol·licitud d'una patent per part de la Universitat de Barcelona.

La nova tècnica es basa en focalitzar un impuls làser a la subsuperfície d'un líquid contingut en un contenidor. Perquè això sigui possible, el líquid ha de ser transparent o dèbilment absorbent de la radiació làser utilitzada. L'absorció

localitzada de la radiació s'aconsegueix mitjançant una gran focalització del feix, i l'ús d'impulsos làser molt curts (femtosegons) n'accentua l'efecte.

La nova tècnica pot presentar dues configuracions possibles. A la primera, anomenada *backward*, el material és ejectat en el sentit contrari de la incidència del làser (d'aquí el nom). És a dir, la radiació làser travessa el substrat, avança a través de l'aire, i finalment penetra lleugerament la superfície líquida fins a ser absorbida. Una fracció de líquid és llavors ejectada cap endarrere, és a dir, cap al substrat. En l'altra configuració, anomenada *forward*, el líquid és ejectat en el mateix sentit que la incidència del làser. En aquest cas, la radiació làser travessa el líquid (ha de ser transparent a la radiació làser) fins a ser absorbida a una curta distància de la superfície lliure. Això provoca l'ejecció de material cap al substrat.

La configuració *backward* requereix que el substrat sigui transparent a la radiació làser. Cal pensar, però, que això no és un impediment per a moltes aplicacions de l'àmbit biomèdic, on es treballa amb substrats transparents. Utilitzant aquesta configuració, s'ha estudiat l'efecte que la distància de focalització entre la superfície lliure del líquid i el punt de focalització del làser té sobre el material dipositat per a una energia determinada. S'ha trobat que existeix un rang de distàncies en el qual es dipositen gotes circulars amb un contorn ben definit. Si el làser es focalitza massa a prop de la superfície lliure, apareixen gotes irregulars i amb satèl·lits. Si el làser es focalitza massa profundament, no es produeix ejecció de líquid. A les condicions òptimes de dipòsit, és possible dipositar grans arrays de gotes amb molta reproductibilitat. A més a més, s'han obtingut resolucions majors que les obtingudes convencionalment amb la LIFT.

La configuració *forward* no imposa cap restricció pel que fa a la transparència del substrat. Amb aquesta configuració es va estudiar l'efecte que l'energia de l'impuls làser té sobre el material dipositat. S'ha trobat que la relació entre volum de gota dipositat i energia de l'impuls segueix una relació lineal, amb una transició abrupta cap a volums grans a partir d'un cert valor de l'energia.

Finalment, i a les condicions òptimes de dipòsit, s'ha provat la viabilitat de la tècnica per al dipòsit de biomolècules. La preparació de diferents arrays d'IgG, així com d'àcid desoxiribonucleic (ADN) ha permès demostrat que les biomolècules, un cop dipositades, preserven la seva funcionalitat. Aquest fet, unit a la gran resolució que es pot obtenir, demostra que la nova tècnica és adequada per a la preparació de biosensors miniaturitzats.